UNIVERSITY OF BIRMINGHAM

PHYSICALLY AND NUMERICALLY MODELLING TURBULENT FLOW IN A PATCHY VEGETATED OPEN CHANNEL

by

OLATUNJI PETER FOLORUNSO

A thesis submitted to

The University of Birmingham

For the degree of

DOCTOR OF PHILOSOPHY

School of Civil Engineering

The University of Birmingham

2014

Abstract

Most open channels are not comprised of uniform boundary roughness but instead in any given cross section consist of different roughness with varying frictional surface resistance. Despite this, most physical modelling work has tended to assume uniform bed roughness in both the streamwise and lateral directions. However, open channels have been modelled assuming a difference in roughness between the bed and the walls of the channel. Whilst this is a reasonable starting point, the reality is much more complex with heterogeneous roughness elements (or roughness 'patches') regularly occurring on the bed of the channel. Given that the bed acts as a source of vorticity, a regular change in bed roughness causes varying levels of vorticity to be present at different cross-sections. The 'new' vorticity, which occurs as a result of changes in bed roughness, interacts with the existing flow structures leading to a complex flow field which can either result in the manifestation of lateral or vertical shear layers depending on the magnitude of the relative roughness distribution. This flow field has implications not only on the conveyance capacity of a channel but also on other parameters such as sediment transport.

This thesis presents results relating to a series of laboratory experiments investigating the velocity field in order to provide an understanding into the flow structures by describing the mechanisms and transport features of heterogeneous (patchy) flexible and rigid strip vegetation flow interaction with gravel roughness which could be used to understand sediment transport in the future. The experimental results were examined in a context of shear layer arising as a result of flexible and rigid vegetation patchy roughness distribution with gravel roughness. It is shown that relative to a gravel bed, the vegetated section of the channel generally resembles a free shear layer. The resistance within the vegetation porous layer reduces the velocity and creates a transition of high velocity flow across the interface at

the top of vegetation; of primary importance is the shear layer at the top of vegetation and roughness boundary regions which are shown to influence and dominate the overall momentum transport. These results have been used to calibrate a numerical model for the depth-averaged streamwise and boundary shear stress distribution using the Shiono and Knight Method (SKM). The model demonstrated approximately 90% accuracy in depth-averaged streamwise velocity distribution in comparison with the experimental data.

Dedicated to **TOLUWANIMI** and **TOBILOBA**

FOLORUNSO

Acknowledgement

My sincere appreciation goes to my supervisors Prof Mark Sterling and Prof John Bridgeman for given me the opportunity to carry out this research through their invaluable support, incredible encouragement and friendship. Thank you for the insightful guidance, feedback, comments and meetings. Completion of this thesis is only made possible with your abundant help.

I would like to thank Mr Mike Vanderstam for his support in setting up the experiments for this research.

I wish to appreciate the financial support provided by the Tertiary Education Trust Fund (TETFUND), Nigeria for this research programme.

Finally, I would like to thank my family and friends who have provided enduring supports and encouragement throughout the years from the start to the completion of this degree.

TABLE OF CONTENTS

LIST OF FIGURES

LIST OF TABLES

NOMENCLATURE AND BBREVATIONS

$A_{1,}\, A_2$	SKM Constant
ADV	Acoustic Doppler Velocimeter
CRS	Cross-section
$EXPT$	Experiment
FSL	Free shear layer
KH	Kelvin-Helmholtz
pdf	Probability density function
PIV	Particle Image Velocimeter
PST	Phase-Space Thresholding filtering method
QRS	Quadrant shear stress
RHS	Right hand side
RMS	Root mean square
SKM	Shiono-Knight Method
SNR	Signal to noise ratio
TKE	Turbulence Kinetic Energy
A	Channel cross-sectional area
A_b	Vegetated bed area
A_f	Vegetation stem frontal area
a_v	Frontal area per unit volume
B	Channels width
C_d	Drag coefficient
C_{int}	Integration constant

∂_e	Turbulence penetration scale
w	Vegetation stem width
d_0	Zero-plane displacement thickness
E	Turbulent energy dissipation
E	Modulus of elasticity
f	Friction factor
F_d	Drag force
F_r	Froude's Number
$\hat{f}$	Fourier transformation function
$f_x.f_y,f_z,$	Body forces
g	Acceleration due to gravity
G	Turbulence generation
H	Flow depth
h_p	Turbulence penetration depth
h_v	Vegetation height
I	Turbulence intensity
I_2	Second moment of area
J	Flexural rigidity
J	Hole size (Quadrant analysis)
k_s	Nikuradse roughness height
l	Mixing length
l	Length spacing
L	Channel length

L_u	Integral length Scale in streamwise direction
m	Width of the volumetric tank
n	Manning's roughness coefficient
n_v	Number of stem per bed area
p	Pressure
P	Wetted perimeter
P_s	Shear production
P_w	Wake production
Q	Discharge
q	Unit flow rate
r	Cross correlation of velocity components
R	Hydraulic Radius
R_e	Reynolds number
R_{uu}	Autocorrelation function in streamwise direction
S_o	Channel bed slope
S_w	Water surface slope
S_f	Friction slope
SK_u	Spectral function
t	Vegetation thickness
T	Time
T_u	Integral time scale in streamwise direction
T_t	Turbulent transport
T_p	Pressure transport

u	Instantaneous streamwise velocity
u'	Streamwise turbulent fluctuation
U	Mean streamwise velocity
U_*	Shear velocity
U_b	Bulk mean velocity
v	Instantaneous lateral velocity
v'	Lateral turbulent fluctuation
V	Mean lateral velocity
v	Kinematic viscosity
w	Instantaneous vertical velocity
w'	Vertical turbulent fluctuation
W	Mean vertical velocity
x	Streamwise direction
y	Lateral direction
z	Vertical direction
z^+	Normalisation of z
z_0	Log-law roughness height
ρ	Fluid density
τ	Shear stress
τ_b	Boundary shear stress
ɳ	Shape of cross-sectional geometry
μ	Dynamic viscosity
∇	Differential operator
Ω	Vorticity

β	Vegetation shape factor
σ	Standard deviation
Γ	SKM secondary flow function
λ	SKM dimensionless viscosity parameter

1 Introduction, Aims and Objectives

1.1 Introduction

Bed roughness is typical of natural rivers; its variability is an important characteristic in open channel flow as this affects the hydrodynamic behaviour of flow. Modelling this behaviour is important in the evaluation of flow characteristics in open channels for meaningful hydraulic predictions and flood management such as conveyance capacity, mass and momentum transfer for effective design of river engineering infrastructures, provision of flood warnings and the protection of biodiversity. Transport characteristics of natural rivers have been shown to be dependent on the bed roughness (Shafi et al., 1997) and by extension provides potential for the exchange of resources between ecological habitats in aquatic environment. Rahman and Webster (2005) have demonstrated that bed surfaces with the similar roughness function may possess different turbulent characteristics as the type and distribution of bed roughness uniquely influence the velocity field.

Uniform roughness is seldom formed in natural rivers, more often, roughness are form in patches, although the effect of individual roughness on the flow can be relatively varied and local, patches are capable of generating significant disturbance to the flow (Jesson et al., 2013). A high level of patchiness (variation in local bed roughness) in rivers is associated with the alteration of flow because of the difference in flow velocities. The velocity profile can become distorted with shear being created at the interface between roughness elements, leading to additional sources of turbulence. Stetzner (1994) demonstrated that in fluvial systems, flow pattern and morphology are factors responsible and control the formation of patchiness. Even when the roughness seems to be fairly uniform, the flow pattern may create considerable spatial variability of the roughness elements. The research outlined in this thesis extends the work of Jesson et al. (2013) by considering the effect that idealized vegetation can exert on the main flow characteristics in a heterogeneous channel. In this case the

hydraulic interaction between gravel and vegetated bed on mean and turbulent flow characteristics is investigated.

Vegetation on the other hand can grow and proliferate in a fluvial environment, whilst the presence of vegetation can cause obstructions to the flow by redistributing velocity fields due to vegetation drag and consequently alter the transport process which is crucial for both ecology and fluvial system. For example, vegetation alters the open channel flows, causing local deposition of sediment (Shiono et al., 2012, Tsujimoto, 1999; Wu et al., 2005). However, vegetation is important for maintaining the quality of river ecology through restoration. Recently, river restoration, i.e. using aquatic vegetation to enhance river ecology, has been applauded (Shiono et al., 2012, Shiono et al., 2009, Velasco, 2003, Ghisalberti, 2006) to maintain the balance of the river ecosystem. Vegetation is no longer regarded as a mere impediment to flow velocity, but rather as a means of providing river restoration, removal of nutrients and producing oxygen in water, stabilization of channels and landscapes for recreational use (Lopez and Garcia, 1998). Vegetation stabilizes sediments by reducing erosion along the channel and in general plays significant roles in providing and maintaining a balance, integrated habitat for other aquatic organisms for ecological management of channels. Hence a trade-off is necessary in minimizing flow resistance to reduce the risk of flooding due to vegetation and river restoration.

Due to the involvement of different roughness elements, the problem of heterogeneous roughness in river flow is complex and requires multiple approaches to be understood quantitatively. However, until recently, only one particular case was investigated using patchiness of smooth and gravel roughness (Jesson. et al., 2012; Jesson et al., 2013; Vermaas et al., 2007; Vermaas et al., 2011). The understanding of this approach is dictated also by the increased demands using vegetation in a restoration context and its consequence for the

fluvial systems. Hence, there is a lack of knowledge on the transport processes and shearing mechanisms in a patchy vegetated heterogeneous flow.

1.2 Aims and Objectives

The overall aim of the current research is to evaluate how the dynamics of the flow field change when heterogeneous roughness involving vegetation is present. Related to this, the research has the following objectives:

i. To investigate the influence that rigid vegetation (akin to 'shrubs') and flexible vegetation (akin to 'grass') have on turbulence generation within an idealised open channel with a patchy roughness distribution.
ii. To evaluate the channel's resistance through calculation of traditional resistance parameters (e.g. Manning's roughness coefficient n and Darcy-Weisbach friction factor f in order to assess the conveyance capacity of the channel).
iii. Detailed high frequency 3-dimensional velocity measurement over three cross-sections of the channel using the Acoustic Doppler Velocimetry (ADV) in order to understand the mean and turbulence characteristics of the flow properties.
iv. To determine the variability of momentum transport and mechanisms responsible due to changes in roughness characteristics.
v. To map the flow field with Particle Image Velocimetry (PIV) to determine the 2-dimensional spatial correlations of the flow variables.
vi. To investigate the applicability of a numerical model (SKM) to reproduce the depth-averaged streamwise velocity and the boundary shear stress.

By providing a description of the patchy vegetated open channel flow through the set objectives and its consequence for flow structure and the transport processes, the study therefore will represents a valid contribution to the theory of patchy vegetated flow and

development of the contemporary fluvial ecology. The developments from the research set the ground for quantitative assessment of local regions of turbulence production and efficient momentum transport in natural rivers with similar patches of roughness for river management.

The thesis is composed of seven chapters. Chapter 1 provides an introduction, aims and objectives of the study, whilst in Chapter 2 the literature review and background to the study are provided. In Chapter 3, the experimental methods, instrumentation and data processing are presented together with extended description of the overall resistance of the channel. Chapter 4 presents the results of the laboratory measurements by describing the mean velocity and turbulence characterisitics of the flow over three cross-sections. Chapter 5 contains the analysis relating to the turbulence flow structures, boundary shear stress and the results for PIV measurement of the flow. Chapter 6 presents the application of the Shiono and Knight Method (SKM) to the experimental data to predict the depth-averaged streamwise velocity and boundary shear stress. Finally, Chapter 7 provides a short discussion of the study and illustrates main conclusions drawn from the research work.

2 Research Background and Literature Review

2.1 Introduction

This chapter provides a general overview of the scientific literature which is appropriate to the work presented in this thesis. The chapter starts with a discussion relating to open channel flow and basic resistance equations in section 2.2. Turbulent flow principles, governing equations and secondary flows are discussed in sections 2.3 to 2.7. Sections 2.8 to 2.9 outline the flow structures in vegetated canopies, and by extension presents the current state of related research in order to show the concepts which the current thesis builds on. The application of Shiono and Knight Method (SKM) are presented and described in detail in section 2.10.

Throughout the thesis, an orthogonal coordinate system is adopted as illustrated in Figure 1. The streamwise direction (x) is in the primary flow direction and perpendicular to the lateral (y) and vertical (z) directions. The corresponding time average velocity components are U, V, W in the x, y and z directions respectively with the associated fluctuating velocity components defined as u', v', w' respectively.

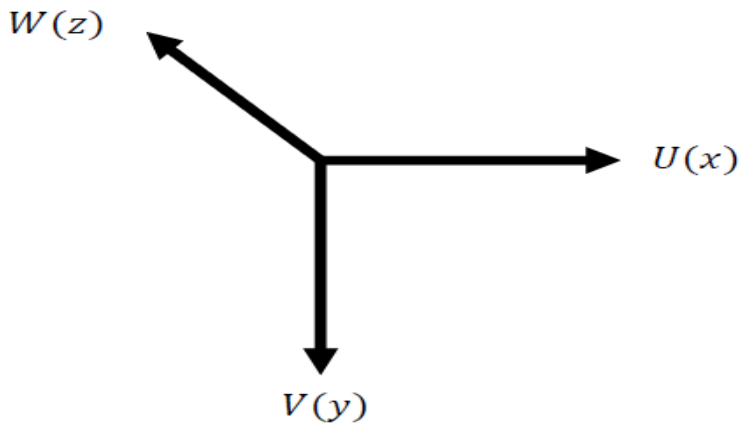

Figure 1: Orthogonal Coordinate System for the Experiment

2.2 Flows in Open Channels

An open channel can be described as a conveyance system in which water flows with a free surface. The term is generally applied to natural and artificial watercourses, ditches and canals, etc.

One of the fundamental features of open channel flow is the variability in the bed roughness. The composition of the river roughness can vary with both elevation and position along the channel. Consequently it is difficult to accurately analyse and obtain satisfactory results for flows in natural channels. Open channel flow characteristic can be altered by the presence of boundary roughness; turbulent flows and the associated transport process are actively influenced by the nature of the boundary roughness elements, these elements in a natural channel include; sand, gravel, aquatic vegetation, etc., with varying morphological forms such as density, shape and heterogeneity from channel reach to reach. One of the effects of boundary roughness is the reduction of the conveyance capacity of the channel due to the presence of resistance.

Whilst the principles discussed in this section are valid for all open channel conveyance system, the primary consideration in this research is to investigate experimentally and numerically, flow characteristics of an idealized heterogeneous channel under uniform steady state condition. Hence, the experimental work is undertaken in a straight channel with a uniform and constant bed slope S_0 and rectangular cross section (Figure 2). All experiments correspond to steady flow such that:

$$\frac{\partial u}{\partial x} + \frac{\partial v}{\partial y} + \frac{\partial w}{\partial z} = 0 \tag{1}$$

where u, v and w are velocities in streamwise, lateral and vertical directions.

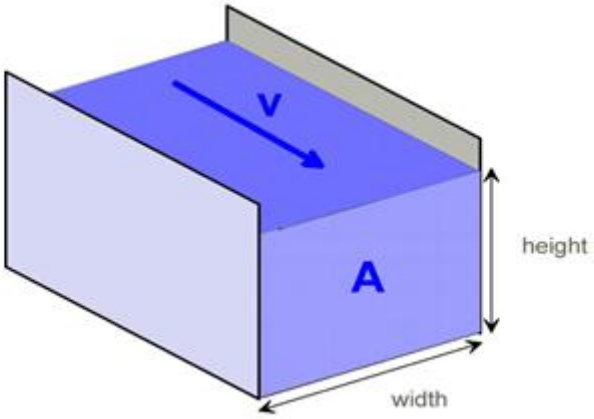

Figure 2: Straight and Rectangular Open Channel Flow

Under uniform flow condition, water depth corresponds to the normal depth. The normal depth depends on the discharge and allows constant depth along the channel for a given discharge. For normal depth, the water surface slope (S_w) is parallel to the bed slope and therefore measurements of S_0 can be used as surrogate for S_w, i.e.

$$S_0 = S_w \tag{2}$$

Applying Newton's second law to the flow, the gravitational forces are balanced by the frictional force acting between the water and the channel bed and the boundary shear stress, the mean boundary shear stress acting on the channel bed τ_b under uniform flow condition may therefore be shown as:

$$\tau_b = \rho g R S_0 \tag{3}$$

where ρ is the water density, g is the acceleration due to gravity, R is the channel hydraulic radius.

The overall boundary shear is often directly associated with the roughness elements and quantifying the effect of these on the flow has been a goal of researchers (Shiono and Knight, 1991; Shiono, 2009; Yen, 2002). Nikudrase (1933) introduced the idea of a roughness

coefficient k_s from artificially roughened pipes, where k_s represents the physical value of grains of sand used to roughened the pipes. Nikudrase (1933) assumed the coefficient k_s to provide a direct relationship between the size of roughness elements and their representation in numerical models. In open channel flow, a direct relationship between the sizes of roughness elements may not hold due to the presence of different forms of roughness elements which may vary both with depth and other parameters. A number of numerical models have been developed to model this large scale effects of bed roughness (resistance) on the flow in order to evaluate the effect of physical features of the boundary roughness elements on flow (Morvan et al., 2008; Rouse, 1965; Shiono and Knight, 1988; Yen, 2002; Carollo et al., 2005). Open channel flow resistance influences channel conveyance capacity and turbulence processes, therefore, accurate quantification and estimation of channel flow resistance are important to predict the conveyance capacity in channels as mitigation against the likelihood of channel flooding. Morvan et al. (2002), and Rouse (1965) classified flow resistance into four components: surface or skin friction, form resistance or drag, wave resistance from free surface distortion, and resistance associated with local acceleration or mean velocity. By using the Darcy Weisbach coefficient f, Rouse (1965) expressed resistance as a function of the following dimensionless symbols (Yen, 2002):

$$f = F'(R_e, K, \eta, N, F_r, U) \tag{4}$$

where R_e = Reynolds number; K= relative roughness, usually express as k_s/R, where k_s is the equivalent roughness height and R is the hydraulic radius of the flow; η is the shape of the cross sectional geometry; N is the nonuniformity of the channel roughness; Fr is the Froude's number; U is the mean velocity and F' represents a function. The symbolic relationship of Equation (4) can be applied to the Manning resistance coefficient n or to any flow resistance parameter (Yen, 2002).

The most well-known example of one dimensional model to quantify resistance in open channel is Manning's equation:

$$U = \frac{1}{n} R^{2/3} {S_f}^{1/2} \tag{5}$$

where the resistance is represented by Manning's n and S_f is the friction slope. Manning's equation will be used in section 3.3 as a theoretical model to calculate the stage-discharge curves for comparison with the experimental data. For Manning's and other one dimensional (1-dimensional) models, the roughness for the whole channel is not explicitly stated but are represented by a single parameter whose value taken as a measure for the overall resistance. Similarly a friction factor f may be used to represent resistance coefficient.

In additional to open channel resistance from boundary elements, secondary flow and shear layers are another features that affect turbulence processes in open channel flow. The secondary flow due to turbulence heterogeneity contributes to the lateral momentum transfer within the flow, while the shear layer produces interfacial vortices due to velocity difference. Shear layers also contribute to turbulent momentum transfer. Shear turbulence is comparable to the turbulence created near the channel bed. These complex mean and turbulence transfer mechanisms affect the overall flow, making understanding their effect on conveyance capacity important. Figure 3 illustrates the secondary flow in a compound open channel flow (Shiono and Knight, 1991).

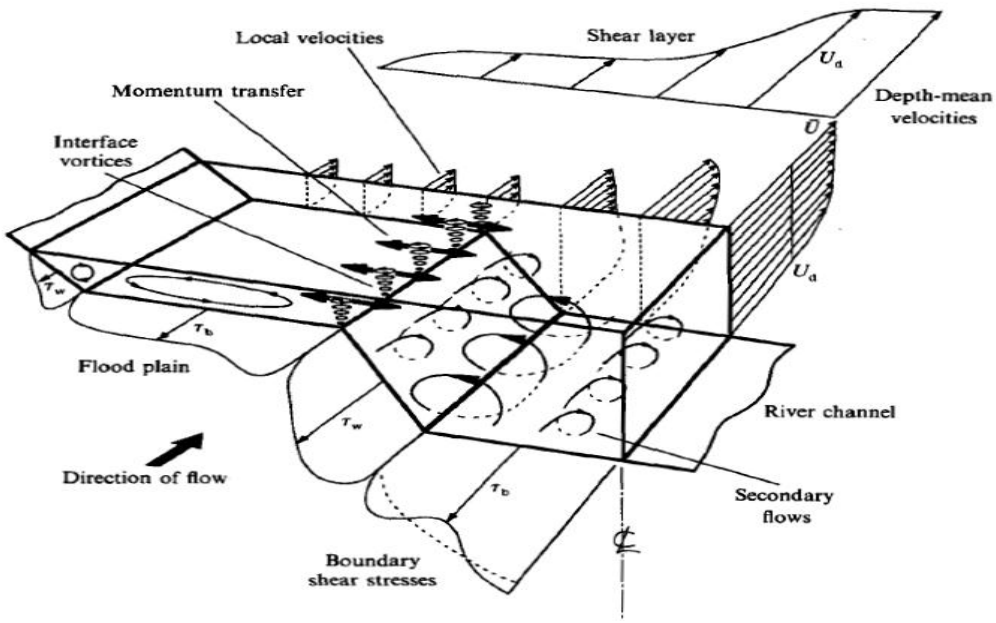

Figure 3: An illustration of secondary flows and turbulent shear stress (Shiono and Knight, 1991)

Another important non-dimensional quantity to analyse flow in open channel is the Froude number in Equation (6). It defines the ratio of the inertial to gravitational forces in order to determine the behaviour of the flow in response to the relative dominance of the internal forces. The Froude number is used to classify flow subcritical ($Fr < 1$) and supercritical flows ($Fr < 1$).

$$Fr = \frac{U}{\sqrt{gL}} \tag{6}$$

where U is the mean velocity, g is the acceleration due to gravity, and L is an appropriate length scale (e.g., the depth of flow).

2.3 Turbulent Flows

Reynolds (1901) examined series of experiments on pipe flow and observed the existence of three types of flow - laminar, transitional and turbulent flow. In laminar flow, fluid particles travels in parallel streamline layers, while in turbulence, the flow is characterised with a

random velocity fluctuation and irregularities (Figure 4). Transitional flow is laminar flow in which intermittent bursts of turbulent flow appear, whose energy is dissipated by viscous forces before the turbulence can develop. In order to characterize the nature of the turbulent flow, the Reynolds number in Equation (7) was developed for pipe flow (Reynolds, 1901). The Reynolds number is a non-dimensional quantity that can be used to characterize the flow and is defined as follows:

$$R_e = \frac{Ud}{v} \tag{7}$$

where d is the pipe diameter and v is the kinematic viscosity of the fluid. Calculating the Reynolds number for a range of pipe flows, Reynolds made classification for $Re < 2000$ as laminar and $Re > 4000$ as turbulent, and ranges in between the flow as transitional (Reynolds, 1901).

The Reynolds number can be calculated for open channels using an appropriate length scale, i.e. the pipe diameter in Equation (7) can be replaced with the channel hydraulic radius R, to give Equation (8):

$$R_e = \frac{4UR}{v} \tag{8}$$

It can be seen from Equation (7) and (8) that $d = 4R$, thus, turbulent flows in open channel are classified based on the Reynolds number in Equation (8) as: flows with $Re < 500$ are classified as laminar, and flows with $Re > 1000$ are considered fully turbulent, however, $Re > 2000$ are usually taken as the upper limit for fully turbulent flow in open channel flow (Chawick et al., 2004). The flows in between the upper and lower limits are considered transitional. Turbulence is due to the inertia of a fluid as a whole, for turbulence to be generated and maintained, inertial forces must exceed the viscous forces, while flows whose inertial effects tend to be small are laminar. Reynolds suggested that the instability that

initiates turbulence and perturbation of a certain magnitude for a given value of Re controls the transition between laminar and turbulent flow.

Turbulence has been described in many ways and being particularly important to the current research, an in-depth discussion of the subject is necessary. The important point is that fluid motion is always inherently unstable and that incipient instabilities in the flow dominate the viscous dissipation, i.e. when viscosity is small, all flows develop a random, chaotic component of motion in both space and time, and exhibit a wide and continuous distribution of length and time scales (Davidson, 2004). Some of the characteristics use to describe turbulence includes (Tennekes and Lumley, 1972; Davidson, 2004):

- Three dimensional fluctuations: turbulence is irregular, random and chaotic. Turbulence is rotational and three dimensional. The random vorticity fluctuations that characterize turbulence are maintained by the process of vortex stretching.
- Continuity: Turbulence is a continuous phenomenon with production and dissipation processes, governed by the equations of fluid mechanics. Even the smallest scales occurring in a turbulent flow are larger than any molecular length scale.
- Diffusion: Turbulence enhances rapid mixing and increased rates of momentum, heat and mass transfer.
- Dissipation: Turbulence energy dissipates through viscosity. Thus, turbulence requires energy in order to maintain its form.
- Turbulence is a manifestation of fluid flows. Most of the dynamics of turbulence are the same in all fluids, whether they are liquids or gases, depending on the Reynolds number.

Turbulent motion is the natural state of most fluids (Davidson, 2004), the implication is that majority of the fluvial flows are mostly turbulent. In fluvial flow, the disturbances associated

with changes in the fluid streamlines due to presence of natural features make such flow more complex with the existence turbulence.

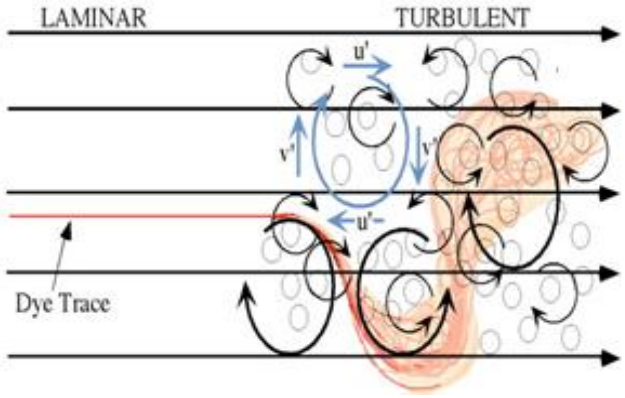

Figure 4: Nature of Laminar and Turbulent Flow (Haywood, 1996)

2.3.1 Turbulence Theory

Fluctuating velocity consists of a random collection of eddies (vortices), the largest of these eddies have a size comparable with the characteristic geometry length scale of the mean flow, however most of these eddies are much smaller depending on the Reynolds number of the turbulence (Davidson, 2004). In turbulent flow, there exists a broad spectrum of eddy sizes with different scales and velocity field within a fully developed turbulent flow. Large-scale turbulent eddies exists with a large Reynolds number, the largest eddies which are created by instabilities in the mean flow are themselves subjects to inertial instabilities and rapidly break up into smaller eddies. The smaller eddies are themselves unstable and they in turn pass their energy on to even smaller structures and so on. Thus, there is a continual cascade of energy from the large scale down to the small with the discontinuity of the cascade when the eddy size becomes so small that cannot be transferred (Davidson, 2004). At this point the viscous forces become significant and the energy is dissipated. Therefore in turbulent flow, large scale eddies are continually created by the mean flow, then breaking up through instabilities into smaller structures with the turbulence energy destroyed when the eddy sizes are so small

for transfer. The turbulent eddy sizes can be described with turbulent length and time scale respectively. The length scale corresponds to the length of fluctuating eddy motions that exists within a turbulent flow. The largest scale is commonly referred to as integral length scale and the smallest scale known as Kolmogorov length scale.

2.3.2 Mean Flow and Turbulence Interaction

The mean flow and turbulence interacts through Reynolds stresses (a full discussion on Reynolds stresses are given in section 2.4.1). Reynolds stresses act as a mechanism for transferring energy from the mean flow into the turbulence. In shear flows however, there is a continual interaction between the turbulence and the mean flow. The mean flow generates, maintains and redistributes the turbulence. Reynolds stresses are created by turbulence and acts on the mean flow, shaping its development and maintaining the turbulent fluctuations as it transfers energy from the mean flow into turbulence. Due to shear, turbulent energy is generated through stretching of vortices by the mean flow, because vortices are aligned in the direction of maximum stretching during shear by the velocity field. This is dictated by the instantaneous velocity field distribution with the vortices evolving and diffusing in the regions where large gradients of velocity (shear) develops. As the vortices are stretched by the mean flow the associated kinetic energy intensify the rotation of the vortices thereby transferring energy from the mean flow into turbulence.

With reference to threshold values of Reynolds number in Equation (8) for turbulent flow in open channels, most of the flows encountered by hydraulic engineers in real situation exhibits turbulence (Reynolds, 1901). Due to disturbances to the mean flow by natural features in open channels, the flow streamlines are broken down into irregularly shaped eddies which cause instability and uneven fluctuations in velocity with time inducing turbulent motion and transport effect known as the Reynolds stresses. These effects are represented in the Reynolds averaged form of Navier Stoke (RANS) decomposition equations (section 2.4.1).

2.3.3 Coherent Structures

Another important feature of turbulence focuses on the existence of coherent structures. This term is used to describe turbulent structures which are organised, in the sense they retain their identity for many eddy generation times and which occur repeatedly in more or less the same form. Nezu and Nakagawa (1993) suggested that coherent structures in open channel turbulence consist of two types, bursting phenomena and large-scale vortical structures and they suggested that both phenomena have different characteristics and location of occurrences. Most relevant to the current work is the busting phenomena because it occurs near the bed and composed of cyclic processes of ejections and sweeps structures (Figure 5). Both ejections and sweeps are transfer mechanisms defined as transporting from the channel bed low velocity fluids with a substantial portion of the fluid ejected into the outer flow, and subsequently, a high velocity fluid approaching the wall and sweeps away the low velocity fluid from the ejection process. Previous research (Yalin, 1972) noted that the busting eddies generated near bed are initially smaller, and then grow until their size becomes equal to flow depth and eventually destroyed. However, some research (Shvidchenkoa and Pender, 2001) noted that only large scale eddies exist within turbulent motions and they give rise to busting phenomena. Hence, while there is an agreement among researchers regarding an existence and general pattern of busting phenomenon, opinion differs about the generation and motion of large scale eddies in open channels. The involvement of complex coherent structures in turbulent open channel flows has generated different views by researchers (Yalin, 1972; Shvidchenkoa and Pender, 2001; Nezu and Nakagawa, 1993; Davidson, 2004, Nezu and Rodi, 1986).

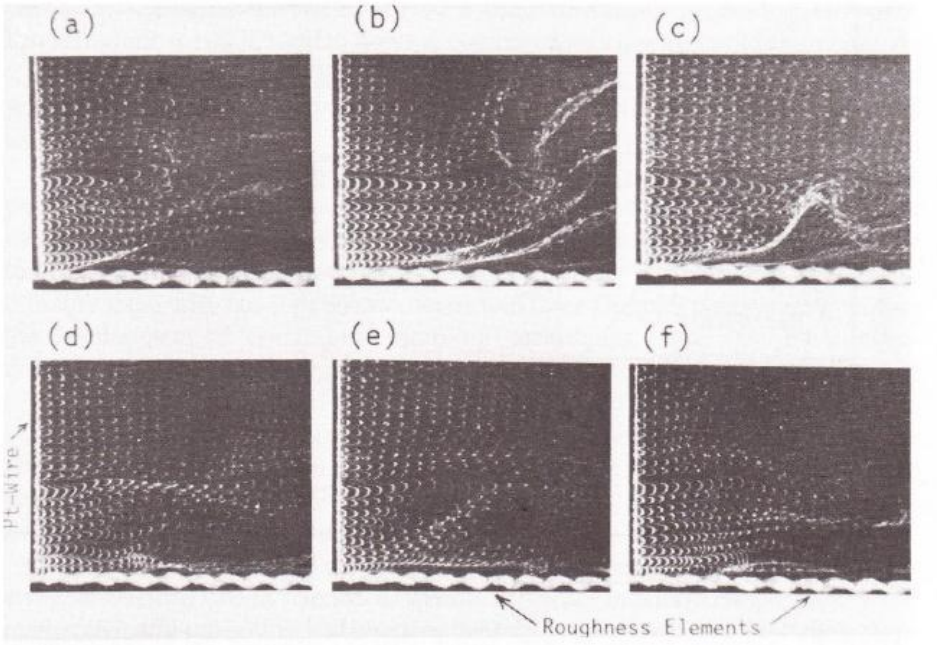

Figure 5: Photographic images of ejection motions, a), b) and c); and sweep motions, d), e) and f) in rough open-channel flows (from (Nezu and Nakagawa, 1993), citing (Reynolds, 1901)).

2.4 Navier-Stokes Equations

The Navier-Stokes equations are set of coupled differential equations which consist of a time-dependent continuity equation for conservation of mass, three time-dependent conservation of momentum equations used to describe the motion of water by the system of differential equations. The Navier-Stokes equations describe how the velocity, pressure, temperature and density of a moving fluid are related. Considering the velocity field equations under mass continuity and momentum conservation equations, the Navier-Stokes equations for incompressible and Newtonian fluids can be written for x-component as (Hinze, 1975):

$$\frac{\partial(\rho u)}{\partial t} + \frac{\partial(\rho u^2)}{\partial x} + \frac{\partial(\rho uv)}{\partial y} + \frac{\partial(\rho uw)}{\partial z} = -\frac{1}{\rho}\frac{\partial P}{\partial x} + \rho f_x + \mu\left(\frac{\partial^2 u}{\partial x^2} + \frac{\partial^2 u}{\partial y^2} + \frac{\partial^2 u}{\partial z^2}\right) \quad (9)$$

where ρ is fluid density, u, v, w are instantaneous velocities in x, y, z directions, t is time, $f_x . f_y, f_z,$ are body forces, μ is the dynamic viscosity.

The continuity equation for incompressible flow is given as (Anderson, 1995):

$$\frac{\partial u}{\partial x} + \frac{\partial v}{\partial y} + \frac{\partial w}{\partial z} = 0 \quad (10)$$

Equation (9) satisfies the momentum equation and Equation (10) represents the mass continuity. These equations are complex and even for the simplest flows analytical solutions are rare (Anderson, 1995). However, they can be solved numerically and they are useful as fundamental basis for modelling three dimensional turbulent flows

2.4.1 Reynolds Averaged Navier-Stokes (RANS) Equation in the x-direction

Considering the velocity to be statistically stationary, the instantaneous velocity can be decomposed into sum of the time averaged and fluctuating components. The velocity fluctuating components act to efficiently transport momentum. The RANS equations are derived by substituting the instantaneous velocities in Navier-Stokes equations by their mean and fluctuating components:

$$u = U + u' \quad (11)$$

where u' represents the fluctuating components (Reynolds, 1895) and taking a time averaged for the x-component: Equation (12):

$$U\frac{\partial U}{\partial x} + V\frac{\partial U}{\partial y} + W\frac{\partial U}{\partial z} = -\frac{1}{\rho}\frac{\partial \bar{P}}{\partial x} + \mu\left(\frac{\partial^2 u}{\partial x^2} + \frac{\partial^2 u}{\partial y^2} + \frac{\partial^2 u}{\partial z^2}\right) - \left(\frac{\partial \overline{u'^2}}{\partial x} + \frac{\partial \overline{u'v'}}{\partial y} + \frac{\partial \overline{u'w'}}{\partial z}\right) \quad (12)$$

(corresponding equations also exist for the lateral and vertical directions). Equation (12) is referred to as Reynolds Averaged Navier-Stokes equations (RANS). The RANS equations are primarily used to describe turbulent flows using the Reynolds shear stresses which are one of the important terms in turbulence modelling; these terms represent the effect of velocity fluctuations or turbulence on the mean flow. These are the bracketed parts of the third terms of the RHS of Equation (12) as the normal, lateral and vertical Reynolds shear stresses. Turbulence can be said to have an effect equivalent to the Reynolds shear stresses in

Equation (12), and are indicators of turbulence transport. However, Reynolds stresses represent the loss of mechanical energy by the main flow due to its interaction with turbulence (Davidson, 2004).

2.5 Statistical Description of Turbulence

The random and unpredictable nature of turbulence requires the description of its motion through statistical measures because the instantaneous motions of turbulence are complicated to understand due to unexpected changes. A statistical description of turbulence involves a time average for stationary flows over multiple realizations to determine the mean occurrence. The velocity will typically be described as a time averaged value denoted by:

$$U = \frac{1}{T} \int_0^T u dt \tag{13}$$

where T is a time longer than the longest turbulent fluctuations in the flow. Example of time series record is shown in Figure (6).

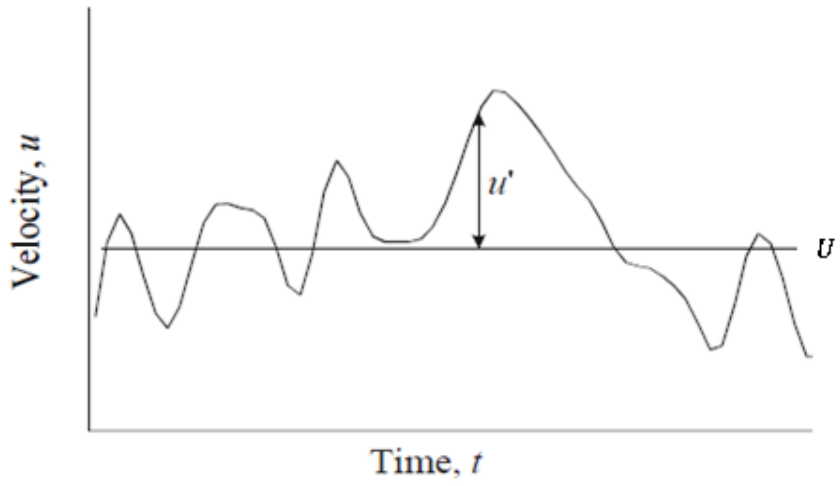

Figure 6 : Schematic Example of Turbulence Time Series Record

2.5.1 Probability density functions and moments

A turbulent variable u at a given point and time can be described by the probability density function (PDF) $P(u)$:

$$\int_{-\infty}^{+\infty} P(u)du = 1 \tag{14}$$

Using the preliminary data in the current research, an example of a pdf distribution for the three velocity components is shown in Figure 7. This is particularly important because, in the statistical theory of turbulence, the probability density function provides a complete probabilistic description that permits the estimation and quantification of turbulent flow variables, for example, the tails of the pdf for flow variables have been reported to be influenced by the scale of eddy motions (Chu et al., 1996). However, to characterize more complex turbulent quantities, such as fluctating velocities, higher order moments are required (Raupach, 1996).

2.5.2 Skweness and Kurtosis

The skewness provides information about the asymmetry of the PDF given as:

$$Skewness\ (\mu_3) = \frac{E(u-U)^3}{(E[(u-U)^2])^{3/2}} \tag{15}$$

Where E is the expectation operator.

For a value of zero skewness, the PDF is symmetric about the mean U, whilst positive and negative skewness gives an indication of a longer tail towards right or left respectively presumably due to momentum transfer in turbulence measurement. The kurtosis characterises the flatness of a PDF and is given by the expression:

$$kurtosis\ (\mu_4) = \frac{E(u-U)^4}{(E[(u-U)^2])^2} \tag{16}$$

A time series with measurements clustered around the mean has low kurtosis and a time series by intermittent extreme events are characterised with high kurtosis.

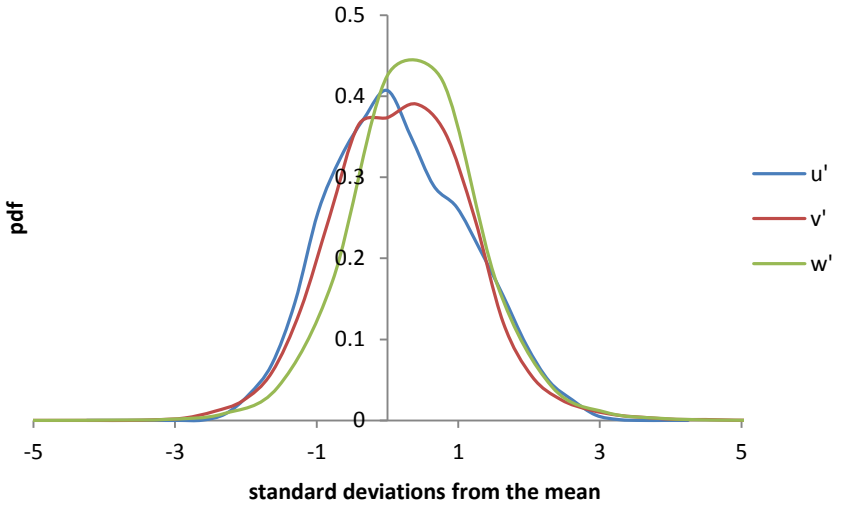

Figure 7: Example of normal distribution of velocity components (preliminary experimental data)

2.5.3 Joint Probability Density Function

Turbulence involves not one, but several random variables dependent on each other for momentum transfer. Therefore it is necessary to define its joint probability density functions (JPDF). For two random flow variables u and w, a joint cumulative probability distribution function $f^*(u,w)$ referred to as the co-variance with a direct physical representation as shown in Equation (17) as:

$$\overline{u'w'} = \iint_{-\infty}^{\infty}(u - U)(w - W)f^*(u,w)dudw \qquad (17)$$

2.5.4 Autocorrelation

The autocorrelation of a random process describes the correlation between values of the process at different points in time, as a function of the two times or of the time difference. It shows the correlation between the consecutive values of the time series. As a time resolved

characteristics for the velocity components, it plays a major role in the analysis of the flow structures and especially for determining temporal and spatial flow scales. It can be computed by shifting the velocity records by a time delay $\tau = \Delta t$ equal to a multiple of the measurement interval, for each time delay, the autocorrelation can be obtained as:

$$R_{uu}(\tau = \Delta t) = \frac{\int_0^T u\prime_{(t)} u\prime_{(t+\Delta t)} dt}{\int_0^T u\prime^2_{(t)} dt} \quad (18)$$

where R_{uu} is the autocorrelation function, u' is the fluctuating part of the velocity, and τ is an increment of time delay (McConville, 2008). An example of the auto-correlation functions for the velocity distributions in Figure 7 are shown in Figure 8. The figure illustrates rapid decay of the velocity components with time, it can be deduced from the figure that more organised structures are observed in the streamwise x velocity component, this may be related to the large scale eddies associated with the streamwise velocity.

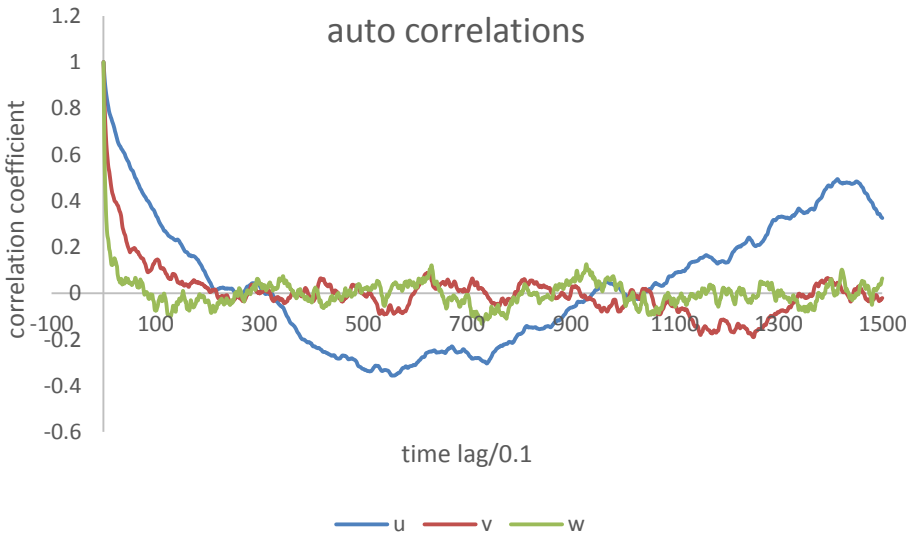

Figure 8: Example of autocorrelation functions (preliminary experimental data)

From the autocorrelation functions, the integral time scale (T_u) can be obtained by evaluating the area under the autocorrelation function which is normally stop when the function crosses the x-axis. Integrating numerically the autocorrelation function in Equation (18) to give integral time scale for streamwise velocity component as shown in Equation (19):

$$T_u \;\; = \int_0^T R_{uu}(t)dt \tag{19}$$

T_u yields a physical interpretation for turbulence, i.e., it is an indication of the average temporal scale of turbulent eddies (Lacey and Roy, 2008). Similarly, an integral length scale is an important parameter in characterizing the structure of turbulence. It measures the longest correlation distance between the flow velocities at two points in the flow field (Hinze, 1975). This can be obtained from Equation (20) as:

$$L_u = \; U \, T_u \tag{20}$$

Cross-correlation is a standard method of estimating the degree to which two series of velocity components are correlated. This gives an indication of how the correlated components can efficiently transfer momentum and other transport parameters.

Considering two series $u'(i)$ and $w'(i)$ where $i = 0,1,2 \ldots . N-1$ the cross correlation r at delay τ is defined as:

$$r = \frac{\Sigma_i \left[(u\prime(i))*(w\prime(i-\tau))\right]}{\sqrt{\Sigma_i \, (u\prime(i))^2} \sqrt{\Sigma_i \, (w\prime(i-\tau))^2}} \tag{21}$$

Figure 9 illustrates examples cross-correlations of the velocity components from the preliminary data of this research.

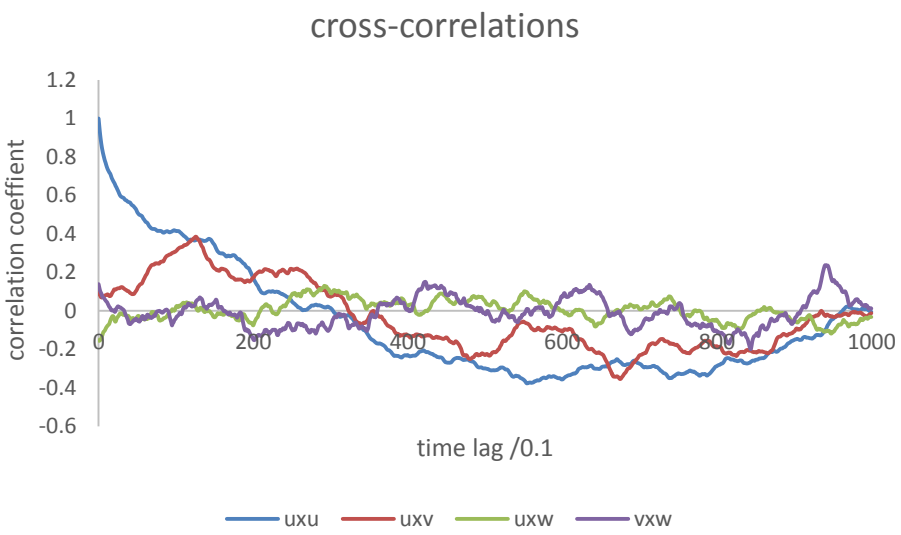

Figure 9: Example of cross correlation functions (preliminary experimental data)

2.5.5 Power Spectral Density

The power spectral density provides information on the frequency distribution of the turbulent kinetic energy per unit mass of the various fluctuating velocity component over the length scale. It permits interpretation in the frequency domain rather than the time domain. This is achieved through the decomposition of the original signal into the frequency domain, by the representation of the original signal in terms of cosine and sine functions using Fourier analysis technique. This process determines the amplitudes and phase of a time varying process, as a function of frequency. The spectrum of a continuous time signal may be calculated using the Fourier transform of a function, $f(x)$, and defined by the following integration (Davidson, 2004):

$$\hat{f}(x) = \frac{1}{\sqrt{2\pi}} \int_{-\infty}^{\infty} f(x) e^{-i\omega x} dx \tag{22}$$

where the transform is denoted by $\hat{f}(x)$, f is frequency and the angular frequency (ω) is equal to $2\pi f$. A stationary random process can be approximated by this series, as illustrated in Figure 10.

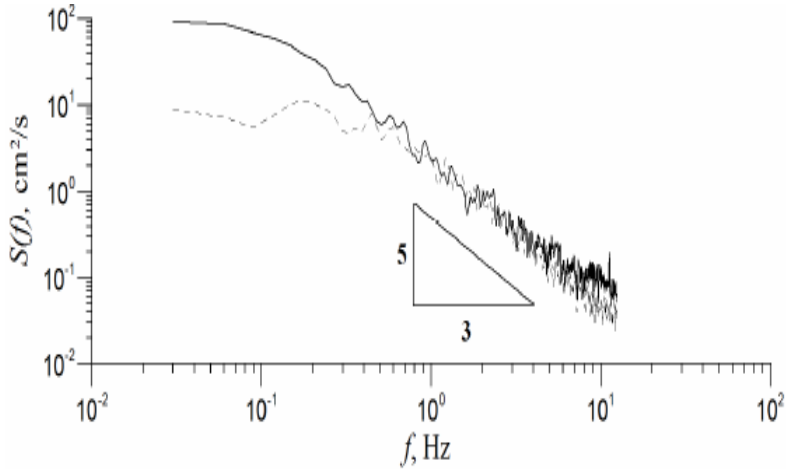

Figure 10: Power spectral density functions showing Komolgoroff's $^{-5}/_{3}$ spectral gradients (Voulgaris and Trowbridge, 1998).

2.5.6 Turbulent Intensity and Kinetic Energy

The magnitude of turbulence can be quantified using the turbulence intensity, i.e,

$$I_x, I_y, and\ I_z\ = \frac{\sigma_x}{U}, \frac{\sigma_y}{U}, and\ \frac{\sigma_z}{U} \tag{23}$$

where σ is the standard deviation of the velocity fluctuation. Experimental observations in open channel flows have shown that the turbulence intensity will be greater near the channel boundary where turbulence is being generated, and decrease with depth away from the boundary towards the free surface (Carollo et al., 2005).

2.6 Boundary Layers

Open channel flows are two-dimensional and are commonly shallow $\left({}^{H}/_{h} \leq 5\right)$ where H is the flow depth and h the roughness height, therefore the effects of the boundary layer and by extension vegetation may extend the flow depth (Shiono and Knight, 1991; Nezu and Nakagawa, 1993; Lane et al., 2012). The effects of the boundary layer represents a no-slip channel condition exerting friction on the flow in which the fluid will have zero velocity relative to the underlying boundary. This generates turbulent structures within the flow

through flow disturbances and subsequently momentum loss. It is an important structure in the idea of velocity profiles and turbulence generation. In fully developed turbulent flow, the boundary layer has composite layers consisting of an inner and outer region (Figure 11).

The inner region typically tends to be smaller than the outer region and is controlled by variables such as the kinematic viscosity, bed roughness and frictional velocity. The mean primary velocity distribution can often be explained by Prandtl's law. This region is classified into the viscous and turbulent sub-regions as illustrated in Figure 11. The viscous sub-region consists of a thin layer with a thickness between 5-15% of the whole boundary layer thickness where viscous force is dominant and the velocity is constant and scales the boundary friction with the mean velocity distribution given as:

$$\frac{U}{U_*} = \frac{U_* z}{v} = z^+ \tag{24}$$

where z is the vertical distance from the channel roughness surface, U_* is the friction velocity, v is the kinematic viscosity.

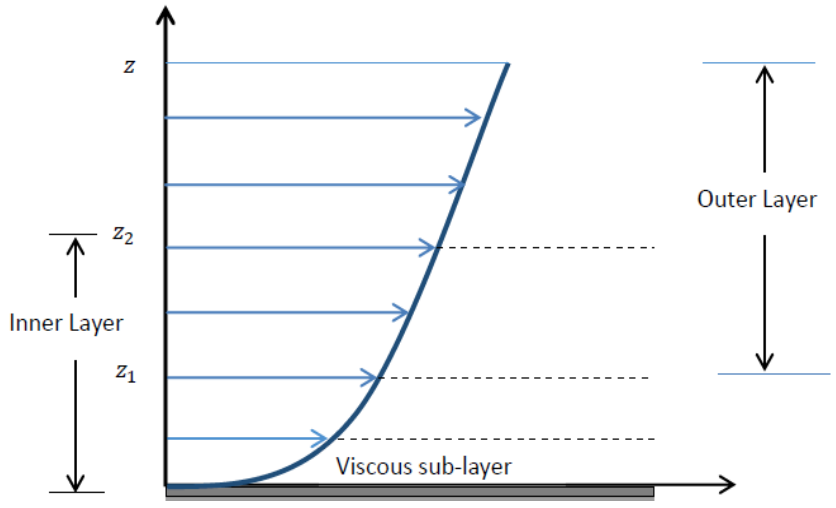

Figure 11: Turbulence Boundary Layer

The vertical distribution of velocity in the turbulent region of the flow with rough bed is often represented by:

$$\frac{U}{U_*} = \frac{1}{\kappa} ln\ \frac{z}{z_0} + C_{int} \quad (25)$$

where k is the Von-Karman constant and C_{int} is the integration constant, the value of $k = 0.41$ has been used as a universal constant by researchers. These constants have been shown to be independent of Reynolds and Froude numbers (Nezu and Nakagawa, 1993). In contrast C_{int} may depend on flow conditions. Equation (25) described the logarithmic velocity profile of a turbulent flow near a boundary with no slip condition. It is often referred to as the log-law of the wall.

The outer region of a turbulent boundary layer is controlled by variables such as the flow depth and the maximum streamwise velocity. The vertical distribution of the mean primary velocity within this region is given by the logarithmic law and wake function outside the logarithm range.

The velocity profile for the outer region of the boundary layer is obtained from the following relationship:

$$\frac{U}{U_*} = \frac{1}{k} ln \frac{z}{z_0} + C_{int} + w(\varepsilon) \quad (26)$$

where $w(\varepsilon) = \frac{2\Pi}{k} sin^2\left(\frac{\pi}{2}\varepsilon\right)$ is the wake function as a correction to the log law at the outer region. Equation (26) is valid for both smooth and rough surfaces which support an indication that at this region, the velocity gradient is independent of the characteristic of the surface roughness. The validity of this law has been checked by researchers for inner and outer region respectively by decreasing or increasing the value of Π (Nezu and Nakagawa, 1993). However, a boundary layer is subject to frequent turbulent burst, in which fluid is ejected from wall with intense vorticity with it. Indeed, these bursts are one of the mechanisms by

which high levels of vorticity are maintained in the boundary layer. Therefore accurate representation of boundary roughness is essential in experimental work aimed to predict river conveyance capacity. Shiono and Knight (1991), and Nezu and Nakagawa, (1993) however noted a boundary layer fully developed to extend the full depth of flow in their works. Such fully developed flow is assumed in the current research.

2.6.1 Turbulence flow Regions

The difference between the boundary sub-layers is important in terms of turbulence production and dissipation. The inner region is a region where turbulent generation exceeds the dissipation ($P > \epsilon$) and this exists near the wall, while in the outer region $\epsilon < P \approx 0$ (Figure 12). The inertial sub-region which corresponds to the intermediate region is the range where the energy flows under a dynamically equilibrium state (Nakagawa et al., 1975) so that $P \approx \epsilon$, the structure in this range is similar to the turbulent energy spectrum expressed by Fourier analysis (section 2.5.5).

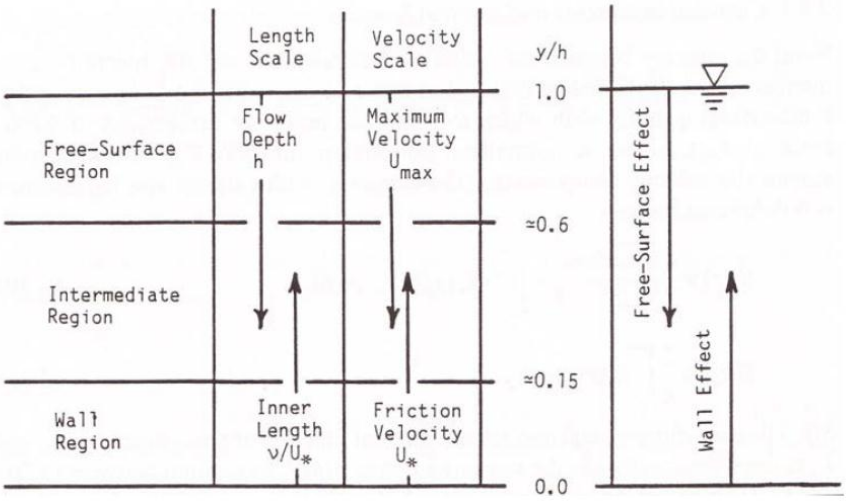

Figure 12： Regions of open channel turbulent flow (Nezu and Nakagawa, 1993)

2.6.2 Similarities between Spectral and Wall turbulence

As noted by (Nakagawa et al., 1975) an evident similarity exists between the spatial and spectral structures of wall turbulence. At a higher Reynolds numbers, the spectral space is divided into three sub-ranges as shown in Figures (13a) and the corresponding spatial structure is shown in Figure (13b). In the inner layer, the turbulent energy produced is larger than the dissipation rate; the excess energy is transported. In outer layer (free surface) corresponding to a viscous sub-range, the turbulent energy production is reduced and the dissipation is cancelled by the transported energy from the inner layer. Between both layers there exists inertial layer in which the production rate is approximately equal to dissipation and this layer corresponds to an inertial sub-range in the spectral space (Figure 13).

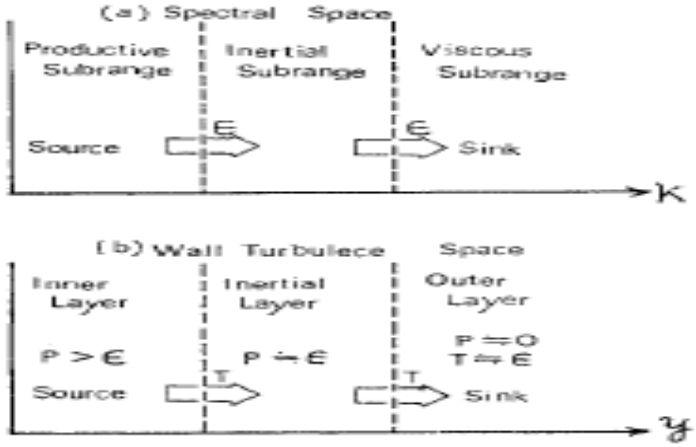

Figure 13: Indicates an existing qualitative similarity between the spatial and spectral structures in turbulence boundary layers. (Nakagawa et al., 1975).

2.7 Secondary Currents in Open Channel Flow

Secondary currents are present in open channels, depending on the flow conditions. They can be classified into two categories (Prandtl, 1952). The first kind of Prandtl's secondary flow is the one generated due to the irregular shape of the channels. The mean flows in such channels are skewed due to curves and bends. This type of secondary flow can often be found in both laminar and turbulent conditions. The second kind of Prandtl's secondary flows are those

generated by the cross-sectional shape and corresponding non-homogeneity of turbulence due to channel boundaries. They are also known as the shear or turbulence driven secondary currents.

The lateral flow v and w in a straight channel are governed by the vorticity (Ω) equation (Nezu et al., 1993):

$$v\frac{\partial \Omega}{\partial y} + w\frac{\partial \Omega}{\partial z} = \frac{\partial^2}{\partial y \partial z}\left(\overline{v'^2} - \overline{w'^2}\right) + \left(\frac{\partial^2}{\partial z^2} - \frac{\partial^2}{\partial y^2}\right)\overline{v'w'} + \upsilon\nabla^2\Omega \tag{27}$$

$$\Omega = \frac{\partial W}{\partial z} - \frac{\partial V}{\partial y} \tag{28}$$

The vorticity Equation (27) accurately governs the secondary motions in open channels (Nezu et al., 1993).

In a more detailed flume experiment, Nezu and Nakagawa, (1984) observed in an open channel with a rectangular cross-section that the aspect ratio (B/H) determines the magnitude of the secondary flow. For open channels, Nezu and Nakagawa set a limit of aspect ratio of 5 to be critical value below which the secondary currents extends to the centre and thereby affect the whole channel. For values of $\left(\frac{B}{H}\right) > 5$ the secondary current is dampen thereby the central part of the channel is unaffected. The central part is defined by (Jesson et al. 2010):

$$\left|\frac{y'}{H}\right| \leq \frac{\left[\frac{B}{H} - \left(\frac{B}{H}\right)_{crit}\right]}{2} \tag{29}$$

Where y' defines the lateral distance from the centre of the channel. Using the critical value of aspect ratio, open channel are classified into two categories: Narrow $\left(\frac{B}{H} < 5\right)$ and Wide $\left(\frac{B}{H} > 5\right)$ open channels (Nezu and Nakagawa, 1993).

Turbulence driven secondary flows are initiated by the effects of the sidewall and the bed roughness (Wang and Cheng, 2005), and later extended in lateral direction to the central region for narrow $\left(\frac{B}{H} < 5\right)$ channels. In wide channels, the magnitude of the corner vortices energy can reduce rapidly. This allows the central region of the channel to be free from the effects of secondary currents. These flows phenomenal have been investigated by Nezu and Nakagawa, (1993); considered to be responsible for the velocity dip in open channels; this is the location of the maximum velocity in the vertical section below the free surface instead of at the free surface (Nezu et al., 1993).

Nakagawa et al. (1975) observed the occurrence of secondary currents due to the anisotropy between v' (transversal velocity fluctuating components) and w' (vertical velocity fluctuating components) and such anisotropy of turbulence has been caused by the development of the complex boundary conditions at channel bed, channel walls and the free surface. The scale of anisotropy between v' and w' is significantly influenced by the boundary roughness and also by channel geometry and the presence of secondary currents influences the cross-sectional distribution of velocity and bed shear stress by generating some undulations in a wave like manner in the cross-sectional direction. The secondary currents in a straight channel with fixed bed are developed as a result of the cross sectional inhomogeneity of turbulence as described out by Prandtl (1952).

Figure 14 illustrates the flow pattern of cellular secondary currents (v', w') in an open channel flow with $B/H = 6.0$, using X-type hot films (Nezu and Nakagawa, 1984). A pair of cellular secondary currents can be seen clearly with the upflow and downflow moving in circular motion.

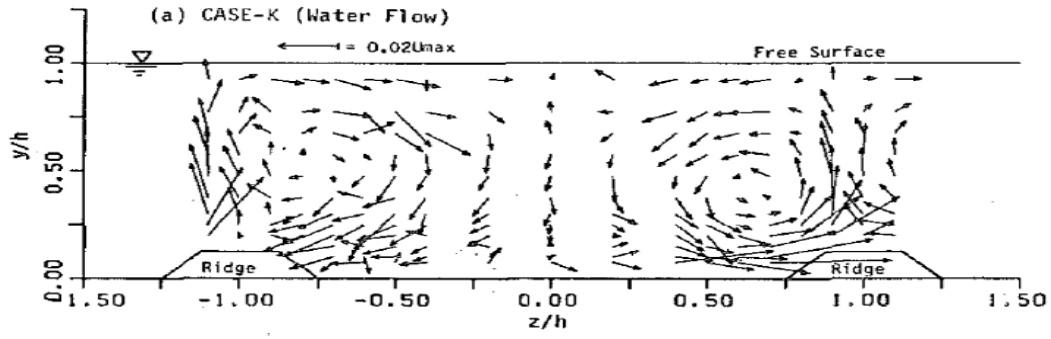

Figure 14: Flow Pattern of Cellular Secondary Currents in Water Channel (Nezu and Nakagawa, 1984)

Investigating the effect of secondary flow on streamwise velocity, Nezu et al. (1993) made a field measurement of secondary flow in a wide $\left(\frac{B}{H} > 5\right)$ straight rivers, as shown in Figure 15. It was observed that the maximum velocity does not appear below the free surface, but at the surface. The results confirmed the absence of velocity dip phenomenon as the aspect ratio is greater than the critical value of 5. Also shown are the isovel lines bulging towards the free surface with corresponding regions of upward and downward flows (Figure 15). Figure 16 illustrates secondary flow cells in half cross section as measured by Nezu and Nakagawa, (1993).

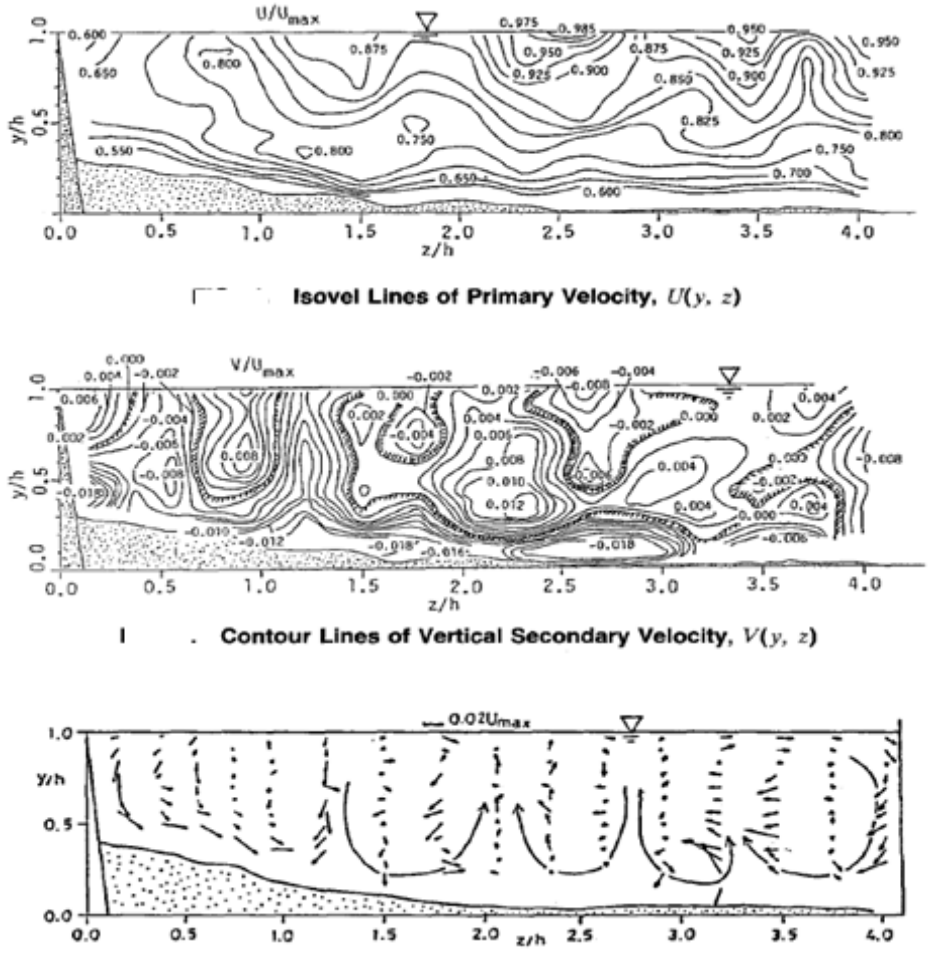

Figure 15: From top: Isovel lines of primary velocity; Contour lines of vertical secondary velocity and Description of secondary currents (Nezu et al., 1993).

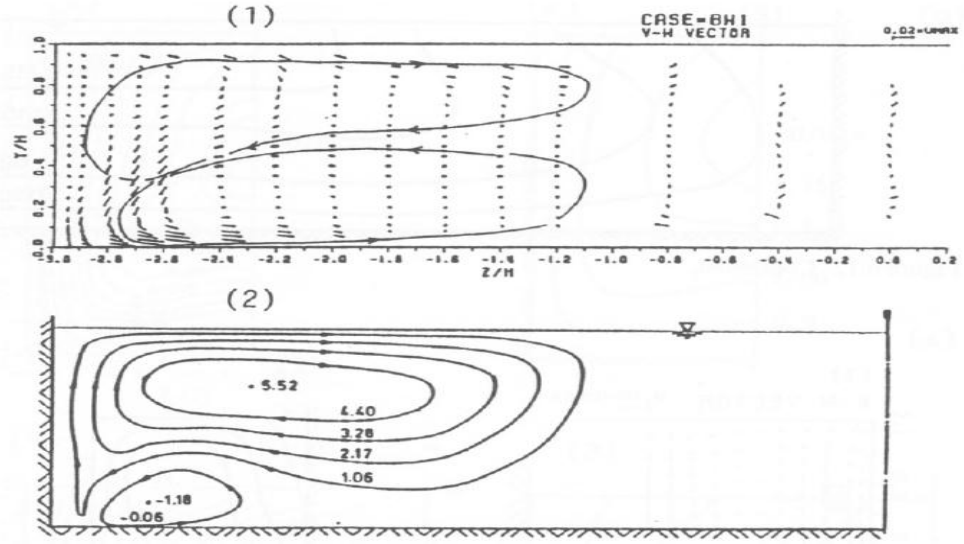

Figure 16: Secondary Flow Cells in Half Cross Section (Nezu and Nakagawa, 1993)

Nezu and Onitsuka, (2001) conducted experiments in a compound channel partly vegetated with cylindrical rods as model vegetation at the floodplain. The actual behaviour of secondary flow within the flow is complex owing to the complexity of vegetation. The results showed weak secondary flow currents over the vegetated region at the floodplain. The secondary flow occurred near the free surface at the main channel and moves towards the vegetated zone as illustrated in Figure 17.

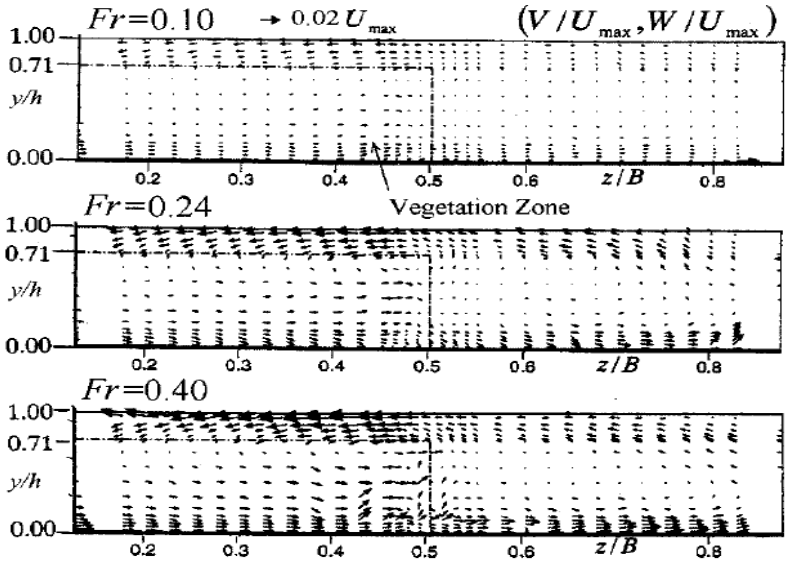

Figure 17: Measured secondary current velocity vectors in a vegetated channel (Nezu and Onitsuka, 2001)

2.8 Flow over Gravel-Beds

Natural gravel beds have been indicated as roughness material that produces coherent macro turbulent flow structure (scaling the roughness height) due to the ensemble of individual roughness elements forming the bed (Hardy et al., 2009). Gravel bed rivers are characterised with complex irregular surfaces with a range of morphological forms (Shvidchenkoa and Pender, 2001). The morphological form combines the individual gravel grain size through particle clusters to form a large scale bed forms. Previous studies over natural gravel beds have shown that coherent flow structures in the near bed region scale with respect to both the

size and sorting of the bed material (Shvidchenkoa and Pender, 2001). Gravel beds are a mixture of sediment of different sizes, it is necessary to determine the particle size distribution and the representative roughness height for the mixture. The former defines the relative amount typically by mass of particles present according to the size of the grains, while the latter defines the length scale of the roughness based on the particle size. The representative roughness height may be difficult to be accurately estimated, for example Nikuradse roughness coefficient k_s represents the physical size of grains (Nikuradse, 1933) which is commonly assumed to be equal to the median d_{50} for practical engineering applications. However, there has been uncertainty on how to accurately define the roughness coefficient k_s for varying types of roughness; in particular k_s may not be appropriate to evaluate roughness coefficient in channels with form drags for example vegetated channel. The assumption of k_s has been shown to be reasonable for a well graded sand bed rivers as a good representative of roughness elements where the grain diameter is less than $d_{50} \leq 0.8mm$ (Hardy et al., 2009). The application of k_s may be more complicated in a natural river where the grain sizes have wider distribution with many other morphological forms.

The near surface turbulence structure over the gravel roughness depends on the viscous length scale $\frac{\upsilon}{U_*}$ (where υ is the kinematic viscosity and U_* is the shear velocity) and the roughness length scale k. The non-dimensional parameter k^+ representing the ratio of the roughness to the viscous length scale as:

$$k^+ = \frac{U_* k}{\upsilon} \tag{30}$$

Equation (30) is used to classify the turbulent flows over the gravel bed into different regimes as follows:

- Hydraulically smooth flow ($k^+ < 5$), this defines the region where the roughness elements are completely submerged within the viscous sublayer with little or no interference with the surface flow.
- Transitionally rough ($5 < k^+ \leq 70$), this is the region where the bed roughness elements are partially submerged within the viscous layer with both the roughness and viscous effects becoming more significant.
- Fully rough ($k^+ > 70$), this is a region where the bed roughness elements protrudes to disturb the viscous and buffer layers and the velocity distributions becomes dependent on the molecular viscosity.

2.9 Flow structure in vegetated canopies

Aquatic vegetation commonly exists in canopies, i.e., the distribution of individual plant elements, for example the plant stem. Aquatic canopies are heterogeneous with varying heights h_v that occupy either only a small fraction of the water depth H $(h_v < H)$ as used in the current research or as being fully emergent $(h_v \geq H)$. Aquatic vegetation can also vary in stem density and geometry in both horizontal and vertical directions. Considering the stem-scale processes and the flow across the boundary layer of an individual leaf, the morphology can be described at a canopy scale (Leonard and Luther, 1995, Luhar et al., 2008). At canopy scale vegetation can be indicated by an average, distributed morphology using the parameter a_v, frontal area per volume. If individual stem has a characteristic frontal area, $A_{f,}$ and the canopy contains n stems per bed area, the canopy has a frontal area index $a_v h_v = nA_f$ (Luhar et al., 2008). The same parameter is used to describe the solidity of terrestrial canopies by Jimenex, (2004). Many types of vegetation have simple stem morphology that can be characterized by the stem width w for which $a_v = nw$. The porosity of the canopy is $\approx (1 - a_v w)$.

Within each canopy, flow is strained to revolve around individual stems and branches, such that the velocity field is spatially heterogeneous at the stem scale. Within the vegetation flow, the simplified momentum balance in most aquatic canopies is given as:

$$\frac{DU}{Dt} = gS_0 - \frac{\partial}{\partial z}\langle\overline{u'w'}\rangle + \frac{1}{2}C_d a U^2 \tag{31}$$

where C_d is the drag coefficient. The momentum balance in equation (31) defines regimes for sparse and dense canopies. For steady and uniform flow $\left(\frac{DU}{Dt} = 0\right)$, the gradient (gS_0) is balanced by the sum of turbulent stress and canopy drag. When the turbulent stress dominates within the canopy, the velocity profile is similar to that of turbulent boundary layer. This is referred to as sparse canopy behaviour (Luhar et al., 2008; Nepf, 2012). When canopy drag is sufficient, the drag discontinuity at the top of the canopy creates an inflection point in the velocity profile, and by this, a similar profile to a free shear layer (FSL) is observed (Raupach et al., 1996; Nepf and Ghisalberti, 2008; Nepf, 2012), this is referred to as dense canopy behaviour. For dense canopies, the inflection point at the top of the canopy leads to the generation of large coherent vortices through the Kelvin-Helmholtz instability (KH), as also seen in free shear layers (Nepf and Ghisalberti, 2008). These large and energetic, coherent vortices dominate mass and momentum exchange between the canopy and the overlying flow (Finnigan, 2000). In a free shear layer, the KH vortices grow continually downstream predominantly through vortex pairing (Winant and Browand, 1974). In a canopy shear layer, however, the KH vortices reach a fixed scale and a fixed penetration into the canopy at a short distance from the canopy's surface (Ghisalberti and Nepf, 2002). Scaling analysis supported by observations show that the penetration scale ∂_e is inversely proportional to the canopy drag, as parameterizes by C_d (Luhar et al., 2008). Figure 18 illustrates the mean velocity and shear stress profiles of spare and dense canopies.

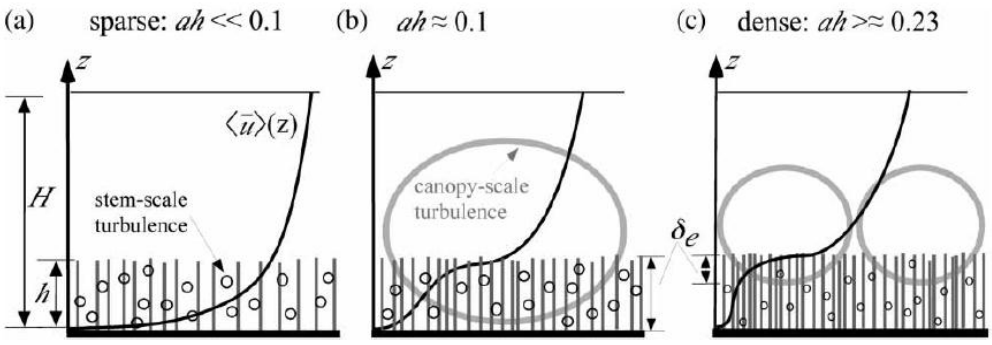

Figure 18: Open channel flow within and above submerged vegetation with sparse and dense canopy (Nepf and Ghisalberti, 2008, Nepf, 2012)

2.9.1 Characteristic of Mean Velocity Profiles in depth limited aquatic Vegetated Flow

Characterising the effect of vegetation on the mean velocity profile has been one of the most significant challenges in understanding the impact of vegetation on flow. Within a flow, vegetation represent blockages and roughness elements, in addition vegetation canopies also acts as a porous medium (Ghisalberti, 2009) which restricts the flow. This effect creates different layers of flow regimes: above and within the vegetation canopy. The longitudinal mean velocity U profile within the canopy differs from the typical boundary-layer model (law of the wall) because of the presence of vertical elements (vegetation stems) into the flow (Velasco et al., 2003) and low values of U are recorded within the vegetation.

A different momentum diffusion mechanism is developed. The flow within the vegetation is characterized by a low longitudinal velocity due to the drag by the vegetation stems. Subsequently, this region is also characterized by a uniform velocity with a low longitudinal velocity gradient. While the velocity profile in non-vegetated channels can be approximated to the boundary layer profile, this may not give accurate approximation in vegetated channels as the porous layer zone creates two layers of flow regimes with a significant impact on the shape of the velocity profile (Figures 18 and 19). Raupach et al. (1996) hypothesized the vegetation layer to be more analogous to free shear or a mixing layer. This is defined as the

region of mixing of two flowing fluids of different velocities. The velocity profile is logarithmic far above the vegetation, the shape of the profile is defined by the zero plane displacement, the friction velocity, and the roughness height (Raupach, 1994).

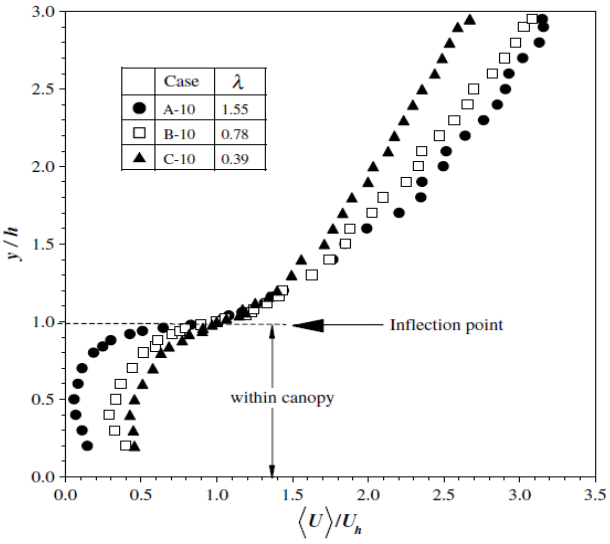

Figure 19: Vertical velocity profile in a submerged vegetated flow (Nezu and Sanjou, 2008)

Ikeda et al. (1996) provided quantitative evidence of the inflection velocity profile above vegetated beds. However, the vertical mean velocity profile within and above a submerged vegetation flow was also idealised by Nezu and Sanjou (2008), they hypothesised that three different velocity regimes exists in submerged vegetation as the (i) vegetation zone, (ii) the shear layer zone and (iii) the boundary layer zone as shown in Figure 20.

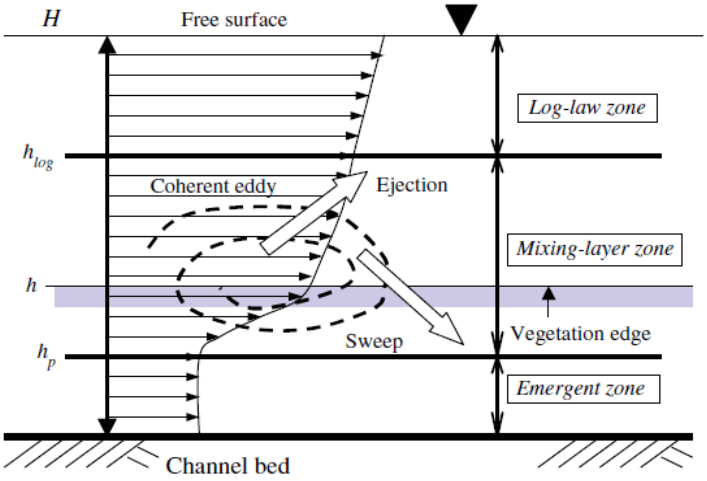

Figure 20: Schematized flow structure for submerged aquatic canopy flow (Nezu and Sajou, 2008)

From Figure 20, within the inner vegetation zone $(0 \leq z \leq h_p)$, h_p is the turbulence penetration depth and z vertical height above the channel bed. The velocity is approximately constant and the vertical turbulent momentum transport is negligibly small due to strong wake effects behind vegetation stems. This region corresponds to the longitudinal zone as reported by Nepf and Vivoni, (2000). In this region the only means of exchange is through longitudinal advection and turbulence is generated by stem wakes effects. This is the closest region to the bed where the flow is pressure driven, turbulence production is dominated by the vegetation stems and therefore the flow profile remain constant (Nepf and Vivoni, 2000). The penetration depth serves as the boundary between the vegetated zone and the free flow in non-vegetated zone.

In the mixing layer zone $(h_p \leq z \leq h_{log})$, there is a free shear layer formed at the interface between flow and vegetation due to different velocities as a result of Kelvin-Helmholtz (KH) instability which may occur in an inflection point in the velocity profile (Nikora, 2009). Turbulence structure in this zone is similar to plane mixing layer and coherent eddies are generated near the vegetation edge due to inflection instability and consequently governs the

vertical momentum (Ghisalberti and Nepf, 2006). The inflection point in the mean profile at the top of the vegetation flow regime is an important feature of the submerged vegetated flow, as it represents a highly unstable region of the high velocity shear which acts as the main source of vegetation shear layer turbulence. This region is characterised by an inflection in the velocity profile and dominated by the large shear vortices.

In the log-law region $\left(h_{log} \leq z \leq H\right)$, flow above the vegetation top is logarithmic and the turbulence characteristics are analogous to those of boundary layers (Finnigan, 2000) and open channel flows with rough beds. A non-logarithmic vertical profile can be observed over the full depth of emergent vegetated flow. A logarithmic structure above the canopy was observed by Nepf and Vivoni (2000) while investigating flow structure in depth-limited vegetated flow. The overflow profile is defined by Equation (32):

$$\frac{U}{U_*} = \frac{1}{\kappa} ln\left(\frac{z-d_0}{z_o}\right) \tag{32}$$

U_* is the shear velocity, **κ** is the von Karman constant taken as 0.41 in open channel flows (Nezu and Rodi, 1986), d_0 is the zero-plane displacement thickness and z_o is the roughness height. The zero plane displacement corresponds to the mean level of momentum absorption (Nepf and Vivoni, 2000):

$$d_0 = \int_0^h \frac{\partial \overline{u\prime w\prime}}{\partial z} z.\partial z / \int_0^h \frac{\partial \overline{u\prime w\prime}}{\partial z} \tag{33}$$

Equation (33) is usually seen as the level to which the effective surface must be raised to make the velocity profile in the inertial sub-layer obey the logarithm law (Raupach and Shaw, 1981).

2.9.2 Transfer mechanism within submerged vegetated flow

The transport structure in submerged vegetated flow is driven by the vegetation shear layer which is responsible for the transfer of energy within the flow. The three main energy transfer mechanisms in vegetated flow include (Nepf and Vivoni, 2000): 1) the transfer of energy from the mean flow to the plant and vice-visa; 2) the transfer of energy from the mean flow into the turbulent kinetic energy and 3) the transfer of energy from turbulent kinetic energy into heat energy due to viscosity. The second and third mechanisms describe the Kolmogorov's (1941) -5/3 turbulence spectral whereby energy is transferred from the mean flow to larger scale eddies which then decay into smaller eddies until dissipation into heat energy. The rate of decay with frequency follows a -5/3 law of frequency. This is a common process in a turbulent flow as discussed in section 2.3.1.

2.9.3 Vegetation motion and interaction with the flow

Plant motion and coherent movement of vegetation stems have been analysed by researchers (Nepf and Vivoni, 2000; Nepf, 2012; Ghisalberti and Nepf, 2006). Importantly, coherent moving of vegetation stems has been used as an evidence of vortices transporting turbulence within the vegetated flow (monami). Similarly, the response effect on the velocity field caused by vegetation motion has been observed (Ikeda et al., 1995). The flexibility of aquatic vegetation has led to a greater spectrum of plant motion in response to the flow in vegetated flow, this can be categorized into four regimes of motion (Nepf and Vivoni, 2000): 1) erect, 2) gently swaying, 3) strong, coherent swaying (monami), and 4) prone. The vegetation motion is a function of the vegetation morphology which includes the stem density and the flexural rigidity. Flexible aquatic vegetation will experience the flow regimes number two and three under normal conditions. In the current work, the second regime of vegetation motion (gently swaying) was observed for flexible vegetation. In particular, the flexural rigidity can be very difficult to accurately measured, therefore, artificial stems are often

scaled with constant rigidity which may give an approximation to the natural stems. This has been a challenge in conducting experiments with artificial vegetation. However, Ghisalberti and Nepf (2002) have shown that the characteristics of shear instabilities are generalised over a ranged of flexibilities, this assertion has made artificial vegetation in a controlled laboratory experiments (e.g., the AstroTurf and the rigid plastic used to mimic vegetation in the current work) to represent reasonable contributions to the theory of vegetation flow like the natural vegetation.

Finally, aquatic plants in natural rivers have greater flexibility and vastly respond to flow stresses. Associated with this phenomenon is the passage of the Kelvin Helmholtz (KH) vortices over the top of a flexible canopy which generate a continuous waving of the canopy called *monami*. It is a coherent motion related to the organised vortices produced by the inflection instability (Okamoto and Nezu, 2009). In canopy shear layer the inflection point corresponds nearly with the top of the canopy ($z_i \approx h$), so that the velocity at the inflection point can be approximated as the velocity at the top of the canopy ($U_i = U_h$), the vortices produced are displaced relative to the inflection point resulting as shown in Figure 21 (Nepf and Ghisalberti, 2008). This depends largely on the density of the vegetation stems.

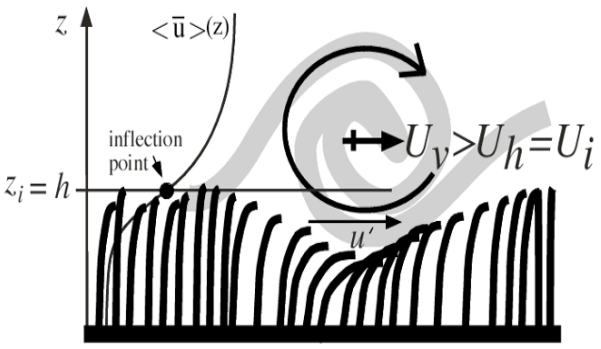

Figure 21: Showing the inflection point and vortex translation speed in canopy shear layer of flexible vegetation (Nepf and Ghisalberti, 2008).

2.9.4 Resistance in Vegetated Channel and Turbulent Kinetic Energy Budget

Vegetation in channels covers a wide range of conditions, from highly flexible low grass stems to dense bushes and rooted trees. The presence of any kind of vegetation in flow introduces resistance into the flow. The conventional open channel resistance equations (e.g. Manning's) have not taken into account the drag force exerted through vegetation stem. A number of researchers (Morvan et al., 2008; Shiono et al., 2012; Tang et al., 2011; Jarvela, 2002; James et al., 2008) have proposed solutions which suggest vegetation resistance through a drag coefficient C_d. The drag coefficient C_d depends on the flow conditions and the specific vegetation characteristics such as the density and flexibility of the canopy. C_d can be determined with the help of modified resistance equations using flow measurements, however it may be difficult to obtain appropriate drag coefficient to represent the vegetation resistance from the measured data. Alternatively the drag force on single stems can be measured directly in the laboratory (James et al., 2008). These approaches have shown that C_d varies strongly with the stem Reynolds number (James et al., 2008).

Another important contribution was made by Kouwen (Kouwen and Unny, 1980) through dimensional analysis of a simple model to evaluate flow vegetation resistance in open channels. The authors observed that flow resistance in vegetated channel depends on the geometric and mechanical properties of plants (density, elasticity) and flow conditions. Plant geometric and mechanical characteristics include plant material density ρ_p, Young's (elasticity) modulus E, second moment of cross-sectional area I_2, and flexural stiffness EI_2. There are also characteristics that quantify the relationship between plants and flow, including the drag C_d and lift C_L coefficients, strain, tension and bending moments (Nikora, 2009).

In order to clarify the structure of turbulence in open channel flow involving vegetation, it is necessary to evaluate the turbulent kinetic energy budget. Turbulent kinetic energy budget explains the relative significance of processes that controls turbulent flow. This varies for open channel flow with or without vegetation. The presence of vegetation in open channel modifies the flow characteristics and creates additional dimension to the balance of turbulence kinetic energy (K). Noticeable is the vegetation resistance on the flow which generates turbulence from wakes production. The modified turbulent kinetic energy (K) in vegetated flow assumed to be steady can be expressed as (Nepf and Vivoni, 2000):

$$\frac{D\overline{\langle k \rangle}}{Dt} = 0 = P_s + P_w + T_t + T_p + \varepsilon \tag{34}$$

where P_s, is the shear production, P_w, the wake production, T_t, turbulent transport, T_p, pressure transport, and ε the dissipation. In a fully developed flow, the largest terms are the shear turbulent production P_s and dissipation ε. Under equilibrium conditions, these terms tends to be in balance and under non-equilibrium conditions, turbulent kinetic energy is transported either through turbulent transport T_t, or pressure transport T_p. Example of turbulent kinetic energy budget is showing in Figure 22 (Nepf and Vivoni, 2000).

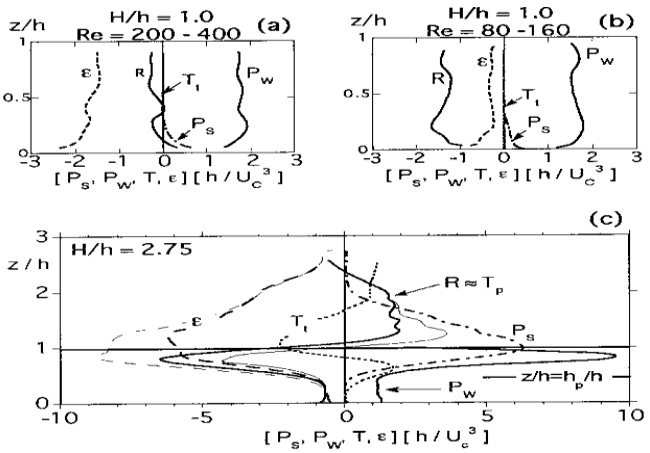

Figure 22: Turbulent kinetic energy for emergent and submerged conditions (Nepf and Vivoni, 2000).

In addition to some of the work mentioned above, a number of studies involving different channel configurations have been carried out whose results may be usefully compared to the results obtained from the experiments presented in this thesis. The work of Jesson (2011) and Jesson et al. (2013) examined flow structures in an idealized heterogeneous channel composed of parallel smooth and gravel sections. Similar to the current work, the channel was split along the centreline into rough side and smooth side and the effect of checkerboard arrangement of alternating rough and smooth sections of 1.83m length was investigated. The work highlighted the importance of the rough-smooth boundary (i.e., the location where the bed roughness changed) on turbulence generation and lateral momentum transfer. Jesson et al. linked turbulence generation and hence momentum transfer throughout the flow to the rough-smooth boundary with the primary momentum transfer in the horizontal direction. The local maxima of the horizontal turbulence propagation were associated with the rough-smooth boundary area with a reduced vertical propagation. An example of vertical profiles of the turbulence intensities measured by Jesson is shown in Figure 23 with the relative value distributions collapsing onto one another and increased turbulence intensities at the rough-smooth boundaries. However, the general magnitude of turbulence parameters appears to be a maximum at the rough-smooth boundary in Jesson's work.

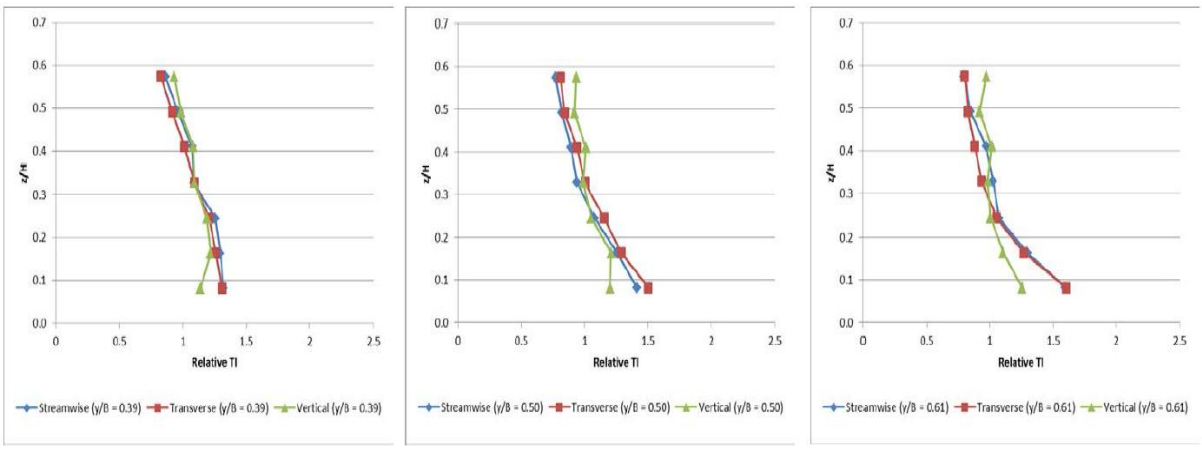

Figure 23: Relative Vertical Turbulence Intensities (Jesson., 2011)

For lateral velocities, Jesson found velocities with RMS values less than 3% of the integrated velocities for all the data set. Jesson's results show secondary flow cells on the smooth side of the channel and noted that the roughness elements on the rough side prevented the formation the secondary cells. At the rough-smooth boundary the results illustrate a strong upward flow as shown in Figure 24.

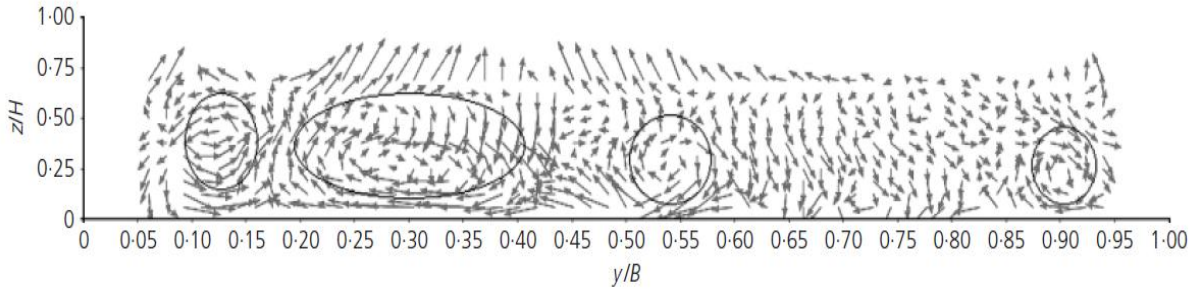

Figure 24: Lateral Distribution of Secondary Flow with RSB at $y/B = 0.5$ (Jesson et al., 2013)

In order to model the effect of vegetation, Tang et al. (2011) incorporated vegetation drag as an additional term in the Reynolds Average Navier-Stokes (RANS) equations through drag force equation (35)

$$F_v = \frac{1}{2}\rho C_D \beta A_v U^2 \tag{35}$$

where C_D is a drag coefficient, β is a vegetation shape factor and A_v is the cross sectional area covered by the vegetation. Modifying the Shiono and Knight Method (SKM) parameter friction factor f, dimensionless eddy viscosity λ and secondary flow term Γ values, Tang et al. using two-panel analytical solution demonstrated that the model predicted the depth-averaged velocity and shear stress distribution in vegetated channel. However, the model supports the rigid emergent vegetation as illustrated in Figure 25.

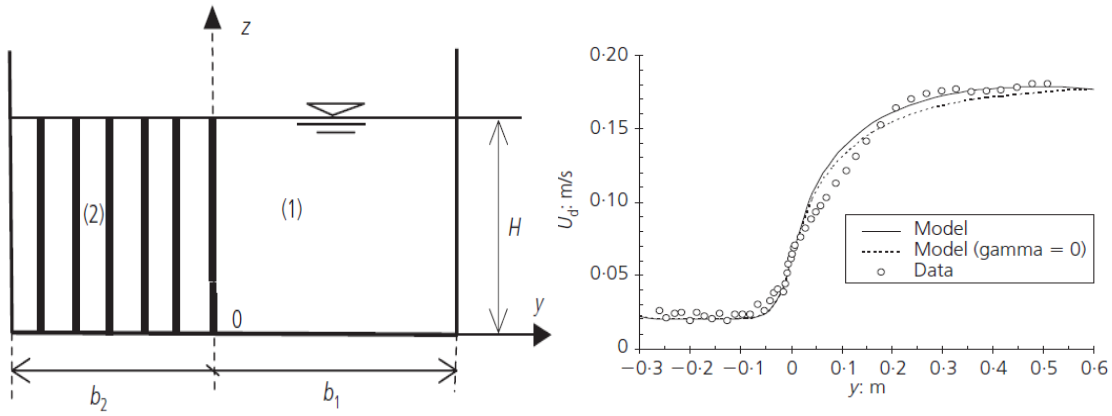

Figure 25: The Cross Section of the vegetated Channel and the Predicted Depth-Averaged Velocity Distributions (Tang et al., 2011).

In the work of Afzalimehr et al., (2011), the turbulence characteristics of flow over submerged vegetation in a flume were examined using two different aspect ratios of $B/H =$ 4 and 5.4 respectively, where B is the channel width. From the result, the secondary current exits in the flow over vegetation with an aspect ratio of $(B/H = 4)$. For this range of aspect ratio, $(B/H < 5)$ noticeable secondary currents due to differential roughness surfaces should be expected above the canopy (Nezu and Nakagawa, 1993), the secondary flow vector changes direction within the flume. This may arise from the low and high momentum fluids been transported by the current from the sides of the channel towards the channel centre. However, more data are needed to fully examine the turbulent flow structures.

Chucksmith et al. (2010) investigated the effects of emergent and submerged natural vegetation on longitudinal mixing using natural vegetation. Chucksmith et al. noted that natural vegetation will introduce more important variables into the flow than artificial vegetation. Injecting dye into a vegetated flow, three-dimensional velocity measurement was made using the ADV and longitudinal mixing in the channel was measured using fluorometery to determine the transport of traceable soluble material through the channel.

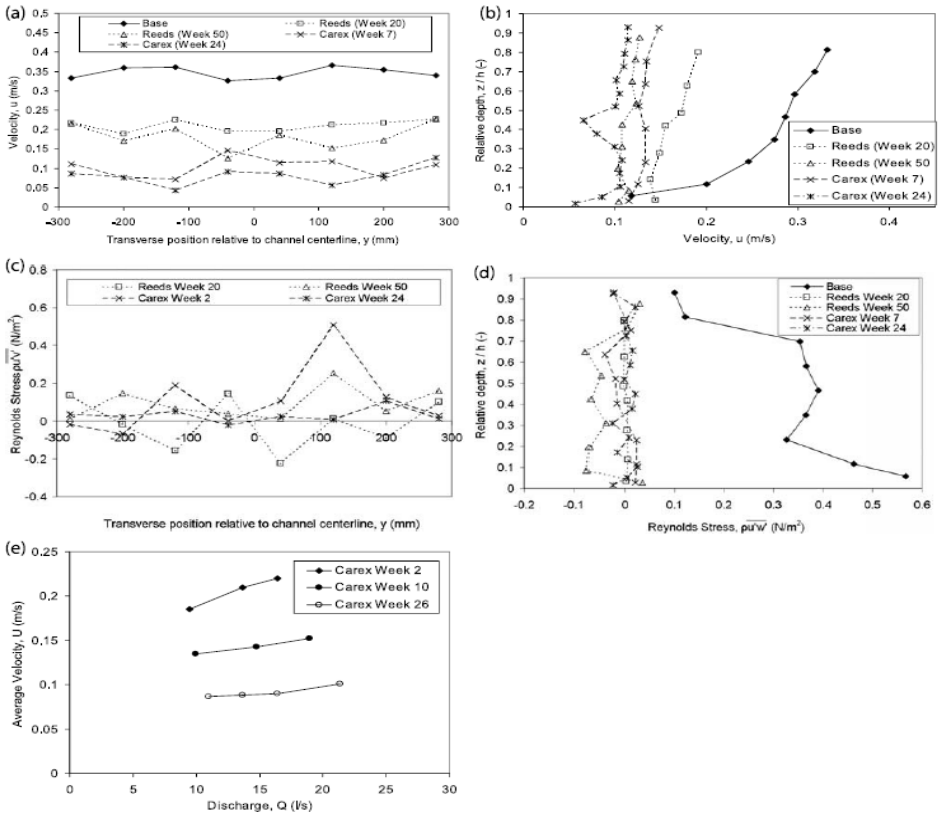

Figure 26: Transverse Profiles of (a) Primary Velocities, (b) Vertical Profile of Primary Velocities, (c) Transverse Profiles of Reynolds Stress, (d) Vertical Profile of Reynolds Stress, and (e) Average Flow Velocity against Discharge for Different Vegetation Ages (Chucksmith et al., 2010)

The results as illustrated in Figure 26 indicate uniform velocity profiles and subsequent reduction in shear dispersion and longitudinal mixing along the flow depth in emergent condition. In submerged conditions there was increased vertical velocity shear due to presence of free region over the top of the vegetation. The vertical velocity shear was found to increase the longitudinal mixing relative to emergent condition. The experiments were performed using uniform vegetation and roughness elements for each of the condition examined (Chucksmith et al., 2010).

Shiono et al. (2012) considered friction factor f and eddy viscosity in the Shiono and Knight Method (SKM) to model vegetated rivers for inbank and overland flows. Velocity and Reynolds stresses were measured with acoustic Doppler velocimetry (ADV) while the

boundary shear stress measured with a Preston tube. The model parameters were calculated using the measured data. Of particular importance is the variation of the model parameter at the shear layer region generated by the vegetation elements. Shiono et al., developed a new analytical solution taking into account the variation of these parameters. This solution was applied to flow in compound channel with vegetation and accurate prediction of the lateral distribution of depth-averaged velocity and boundary shear stress was achieved.

The flow structures in straight compound channels with and without one-line emergent vegetation along the floodplain edge have been investigated by Sun and Shiono (2009). The velocity and shear stress distribution were significantly reduced in vegetated case compared to those without vegetation. Using vegetation density and flow parameters, Sun and Shiono developed new formulae for resistance factors for with and without vegetation and the equations found to give a good prediction of drag force for one-line vegetation. The force balance approach was adopted to calculate the discharge using the predicted drag force ratio and compared with the discharge predicted by the new formula.

Omran and Knight (2006) obtained boundary shear stress in open channel using the Shiono and Knight Method (SKM) through proper specification of the secondary flow term using the position and rotational direction of the secondary cells. The values of secondary flow term were shown to change in sign laterally depending of the direction of the secondary flow cells. Omran and Knight applied the method with linear variation of friction factors to the experimental data, accurate results for both depth averaged velocity and boundary shear stress distributions were obtained for different set of simulations when compared with the experimental data.

Wang and Cheng (2005) conducted flow measurement experiments using a two-dimensional Laser Doppler Anemometer (LDAs) system over longitudinal bed strip roughness and

longitudinal ridges and troughs, in this case, the presence of secondary flows altered the distribution of the primary velocity and Reynolds stresses, and therefore deviates from those observed for 2D open channel flows. From their experiment Wang and Sheng (2005) obtained analytical formulae to modify the velocity and shear stress distribution from longitudinal strips by a function proposed in log-wake form, the formulae matched the tranverse roughness variation for their data. Figure 27 illustrates the secondary flow vector of the longitudinal bed strip roughness from their experimental data.

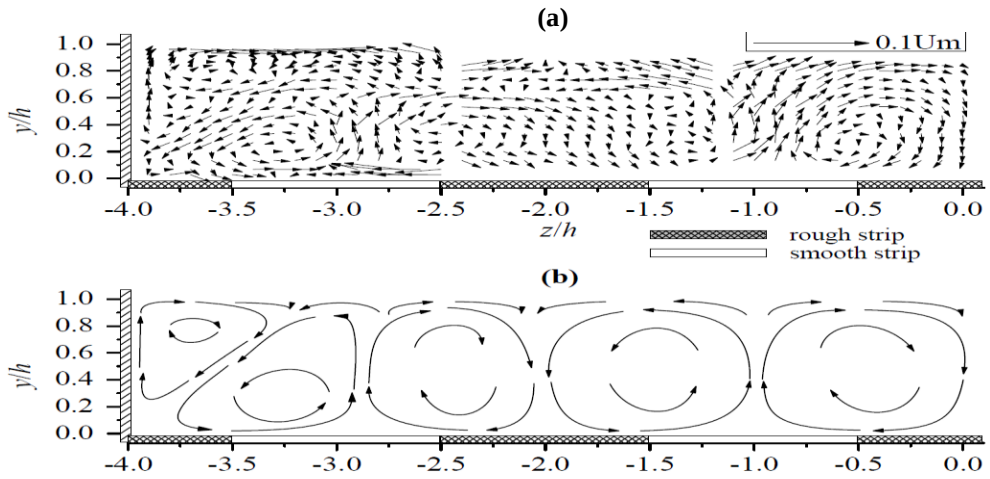

Figure 27: Secondary flow vector the longitudinal bed strip roughness (Wang and Cheng, 2005).

Further to the work highlighted above, Wang and Cheng (2006) examined the time-mean secondary flow structure using similar bed configuration of alternated smooth and rough bed roughness. Consistent with previous research on smooth and rough bed, the upflow was observed over the smooth bed and downflow over the rough bed. With the high aspect ratio for the experiment $\left(\frac{B}{H} > 5\right)$, the central region of the flow was free from the side wall effects necessitating the creation of secondary flows at the central region due to only heterogeneous roughness effects only as illustrated in Figure 28.

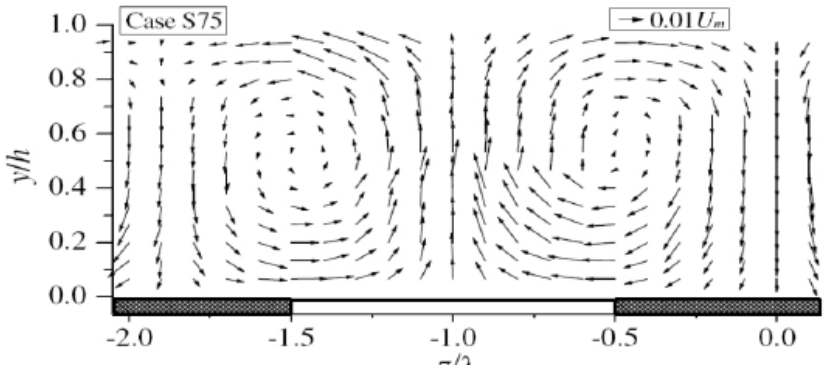

Figure 28: Velocity Vectors (Wang and Cheng, 2006).

McLelland et al. (1999) investigated the mean and turbulence flow structures over a self-formed heterogeneous channel bed from a bimodal sand and gravel bed mixture material. Stripes of different roughness were naturally formed after approximately 40 minutes and remain stable for about 15 hour lifetime of their experiments. The self-formed beds have similar size of roughness elements with rough stripes having $D_{50} = 1.21mm$ and smooth $D_{50} = 0.87mm$. A two-dimensional measurement of velocity was made using a Laser Doppler Anemometer (LDA). From their results as illustrated in Figure 29, streamwise velocity dip was observed near the free surface. The turbulence anisotropy due to heterogeneous bed-form generates secondary flow cells within the half channel width thereby producing lateral variations in the boundary shear stress. The interaction of the secondary flow cells and the bimodal bed material generates lateral bed forms with similar distribution at the channel centre. The similar distribution indicates no lateral variation with roughness and the bed serving as the only source of turbulence generation. This mechanism may have similar effect to turbulent processes over symmetrical roughness.

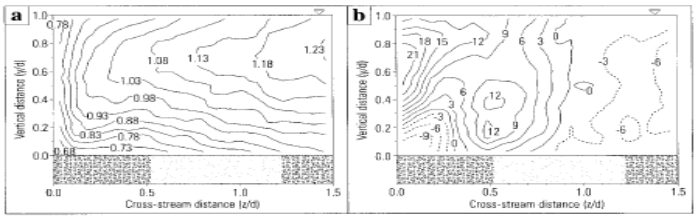

FIG. 4. Contour Plots of: (a) Dimensionless Streamwise Velocity (U/U_m); and (b) Dimensionless Vertical Velocity ($V/U_m \times 10^{-3}$) in y, z-plane. Flow Is into Page. Plot Shows Flow in Half of Channel with Location of Fine- and Coarse-Grained Sediment Stripes Being Illustrated below Contours

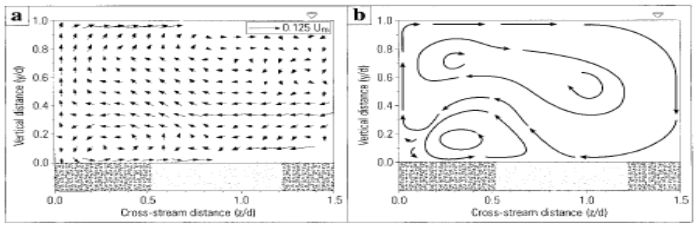

FIG. 5. (a) Vector Plot of Pattern of Secondary Circulation with Cross-Stream Velocities Calculated using Eq. (3); (b) Schematic Plot of Inferred Pattern of Secondary Flow. Flow Is into Page and Stripe Locations Are Shown below Contours

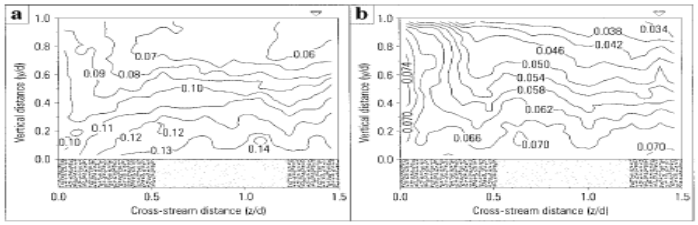

FIG. 6. Contour Plots of: (a) Dimensionless Downstream Turbulence Intensity (u'_{rms}/U_m); (b) Dimensionless Vertical Turbulence Intensity (v'_{rms}/U_m). Flow Is into Page and Stripe Locations Are Shown below Contours

Figure 29: Shown McLelland et al., results (McLelland et al., 1999)

The effect of bed roughness on scalar fluctuations in turbulent boundary layer has been studied by Jackson et al., (2007). The bed roughness was varied to generate smooth, transitional rough and fully rough bed with the velocity field measured in horizontal planes using Planar Laser induced fluorescence (PLIF) technique. From the study, the variance of the fluctuation decreases as the bed roughness decreases and accelerates the approach of the PDF towards a Gaussian distribution (Jackson et al., 2007).

In order to know the extent and length of shear layer in vegetated shear flow due to obstruction, Ghisalberti and Nepf (2004) conducted experimental work to study the limited growth of vegetated shear layers in submerged vegetation flow. The experiments conducted in a laboratory flume showed that the development of the shear layer is prevented at an equilibrium point where the turbulent kinetic energy due to shear balances its dissipation due

to drag in vegetation elements (Ghisalberti and Nepf, 2004). Using the equilibrium condition, Ghisalberti and Nepf proposed a one dimensional numerical model to predict the mean velocity profiles within the shear layers. Using the model for their experimental data, good agreement was achieved. Due to the difficulty and lack of adequate description of drag coefficient of submerged vegetation in the model, field application of such model may be limited.

The characteristic of shallow flows over a permeable medium using submerged vegetation was studied by Ghisalberti, (2009). The study investigated the length required for the development of mixing layer in vegetated flow. The results showed that the length required for mixing to develop scaled upon the drag and the vegetation length. They also observed coherent momentum transport in a narrow frequency range and a reduction in the vegetation drag due to coherent waving (monami). Figure 30 illustrates the mean streamwise velocity and mixing layer length as obtained by Ghisalberti, (2009).

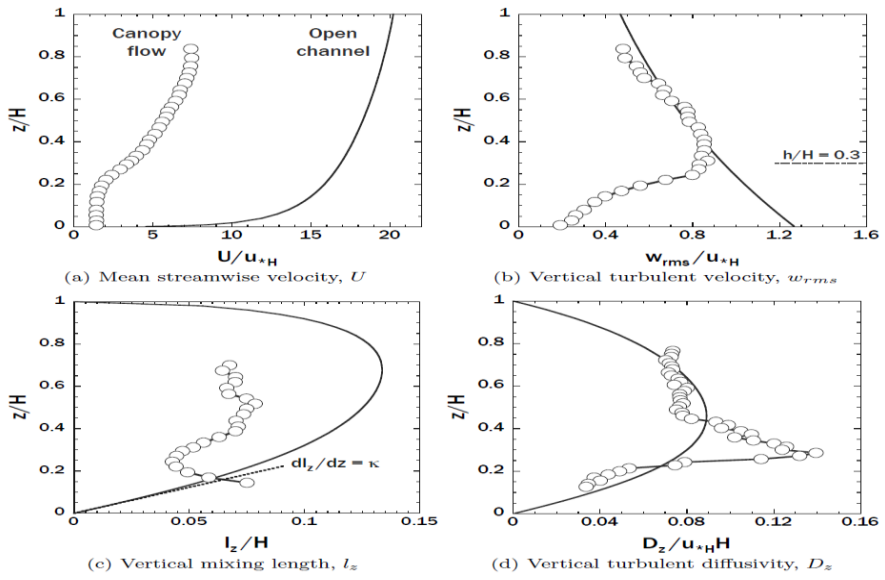

Figure 30: Experimental Results of the Shallow Flow over Permeable Submerged Vegetation (Ghisalberti, 2009)

Ghilsalberti and Nepf (2002) classified aquatic flows with submerged vegetation as a mixing layer rather than a boundary layer due to the vertical discontinuity of the vegetation drag at the vegetation top with the creation of an inflectional point in the velocity profile which the authors described to resemble the hyperbolic tangent profile of a pure mixing layer. It was noted that the inflectional profile results in the development of vortices which causes the instantaneous streamwise velocity increase at the top of the vegetation as the vortex passes. This effect was further noted to create localized regions of plant deflection through coherent waving phenomenon called monami (Ghisalberti and Nepf, 2002).

Turbulence measurements were conducted using the 2-dimensional laser Doppler anemometer to study the dispersive properties of vegetated open channel flows by Nezu et al., (2006). In their work, it was found that the vegetation density strongly correlates with the turbulence structure. The dispersive contributions to turbulence due to vegetation were examined through the kinetic energy budget to reveal the shear and wake generation. Of particular significance was the large value of wake generated turbulence which was comparable or larger than the shear turbulence generation. This is an indication that wake generation plays an important role within the vegetation by complementing the shear turbulence generation in submerged vegetated flow (Nezu et al., 2006).

Measurements at several locations within the vegetation to obtain velocity and turbulence intensity profiles through an array of rigid vegetation have been undertaken by Liu et al. (2008). The study was to observe the changes in the flow characteristics as it flows through the rigid dowels. ADV was used for velocity measurement. The velocity within the vegetation array remains constant with depth and the velocity profile becomes logarithmic above the vegetation element. The maximum turbulence intensities are found at the boundaries between the vegetation elements and the free flow with the formation of coherent

vortices for significant mass and momentum transport. Figure 31 compares the mean velocity profiles under various conditions of dowel roughness.

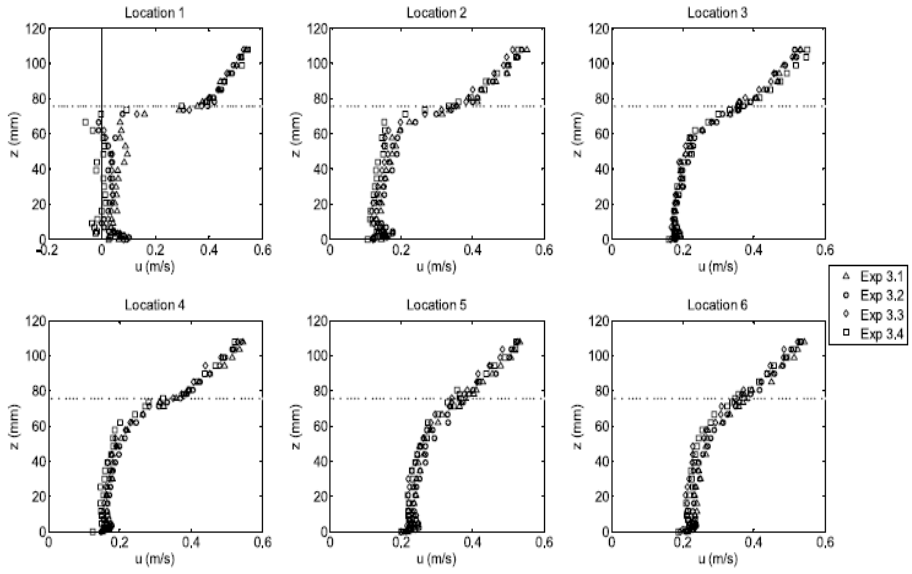

Figure 31: Comparison of the mean velocity profiles under various conditions of dowel roughness (Liu et al., 2008)

The behaviour of turbulent open channel flows over permeable and impermeable beds has been examined by Manes et al. (2009). The purpose was to provide a better understanding of how the surface and the subsurface flow within the permeable bed interact and influence each other. Velocity measurements were taken over and within a permeable bed made of five layers as illustrated in Figure 32. The results confirmed that bed permeability can significantly affect flow resistance with the friction factors increasing for permeable bed as the Reynolds number increases. The flow measurements within the permeable bed show significant transport of turbulence at the roughness interface and the transport at the lower bed driven by pressure fluctuations.

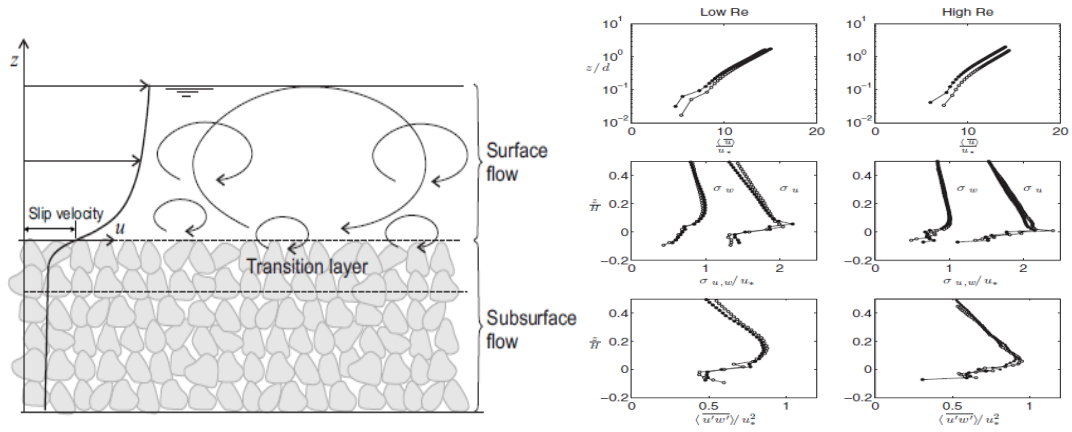

Figure 32: Flow Subdivision in Open Channel Flow over Permeable Beds, and the Averaged Velocity and Shear Stress Vertical Distributions (Manes et al., 2009)

Vermaas et al. (2011) investigated the contributions of momentum exchange of various mechanisms through laboratory flume experiments using a channel bed with two parallel patches of different roughness (smooth and rough), the authors identified three mechanisms for momentum exchange as distinguished by the secondary flow and turbulence mixing; they calculated the momentum transfer through secondary flow and turbulent mixing using Equation (36) and Equation (37) respectively.

$$T_{mix} = \frac{1}{H}\int_0^H \left(\overline{-u'v'}\right) dz \tag{36}$$

$$T_{sec} = \frac{1}{H}\int_0^H \left(-U\left(V - \frac{1}{H}\int_0^H V dz\right)\right) dz \tag{37}$$

The momentum contributions from secondary current and from turbulence mixing were found to be in the same order of magnitude and this reflects the peak in momentum gradient associated with the transverse depth averaged mass transfer in the developing mixing layer. As the water depth increases the contributions to momentum exchange by secondary current exceeds the contribution by the turbulent mixing. Furthermore, Vermaas et al. described the total longitudinal momentum gradient for the flume width using Equation (38)

$$\frac{\partial M_t}{\partial x} = \frac{4\rho D V_{100}}{B} \int_{x=0}^{L} V_{100} dx \tag{38}$$

where V_{100} is the depth averaged transverse velocity at the roughness interface, D is the transverse momentum exchange, B is the channel width, M_t is the momentum transfer. The authors observed that the longitudinal gradient in momentum associated with transverse depth-averaged mass transfer is approximately proportional to the depth mean transverse velocity as illustrated in Figure 33.

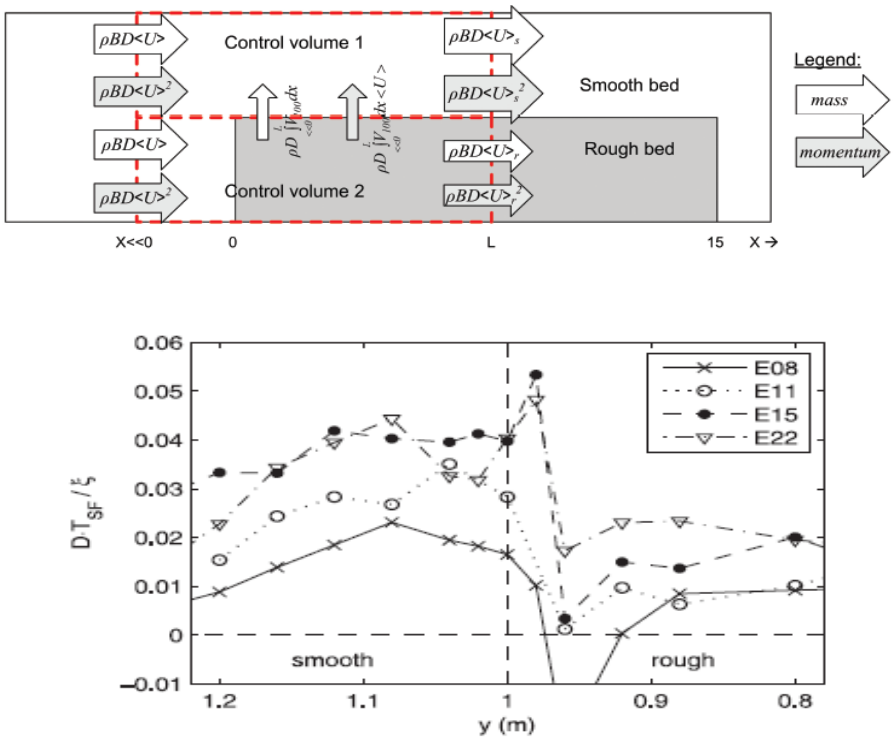

Figure 33: Mass and Momentum Balance set up and the Distribution of the Momentum Transfer by Horizontal Turbulence Mixing (Vermaas et al., 2010)

The generation of shear layer at interface between the vegetation and the underlying water flow has been linked to the flow penetration into the vegetated bed (Nepf and Vivoni, 2000). The thickness of this interface is a function of the flow and plant characteristics and this can be determined by the distance the flow can penetrate into the canopy. As a measure of flow penetration, Nepf and Vivoni (2002) proposed the penetration depth to be located at a

distance from the top of vegetation to the point where turbulent shear stress decays to 10% of its maximum value Figure 34. Nikora and Nikora (2010) proposed the determination of penetration depth using vertical distribution of other components of Reynolds stress tensor or their combinations (normal and shear turbulent stresses). The estimates of penetration depth from shear stresses are found to be more closely correlated with the normal stress profiles which suggests the method being satisfactory (Nikora and Nikora, 2010).

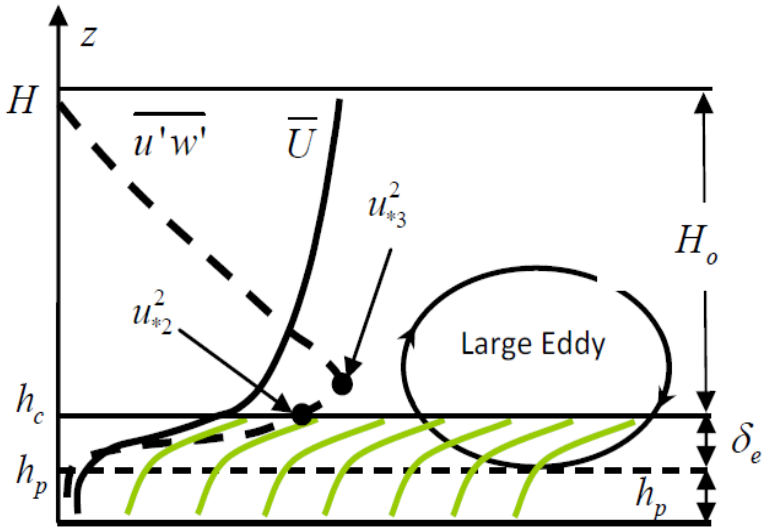

Figure 34: The Penetration Depth (h_p) of the Turbulent Shear Stress

Nezu and Sanjou (2008) investigated turbulence structure and coherent motion in vegetated canopy open-channel flows. The purpose of the work was to investigate the effects of rigid vegetation density on turbulence structure for constant flow depth. The authors described the velocity distribution only near the vegetation edge by the exponential law of Equation (39):

$$\frac{U}{U_h} = exp\left(\propto \left({}^{H}/_{h_v} - 1\right)\right) \tag{39}$$

in which $\propto \equiv \left(\frac{C_d a h^3}{4l^2}\right)^{1/3}$ becomes a constant value if the mixing length l is constant within the canopy, U is the mean velocity, U_h is the velocity at the top of vegetation, h_v is the vegetation height and H represents the flow depth. The drag coefficient was estimated from the momentum Equation (40):

$$\frac{\partial}{\partial x}\left(\frac{-\overline{uw}}{u_*^2}\right) = \frac{1}{2} C_d a \left(\frac{U}{u_*}\right)^2 - \frac{1}{H-h} \tag{40}$$

From their results, the vertical Reynolds stress attains a maximum value near the vegetation edge; while a decrease in the Reynolds stress was also observed within the canopy due to the drag in the vegetation elements. In conclusion, vegetation elements obstruct momentum transfer within the vegetation. Hitherto in the experiment, the turbulence penetration into the canopy was examined with vegetation density; the study revealed that the penetration of Reynolds stress into the canopy increases as the vegetation density becomes smaller. This inferred that the effects of vegetation density on turbulence structure are reduced at sparser density. The distribution of turbulence intensities in their work was based on the equilibrium state equations of turbulent kinetic energy for two dimensional open channel flow as proposed by Nezu, (1977) using the following equations (Nezu, 1977):

$$\frac{u'}{U_*} = 2.3\exp(-\varepsilon) \tag{41}$$

$$\frac{v'}{U_*} = 1.27\exp(-\varepsilon) \tag{42}$$

where $\varepsilon = (y-h)/(H-h)$

Equation (41) and Equation (42) are described by Figure 35. The maximum streamwise turbulence intensity attains a maximum at the top of the vegetation, whereas the vertical

turbulent intensity attain maximum below the vegetation. The magnitude of both streamwise and vertical intensities is seen to become similar in the case of dense vegetation.

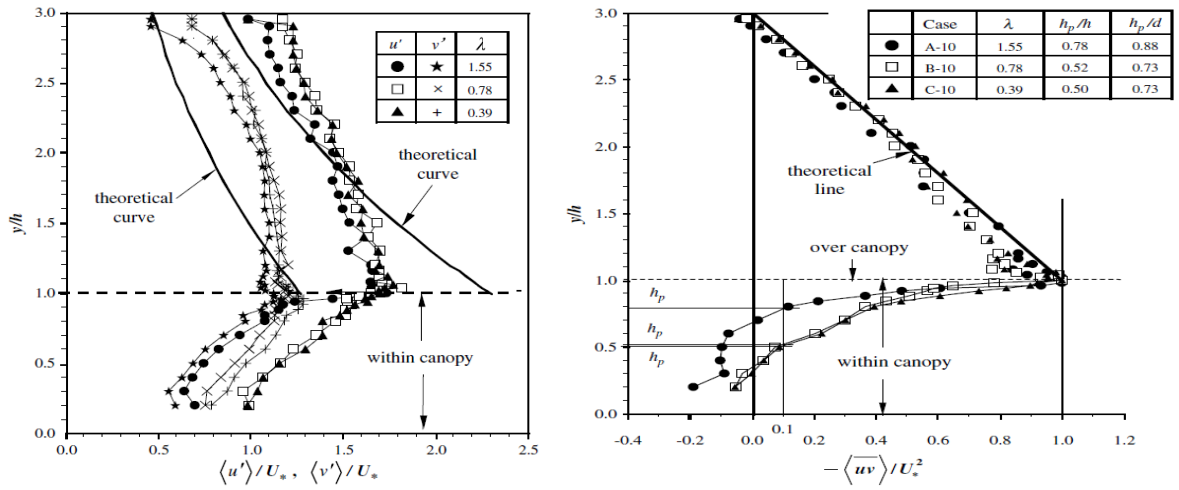

Figure 35：Averaged Turbulence Intensities and Shear Stress (Nezu and Sanjou, 2008)

Finally, Jarvela (2002) studied the flow resistance of natural grasses, sedges and willows in the laboratory flume to investigate the effect of density and vegetation type on flow velocity. The vegetation was investigated in various configurations under submerged and emergent conditions. The results showed significant variation in friction factor (f) with flow depth, velocity and vegetation density. He found that the friction factor mostly depended on the relative roughness in the case of grasses and flow velocity in the case of willows. Friction factor (f) appears to increase with depth for leafless willows. The friction factor (f) decreases with increasing Reynolds number for grasses and sedges but remain independent with leafless willows (Figure 36).

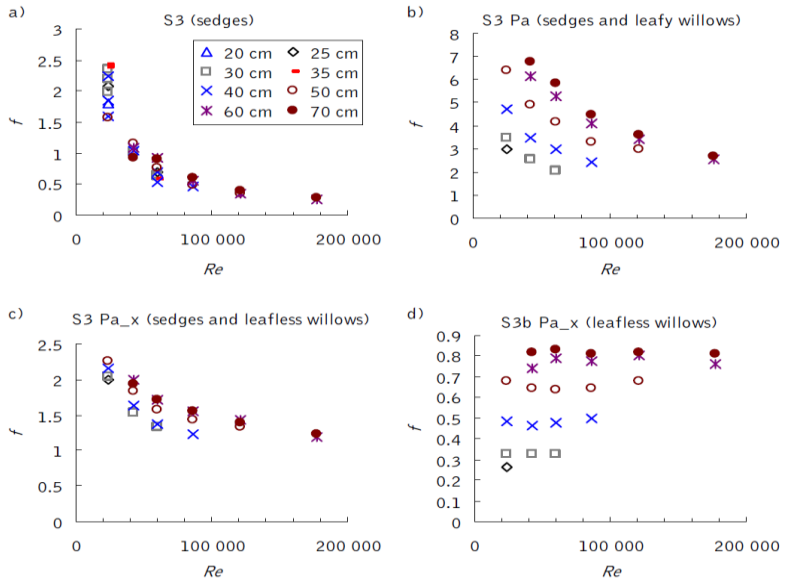

Figure 36：Variation of Relative Roughness with Friction Factor f and the Reynolds Stress (Jarvela, 2002)

The results showed good correlation of the friction factor with natural grass and sedges and weaker correlation of friction factor with series of leafless willows under similar conditions. This indicates that relative roughness may not only be appropriate to estimate friction factor.

In conclusion, many studies on aquatic plants have been undertaken, yet no attention has been paid to how heterogeneous roughness involving patchy aquatic vegetation such as grass and shrubs influence flow behaviour and characteristics. Hence lack of knowledge on the transport processes and shearing mechanisms in a patchy vegetated heterogeneous flow. This research is therefore to evaluate how the dynamics of the flow field change when heterogeneous roughness involving vegetation is present in order to mitigate flood risk.

2.10 Shiono and Knight Method

The Shiono and Knight method (SKM) (Shiono and Knight, 1988, Shiono and Knight, 1991) is a two-dimensional mathematical model based on the Reynolds Averaged Navier-Stokes (RANS) equations for steady uniform flow in the streamwise direction. In order to predict the lateral variation of depth-averaged velocity and boundary shear stress in open channel, the depth-averaged momentum equation is solved for steady uniform turbulent flow. The equation for the longitudinal streamwise component of momentum may be combined with the continuity equation to give (Shiono and Knight, 1991):

$$\rho\left[\frac{\partial(UV)}{\partial y}+\frac{\partial(UW)}{\partial z}\right]=\rho g S_0+\frac{\partial(-\rho\overline{u\prime v\prime})}{\partial y}+\frac{\partial(-\rho\overline{u\prime w\prime})}{\partial z} \tag{42}$$

Equation (42) includes the secondary flow terms in the bracketed part of the LHS, while the bracketed parts of the second and third terms on the HRS are the horizontal and vertical Reynolds stresses respectively. Assuming that $W(H)=W(0)$, the depth-averaged of Equation (42) is:

$$\frac{\partial(\rho UV)_d}{\partial y}=\rho g S_0+\frac{\partial(-\rho\overline{u\prime v\prime})_d}{\partial y}+\frac{\partial(-\rho\overline{u\prime w\prime})_d}{\partial z} \tag{43}$$

where:

$$(\rho UV)_d=\frac{1}{H}\int_0^H \rho UV \tag{44}$$

Considering the forces on a fluid element and conservation of momentum, Equation (43) can be shown to be equivalent (Shiono and Knight, 1988) to:

$$\frac{\partial H(\rho UV)_d}{\partial y}=\rho g H S_o+\frac{\partial H(-\rho\overline{u\prime v\prime})_d}{\partial y}-\tau_b\left(1+\frac{1}{s^2}\right)^{\frac{1}{2}} \tag{45}$$

where τ_b is the boundary shear stress, s is the side-slope.

The following assumptions form closure to Equation (45):

$$U_d = \frac{1}{H}\int_0^H U dz; \tau_b = \left(\frac{f}{b}\right)\rho U_d^2;\ \bar{\tau}_{yx} = \rho\bar{\varepsilon}_{yx}\frac{\partial U_d}{\partial y};\quad \bar{\varepsilon}_{yx} = \lambda U_* H; U_* = \left(\frac{1}{8}f\right)^{\frac{1}{2}} U_d.$$

Equation (45) can be rewritten as:

$$\rho g H S_o - \frac{1}{8}\rho f U_d^2\left(1+\frac{1}{s^2}\right)^{\frac{1}{2}} + \frac{\partial}{\partial y}\left\{\rho\lambda H^2\left(\frac{f}{8}\right)^{\frac{1}{2}} U_d\frac{\partial U_d}{\partial y}\right\} = \frac{\partial}{\partial y}\left[H(\rho UV)_d\right] \qquad (45a)$$

2.10.1 The Analytical Solution

An analytical solution was developed for Equation (45a) by Shiono and Knight (1991) for the depth averaged velocity U_d for constant depth region using the eddy viscosity model as:

$$U_d = [A_1 e^{\gamma y} + A_2 e^{-\gamma y} + k]^{\frac{1}{2}} \qquad (46)$$

and in side-slope regions:

$$U_d = [A_3\xi^{\alpha_1} + A_4\xi^{-\alpha_1-1} + \zeta\xi + \eta]^{\frac{1}{2}} \qquad (47)$$

where:

$$\gamma = \left(\frac{2}{\lambda}\right)^{\frac{1}{2}}\left(\frac{f}{8}\right)^{\frac{1}{4}}\frac{1}{H} \qquad (48)$$

$$k = \frac{8gS_0H}{f}(1-\beta) \qquad (49)$$

$$\beta = \frac{\Gamma}{\rho g S_0 H} \qquad (50)$$

$$\alpha_{1=} -\frac{1}{2} + \frac{1}{2}\left[1 + \frac{s(1+s^2)^{\frac{1}{2}}}{\lambda}(8f)^{\frac{1}{2}}\right]^{\frac{1}{2}} \qquad (51)$$

$$\zeta = \frac{gS_0}{\frac{(1+s^2)^{\frac{1}{2}}}{s}\left(\frac{f}{8}\right) - \frac{\lambda}{s^2}\left(\frac{f}{8}\right)^{\frac{1}{2}}} \tag{52}$$

$$\eta = -\frac{\Gamma}{\frac{(1+s^2)^{\frac{1}{2}}}{s}\rho\left(\frac{f}{8}\right)} \tag{53}$$

where λ is the dimensionless lateral eddy viscosity coefficient, f is the Darcy-Weibach friction factor, Γ the secondary flow term, ρ the water density, g the gravitational acceleration and S_0 the bed slope, k is a coefficient constant and ξ is the depth function on the side-slope. The unknown A_1 to A_4 are evaluated through the application of the appropriate boundary conditions to Equation (46) (Shiono and Knight, 1991).

2.10.2 Calibration coefficients f, λ, and Γ

The SKM is governed by the three calibration coefficient f, λ, and Γ which must be known before Equation (46) and (47) could be used. The parameter f and λ are both positive, and are connected to the boundary shear stress. The friction factor f has been shown to have the most influence on the SKM model, this is followed by the secondary flow term Γ, with λ less important (knight and Abril, 1996) and therefore to simplify the calibration procedure, constant and standard value of λ can be imposed on all panels ($\lambda = 0.07$) (Elder, 1954). In the SKM application, both f and λ are assumed to be constant for a given panel, but f may be varied laterally between panels by using common f values at the panel boundaries and assumes that f varies linearly between these values as shown in Figure 37 (Omran and Knight, 2006, Knight et al., 2007).

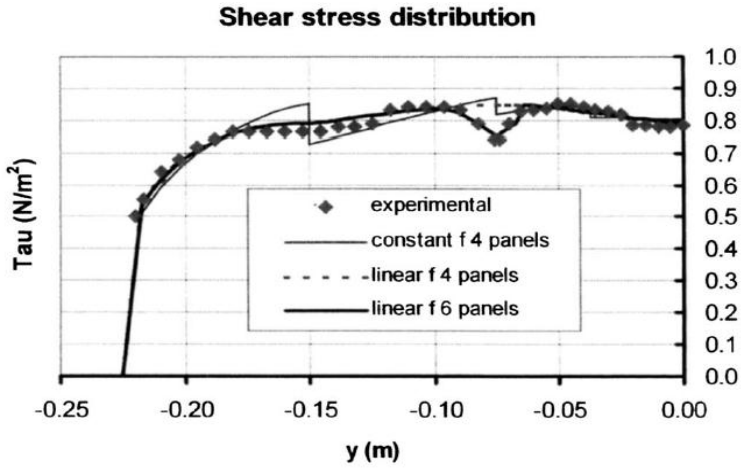

Figure 37: SKM Shear Stress Distribution (Knight et al., 2007)

The secondary flow term Γ shows the gradient of the force per unit length due to secondary flow. Figure 38 shows the secondary flow representation of a trapezoidal channel, secondary current cells and their signs due secondary flow rotation (Omran and Knight, 2006). It can be seen from the figure that the depth-averaged $(UV)_d$ value of secondary flow term can either be positive or negative depending on the rotational direction of the secondary current cell. The panel locations therefore depend on the rotational status of the secondary current cell. Therefore, the secondary flow term Γ may require calibration in order to model the depth-averaged velocity distribution. However, Abril and Knight (2004) have shown a relationship between the secondary flow term Γ and the friction factor f. For higher value of f, a higher value of Γ/H is required to calibrate the model (Abril and Knight, 2004).

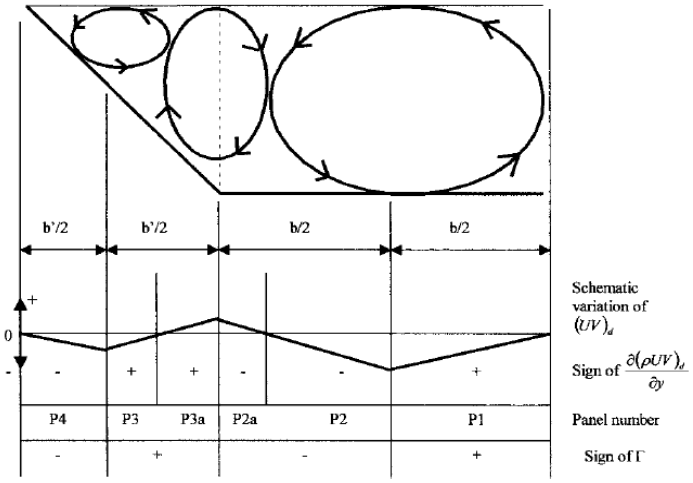

Figure 38：Secondary current cells, secondary flow term and panel locations (Omran and Knight, 2006, Knight et al., 2007).

3 Experimental Methods, Instrumentation and Data Processing

3.1 Introduction

This chapter outlines the experimental data collected and discusses the setup and methods used to collect the data. The data is used to evaluate the channel's resistance through calculation of traditional resistance parameters (e.g. Manning's roughness coefficient n and Darcy-Weisbach friction factor f) in order to assess the conveyance capacity of the channel. Details relating to the data acquisition and experimental setup are presented and discussed in section 3.2. Section 3.3 discusses the stage-discharge experiments, whilst the point velocity measurements with an acoustic Doppler velocimeter (ADV) and Pitot tube are presented in sections 3.4 and 3.5 respectively. Section 3.6 discusses the processing of the velocity data to filtering extent. Finally, the normal depths of flow and velocity measurement obtained from particle image velocimetry (PIV) are presented in section 3.7.

3.2 Experimental Setup

The experiments were conducted in a 22m long rectangular re-circulating flume of width $B = 614mm$ and depth $H = 365mm$ at the University of Birmingham. The flume has sidewalls made of glass with a honeycomb section installed at the inlet to eliminate swirl and prevent any effects which can be attributed to the entrance. The flume is fed from an overhead water tank located approximately 15m above the flume with a capacity of 10,000 gallons (45,460.9 litres). In turn, the overhead tank is supplied by an underground water tank with a capacity of 62,000 gallons (281,857.7 litres). The water surface profile in the flume is controlled by an adjustable downstream tailgate which allows the setting of the flow depths to achieve normal depth flow. The set-up of the experimental flume is shown in Figure 39.

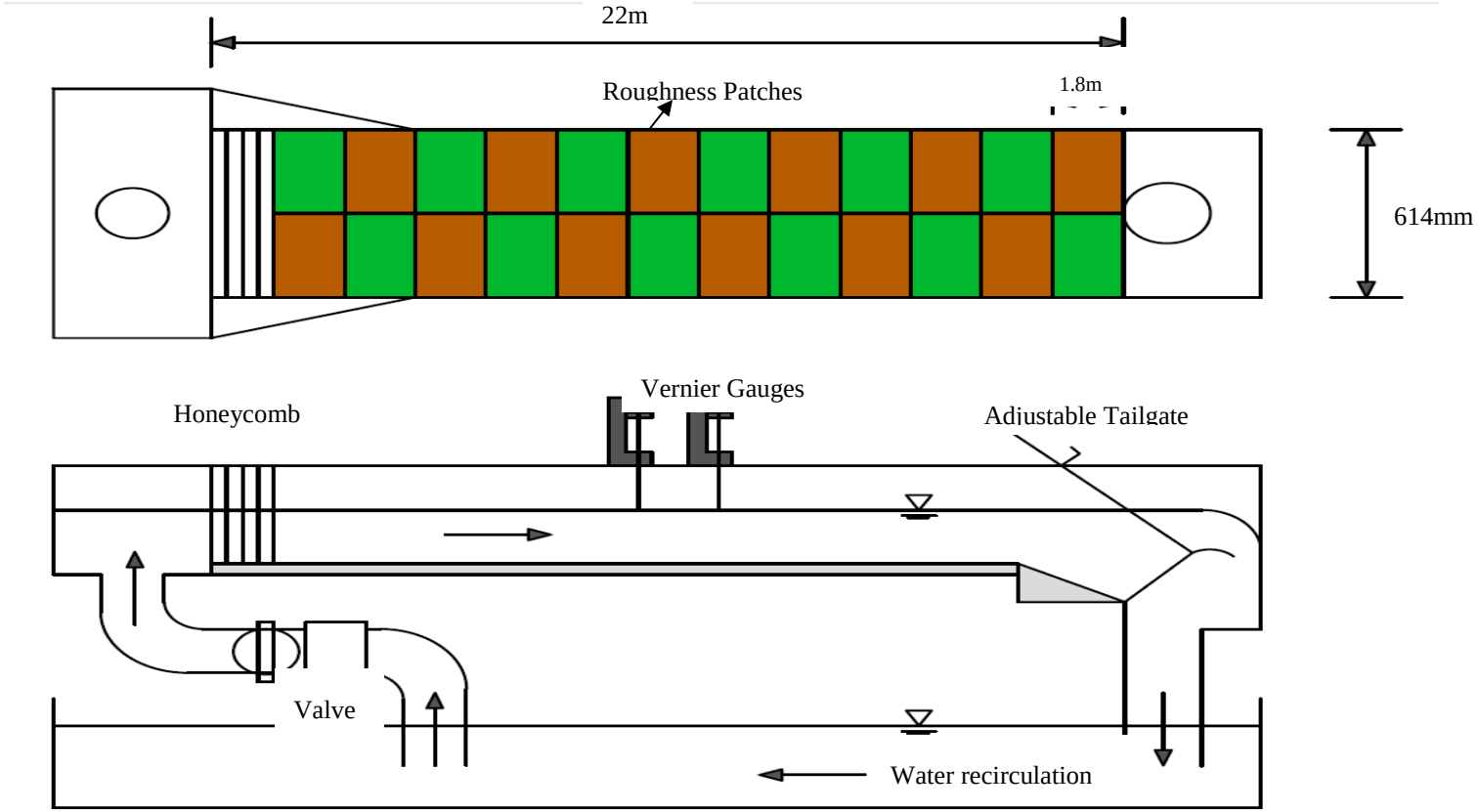

Figure 39: Schematic of the Experimental Channel

The water depth within the flume was measured in the longitudinal direction using Vernier pointer gauges with an accuracy of $\pm 0.5mm$ and situated at approximately 1m intervals along the streamwise length of the channel (Figure 40).

Figure 40：Venier Gauge for Water Depht Measurement

In keeping with Jesson et al. (2013), patches of roughness of length 1830mm by width 307mm were installed in an alternating fashion as illustrated in Figure 41. The first bed configuration examined consisted of a patch of submerged vegetation which was composed of artificial grass (Astroturf) and assumed to be akin to flexible vegetation as shown in Figure 41a. Next to the Astroturf was gravel of d_{75} = 10mm (Figure 41a). The gravel and Astroturf alternated along the length of the channel every 1.83m (~3B) as shown in Figure 41. For the second bed configuration the Astroturf was replaced by inflexible plastic dowels of width 15mm vertically fixed using $20mm$ grid spacing (see Figure 41b). The plastic dowels spacing was chosen to reproduce the staggered distribution of rigid vegetation roughness in aquatic environment (Figure 41b) based on the critical spacing ratio of $\left({}^{l}/_{w} > 1\right)$ suggested by Igarashi (1984) and Sun and Shiono (2009) which produces vortex shedding behind each rigid vegetation element.

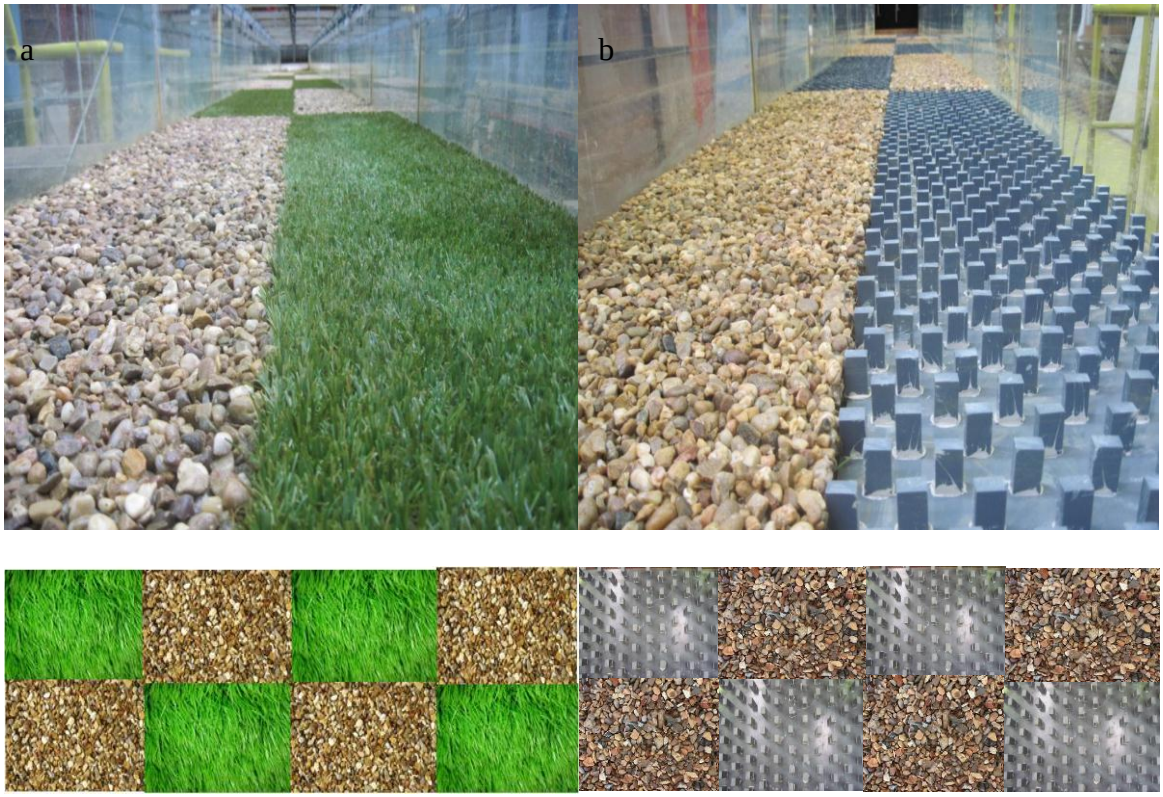

Figure 41: Bed Roughness Configuration Plan View of Roughness Patches for Experiment One and Two

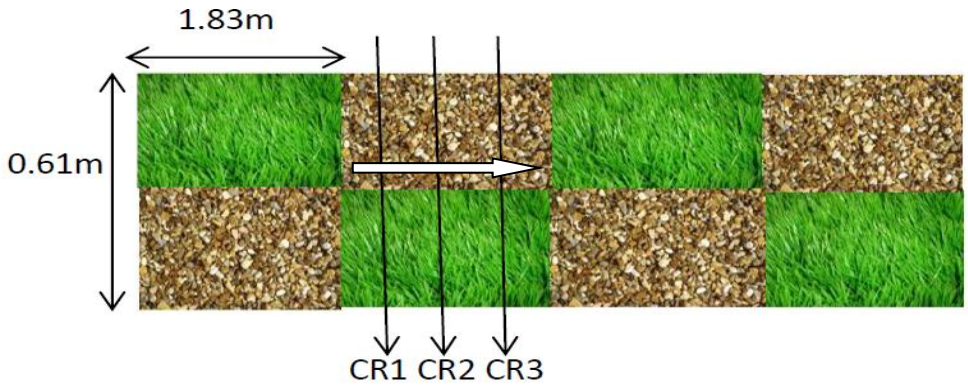

Figure 42: The Length of Patches and the Measured Cross Section Positions. The arrow indicates the streamwise flow direction whilst CRS1, CRS2 and CRS3 represents cross-section one to three.

Vegetation parameters were measured using a digital Vernier Caliper with accuracy $0.01mm$, the stem height h_v, stem width w and stem thickness t of the modelled after artificial grass (Astroturf) were measured to be $26mm, 1mm\ and\ 0.15mm$ respectively; each plant

consisting of 16 stems joined together to form a bunch of $2.3mm$ diameter, the coverage areal density of the grass bed was estimated to be approximately $15625\ plants/m^2$. The parameters of the thick plastic dowel were measured to be $26mm$ high, $15mm$ wide and thickness of $10mm$ with an areal density of $800\ plants/m^2$. These properties are summarized in Table 1.

	h_v	w	t	Areal Density
Grass	$26mm$	$1mm$	$0.15mm$	$15625 plants/m^2$
Rigid	$26mm$	$15mm$	$10mm$	$800 plants/m^2$

Table 1: Summary of Vegetation Structural Properties

Using the size distributions of the vegetation stem, the frontal area per unit volume a_v was calculated at vertical height $\Delta z = 0.5mm$ interval as:

$$a_{v(z)} = \frac{w_{(z)} n_v}{A_b} \tag{54}$$

where A_b is the bed area, n_v is number of vegetation stem per bed area. For the experimental grass and rigid strip, the average frontal area per unit volume were $62m^{-1}$ and $12m^{-1}$ respectively. The vegetation stem flexural rigidity for experimental grass was determined using:

$$J = EI_2 \tag{55}$$

where E is the modulus of elasticity and I_2 is the second moment of area. For the experimental grass the flexural rigidity J was obtained as $2.83 \times 10^{-6}\ Nm^2$.

The gravel sample was characterised by sieve analysis. The gravel particle size distribution was analysed using BS 1377: Part 2: 1990 with a mechanical test sieve diameters 14mm, 10mm, 6.3mm, 5mm, 3.35mm, and 2mm. The gravel was shown to have D_{75} = 10mm, and D_4 = 5mm, where the subscript gives the percentage of the grains passed through the sieve

sized diameter. The gravel was attached to the bed with a layer of waterproof adhesive. The grains were densely packed and pressed into place to ensure a bond of the particles.

In what follows, these roughness configurations are referred to as EXPT1 and EXPT2 for the first and second bed configurations respectively. In addition, the gravel region of the bed extends over a distance of $0 \leq {}^{y}/_{B} \leq 0.5$ with the roughness boundary located at ${}^{y}/_{B} = 0.5$, and the vegetated region extending over $0.5 \leq {}^{y}/_{B} \leq 1.0$, where y is the lateral distance in transverse direction and B is the channel width.

Velocity measurements were undertaken at three cross-sections hereafter referred to as CRS1, CRS2 and CRS3 at distances of 17.5m, 18.05m and 18.6m respectively downstream from the channel inlet. The numbering sequence is summarized in Table 2 as positions downstream the roughness switch (see Figure 42). From Table 2, CRS1 indicate the first cross-section downstream the roughness switch, CRS2 is the middle cross-section of the roughness strip, and CRS3 is the cross-section upstream the next roughness switch as illustrated in Figure 42. Analysis of velocity data reported in section 3.7 illustrates that the flow was fully developed at these measurement locations.

Cross-Section	$x_{distance\ from\ switch}\ (m)$
CRS1	0.35
CRS2	0.90
CRS3	1.45

Table 2: Measured Cross-Section Positions Relative Roughness Switch

3.2.1 Discharge Measurement

The discharge was measured using a Kent-Taylor $102mm$ Magmaster flow meter with a $\pm 0.2\%$ accuracy which was installed in a pipe leading from the header tank which fed the channel. To verify the accuracy of the flow meter, the discharge was checked manually by directing the outflow from the flume into volumetric tanks of width $m = 1.5$m and breadth $d = 1.5$m and the discharge calculated volumetrically using Equation 54:

$$Q_{tank} = \frac{\Delta d * m * d}{\Delta t} \tag{54}$$

where Δd is the change in water depth in the tank and Δt is the time interval over which the depth changes in the tank. Using both methods, the difference in discharge was investigated over a range of flow rates $(0.0020 - 0.085 m^3 s^{-1})$. Table 3 shows the calculated discharge value of the volumetric measurement in comparison with the flow meter value. It can be seen from the table that the difference in discharge from both method is less than 2% at low discharges and approximately 0.5% at high discharges.

$Q_{gauge}(ls^{-1})$	$Q_{tank}(ls^{-1})$	Error Difference (%)
10.4	10.2	1.92
26.9	26.6	1.12
40.7	40.4	0.74
55.5	55.3	0.36
60.7	60.4	0.49

Table 3: Discharge Comparison Calculated from the Volumetric Tank and the Flowmeter

In what follows, the experiments were undertaken for two discharges (Q). The first discharge was 30.0 l/s and corresponded to a flow depth (H) of $130mm$ and width to depth ratio ($^{B}/_{H}$) of 4.7. The second discharge of $40l/s$ corresponded to a depth $142mm$ and a $^{B}/_{H}$ value of 4.3. The experiments were conducted in fully developed flow conditions and relate to sub critical, uniform flow as shown in section 3.7.

3.2.2 Bed Slope

The bed slope of the channel was measured by setting a horizontal water surface which was used as a datum.

The water depth was measured longitudinally using the 21 Vernier gauges stationed along the channel and the channel bed slope calculated from the water depth measurements. The uncertainty in the depth measurement is estimated as $\pm 0.5mm$. Two methods were used to calculate the bed slope, S_o. The first method is the least square regression method of the form $y = ax + b$, where a and b define the slope and the intercept respectively. Figure 43 illustrates the channel bed slope using the least square regression method with two different quantities of water for both EXPT1 and EXPT2. The slopes are consistent for the two quantity of water measured.

The second method was used to verify the consistency of the linear regression method. Defining H_i and Δx_i as the depth at the i^{th} guage and the distance of the i^{th} gauge from the $(i-1)^{th}$ gauge respectively, for N gauges the first to last mean was calculated (Jesson, 2011) as:

$$S_o = \frac{H_N - H_1}{\sum \Delta x_i} \tag{56}$$

The calculated bed slopes using both methods are given in Table 4.

Experiment	Quantity of Water	Regression Method	First-to-Last Method
EXPT1	Depth 1	0.0008±0.0001	0.0008±0.0001
EXPT1	Depth 2	0.0008±0.0001	0.0008±0.0001
EXPT2	Depth 1	0.0011±0.0001	0.0011±0.0001
EXPT2	Depth 2	0.0011±0.0001	0.0011±0.0001

Table 4: Calculated Bed/Water Surface Slope Results

Given the constraints of constructing the experimental channel, the channel bed slopes are slightly different due to the different roughness distribution.

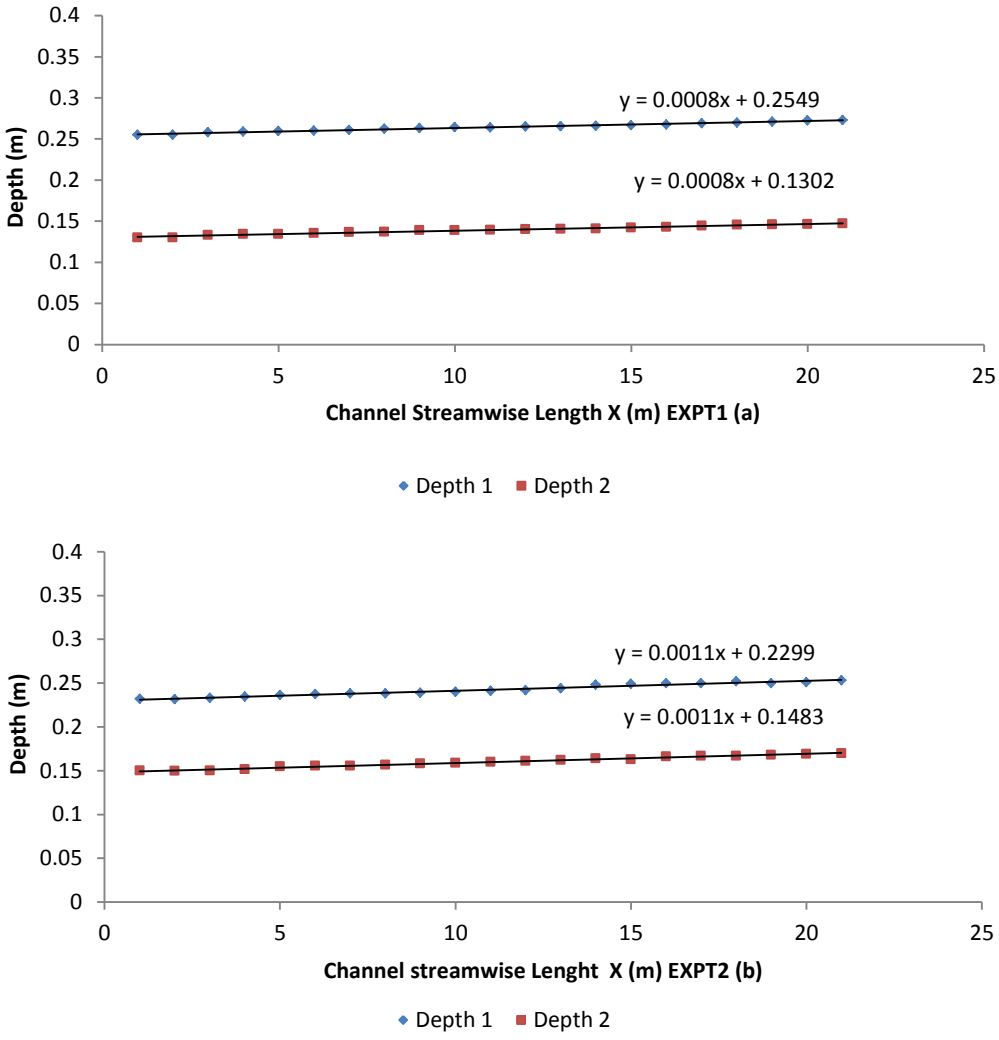

Figure 43: Bed Slope for (a) EXPT1 and (b) EXPT2

To examine the lateral variation in water levels, three series of measurement were undertaken in the transverse direction at the measured cross-sections over a distance of 0.6 meters. The measurements were taken with respect to a movable transverse carriage on which a Vernier gauge was attached. Figure 44 illustrate the lateral water surface profiles of at the measured cross-sections (CRS1, CRS2 and CRS3). The figures show approximately a $\pm 0.1mm$ variation in water surface level for all the three cross sections measured and is within the measurement accuracy of $\pm 0.5mm$.

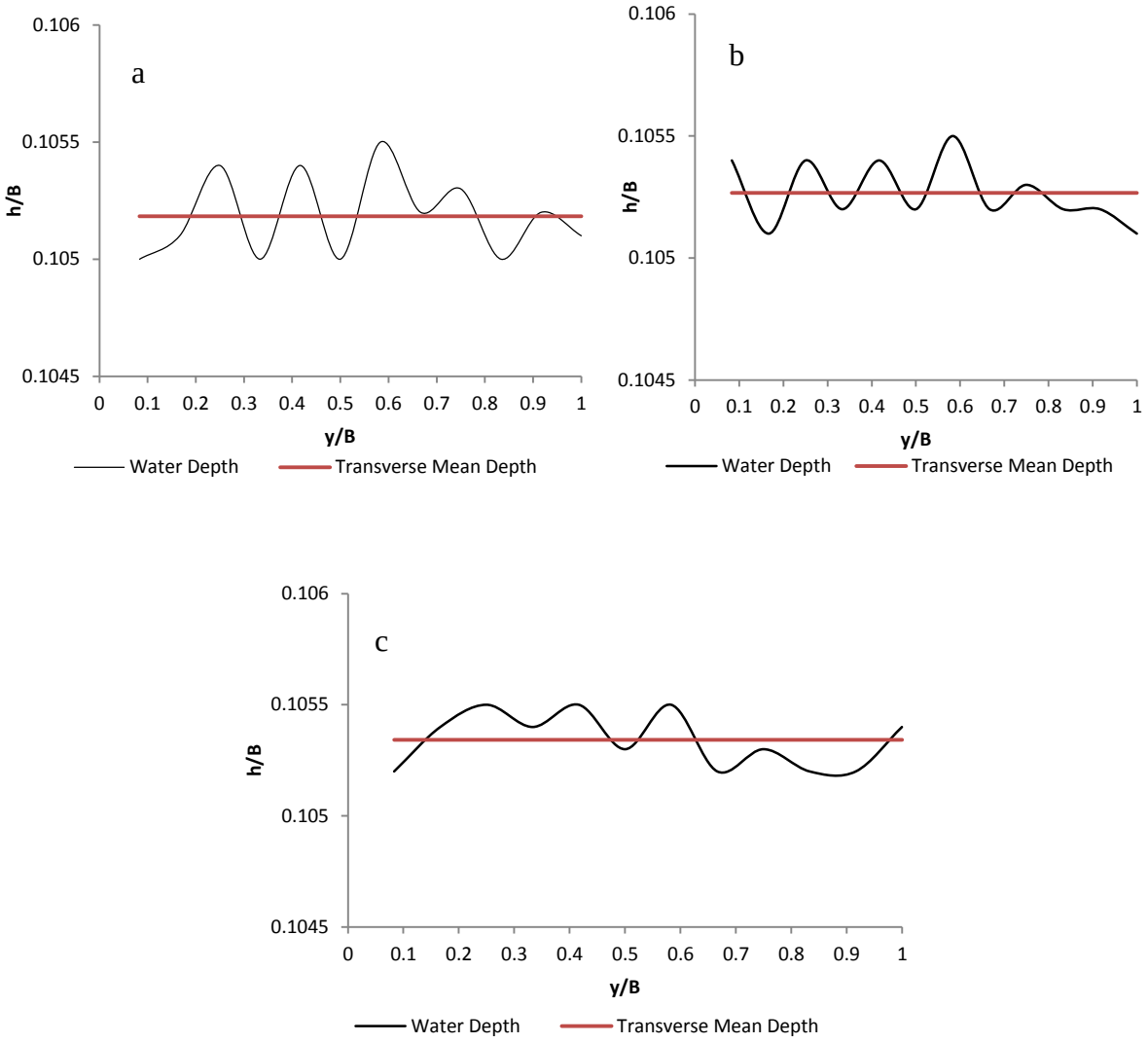

Figure 44: Lateral Variation of Water Surface Profile (a) CRS1, (b) CRS2 and (b) CRS3

3.3 Stage-Discharge Experiment

In order to construct a stage discharge curve for the experimental channel, it is necessary to find the normal depths at a number of different discharges. For each selected discharge, the tailgate was adjusted and the water depths measured using the Vernier gauges along the channel. The water surface slopes were calculated from these measurements. This process was repeated five times, with the adjustment of tailgate to give two positive water surface slopes (M1 profiles), two negative (M2 profiles) and a near zero water slope (see Figure 45). The water depth was measured at 17.5m downstream, a location within the measured cross-

sections for all the adjusted tailgate heights. Plotting the water surface slope and the corresponding depth as shown in Figure 45, normal depth was evaluated graphically. From the figure, water surface slope is zero for a tailgate height of 135mm with the corresponding depth of 222mm, which gives the normal depth for this flow discharge.

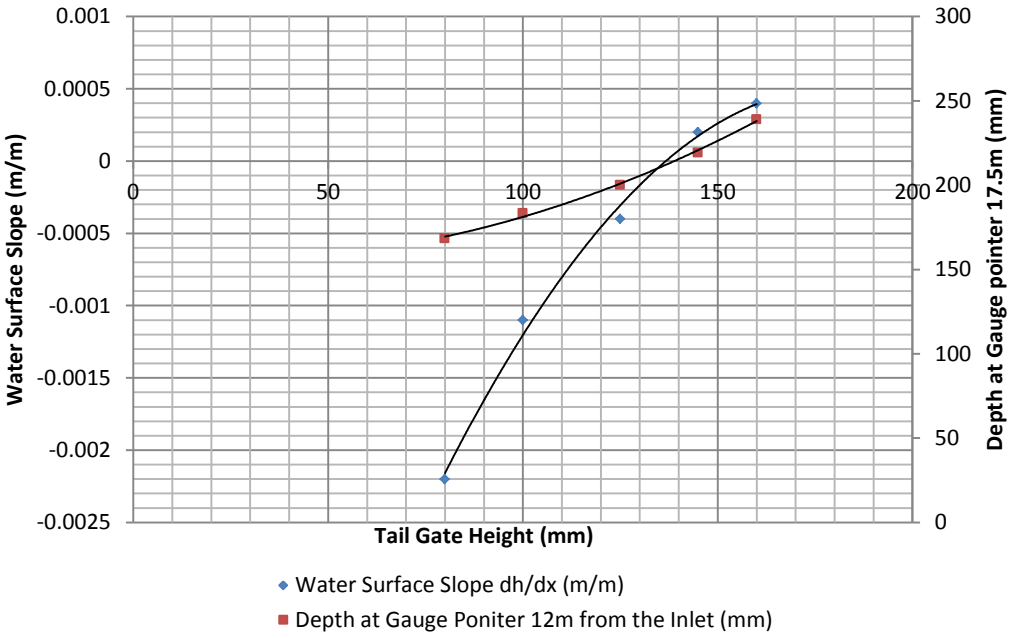

Figure 45: Example of Water Surface Slope and Depth versus Tailgate Height Graph

This process was repeated for a total of twelve discharges over a range of flow rates $(0.004 - 0.085 m^3 s^{-1})$. The normal depth criterion is necessary to obtain a true uniform flow which will allow the mean flow properties to remain unchanged for a reach around the measurement sections. Due to minor variation in water surface, the water depth was measured to an accuracy of $\pm 0.5 mm$ and the discharge measured to an accuracy of $0.2 ls^{-1}$ due to fluctuations in discharge readings. The stage-discharge curve for the experimental channel was constructed for EXPT1 and EXPT2 using the different roughness configurations shown in Figure 42.

The stage-discharge curves were constructed for theoretical models as a way of comparison with the experimental results, theoretical curves were calculated from:

1. Manning's equation, using roughness coefficient n value of 0.020 for gravel bed as recommended by Chow (1959).
2. Manning's equation, using the n value for grass, $n = 0.035$ (Wilson and Horritt, 2002; Chow, 1959).
3. Manning's equation, using the n value for rigid vegetated channel, $n = 0.040$ (Arcement and Schneider, 1984; Chow, 1959)

Additionally, a number of composite channel analysis methods were used to evaluate the channel resistance:

- Cox Method
- Lotter Method
- Colebatch Method
- Segmented Conveyance Method

The composite analysis methods above calculate a composite Manning's Roughness (n_c) coefficient for the channel using different formulae as provided in Appendix D. The segmented conveyance method however uses divided channel method to calculate total conveyance of the channel. These methods are applicable in evaluating the composite channel resistance for conveyance capacity estimation.

The curves are obtained through the algebraic power equation of the form $Q = AH^B$ where A and B are positive constants and H is the normal flow depth. The selected discharges ranged from low to high flow rates ($0.0020 - 0.1 m^3 s^{-1}$).

Figure 46 illustrates the stage-discharge curves for EXPT1 and EXPT2. The power curves fit with correlation coefficient, R_{cc}, such that $R_{cc}^2 = 0.9991$ and $R_{cc}^2 = 0.9989$ for EXPT1 and EXPT2 respectively. From the correlation coefficients, it can be seen that the stage-discharge

curves for the experimental channel follows the standard form for open channel flow for both roughness configurations. Moreover, the results show some similarities in the stage-discharge relationship with increasing gradients at low flow rates (Figure 47) relative to higher flow rates.

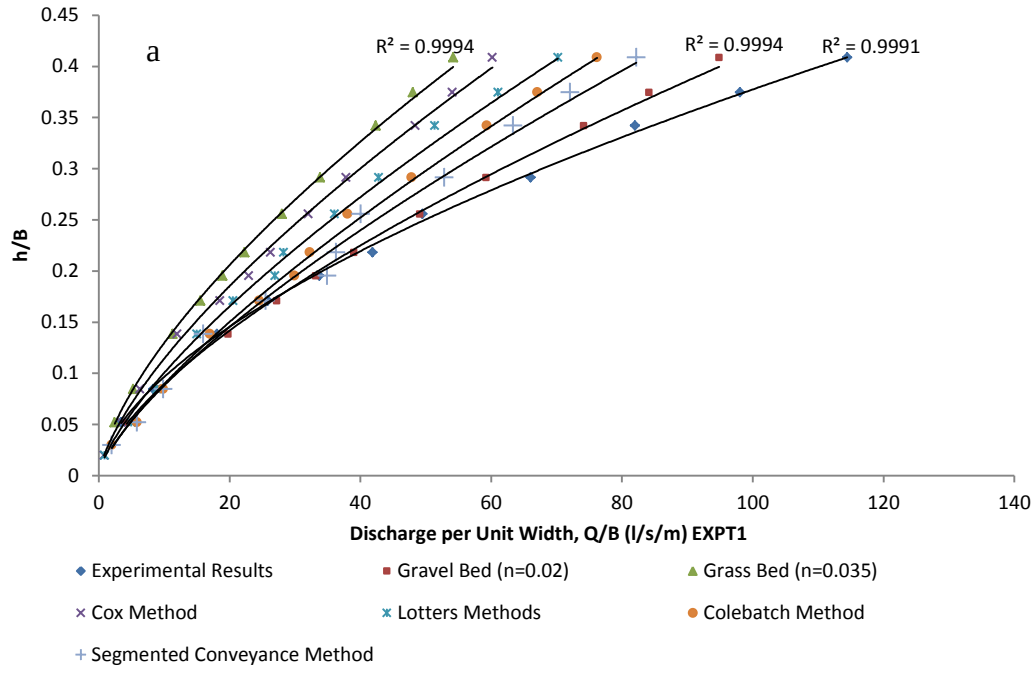

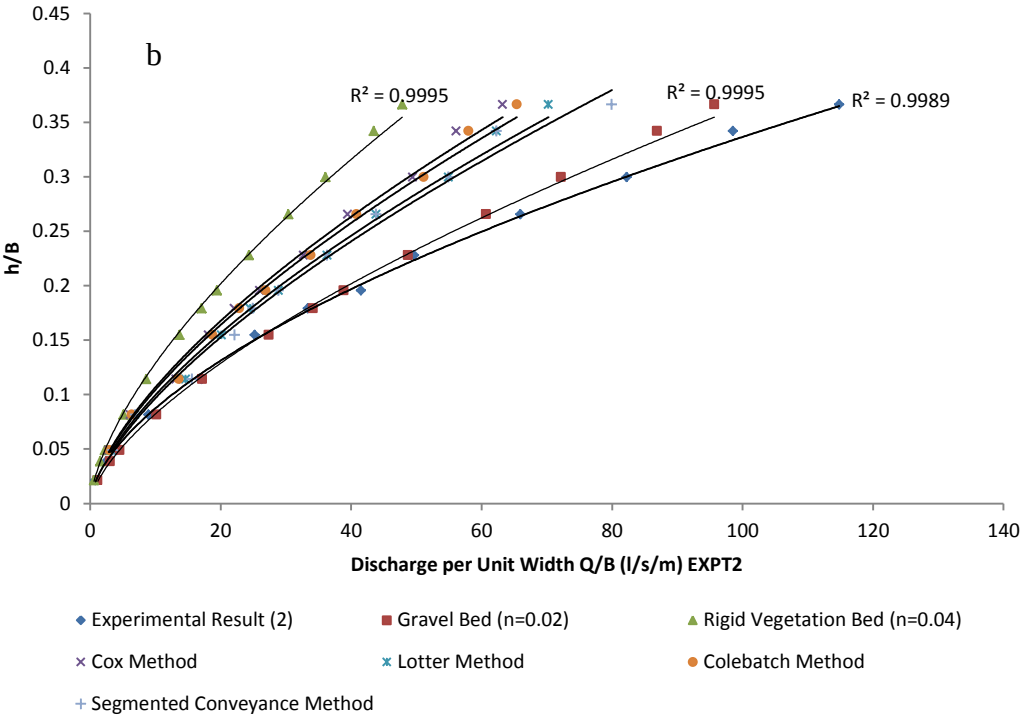

Figure 46: Stage-Discharge Curve in Comparison to Manning's Theoretical Model for Gravel and Vegetated Bed, (a) EXPT1, (b) EXPT2

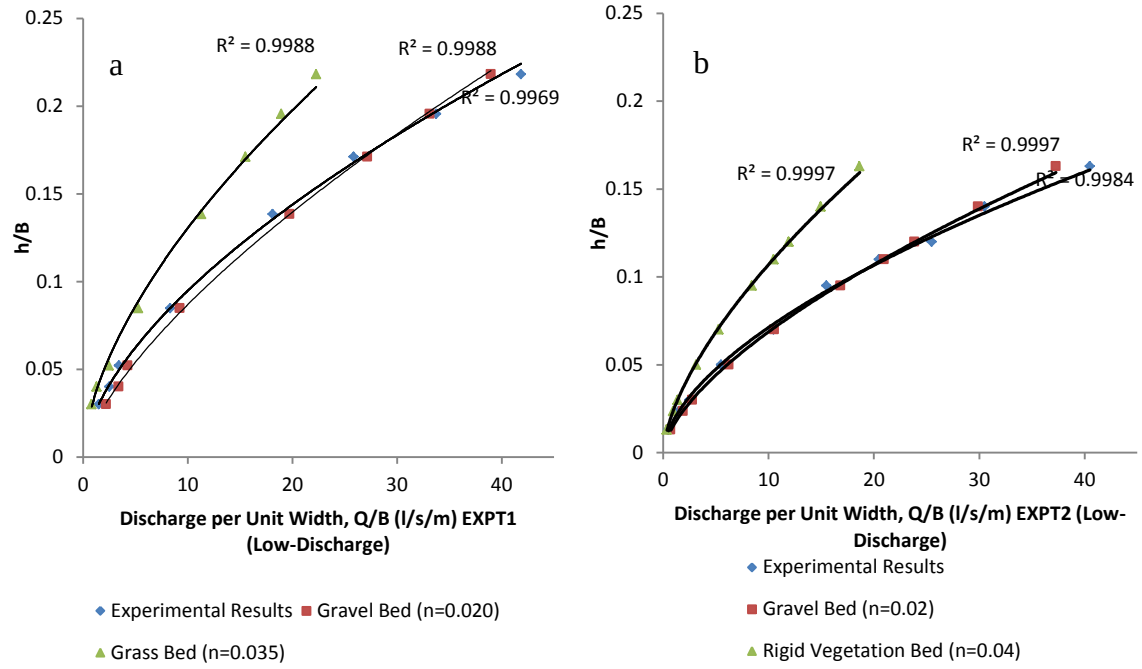

Figure 47: Stage-Discharge Curve in Comparison to Manning's Theoretical Model for Gravel and Vegetated Bed (Low-Discharge), (a) EXPT1, (b) EXPT2

As can be seen from Figure 46, for a given discharge; the stage-discharge curves of both EXPT1 and EXPT2 tending to be different as the discharge increases. A higher stage is recorded for EXPT1 relative to EXPT2 given an equivalent discharge (Figure 48). This can be attributed to a more hydraulically rough section in EXPT1, which causes a deceleration of the flow velocity in EXPT1 (Figure 49) given that Q is constant increases h relative to EXPT2 as shown in Figure 48. The bulk mean velocity U_b in Figure 49 was calculated from $\left(U_b = \frac{Q_s}{A}\right)$ where Q_s is the actual selected discharge and A is the channel cross-section area (Bh), B is the channel width and h is the normal depth.

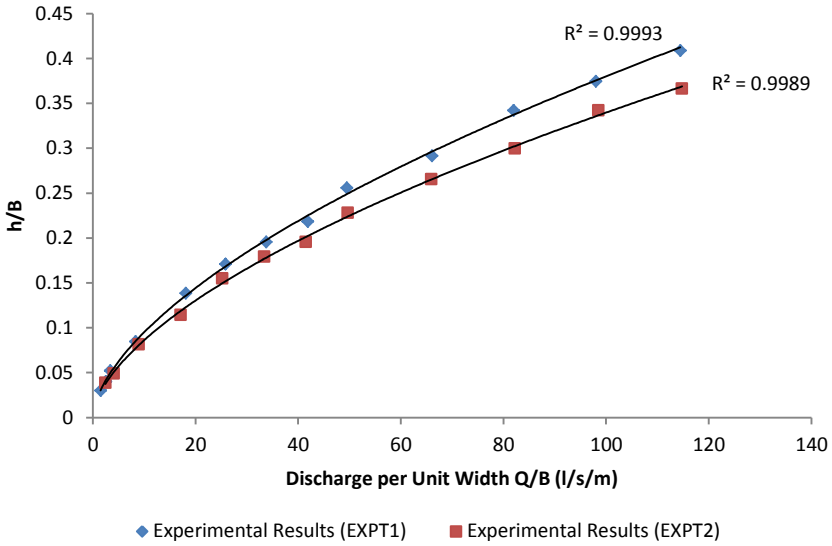

Figure 48: Stage-Discharge Curve for EXPT1 and EXPT2 showing increase in Stage in EXPT1 for a given Discharge

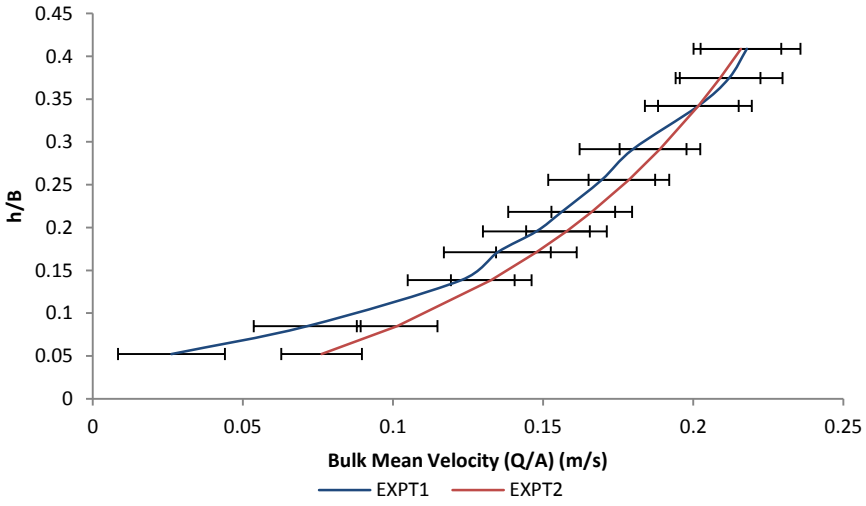

Figure 49: Channel Mean Velocity (Q/A) for EXPT1 and EXPT2

Comparing the stage-discharge curves from the experimental data and the Manning's theoretical curves, the curves can be seen to show some relative roughness effects for gravel and vegetated beds based on the standard roughness coefficients n adopted. The Manning's theoretical model underestimated the discharge for a given h for both EXPT1 ($n = 0.020$)

($n = 0.035$) (Figure 46a) and EXPT2 ($n = 0.020$) ($n = 0.040$) (Figure 46b) respectively. The underestimation is more apparent with the vegetation bed showing increased divergence from the experimental data relative to the gravel bed. However, the difference between the experimental and theoretical curves can be attributed to the different standard coefficient n adopted which show to have greater impact when the channel is assumed to be fully vegetated using the standard coefficient n = 0.035 and 0.040 for grass and rigid vegetation respectively. The underestimation is equally noticeable at low flow rates $\left(\frac{Q}{B} \leq 40\right)$ (Figure 47). For the gravel bed, the theoretical model slightly underestimated the discharge when compared to the experimental results Figure 46. It should be noted that the theoretical curve for vegetated bed increased higher with stage relative to the gravel bed and experimental result.

For a different composite channel analysis method of evaluating channel resistance, it can be seen from Figure 46 some differences relative to the experimental data. While the results vary depending on the roughness coefficient, the composite methods underestimated the discharge relative to the experimental data. The segmented conveyance discharge method often produces higher discharges relative to the other methods. However, the methods produce more variability in EXPT1 relative to EXPT2 (Figure 46a and 46b).

3.3.1 Variability of Manning's Roughness Coefficient (n) and Friction Factors (f)

The estimation of Manning's roughness coefficient n and friction factor f are essential in describing the channel resistance and its effects on the subsequent velocity and shear distributions in open channel system (Chow, 1959). The value of roughness coefficient n for the experimental channel was calculated from the measured discharge and normal depth using Equation (5).

The experimental results indicate a variation in roughness coefficient between EXPT1 and EXPT2 for a given discharge and normal depth. Figure 50 show the variation of the

Manning's roughness coefficient n with normalised stage h. As one may expect from the figure, the effects of bed roughness is more pronounced near bed $\left(\frac{h}{B} < 0.1\right)$ with an increased area of flow deceleration close to the channel bed (Figure 49). The hydraulic resistance of the channel is at maximum in this region of the channel bed. As the flow depth increases over the bed, the bed hydraulic resistance as define by n steadily decreases, supporting the fact of a reduced effect of the bed roughness with height above the bed. This can be related to the reduced near bed velocity field which will be demonstrated in chapter 4.

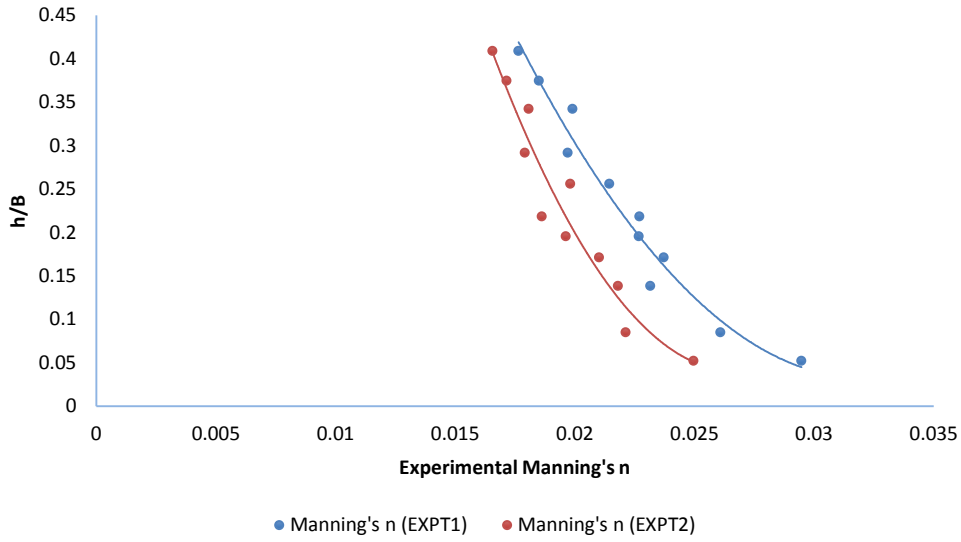

Figure 50: Variation of Manning's n with Flow Depth for EXPT1 and EXPT2

It should be noted that the maximum roughness coefficient values for the current roughness configurations are greater than those observed by Jesson et al. (2013) for their two roughness investigated. A maximum Manning's n value of 0.016 was suggested for smooth and gravel bed configuration by Jesson et al. (2012; 2013). However, the maximum values of Manning's roughness n obtained for both EXPT1 and EXPT2 suggests relatively a rougher experimental

channel. Furthermore from Figure 50, variations observed in the resistance coefficient with flow depth indicate a non-uniform Manning's roughness coefficient n for the flow in contrary to Wilson and Horritt (2002) who observed uniform roughness coefficient while measuring flow resistance of submerged vegetation.

The friction factor f was calculated from the Darcy-Weisbach equation as:

$$f = \frac{8gRS_0}{U^2} \tag{57}$$

where g is the acceleration to due gravity. Figure 51 show the distribution of friction factor (f) with stage $\left(\frac{h}{B}\right)$. The distribution of the friction factors in the figures shows similar effect to Manning's coefficient distribution shown in Figure 50. It can be seen from these figures that the friction factor f for both experimental and theoretical data decreases progressively with increasing stage. The maximum Darcy-Weisbach friction factor observed for the experimental data in this study corresponds to 0.159 and 0.115 for EXPT1 and EXPT2 respectively. In both cases as would be expected, the maximum friction factor is observed near the channel bed and the distribution decreases with stage. Considering the friction factor for theoretical curves in the figures, the vegetation bed exerts more friction on the flow than the gravel bed. This supports the retarding effect of vegetation shown in the stage-discharge curves (Figure 46). Furthermore, from Figure 51, the friction factor for gravel bed is tending towards constant value as the stage increases and becoming approximately linear at high stage $0.15 \leq \frac{h}{B} \leq 0.41$, similar effect is observed for the experimental data. In all cases, the minimum value of f is obtained for the highest discharge (Figure 52) for both experimental data and the theoretical values. The higher friction factor f for rigid bed in EXPT2 further confirmed that the theoretical value of n selected for rigid vegetation overestimated the resistance relative to the experimental results.

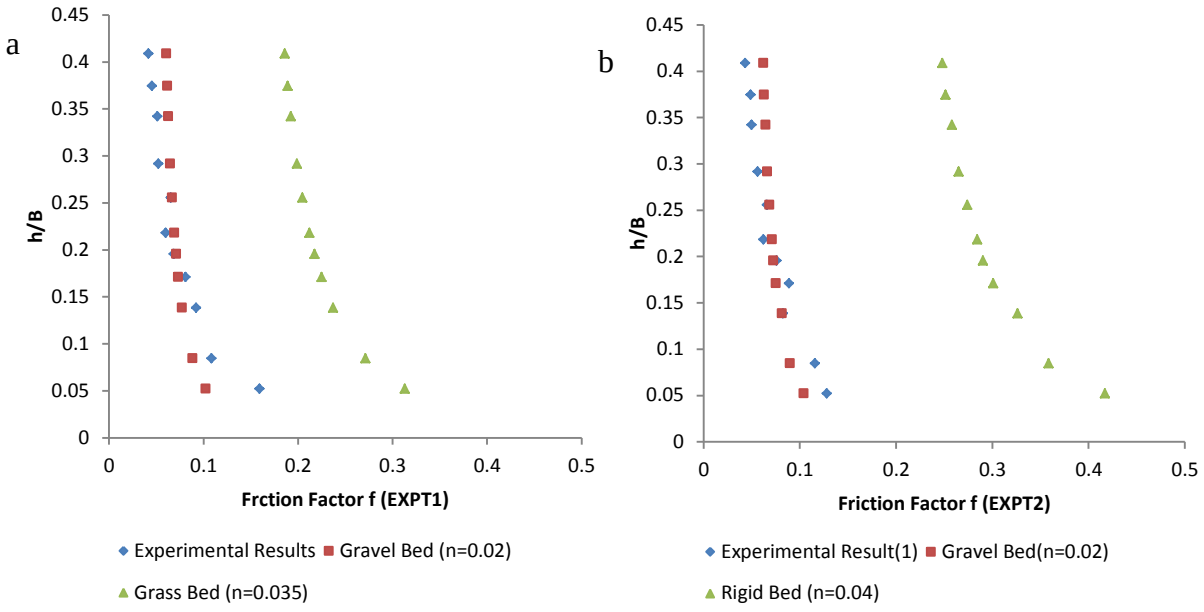

Figure 51: Variation of the Friction Factor with Flow Depth for the Experimental Data and Manning's Theoretical Data, (a) EXPT1, (b) EXPT2

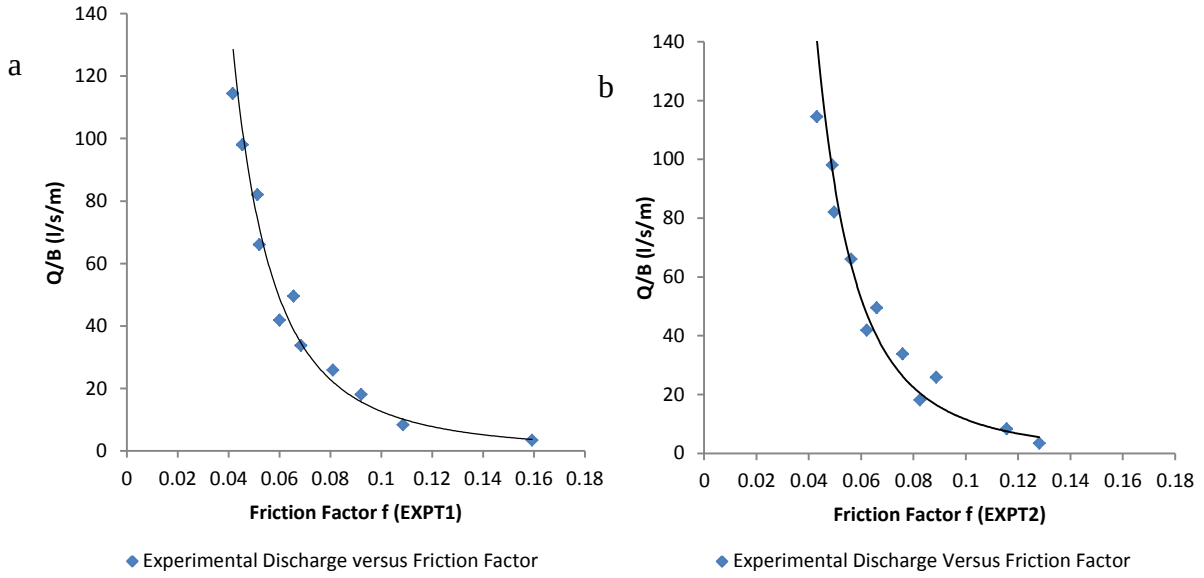

Figure 52: Variation of Friction Factor with Discharge, (a) EXPT1, (b) EXPT2

Figure 53 illustrates the variation of friction factor f with the Manning's coefficient n. The figure shows the friction factor to be approximately proportional to the Manning's coefficient

n. This is a reasonable behaviour since both n and f measures the resistance associated with the roughness material underlying the flow.

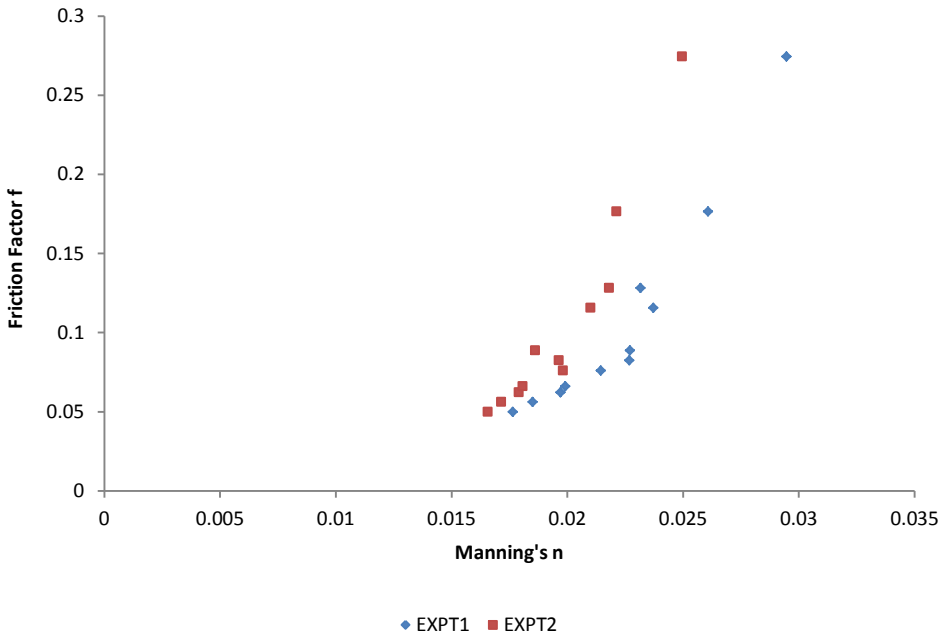

Figure 53: Variation of the Friction Factor with Manning's n for EXPT1 and EXPT2

3.4 Velocity Measurement with Acoustic Doppler Velocimetry (ADV)

An Acoustic Doppler Velocimeter (ADV) is based on the principle of the Doppler shifts and can be used to measure the velocity of suspended particles in the water. Assuming that these particles move with the same velocity as that of the water, it is possible to obtain an insight into the water velocity. An ADV measures the three components of velocity at a rate specified by the user (up to frequencies of 200 Hz) and within a relatively small sampling volume. The standard configuration of the sampling volume is approximately 6mm in diameter and 9mm in height (Chanson et al., 2007). The sampling volume for Vectrino occurs 5cm away from the central transducer (Nortek, 2004).

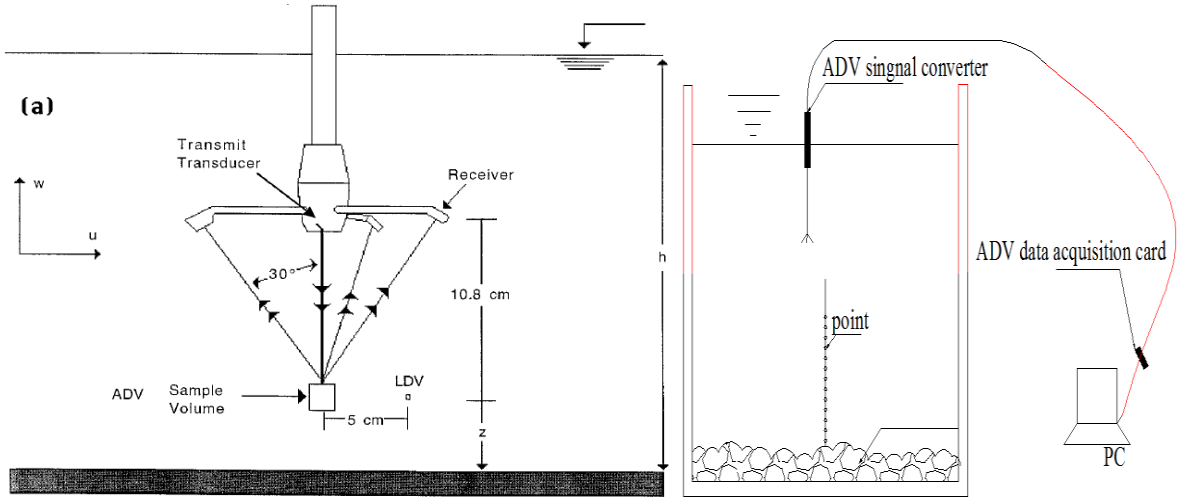

Figure 54: Diagram showing the ADV principle of operation with transmitter, receiver layout and installation configuration for data collection (Voulgaris and Trowbridge, 1998)

An ADV consists of a transmitter and four receivers and operates by emitting acoustic impulses of known duration and frequency from a transmitting transducer (Figure 54). The three receiving transducers are used to measure the backscatter from particles in the water arising from the emitted wave. For further details the reader is directed towards Voulgaris and Trobridge (1998) and Ha et al. (2009).

ADV system simultaneously record nine values within each sample collected, these include: three velocity components, three signal to noise ratio values, and three correlation values. The signal to noise ratio and correlation values are used primarily to determine the quality and accuracy of the velocity data.

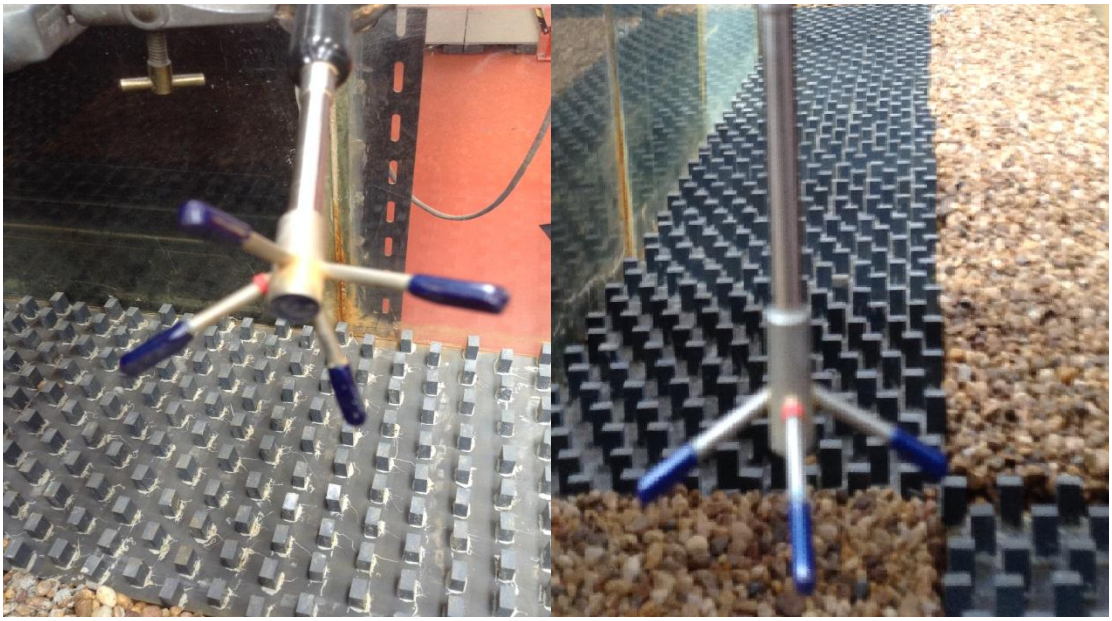

Figure 55: The ADV Probes

In research contained in this thesis, Nortek Vectrino acoustic Doppler velocimeter (ADV) VNO-0334, (ADV) VNO-0560 probes used consisted of a transmitter, and four receivers equally spaced at 90° intervals around the transmitter, angled at 30° to the transmitter axis (Figure 55). The velocity was recorded in a sample approximately 50mm below the probe end (Lohrmann et al., 1994). Further details relating to the ADV can be found in Lohrmann et al. (1994) and Lane et al. (1998).

3.4.1 Error Sources and Accuracy of ADV Measurements

The data obtained from an ADV is subject to uncertainties relating to the experimental conditions, e.g., probe alignment, measurement volume and signal aliasing. These uncertainties affect and compromise the accuracy of measurements. Misalignment of the probe can have a direct impact on the interpretation of velocity components and corresponding higher order statistics.

Another source of error in ADV measurement is the Doppler noise. Doppler noise can be described as an error due to Doppler backscattering principle in calculating velocities

(Lohrmann et al., 1994). Whilst this does not influence the mean velocity, it adds a positive bias to the high-frequency range of the power spectrum, affecting the turbulence statistics (Daniel et al., 2007). The cause of Doppler noise is related to three main reasons: particles entering and leaving the sampling volume during the interval between pulses, turbulence at scales smaller than the measuring volume, and beam divergence (Nikora and Goring, 1998). The Doppler noise produces no correlation of the signal in comparison to signals without noise. Consequently, the temporal scales obtained from this function are biased; the velocity spectra for primary velocity components are significantly affected by the presence of the Doppler noise compared to the vertical velocity component where the noise is negligible (Lohrmann et al., 1994; Nikora and Goring 1998).

The Nyquist frequency is the limiting frequency which detects signals of composite frequencies up to half the sampling frequency (Kaimal and Finnigan, 1994). This determines the resolution (highest detectable turbulent fluctuation frequency) of the ADV measurements by sampling signals of different frequencies of the time velocity measurements in turbulent flow. The sampling frequency of the Nortek Vectrino used in this research is 200Hz given a Nyquist frequency of 100Hz. This is one of the main parameters used to examine the noise effects on the turbulence parameters as the energy level of the white noise can be identified in a power spectrum as a flat plateau at high frequencies. Nikora & Goring (1998) suggested that the turbulent energy spectrum may be split into two parts, with the division at the frequency for which the turbulent energy equals the Doppler noise energy. This is illustrated in Figure 56 with the characteristic frequency denoted as ω_b. This method becomes a good approximation to determine the noise energy level.

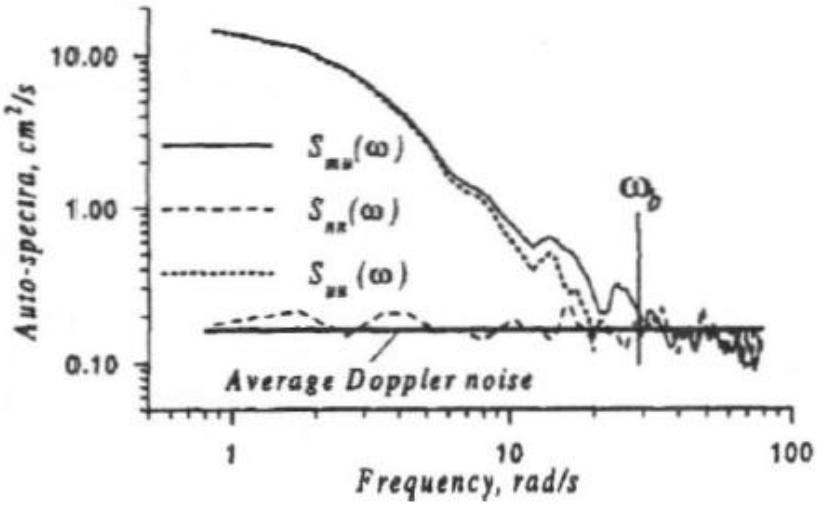

Figure 56: Turbulent Energy Spectrum and Doppler Noise Spectrum (Nikora and Goring, 1998)

Correlation and signal to noise ratio are filtering parameters in ADV to indicate the quality of the velocity measurements. Correlation and signal to noise ratio are the real time outputs the ADV provides for quality measurements. They are used for phase shift estimation. Correlation values ranges from 0% to 100%. The closer the correlation is to 100%, the less polluted, noisy and more reliable a velocity measurement is. Nortek (2004) recommended 70% minimum acceptable correlation of the velocity components and any measurements with a correlation of less than 70% are discarded (Lane et al., 1998). However, it has been suggested that correlation is not necessarily a good filtering parameter for turbulent flow as it is strongly affected by high-frequency fluctuations (Cea et al., 2007). Similarly, the ratio of the signal strength to the noise ratio (SNR), is output by the Vectrino ADV. SNR is a measure of the relative quality of acoustic signal received by the ADV. It is recommended that a SNR of at least 15 is achieved in order to obtain good data (Lohrmann et al., 1994). This correlation, when used with SNR, provides a better way to gauge the quality of the ADV measurement.

3.5 Point Velocity Measurement

Velocity measurements were undertaken at the relevant cross sections (CRS1, CRS2, and CRS3), using a combination of a Nortek Vectrino acoustic Doppler velocimeter (ADV) and a $4mm$ diameter Pitot static tube for the areas in which the ADV could not be used due to its physical size, i.e., approximately 40mm near the free surface, the near channel sidewalls and within the vegetation,

Velocity data were collected in $10mm$ by $10mm$ grid spacing in the yz plane at the three cross-sections (CRS1, CRS2 and CRS3) with the first measurement taken at $10mm$ above the channel bed (within the sampling volume of the Vectrino). The measurement grid is illustrated in Figure 57. The grid was adopted in order to represent a trade-off between making the measurement within the time frame and achieving a high resolution. Because of the influence of the channel walls on the ADV's performance, measurements with the ADV were undertaken up to $30mm$ to the channel side walls and the remaining completed by the use of the Pitot-static tube.

For each cross-section, a vertical profile of velocity data was collected from the middle of the channel ($y = 307mm$) towards the channel sidewalls at the specified interval resulting in approximately 659 measured points for a full cross-section (using lower discharge). For each vertical profile the maximum measurable height with ADV was $30mm$ below the free surface. The number of points in the vertical profile ranged between ten for ADV and thirteen for the full depth as completed by the Pitot - static tube. The ADVs were mounted on a carriage which could be moved along the streamwise length of the flume and can be controlled in lateral and vertical directions. The second ADV was position at a fixed position 120mm upstream the measured cross-sections and the measuring probe. The second ADV recorded the consistency of the velocity measurement with the subsequent velocity difference

between sections. The variation seen with the fixed probe varies between 3.4% - 6.5% for both experiments.

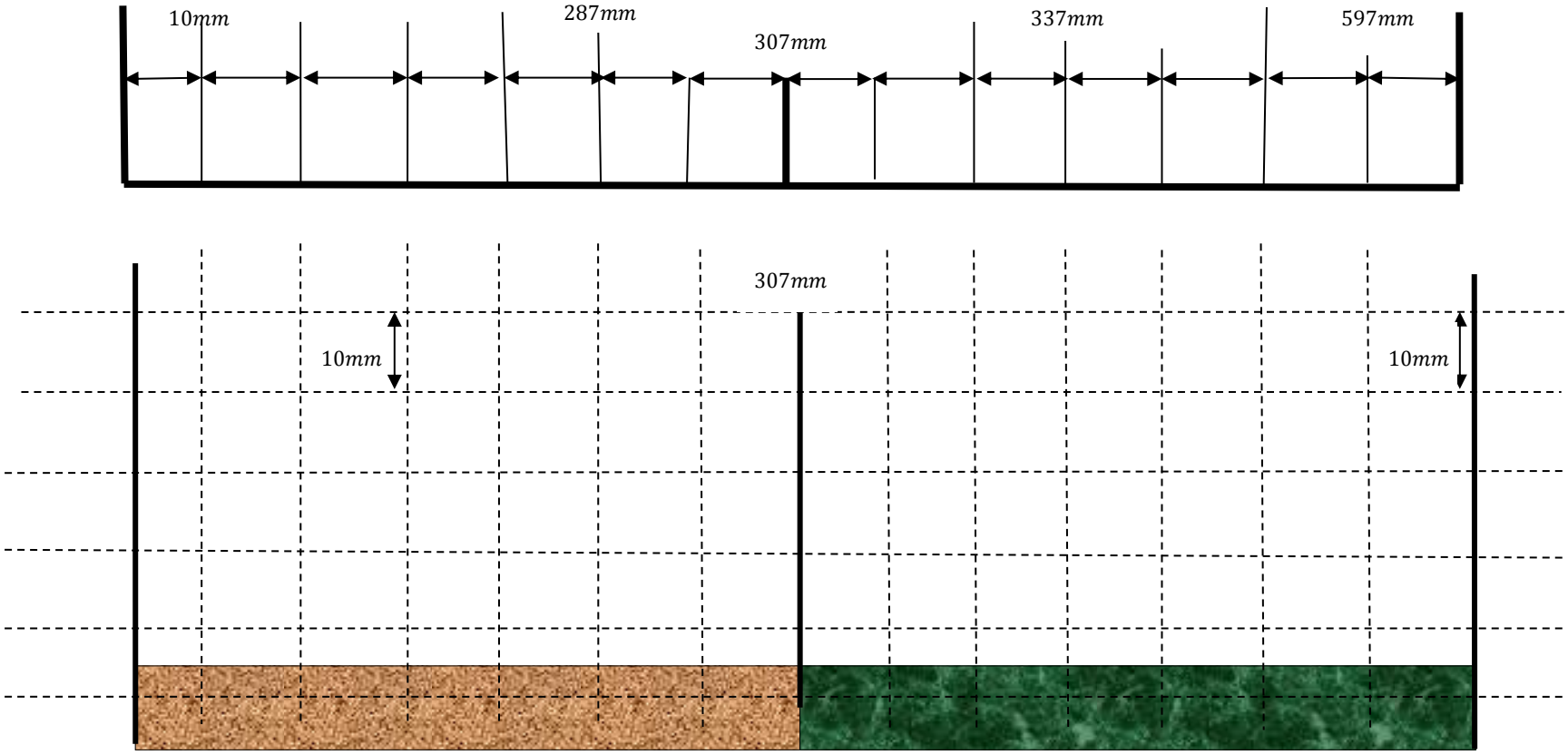

Figure 57:The Measuremet Grid Adopted

An important assumption in using the ADV is that the flow particles in the water have similar velocity as the water velocity, therefore to have accurate data, there must be enough particles in the water to scatter the emitted acoustic impulse and reflect back to the receivers. Due to the clarity of the water used in the laboratory, an electrolyser was used to produce small water bubbles as surrogate for water particles which improves the ADV signal. Using this method in the current experiment, the signal to noise ratio (SNR) exceeded 20 and the correlation coefficients of the ADV signals for the velocity components ranged within 85% - 98%. This method was considered more reliable and reproducible than the alternative, which involves addition of seeding particles to the water. The electrolyser consisted of two grids of fine wire spanning the channel placed approximately 1m upstream of the ADV probes, and connected to a power supply to act as an anode and cathode for the generation of hydrogen bubbles through hydrolysis.

The ADV used have the ability to measure the three orthogonal velocity components simultaneously at a point using a maximum frequency of 200Hz to provide temporally averaged mean velocity and turbulence parameters in streamwise, lateral and vertical directions. The ADV measurement data resolution can be compromised by the amount of data recorded (sample rate) and the length of time used to sample the data (sample length). Collecting data samples in over long periods of time is time consuming; however, insufficient data can lead to misleading results. To achieve a balance between the number of data collected and the time to sample the data, a convergence test based on (Buffing-Belanger and Roy, 2005) was performed to obtain the optimum sample length. To determine the sample length and sample rate for the velocity measurements in the current research, point velocity (u) measurements were undertaken in (y, z) coordinate in the gravel region $(87, 10)$ and in the vegetation region $(467, 10)$ using sampling rates of 100Hz and 200Hz and sample lengths of 5, 10, 15, 20, 25, 30, 40, 50, 60, 90 and 120 seconds. The standard deviation of the

velocity u was plotted against the sample length as shown in Figures 58 and 59 for 100Hz and 200Hz respectively. These figures indicate that for samples of length 60s and greater, the variation between successive values of standard deviation were reduced, i.e., the standard deviation tended towards a constant value. Hence, a sample length of 60 seconds was adopted for the current research. At the adopted duration, the sampling rate affected the standard deviation by approximately 2% when the sample rate was increased from 100Hz to 200Hz (Figures 58 and 59). This variation is within the range observed by others (Jesson et al., 2013; McLelland and Nicholas, 2000) and is within the level of uncertainty associated with the velocity measurements. Similar behaviour was observed for both EXPT1 and EXPT2 respectively. A sampling frequency of 200Hz was adopted for the current since this permitted a greater resolution of the velocity data.

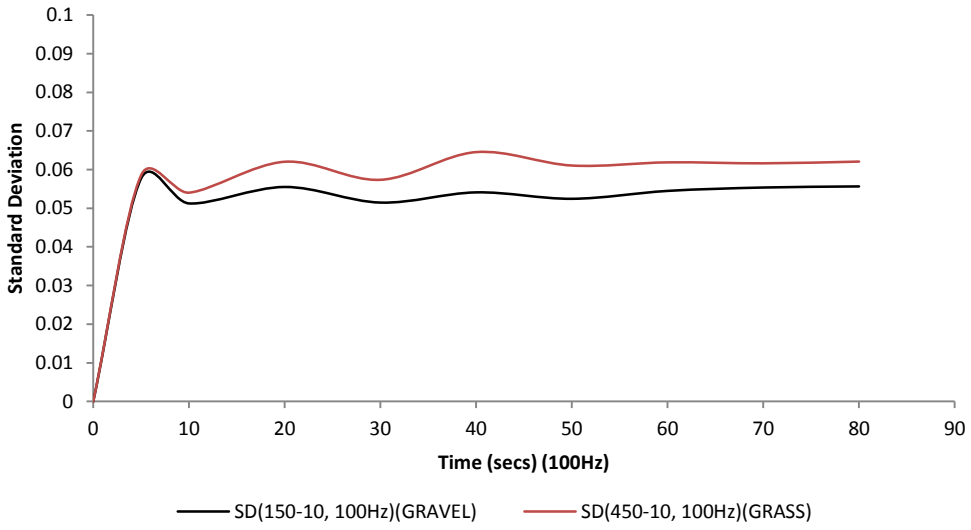

Figure 58: Variation of Standard Deviation of u with Sample Length (100Hz)

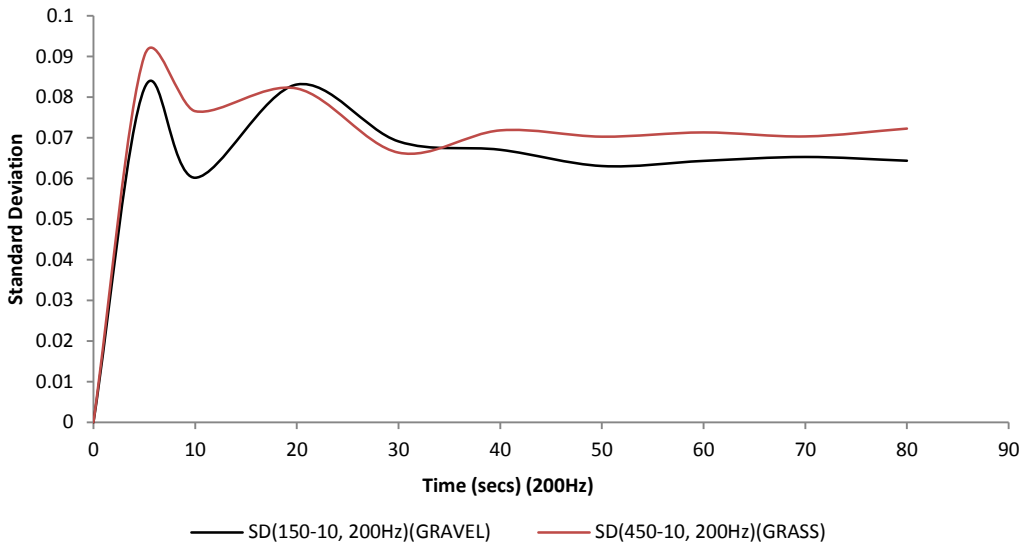

Figure 59: Variation of Standard Deviation of u with Sample Length (200Hz)

Using an ADV to sample data for 60 seconds with a sample rate of 200Hz provides 12000 data per minute for a measured point. The total number of points at which velocity data is collected in a cross-section by ADV is 590. Hence, the process generates a large amount $(i.e. 12000 \times 590)$ of data that need to be processed and converted into a meaningful form. The steps followed in processing the data are illustrated in Figure 60. The ADV Polysync software developed by Nortek was used for data acquisition. Polysync create files with "VNO" file extension for every single measured point. The files were converted to the ADV, HDR and DAT formats after data acquisition. The obtained files are transferred to MATLAB and Excel worksheet for data statistic and final post processing.

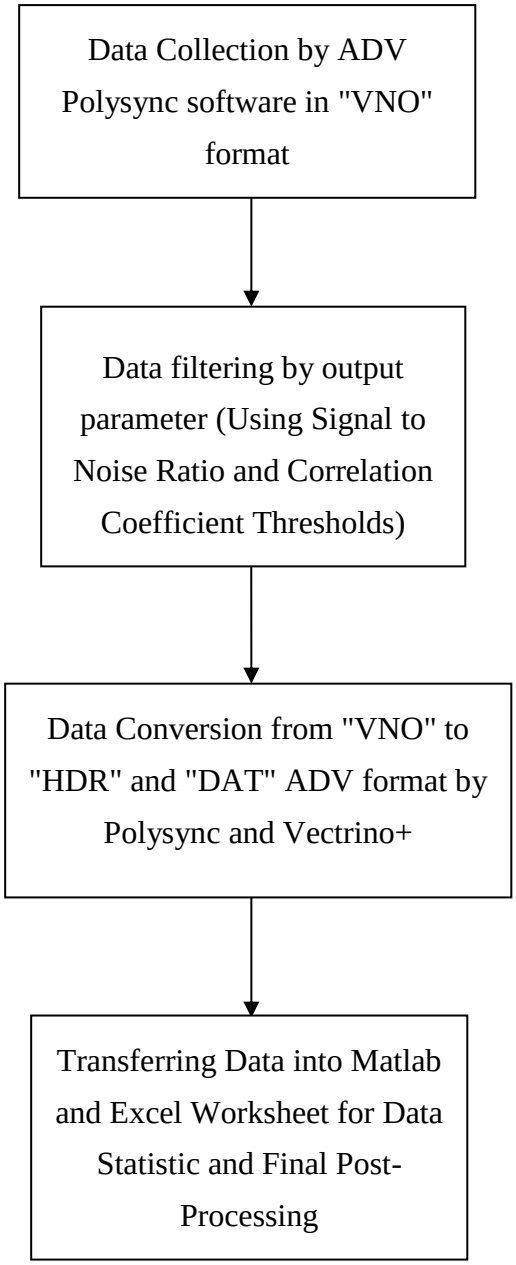

Figure 60: Data Processing Flow Chart

In order to provide a complete set of velocity data at a cross section, a Pitot - static tube was used to measure the velocity in these regions using the same grid spacing. The Pitot-static tube was connected to an inclined water manometer (Figure 61).

Figure 61: Manometer for Pitot - static tube

The uncertainty analysis provides an approximate value of 0.0167 (1.67%) associated with the Pitot-static tube. This uncertainty corresponds to $1mm$ uncertainty in the evaluaton of the water level in the manometer which is considered to be acceptable for the current research. To validate the use of Pitot - static tube and the ADV velocity measurement, a vertical profile was taken at the roughness boundary region using both the ADV and the Pitot-static tube. Figure 62 compares the result from both instruments. From the figure, it is apparent that the measurements made by both instruments are similar, indicating the consistency of both instruments.

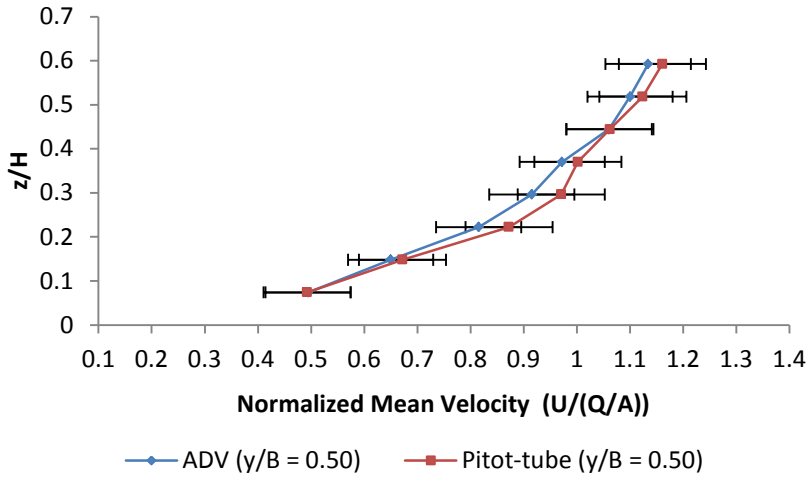

Figure 62: Comparison of ADV and Pitot-Static Measurement (EXPT1)

3.6 Data Processing

Spikes and outliers are created in the ADV data due to Doppler noise or poor signal to noise ratio as a result of inadequate particles in the flow to reflect the sound impulse signal. To process the ADV raw data, a filtering process was applied to remove spikes and noisy data in the time series signal. The ADV data in the current work was filtered for:

- Low signal to noise ratio
- Low correlation coefficient of the velocity components
- Large deviation in velocity signal amplitude (Noise).

Using the output signal of the ADV Polysync software, data points with poor signal to noise ratio and low correlation were filtered out at the point of collection using correlation and signal to noise thresholds. In line with the suggested recommendation by the manufacturer (Nortek), the correlation coefficient was set to 80% as minimum threshold value for all the three components. To monitor the acoustic signal, a minimum threshold value of 15 is suggested for signal to noise ratio (Nortek, 2004), and a minimum value of 20 was set for the current experiments. All the data points were observed to pass through these filtering and the

process removed about 80% of the spikes. The signal to noise ratio exceeds 20 and the correlation coefficient fluctuates between 85% and 98%. The remaining "spikes" in the velocity signal were further despiked using Phase-Space Threshold despiking algorithm proposed by Goring and Nikora (2002). Due to the controlled output signal for the correlation coefficient and the signal to noise ratio at the point of collection, the sampled data contained fewer spikes that the filtering was able to identify and remove.

The Phase-Space Threshold Method uses a phase-space plot in which the sampled velocity time series and their derivatives are plotted against each other to form points which are enclosed in an ellipsoid. The ellipsoid is defined by the sample mean and standard deviation and the points outside the ellipsoid are taken as spikes. The filtered signals by correlation - signal to noise ratio and phase-space thresholds are shown in Figure 63 and 64 over the gravel and vegetated bed for EXPT1. The signal is apparently good at point of collection after applying signal to noise ratio and correlation coefficient threshold value (Figure 63a and Figure 64a). However, it is noticeable that there are still significant outliers which are addressed when the phase space method is used (Figure 63b and 64b). Once filtered, the signals with poor quality are discarded; for replacement, the discarded data were replaced by the overall mean value of the sampled data. The PDF of the filtered data are presented in Figure 65 for both correlation - signal to noise ratio and phase-space threshold values. It can be seen that the PDF of the phase-space filtered data is approximately Gaussian and normally distributed (Figure 65a), whilst the PDF of the correlation-signal to noise filtered data is characterised by long tails apparently to the left side of the PDF curve (indicating that spikes are located in the PDF tails), with some part of the distribution deviating from Gaussian distribution (Figure 65b). This deviation suggests that correlation and signal to noise ratio may not be a complete filtering parameter for turbulent flow as it is strongly affected by high frequency fluctuations (Cea et al., 2007). Figure 66 illustrates the power spectral of the

phase-space filtered velocity data, it can be seen that the resulting spectral distribution illustrates the different frequency ranges of the turbulent kinetic energy.

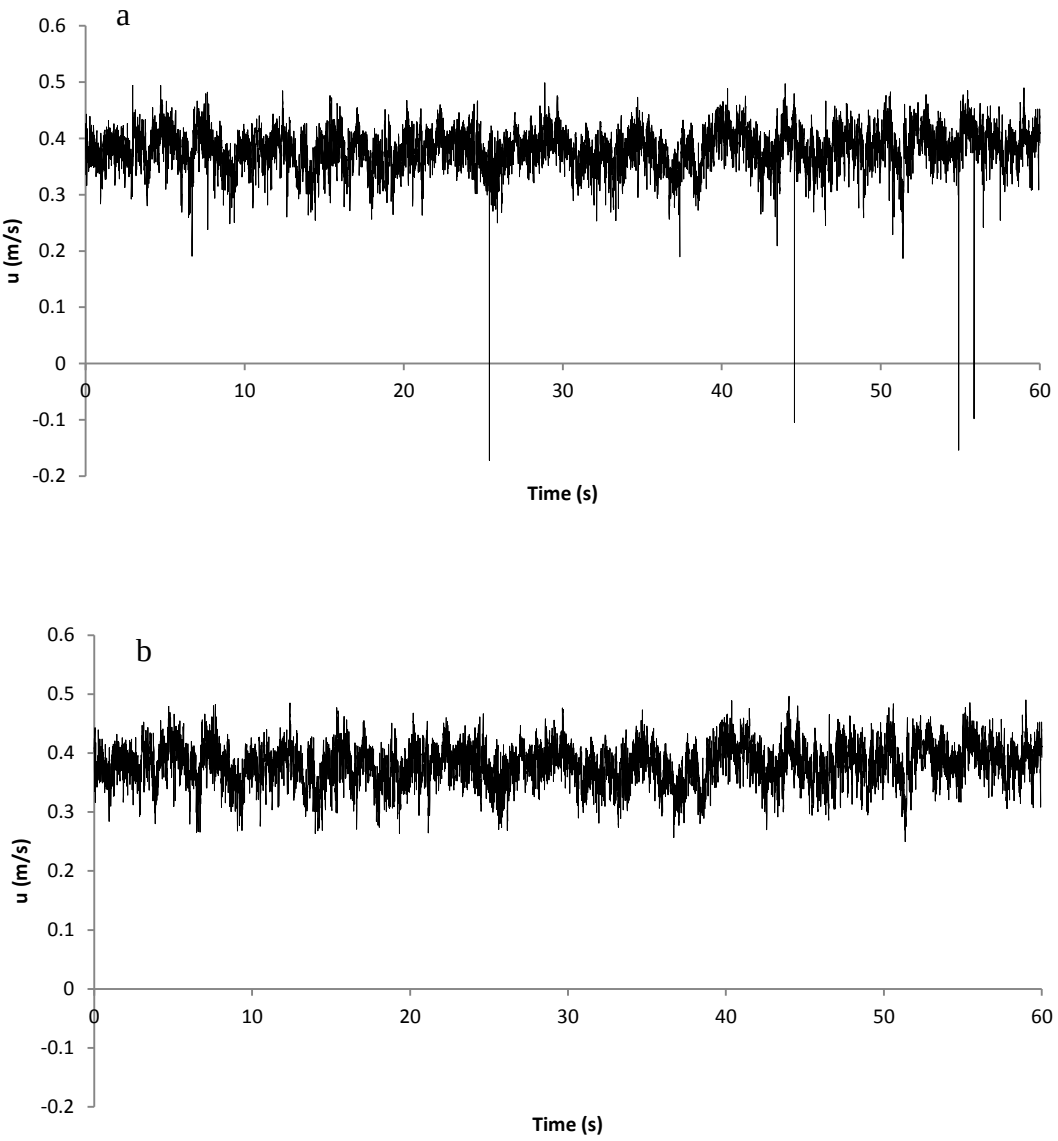

Figure 63: ADV Velocity Time Series over the Gravel Bed (EXPT1): (a) Output signal after correlation and signal to noise ratio threshold application, (b) Filtered signal using Phase-Space Threshold

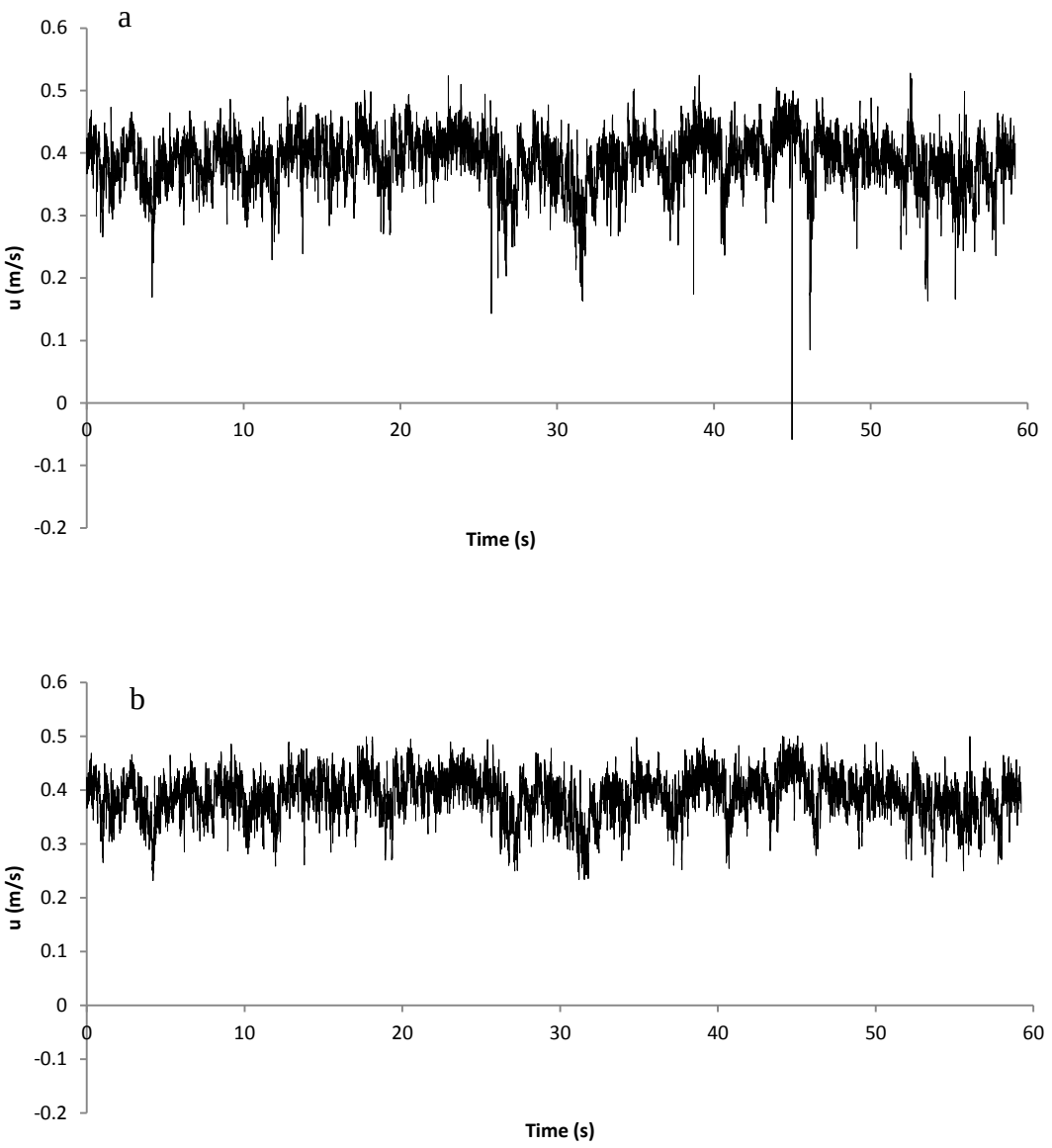

Figure 64: ADV Velocity Time Series over the vegetated bed (EXPT1): (a) Output signal after correlation and signal to noise ratio threshold application, (b) Filtered signal using Phase-Space Threshold

Due to manual probe alignment and the difficulty associated with precisely orientating the probe, it is necessary to transform the measured data to the true coordinate system of the channel flow in the streamwise, lateral and vertical directions. Due to the large volume of data in the current work, each set of measurement made in one session with the probe in a particular position are treated for the same rotation correction by applying a technique to determine the angles necessary to place the probe into the orthogonal coordinate system.

Since a set of measurement made in one session is assumed to have same probe misalignment. A series of two rotations to place the probe into a true coordinate system was applied, this gives new velocities as:

$$u_1 = u\cos\theta + v\sin\theta \quad (58)$$

$$v_1 = -u\cos\theta + v\sin\theta \quad (59)$$

$$w_1 = w \quad (60)$$

where

$$\theta = \tan^{-1}\left(\frac{U}{V}\right), \quad (61)$$

and

$$U = \frac{1}{N}\sum_{set} u \quad (62)$$

$$V = \frac{1}{N}\sum_{set} v$$

the subscripts denotes the velocities rotation, u, v and w are the streamwise, lateral and vertical point velocities, the second rotation gives the final velocities as:

$$u_2 = u_1\cos\emptyset + w_1\sin\emptyset \quad (63)$$

$$v_2 = v_1 \quad (64)$$

$$w_2 = -u_1\cos\emptyset + w_1\sin\emptyset \quad (65)$$

where

$$\emptyset = \tan^{-1}\frac{W_{1m}}{U_{1m}} \quad (66)$$

W_{1m} and U_{1m} are the mean set of velocities from first rotation. This is a double rotation method which aligns the x-axis with the mean streamwise velocity, hence minimising the values of y and z axes of the velocity components. The method allows the correction of probe misalignment given probe rotation angles. These angles represent the amount of rotation needed to place the probe into the desired coordinate system (James et al., 2000) which has

been taken as the orthogonal coordinate system described in section 2.1. The maximum rotation corrections applied in the current research are shown in Table 5.

After data processing, each point measurement of velocity was temporally averaged over 60 seconds at a rate of one sample every 0.005s which was considered long enough to capture the lowest frequency fluctuations in the flow.

CROSS SECTION	EXPT1		EXPT2	
	θ degrees	∅	***θ*** degrees	∅
CRS1	1.7	0.2	2.8	0.2
CRS2	1.6	0.1	2.5	0.2
CRS3	1.7	0.2	2.9	0.5

Table 5: Maximum Values for Rotation Correction about y and z axes

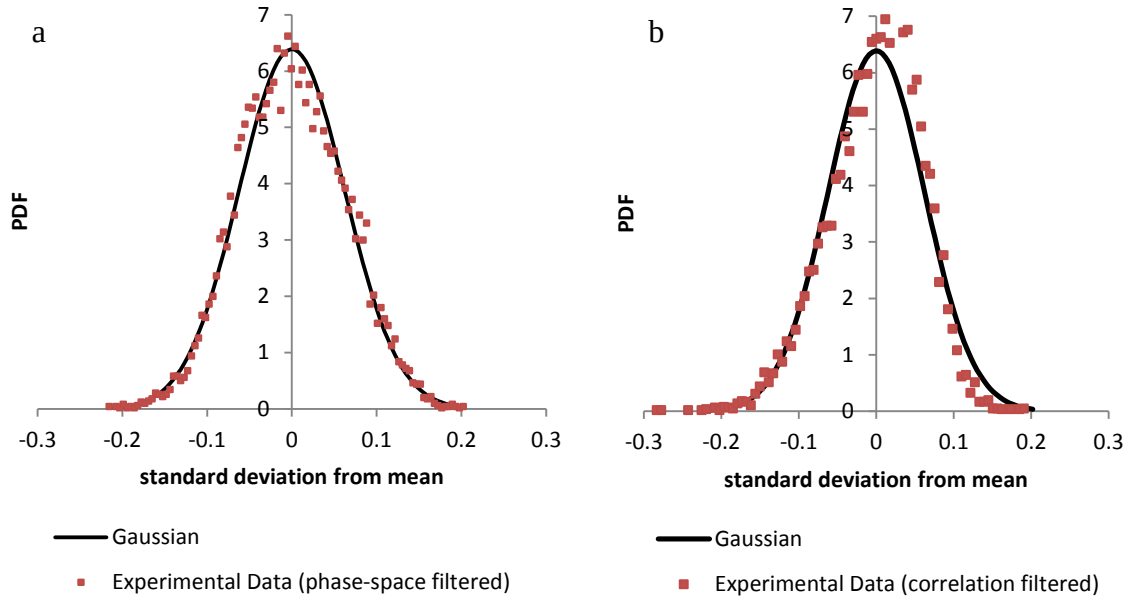

Figure 65: PDF Distribution $\left(\frac{y}{B} = 0.5, \text{EXPT1}\right)$ of (a) Filtered Data (phase-space); (b) Filtered Data (Correlation-signal to noise ratio)

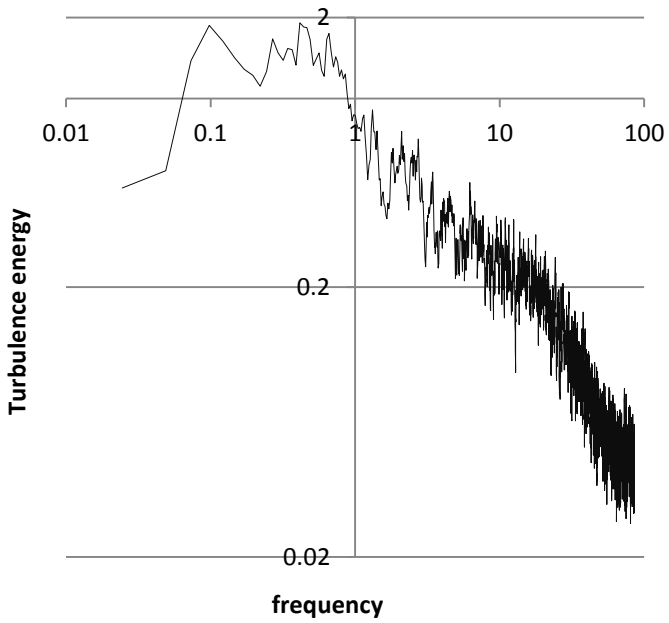

Figure 66: Power Spectral of the Filtered Data (phase-space) $\left(\frac{y}{B} = 0.5, \text{EXPT1}\right)$

3.7 Normal depth flow

In order to verify the suitability of the measured cross-sections for flow development, the vertical velocity profile was measured at the relevant cross-sections (CRS1, CRS2 and CRS3). Figure 67 show the vertical velocity profile of the measured cross-sections undertaken at the roughness boundary region $\left({}^{y}/_{B} = 0.5\right)$ of the measured sections. From Figure 67, it can be seen that, the vertical profiles at the measured cross-sections are identical (within the uncertainty limits) for both EXPT1 and EXPT2. The results demonstrate that the flow is fully developed and uniform at the measured cross-sections.

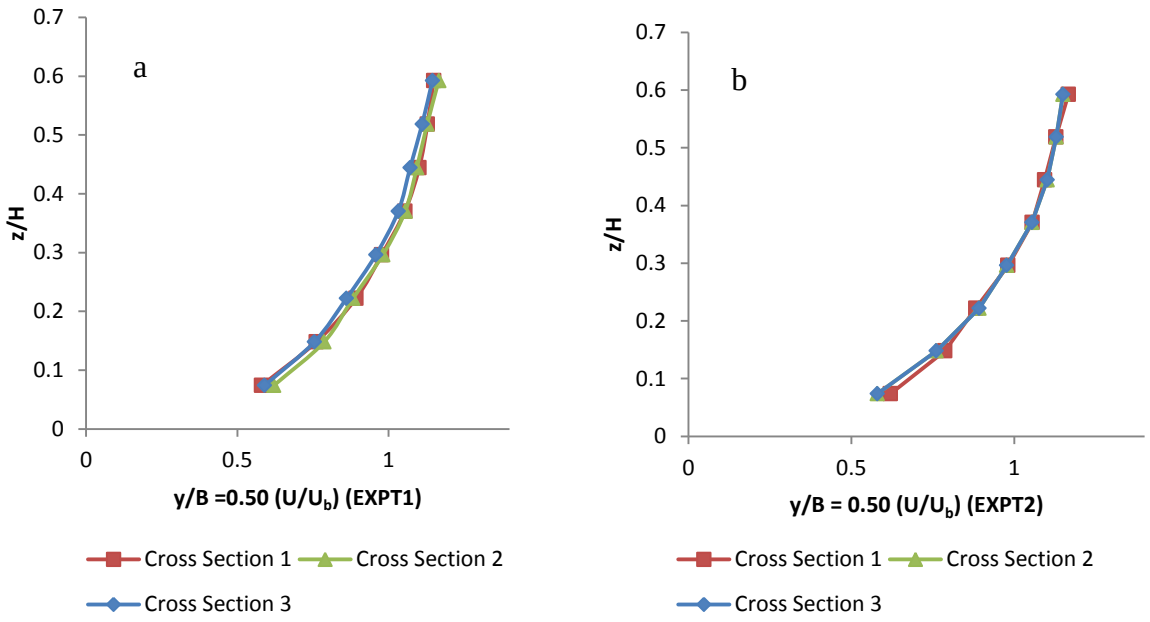

Figure 67: Vertical Distribution of Mean Velocity *U* at the three Cross-Sections Measured; (a) EXPT1; (b) EXPT2

3.8 Velocity Measurement with Particle Image Velocimetry PIV

Particle Image Velocimetry (PIV) is an optical technique of flow measurement which involves illumination by a light source of flow particles and the particles images recorded by a digital camera as shown in Figure 68.

Figure 68: The high definition PIV Camera

As described by Buchhave (1992), the PIV technique can be regarded as an efficient way of measuring a whole flow field velocity structure of a flow region. PIV uses methods that are characterized by the recording of the displacement of flow particles within the flow region being measured. The principle of a PIV involves seeding the flow with small particles, tracking the motion of those particles using digital camera and laser beam. As with an ADV, it is assumed that the seeded particles move at the same speed as the surrounding flow.

The particle image velocimetry (PIV) measurements in the experiment detailed outlined section 5.5 consisted of a computer and software (rtControl) for the data collection and processing, a PIV camera with 640×480 image resolution (Figure 68) and timing-synchroniser (PIV, 2009) (Figure 69).

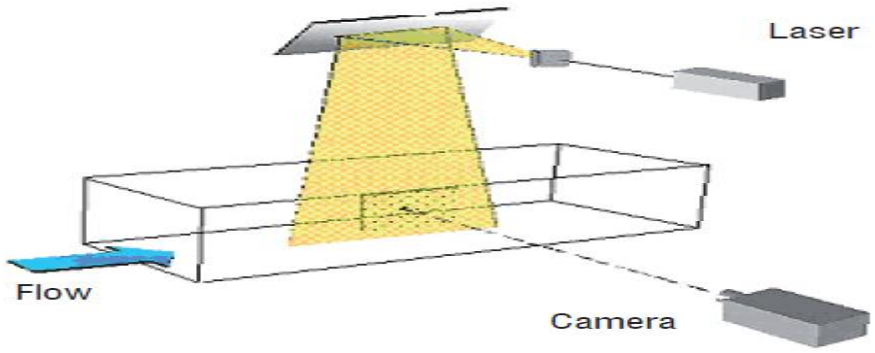

Figure 69: PIV Experimental Set-up

The optimum analysis to find the displacement and direction of the vectors is a two-dimensional fast Fourier transform (FFT) using the cross correlation method for PIV image analysis. As the image information is recorded in two separate exposures, one for the first illumination and another for the second illumination, a cross-correlation is applied to find the displacement (Adrian, 1988).

A cross correlation method splits the two images into small sub-windows or interrogation areas and then uses a fast Fourier transform (FFT) on each sub-windows or interrogation area. The signal strength for a single sub-window is compared between the first and second image to determine a mean and common displacement between the two peaks. The correlation produces vector for that sub-window with the processes repeated to build a vector map for the measurement plane (this is further discussed in section 5.5.2).

In the PIV experiments detailed in section 5.5, the upstream of the area of interest and the field of view (FOV) is located the hydrolyser that generates micron-sized bubble particles in the flow (section 3.5). In addition to this is an injection of uniform concentration of 100 μm polyamide seeding particles near bed $1m$ upstream the FOV. Given the low flow condition of the experiment ($Q = 7.5\ l/s$), the bubble density and particle concentration into the flow was

optimised, this increased the representation of velocity vectors in the flow. The flow was then illuminated with a sheet of monochromatic light from a pulsed laser.

4 Mean Velocity and Turbulence Characterisitics

4.1 Introduction

In this chapter, the velocity data is examined in terms of mean and turbulent parameters. Attention is focussed on the vertical distributions at selected lateral locations over the gravel bed $\left({}^{y}/_{B} = 0.24\right)$, the boundary roughness $\left({}^{y}/_{B} = 0.50\right)$ the over the vegetation bed $\left({}^{y}/_{B} = 0.73\right)$. Attention is also focussed on the comparison between the two different roughness configurations (EXPT1 and EXPT2) using the lower flow rate $(30 l/s)$. However, where appropriate, comparisons and discussions between results for higher and lower flow rates are provided. Despite the different flow rates $(Q = 30\, l/s)$ and $(Q = 40\, l/s)$ used for the current experimental work, it is noted that the flow characteristics are qualitatively similar as the flow property distributions remain consistently demonstrating same mechanisms, except for a change in magnitude of some properties due to higher flow rate, hence for clarity and brevity, a fraction of the results for higher flow rates $(Q = 40\, l/s)$ are presented (Appendix E). The lateral distributions of the depth-averaged (denoted with subscript d) values are also presented when considered appropriate.

4.2 Probability Density Distributions of Turbulent Velocities

As shown in section 2.5.1, a probability density function $P(u)$ of a random variable u follows a Gaussian distribution:

$$P(u) = \frac{1}{\sqrt{2\pi {\sigma_u}^2}} e^{-(u-U)^2} \qquad -\infty < x < \infty \tag{67}$$

where σ_u is standard deviation of the random variable with U denoting the mean streamwise velocity). Probability density functions which differ from a Gaussian distribution may suggest certain features within the flow, e.g., extreme values arising from coherent structures.

The pdf from the streamwise velocity fluctuation u' for different locations are shown in Figures 70 and 71. The pdf values have been normalized by Equation (68) in order to compare and contrast the fluctuating velocity distribution with Gaussian distribution for all the locations.

$$P(u) = P\left(\frac{u-U}{\sigma_u}\right) \tag{68}$$

The shape of the fluctuating velocities were obtained by evaluating the kurtosis and skewness of the representative points. As shown in section 2.5, skewness quantifies the symmetry of a distribution with respect to its deviation from the mean. A symmetrical distribution has a skewness equal to zero. Kurtosis describes whether the shape of data distribution is peaked or flat relative to a normal distribution, a higher kurtosis tend to exhibit a distinct peak near the mean. For quantitative comparison with the Gaussian distribution, the skewness and kurtosis factors for all the locations and cross-sections are presented in Table 6.

Figures 70 and 71 illustrates the pdf of the streamwise turbulent velocity at different locations for EXPT1 and EXPT2 respectively. In the figures, the vertical axis represents the probability density functions multiplied by the corresponding standard deviation $P(u)(\sigma_u)$ and the horizontal axis represents the number of standard deviations from the mean. As can be seen, the distribution of the streamwise turbulent velocity appears to be qualitatively Gaussian in all the cross-sections. However, for EXPT1, the pdf in CRS3 over the gravel bed $\left({}^{y}/_{B} = 0.24\right)$ exhibits higher kurtosis (peakedness relative to normal distribution) but nearly Gaussian-distributed ($\mathrm{S} = -0.0456, \mathrm{K} = 0.3343$) Figure 70a, where S and K are the skewness and kurtosis respectively. This kurtosis distribution of the fluctuating velocity is similar to that obtained for CRS1 over the flexible vegetated bed $({}^{y}/_{B} = 0.73)$ as illustrated in Figure 70c. This can attributed to the location of maximum streamwise velocities being

displaced between regions of different cross-sections due to heterogeneous roughness (the following sections will discuss this in detail). However, over the flexible vegetated bed ($^{y}/_{B} = 0.73$) in EXPT1 (Figure 70c), the velocity fluctuations slightly deviates from Gaussian, given negative skewness ($S = -0.6903, -0.5266, -0.5955$) for CRS1, CRS2 and CRS3 respectively. This is attributed to the possible effect of flexible vegetation roughness on the flow: as the flow accelerates over the preceding gravel bed to the new flexible vegetated bed in EXPT1, the velocity of the flow decreases due to vegetation stem density as will be shown later in the following sections. It can therefore be suggested that, the flow deceleration due to vegetation stem density produces an asymmetric velocity fluctuation over the vegetated bed due to more distortion of large scale structures, thereby becoming more asymmetric and in turn manifested in the actual fluctuations. It should be noted however in Figure 70b that the probability density functions for the fluctuating velocities show qualitative similarities in shapes with Guassian distribution for all the cross-sections at the roughness boundary region ($^{y}/_{B} = 0.50$) in EXPT1, confirming the uniform flow for the experiment. The distribution is seen to be symmetric about the mean value and the width of the distribution increases on both sides relative to gravel $\left(^{y}/_{B} = 0.24\right)$ and vegetated $\left(^{y}/_{B} = 0.73\right)$ regions respectively, hence the pdf show flat peak ($K = 0.1216, 0.1237, -0.0476$) corresponding to Figure 70b at the boundary region. Such flat peaks and increased pdf widths are not formed over the gravel and vegetated regions in EXPT1.

In EXPT2 (Figure 71), the pdf exhibits extended long tails at both sides relative to EXPT1. As can be see from the figure, the pdf of streamwise velocity fluctuations demonstrate near Gaussian behaviour at every region and for all the cross-sections with lower kurtosis relative to EXPT1. At the boundary region $\left(^{y}/_{B} = 0.5\right)$ however, the pdf is negatively skewed in

EXPT2 (Figure 71b) relative to EXPT1 (Figure 70b). This asymetry may be attributed to the enhanced lateral transport of momentum at the boundary region in EXPT2 (detailed analysis are presented in sections 4.7 and 4.8). The skewness of the streamwise turbulent velocity over the vegetated bed in EXPT1 (Figure 70c) and at the roughness boundary region in EXPT2 (Figure 71b) highlights the differences in flow behaviour which occurred at the different regions of the channel bed. The major asymmetry of the distribution appears to be located in these regions of the channel. This may not be unexpected since these regions are the high shear regions (Sections 4.7 and 4.8) which leads to frequent momentum transfer. It appears from Figure 71 that the fluctuating streamwise velocities may have a more Gaussian pdf in EXPT2 relative to EXPT1, the distribution however exhibits long tail (negative skewed) at the roughness boundary region ($^{y}/_{B} = 0.50$).

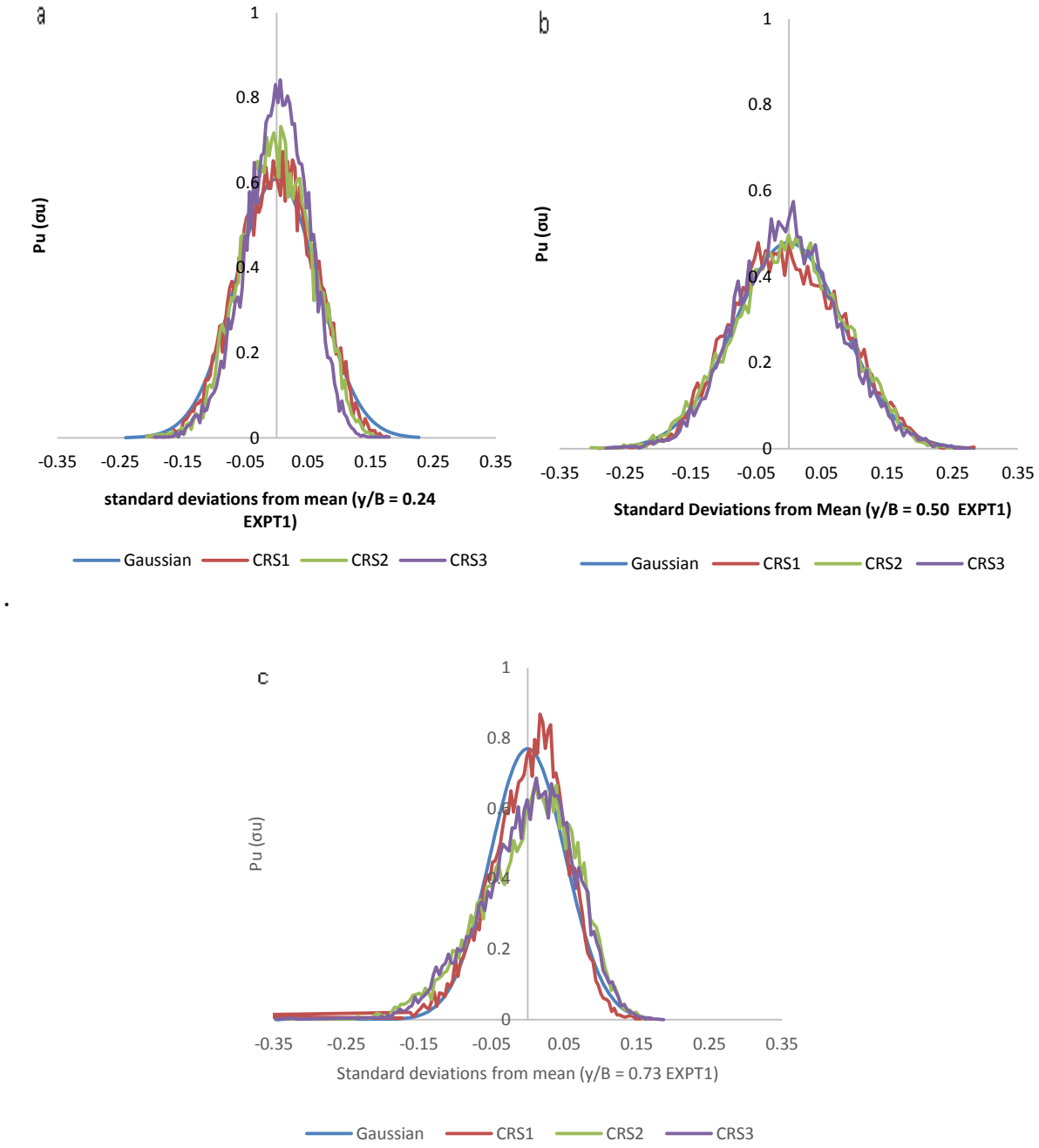

Figure 70: **Probability density function of streamwise velocity fluctuations near bed for (a) gravel, (b) boundary and (c) vegetated regions (z/H = 0.07) (EXPT1)**

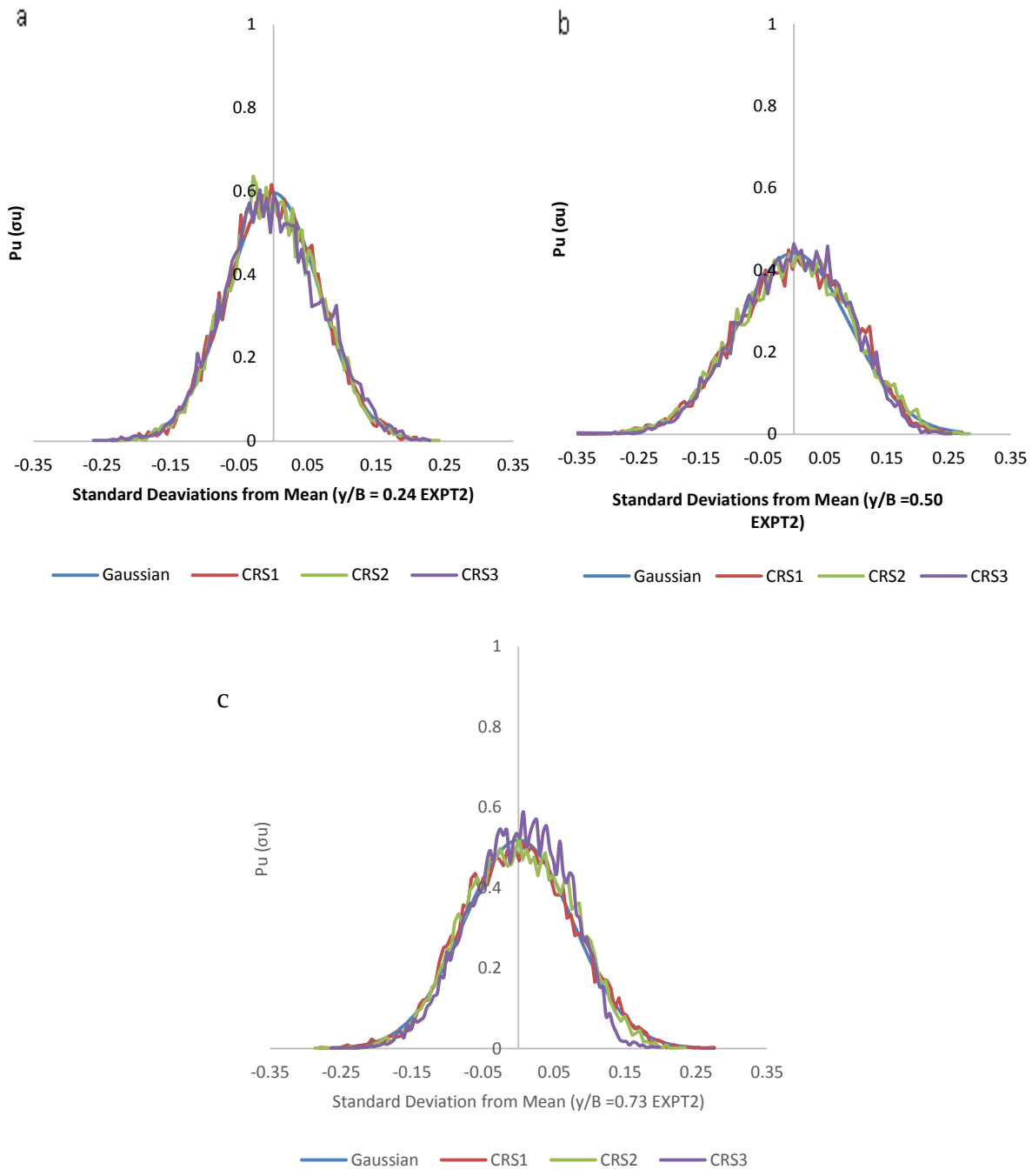

Figure 71: Probability density function of streamwise velocity fluctuations near bed for (a) gravel, (b) boundary and (c) vegetated regions (z/H = 0.07) (EXPT2)

	EXPT1			EXPT2		
	CRS1	**CRS2**	**CRS3**	**CRS1**	**CRS2**	**CRS3**
$y/_B = 0.24, z/_H = 0.07$				$y/_B = 0.24, z/_H = 0.07$		
Kurtosis	0.146	0.268	0.334	0.096	0.092	0.094
Skewness	-0.070	-0.069	-0.045	0.051	0.051	0.054
$y/_B = 0.50, z/_H = 0.07$				$y/_B = 0.50, z/_H = 0.07$		
Kurtosis	0.121	0.123	-0.047	0.072	0.081	0.078
Skewness	0.0518	-0.025	0.050	-0.230	-0.213	-0.281
$y/_B = 0.73, z/_H = 0.07$				$y/_B = 0.73, z/_H = 0.07$		
Kurtosis	0.3036	-0.1476	0.1220	0.121	0.119	0.120
Skewness	-0.6903	-0.5266	-0.5955	0.073	0.070	0.071

Table 6: Kurtosis and Skewness values for EXPT1 and EXPT2

From Table 6 the values of skewness over the flexible vegetated region ($^{y}/_{B} = 0.73$) in EXPT1 and roughness boundary region ($^{y}/_{B} = 0.50$) in EXPT2 are much greater with negative values than those at the gravel ($^{y}/_{B} = 0.24$) region; these regions of high negative skews are assumed to be the shear regions, as demonstrated in sections 4.7 and 4.8. These values confirmed the pdf distributions shown in Figure 70 and Figure 71. The negative skewness can be attributed to the large scale vertical and horizontal motions induced by significant shear layer over the vegetated bed in EXPT1 and the roughness boundary region in EXPT2 respectively (detailed discussions are provided in section 4.8 where these behaviours are confirmed). The kurtosis values are higher in EXPT1 relative to EXPT2, with higher values indicating a sharp peaked distribution suggesting intermittent extreme event over the vegetated region in EXPT1, this behaviour in EXPT2 with lower kurtosis values indicates flat distributions of streamwise turbulent velocity. More symmetrical distributions of turbulent velocities occur for increased distance above the bed ($^{z}/_{H} = 0.61$) due to less significant effects of the bed roughness at the upper region of the flow as illustrated in Figure 72 and 73. It should be noted that the differences outlined between the normal distribution and the data collected leads to assume that the flow is normal.

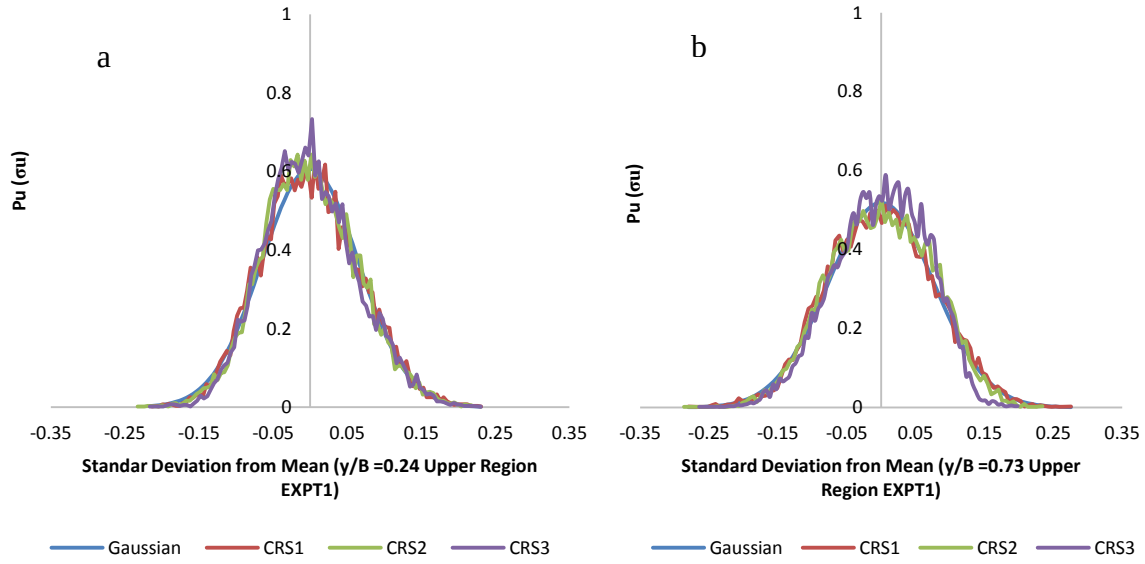

Figure 72: Probability density function of streamwise velocity fluctuations at upper region (z/H = 0.61) (EXPT1)

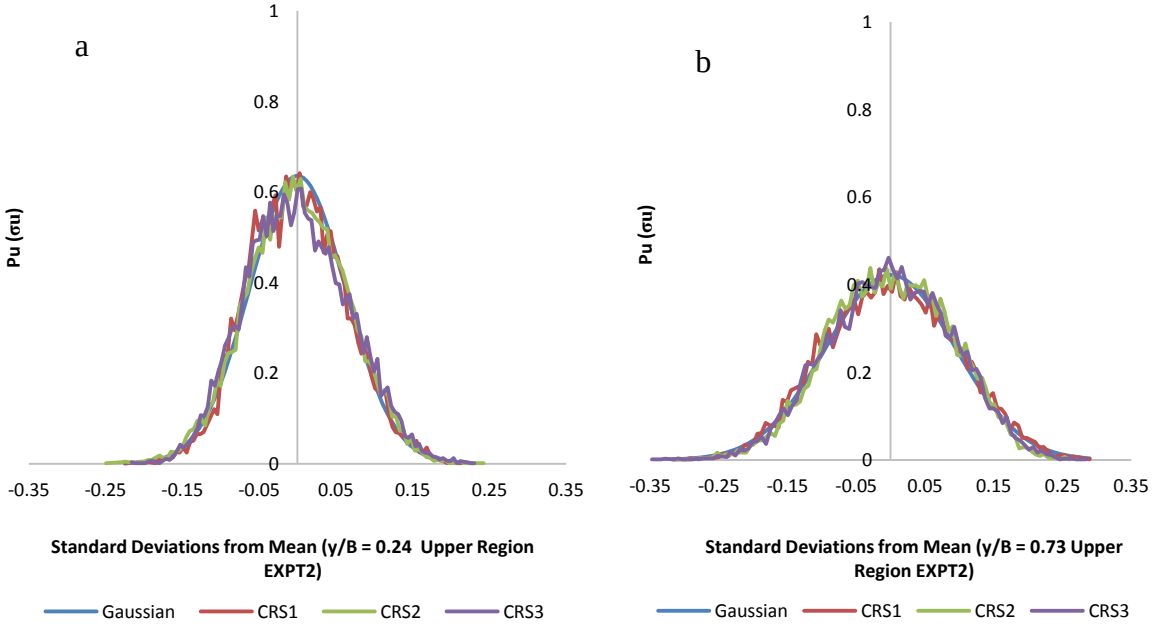

Figure 73: Probability density function of streamwise velocity fluctuations at upper region (z/H = 0.61) (EXPT2)

4.3 Distribution of time-averaged (mean) velocity and turbulence properties

The mean velocity (U) was obtained for each measured point and normalized by the theoretical velocity $U_b = \left({}^{Q}/_{A}\right)$ where A is the cross sectional area of flow. To provide an indication of the degree of reliability of the data collected, the time averaged velocity data at each point was numerically integrated and compared to U_b. The theoretical velocity along the channel yields a value of $0.382 ms^{-1}$ for both EXPT1 and EXPT2 respectively. These values compare favourably with the numerically integrated velocity values along the cross-section with maximum difference within 4% for EXPT1 and EXPT2 respectively as illustrated in Table 7; this result is considered appropriate for the current work as it does not only indicates sufficient number of measurements to capture the localised effects of the bed roughness over the cross-sections but as a confirmation of the accuracy of the ADV measurements. All the point mean velocity values and the depth averaged values have been scaled to a dimensionless values using the theoretical velocity, i.e., $[U/U_b]$.

Cross-sections	$\boldsymbol{U_{Q/A}(ms^{-1})}$	$\boldsymbol{U_{\mathrm{i}}(ms^{-1})}$	% Difference
EXPT1CRS1	0.382	0.368	3.6
EXPT1CRS2	0.382	0.370	3.0
EXPT1CRS3	0.382	0.370	3.0
EXPT2CRS1	0.382	0.389	-1.8
EXPT2CRS2	0.382	0.392	-2.6
EXPT2CRS3	0.382	0.392	-2.6

Table 7: Mean velocity difference from the numerically integrated and the theoretical values

Figures 74 and 75 illustrate the lateral distribution of normalized streamwise velocity $[U/(Q/A)]$ for the three cross-sections. To enable comparison between the cross-sections, the entire field was equally mapped across the sections. Figures 74 and 75 shows some significant differences between the flexible and rigid patches in EXPT1 and EXPT2, in particular the distribution of the relative mean streamwise velocity in which the flexible vegetation appears to decelerate the near bed $\left({}^{z}/_{H} \leq 0.2\right)$ flow in EXPT1 and the rigid vegetation accelerate the flow in EXPT2. In EXPT1 (Figure 74), the flow is approximately symmetrical for $0.3 \leq {}^{z}/_{H} \leq 0.4$ across the section. Intuitively, the velocity maximum appears at the free surface within the roughness boundary region and progressively reduces towards the channel bed, the contours of the mean streamwise velocity at the lower region $\left({}^{z}/_{H} \leq 0.2\right)$ of the flow varies according to the bed roughness. It can be seen from the contour that the faster region of the flow is towards the gravel region $\left(0 \leq {}^{y}/_{B} \leq 0.5\right)$. With further reference to the near bed $\left({}^{z}/_{H} \leq 0.2\right)$ (Figure 74), the flow decelerates over the flexible vegetated region $\left(0.5 \leq {}^{y}/_{B} \leq 1.0\right)$, this reflects the different resistance to the flow as induced by the channel bed roughness. It is suggested that the flexibility and the relative density of the vegetation in EXPT1 reduces the flow velocity near bed, while the flow accelerates over the gravel bed. Comparison between the cross-sections (CRS1, CRS2 and CRS3) illustrates the stabilisation and downstream development of the flow as the distance from the change in roughness increases with subsequent displacement of maximum streamwise velocity between regions of different cross-section (Figure 74).

The result for EXPT2 (Figure 75) show clear regions of the maximum averaged streamwise velocity away from the roughness boundary region, the concentration of the mean streamwise velocity appear at the free surface on both gravel and vegetated regions, while the minimum averaged velocity is located at the roughness boundary region as illustrated in Figure 75. In

this case, the roughness combination is assumed to exert stronger influence on the flow at the boundary region.

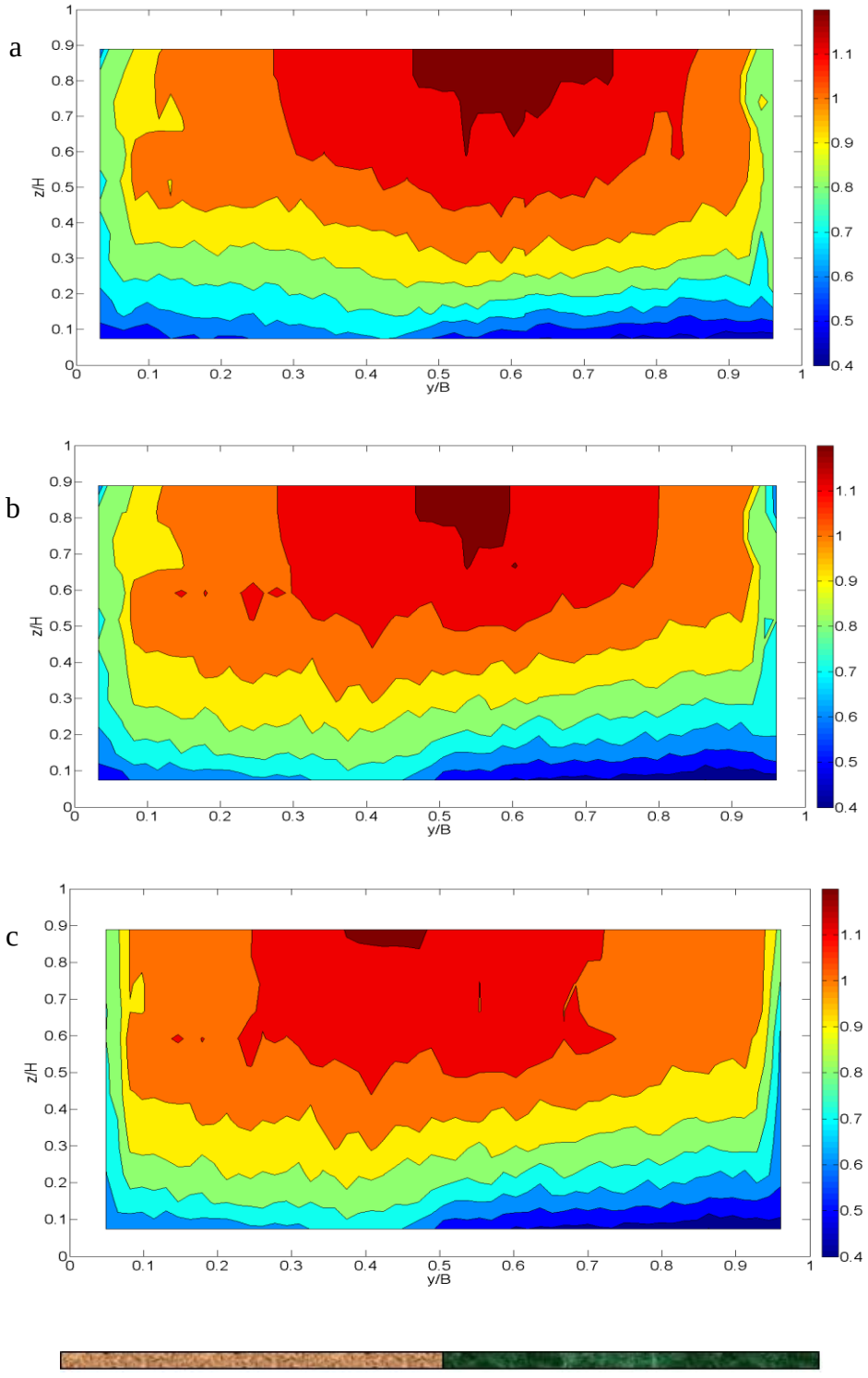

Figure 74: Relative (U/U_b) Distribution CRS1 (a) to CS3 (c) (EXPT1).

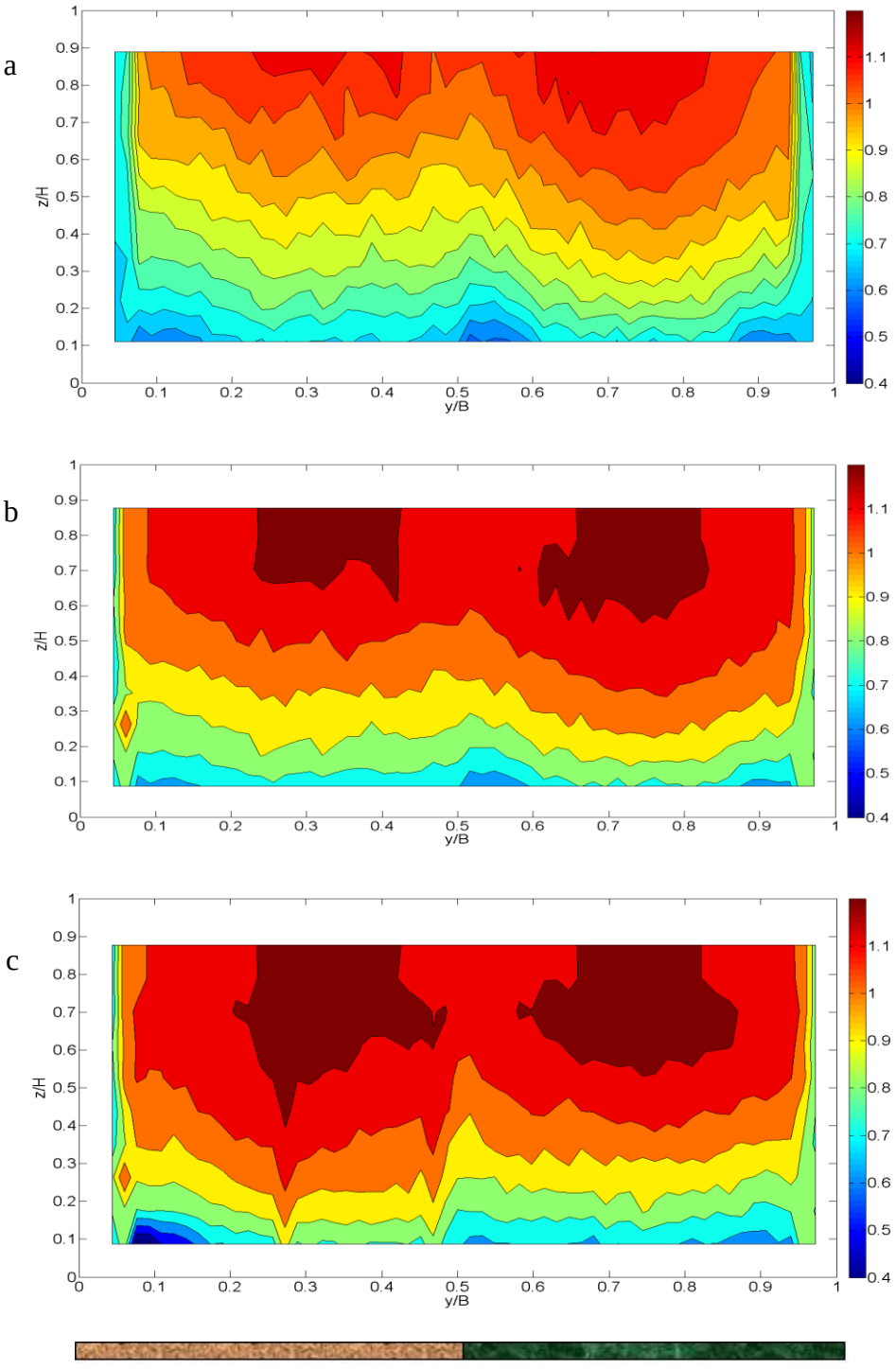

Figure 75: **Relative** (U/U_b) **Distribution CRS1 (a) to CS3 (c) (EXPT2).**

For the higher flow rate $(40l/s)$, the features of the U distribution are generally similar to the lower flow rate described above. A difference can be noticed at the upper region where the

flow is more concentrated within the roughness boundary region $\left(0.4 \leq {}^{y}/_{B} \leq 0.6\right)$ in EXPT1 and over the gravel and rigid vegetated bed in EXPT2 (Figure 76). The flow accelerates near bed in both EXPT1 and EXPT2 relative to lower flow rate as illustrated in Figure 76 for CRS3.

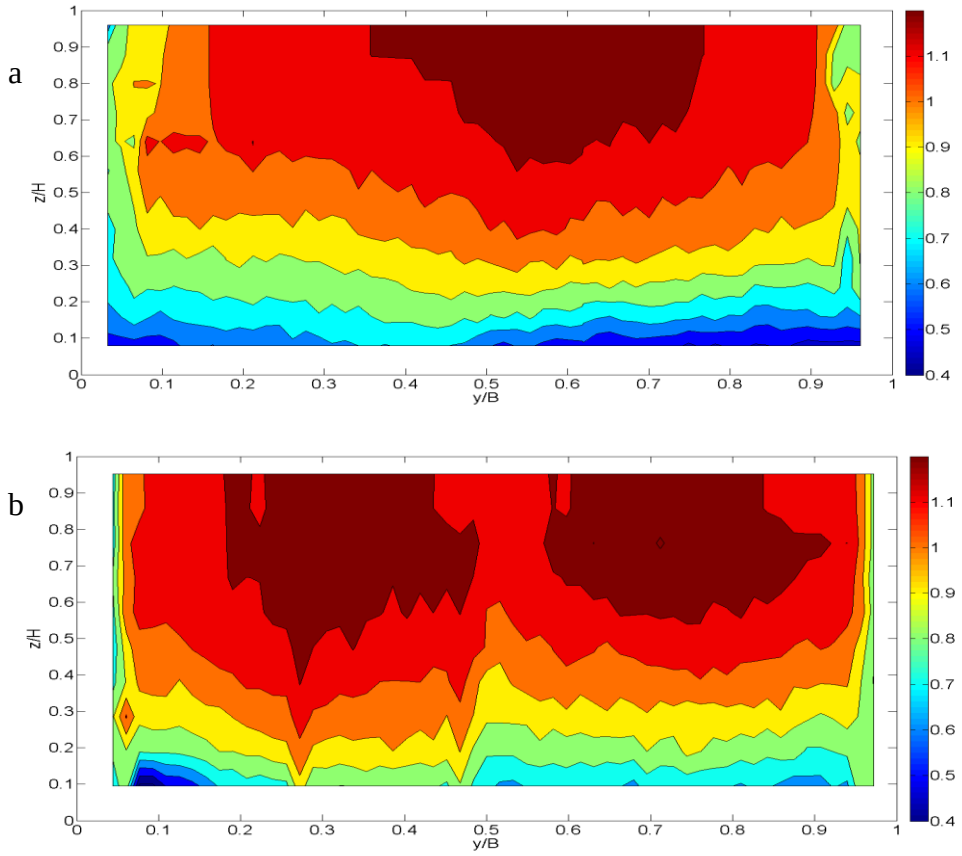

Figure 76: Relative Distribution (U/U_b) Distribution EXPT1 (a) EXPT2 (b) for higher flow rate (40l/s) at CRS3.

Figures 77 and 78 compare the vertical mean velocity (U) profiles for three cross sections over the vegetated and gravel bed. These figures confirm that the presence of vegetation retards the flow near the bed $\left({}^{z}/_{H} \leq 0.2\right)$ with much lower value of velocity over the vegetated region $\left({}^{y}/_{B} = 0.73\right)$ (Figure 77c) relative to gravel region $\left({}^{y}/_{B} = 0.24\right)$ (Figure 77a) in EXPT1. In contrast, the flow at the upper portion exhibits higher velocity above the vegetated bed and smaller velocity over the gravel bed. This is attributed to the retardation

flow over the vegetated bed due to vegetation flexibility and stem density, thereby forcing more flow to accelerate at the free surface. In EXPT2, the mean velocities are approximately constant over a large proportion of the two bed roughness at a given height as illustrated in Figure 78. However, Figure 78a demonstrates near bed $\left({}^{z}/_{H} \leq 0.2\right)$ deceleration over the gravel bed relative to vegetated bed (Figure 78c). The effect of the near bed acceleration over the vegetated bed in EXPT2 on the vertical shear is given in section (4.8).

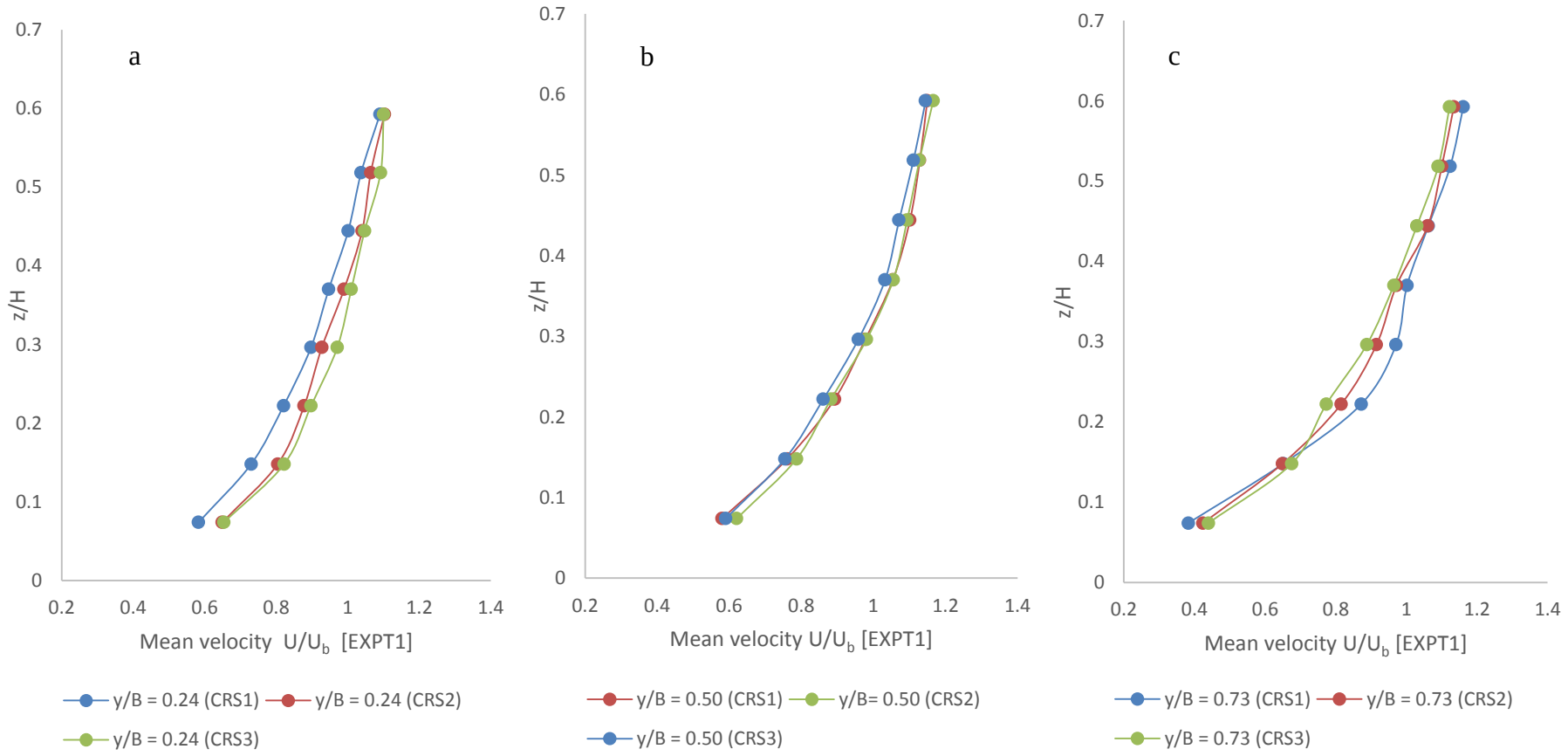

Figure 77: Vertical distribution of the mean velocity *U* over (a) the gravel $\left({}^{y}/_{B} = 0.24\right)$, (b) the boundary $\left({}^{y}/_{B} = 0.50\right)$ and (c) the vegetated $\left({}^{y}/_{B} = 0.73\right)$ regions (EXPT1)

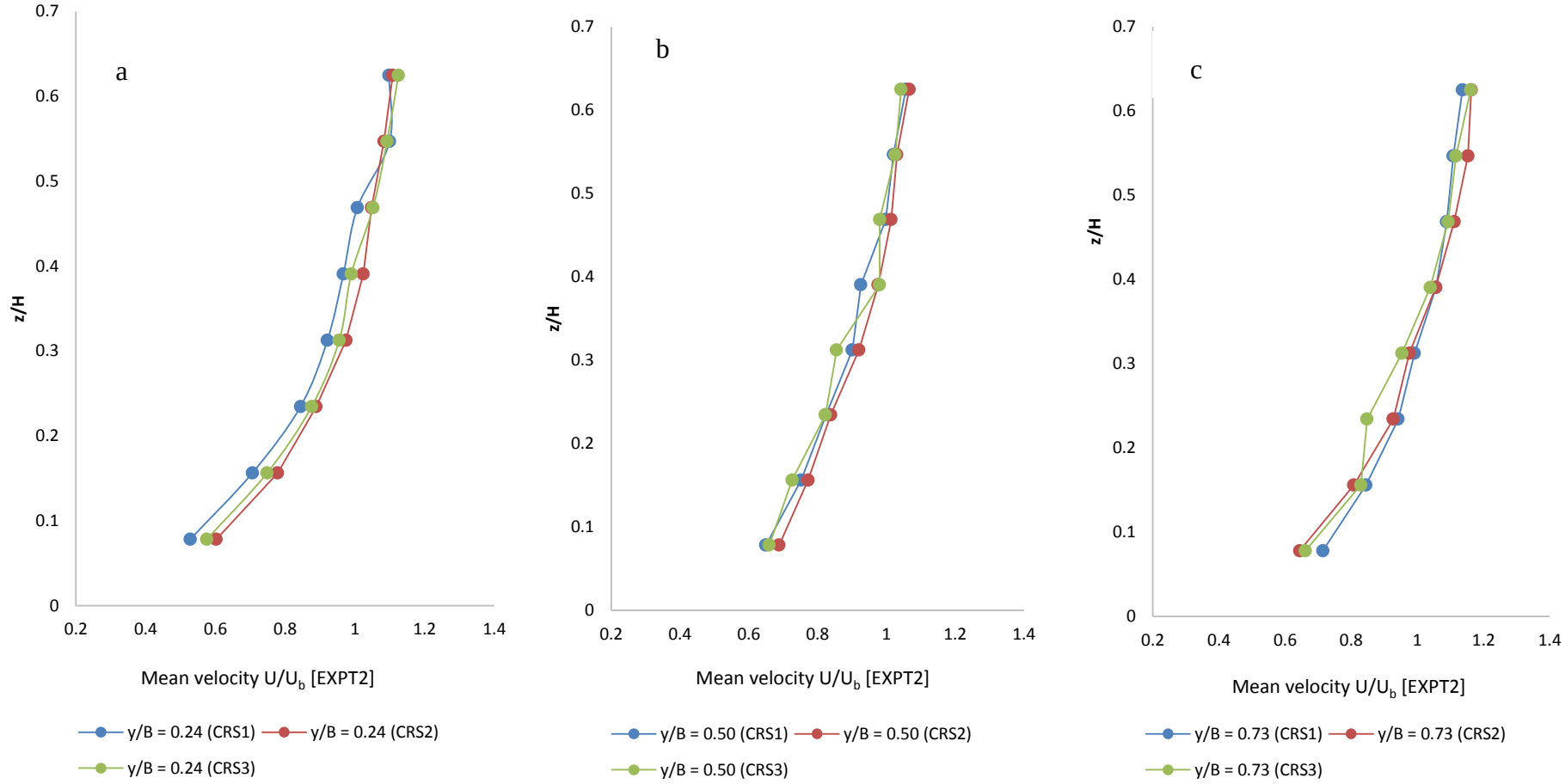

Figure 78: Vertical distribution of the mean velocity *U* over (a) the gravel $\left({}^{y}/_{B} = 0.24\right)$, (b) the boundary $\left({}^{y}/_{B} = 0.50\right)$ and (c) vegetated $\left({}^{y}/_{B} = 0.73\right)$ regions (EXPT2)

The vertical profiles of the mean velocity are explored further to examine the flow distribution within the vegetated bed. Measurements were undertaken for three vertical points using a Pitot - static tube ($4mm$ diameter) and the vertical distributions of streamwise velocity are shown in Figure 79. Vegetation stems were removed within an area $0.03m^2$ to allow the tube into vegetation zone. The flow within the vegetation is at a smaller spatial scale $\left({}^{z}/_{H} \leq 0.07\right)$ but the measurements revealed low velocities compared to the value at the vegetation top as measured using the ADV, suggesting two layer flows over vegetated bed, identifying an inflection in EXPT1 and the possibility of vertical shear. The analysis of the dynamics of vertical with horizontal shear is explored in section 4.8. However, the figure suggests larger boundary layer structure over the vegetated bed in EXPT2 relative to EXPT1 due to vegetation stem spacing (Figure 79). Similarly for higher flow rate $(40l/s)$ the vertical profile over the vegetated bed as shown in Appendix E (Figure 167) demonstrates reduction in the inflection with much greater boundary layer in EXPT1 (Figure 167, (Appendix E)) relative to lower flow rate (Figure 79). This suggests interference of boundary layer over the vegetated bed at higher flow rate $(40l/s)$ in EXPT1. The effect of reduced inflection on turbulent intensity and Reynolds stress is further examined in sections 4.5 and 4.7.

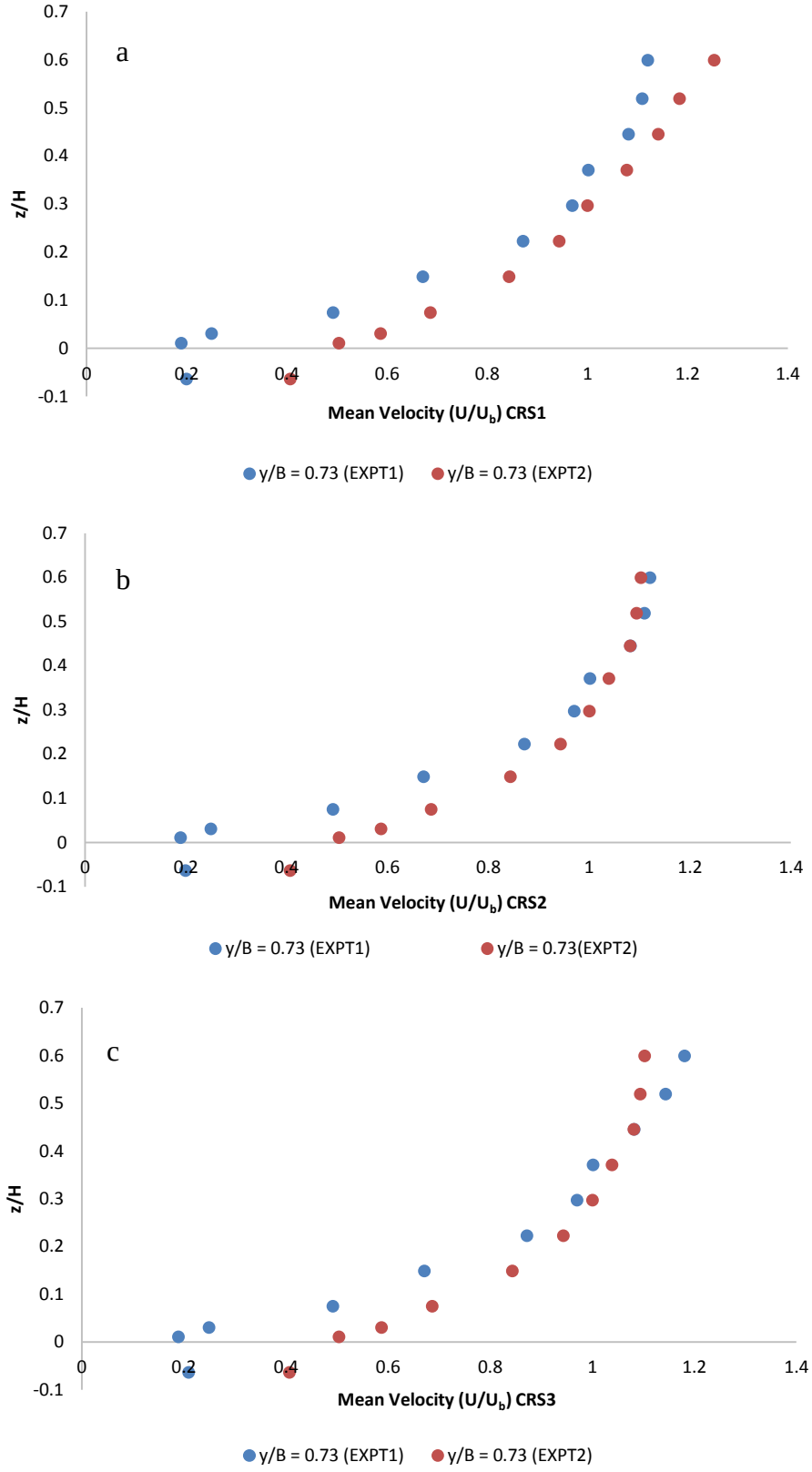

Figure 79: Vertical velocity profiles over vegetated bed with porous layer for all the cross sections (EXPT1 and EXPT2), CRS1 (a) to CS3 (c).

Figure 80 shows transverse profiles of streamwise velocity for selected elevations. All the profiles demonstrate the nature of flow over the roughness surfaces. With respect to EXPT1, the flexible vegetation retards the transverse profiles relative to gravel bed, while the figure suggests acceleration of the flow over both the gravel and rigid vegetated bed with minimum averaged velocity located at the roughness boundary region in EXPT2. Generally it can be seen that all transverse profiles indicate a change in lateral shear (i.e. changes in dU/dy at the interface $\left({}^{y}/_{B} = 0.5\right)$ between the gravel and vegetated sections). As indicated in Figure 80, lateral velocity difference is noted in both EXPT1 and the EXPT2. What is also interesting is the indication in EXPT2 that the gravel surface tends to be rougher than the rigid vegetation.

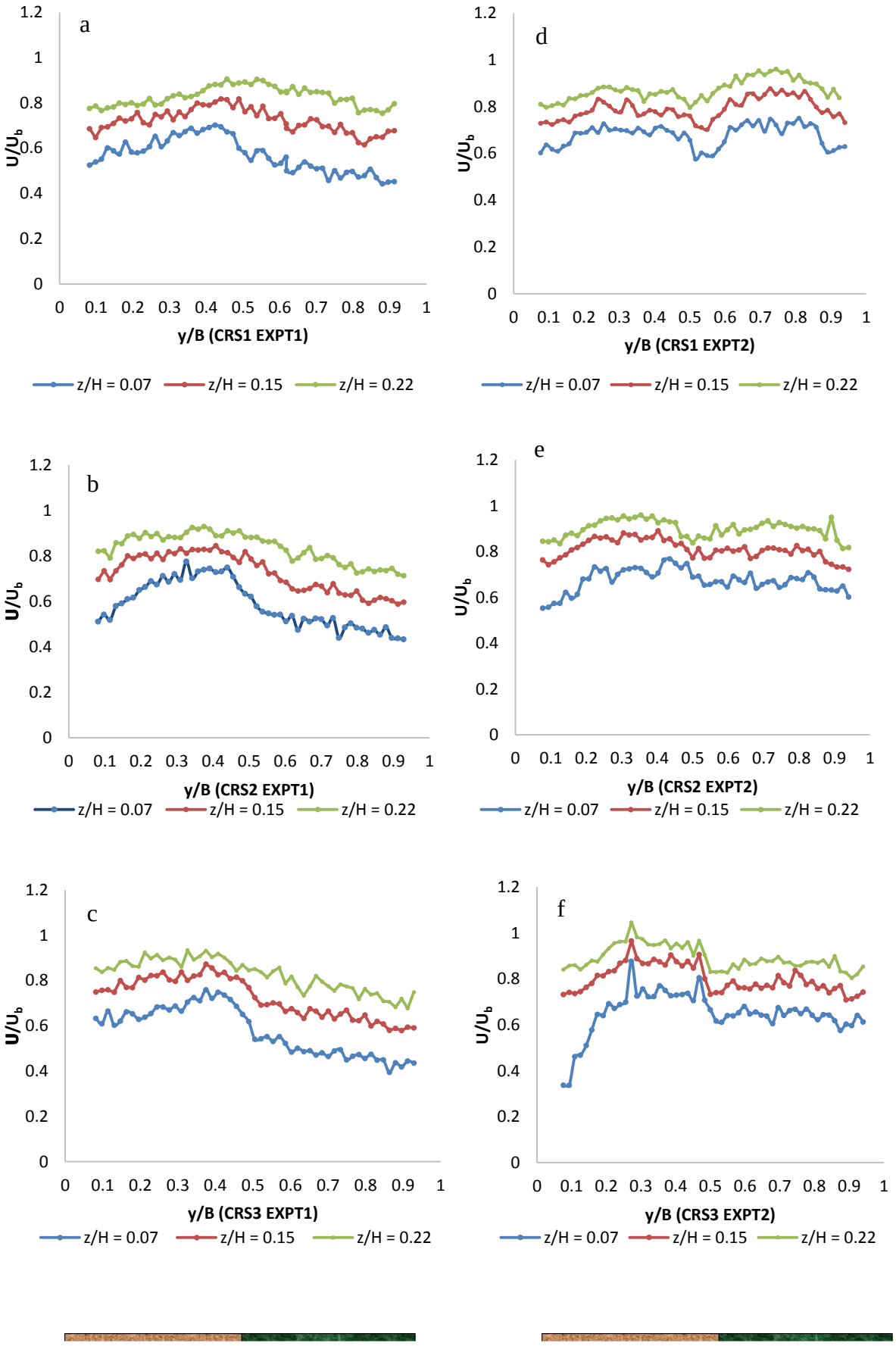

Figure 80 : Lateral velocity profiles for EXPT1 and EXPT2. CRS1 (a-d) to CS3 (c-f)

Figure 81 compares the depth averaged streamwise velocity $U_d = \frac{1}{H}\int_0^H Udz$ of each cross-section for EXPT1 and EXPT2 respectively, where U_d is the depth averaged streamwise velocity, and H is the depth of flow. The values are normalized by the channel theoretical velocity $U_b = \left({}^{Q}/_{A}\right)$. The distributions in Figure 81 illustrate the relative effects of the bed roughness on local streamwise velocities; the mean flow structure is considerably different in both EXPT1 and EXPT2 with the distributions showing different regions of maximum velocity for both experiments (Figure 81). For EXPT1 velocity maximum is observed at the free surface near the boundary region over the vegetated bed $\left({}^{y}/_{B} = 5.6\right)$ in both CRS1 and CRS2 (Figure 81a and 81b), whilst by CRS3 (Figure 81c), the maximum velocity has switched to the gravel region $\left({}^{y}/_{B} = 0.3\right)$. This is attributed to the secondary flow (section 4.4) redistributing the flow along the channel section. The flow resistance at the roughness boundary is apparent in EXPT2 with a velocity dip at the boundary region when compared with EXPT1, this suggests lateral momentum transfer at the boundary region in EXPT2; the minimum streamwise velocity (U) at this region approaches to the channel bed thereby creating velocity dip within the region $({}^{y}/_{B} = 0.45 \sim 0.55)$. This is in contrast to EXPT1 in which the results show the maximum mean streamwise velocities within the roughness boundary region $\left({}^{y}/_{B} \cong 0.5\right)$. The regions of maximum velocity are located over the gravel and vegetated bed in EXPT2.

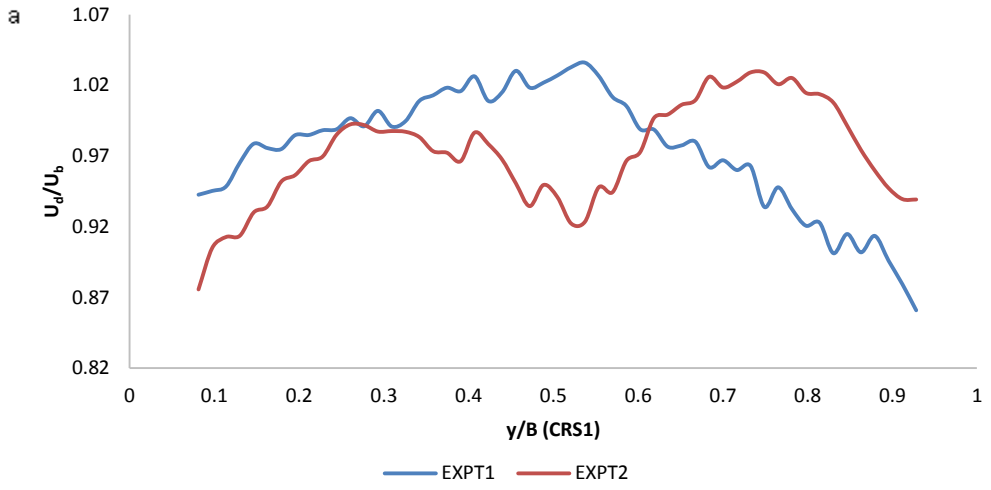

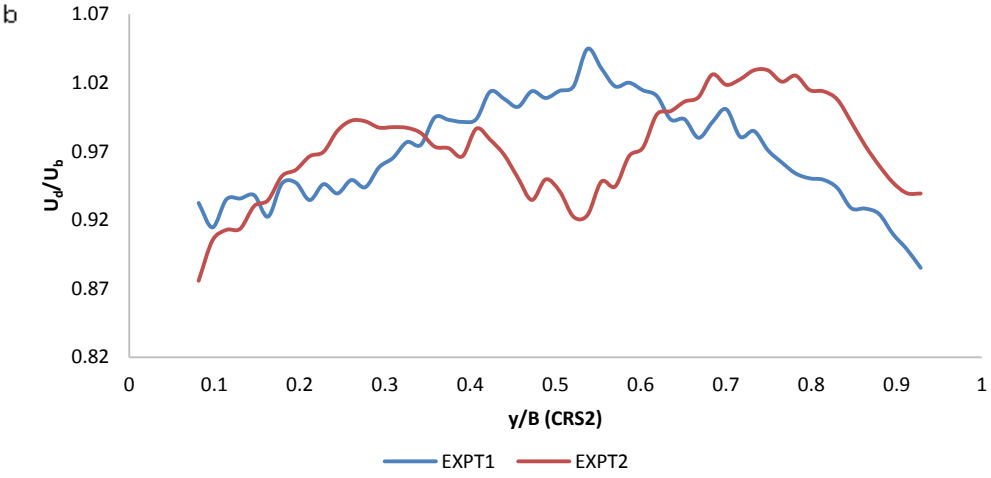

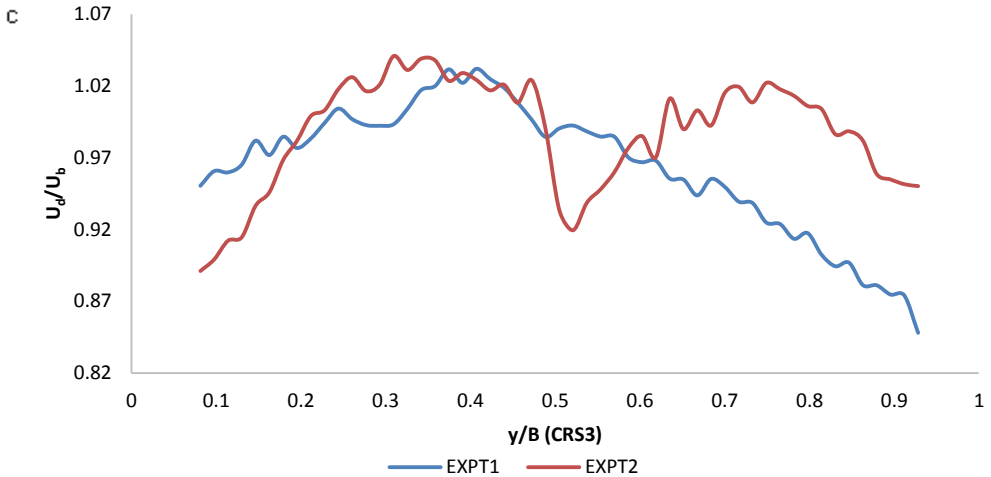

Figure 81: Depth averaged velocity U_d for EXPT1 and EXPT2, CRS1 (a) to CS3 (c)

The depth averaged velocity distribution in Figure 81 is consistent with the result of Okamoto and Nezu (2009) who observed significant momentum absorption over the oscillating canopy relative to the rigid canopy while conducting a series of experiments with artificial vegetation.

The mean velocity vertical distributions correspond with the logarithmic profile over the gravel bed thus indicating the flow to have characteristics akin to a two-dimensional structure shown in Figure 82a. In the case of vegetated bed Figure 82c, the logarithmic distribution is better observed in EXPT2 and above the vegetated zone in EXPT1 (Nepf and Vivoni, 2000) while there is divergence from logarithmic profile within the vegetated bed in EXPT1 as illustrated in Figure 82c. The results confirmed the larger boundary layer structure in EXPT2 relative to EXPT1.

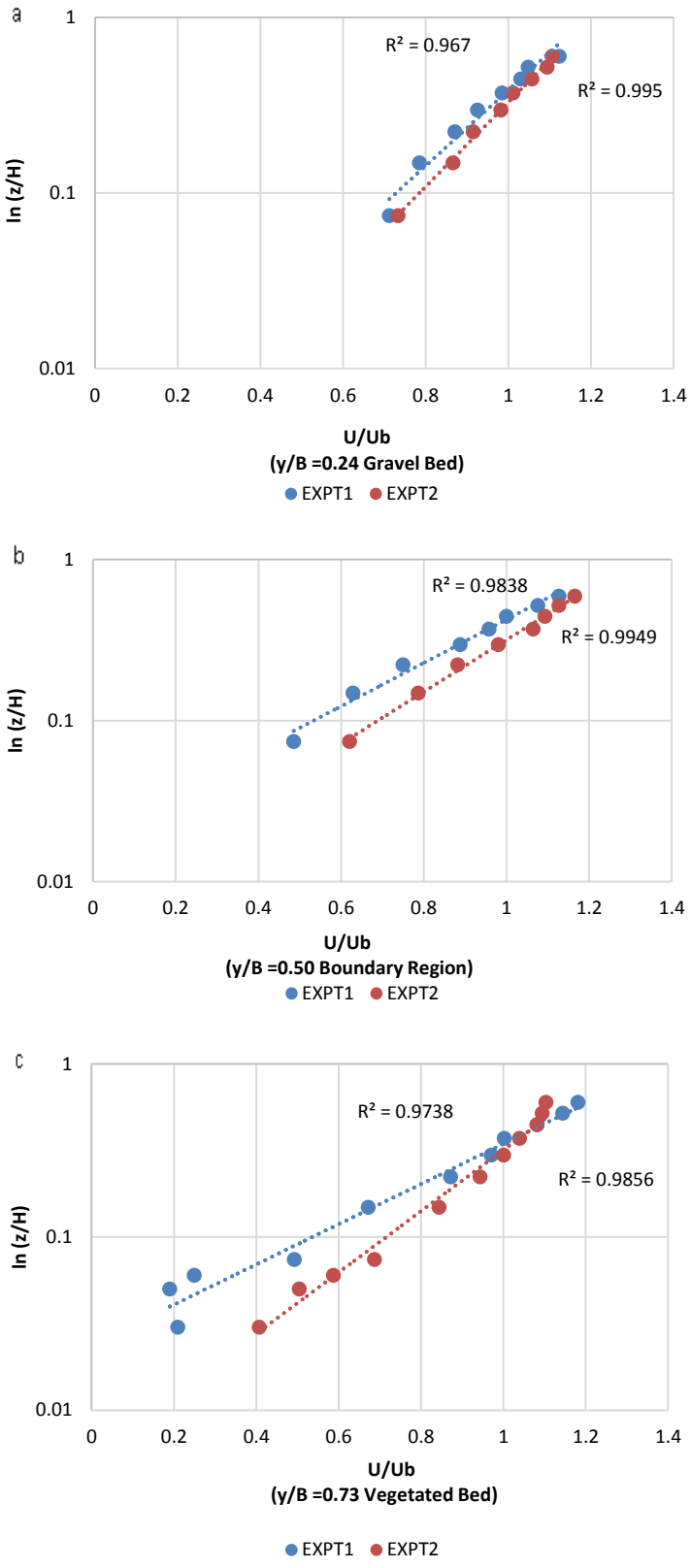

Figure 82: Logarithmic Distribution of the Mean Streamwise Velocity (EXPT1 and EXPT2), Gravel (a) to Vegetated region (c) for CRS3

4.4 Secondary Flow

Secondary flow vectors were obtained by calculating $(V^2 + W^2)^{\frac{1}{2}}$, where V and W are the mean lateral and vertical velocities respectively, the results of which are shown in Figures 83 and 84. As a check, these values were numerically integrated over the cross section and the resultant velocities were found to be closed to zero, for example (3.33×10^{-3}). The maximum calculated mean vector is within 3% of the mean streamwise velocity (U) for both EXPT1 and EXPT2 and as such is in keeping with the values found elsewhere (Nezu et al., 1993, Jesson et al., 2013, Wang and Cheng, 2006). Figures 83 and 84 illustrate the distributions of the secondary flow vectors. Based on these figures it can be seen that CRS2 and CRS3 show more definite vector directions relative to CRS1 because the flow structures begin to stabilize as the distance from the change in roughness increases due to downstream development of the flow.

For EXPT1 Figure 83, the direction of the secondary flow vector is similar to those observed for rough and smooth strips by Wang and Cheng (2006); Jesson et al. (2013), and Vermaas (2009). A visual inspection shows that the magnitude of secondary flow over the gravel bed $\left(0 \leq {}^{y}/_{B} \leq 0.5\right)$ in EXPT1 is relatively large with occurrence of down-flow, and up-flow over the flexible vegetated bed $\left(0.5 \leq {}^{y}/_{B} \leq 1.0\right)$. At the lower region $\left({}^{z}/_{H} \leq 0.2\right)$ of the flow, the transverse motion is directed from the gravel bed towards the flexible vegetated bed, and at the upper region $\left({}^{z}/_{H} > 0.2\right)$, the flow tends to be transported laterally in the opposite direction (although it is acknowledged that interpretation of secondary flow vectors is not definitive of the flow's actual behaviour). The direction of the flow vectors indicates a transfer of low momentum fluid from the vegetated region to the gravel region. The boundary region $\left({}^{y}/_{B} = 0.5\right)$ is apparently characterized by downflow into the vegetated bed. It can be seen from Figure 83 that, the secondary flow moves upward the near bed low velocity fluid

due to resistance of the vegetated region and transport same to the gravel region near the free surface, whilst on the gravel side downflow occurs which transport the high velocity fluid near the free surface down the lower portion of the flow, at this region the flow is transported laterally into the vegetated region. The upflow over the vegetated bed $\left(0.5 \leq {}^{y}/_{B} \leq 1.0\right)$ is induced by the retardation of the near bed streamwise flow due to vegetation stem density. It will be noted that due to the bed configuration, a relatively higher velocity will flow from the previous gravel bed to the new vegetated bed where the flow velocity is retarded - continuity suggests that the low velocity fluid is therefore transported upward by the secondary flow and direct towards the gravel region. This feature is consistent for all the cross-sections as indicated in Figure 83.

The secondary flow vectors in EXPT2 (CRS3) however suggests the appearance of the developing secondary flow cells moving in clockwise direction over the gravel bed $\left(0 \leq {}^{y}/_{B} \leq 0.5\right)$ (Jesson. et al., 2012; Knight et al., 2007; Nezu and Nakagawa, 1984; Wang and Cheng, 2005; Jesson et al., 2013), with the circulation demonstrating strong up-flow at the roughness boundary $\left({}^{y}/_{B} = 0.5\right)$ (Figure 84), the flow cells in clockwise direction appear to dominate momentum transfer between the gravel and vegetated bed strips (Figure 84). This suggests that, the contribution of the secondary flow is significant at the roughness boundary region in EXPT2. However, the results indicate evidence of downflow over both roughness regions. The directions and circulations of these secondary vectors are consistent along the channel CRS2 and CRS3.

In keeping with the findings of Figures 74 and 75, the lateral distribution of the streamwise velocity over the vegetated bed region in EXPT1 (Figure 74) corresponds to the region of upflow in Figure 83. In this region$\left(0.6 \leq {}^{y}/_{B} \leq 0.9\right)$, the mean flow decelerates near bed. The mean streamwise velocity increases towards the free surface at approximately $\left(0.2 \leq\right.$

$y/_B \leq 0.5)$ which forms the region of downflow over the gravel region as evidenced in Figure 83. In EXPT2 the minimum mean streamwise velocity at the boundary region $(y/_B = 0.5)$ in Figure 75 corresponds to the region of upflows in Figure 84. This is consistent with the findings of Jesson et al., (2013) who observed the existence of the relatively strong upflows near the rough-smooth boundary.

a

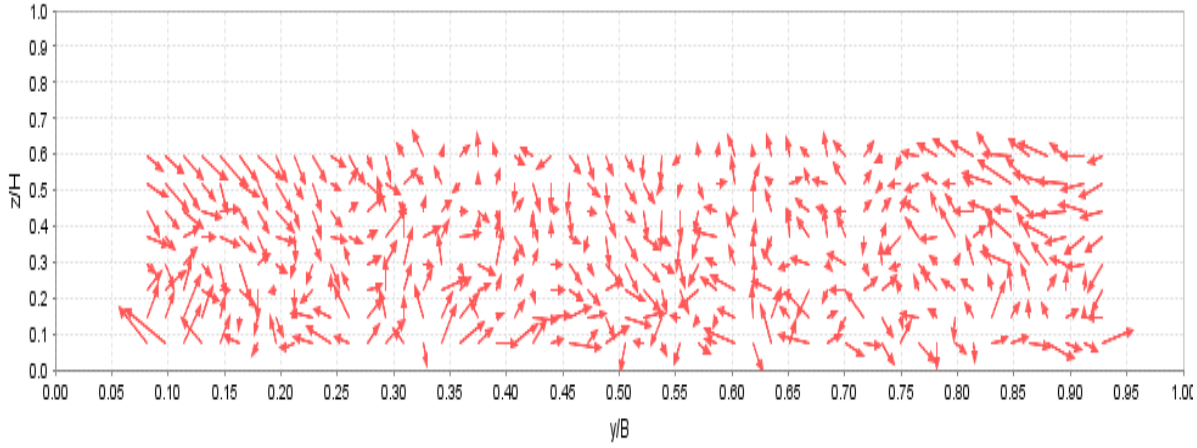

b

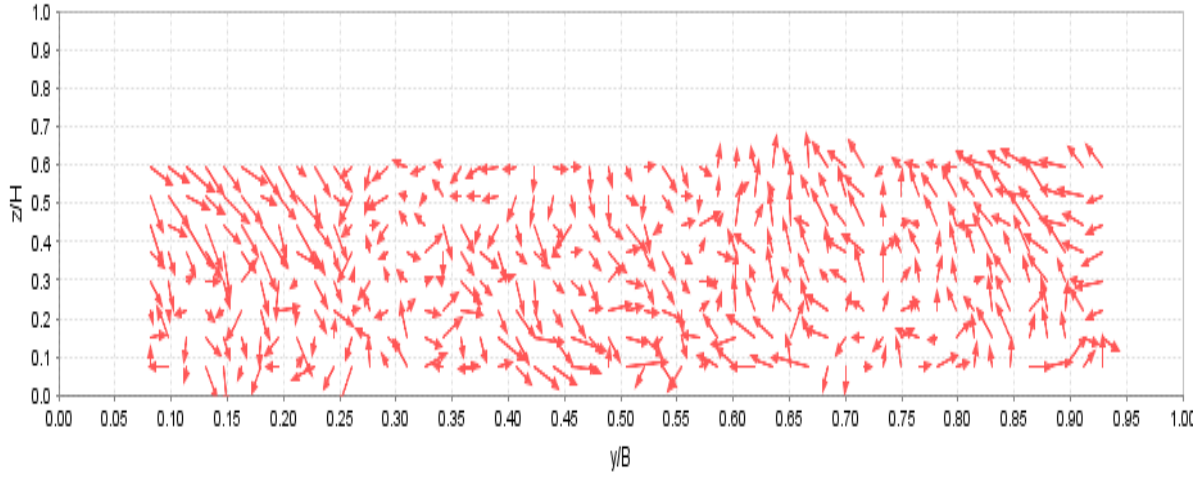

c

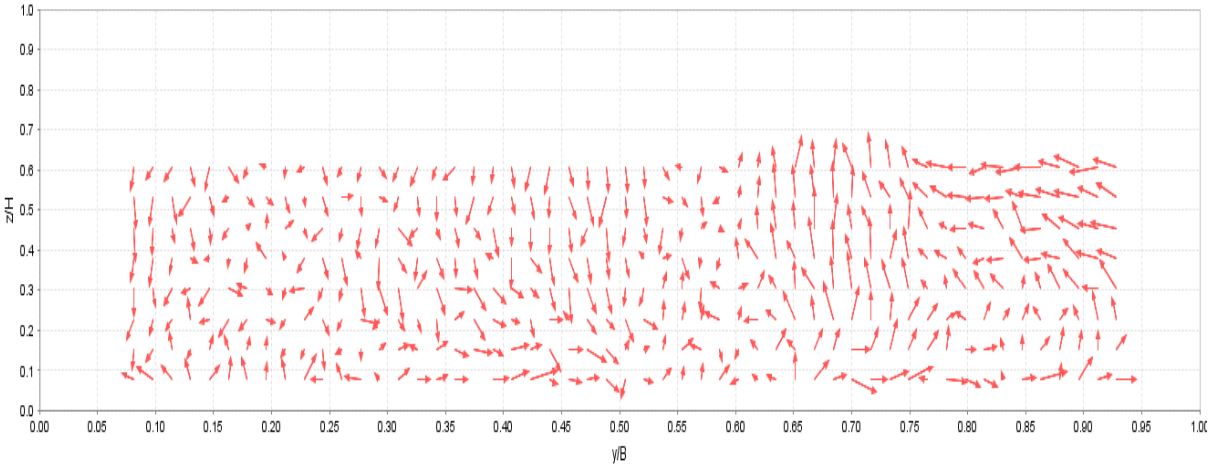

Figure 83: Lateral flow distributions (EXPT1) CRS1 (a) to CS3 (c)

a

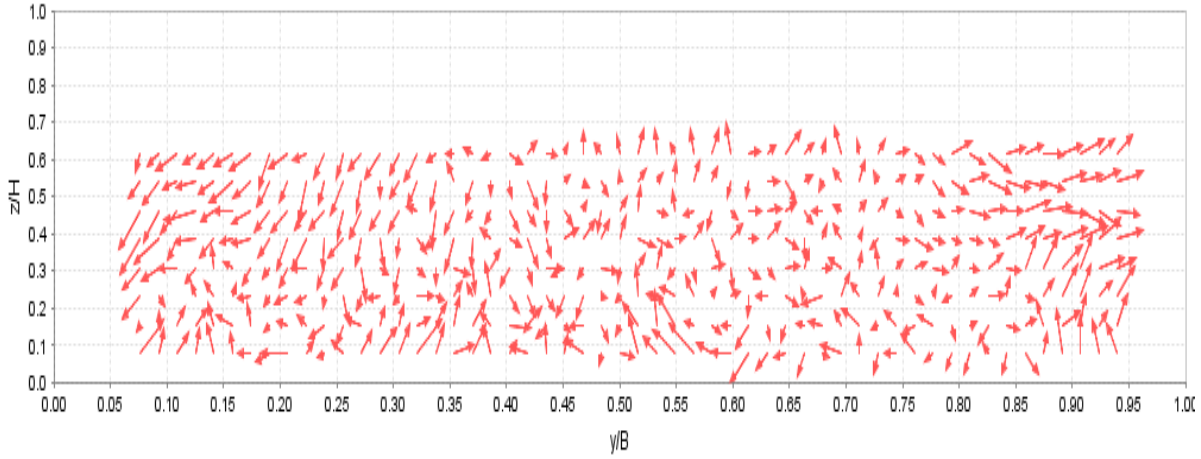

b

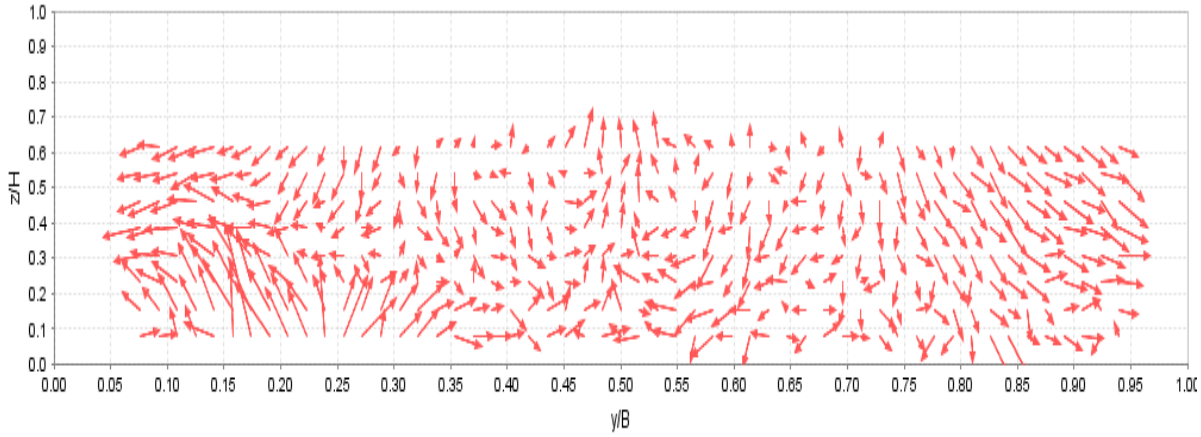

c

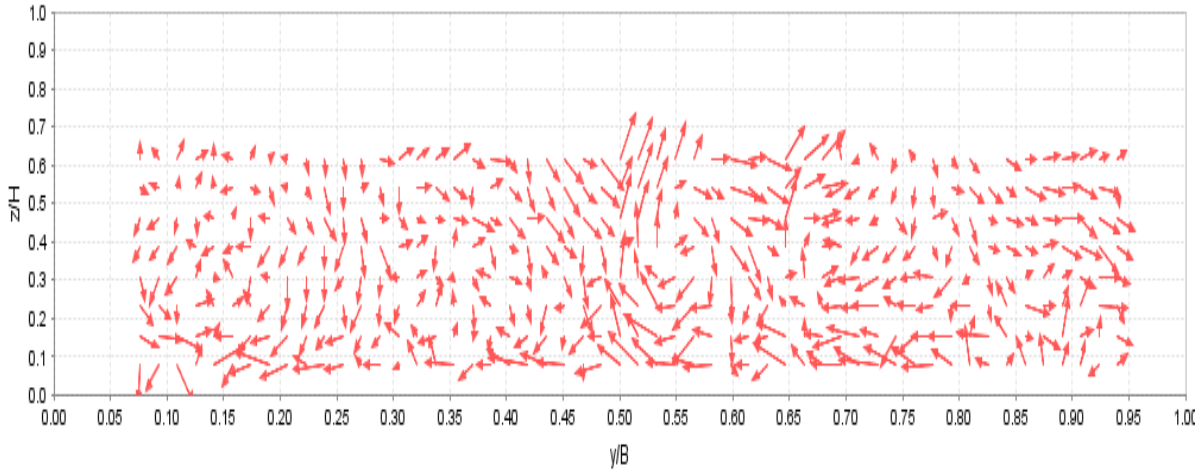

Figure 84: Lateral flow distributions (EXPT2) CRS1 (a) to CS3 (c)

4.5 *Turbulent intensity*

Turbulence intensity is an important characteristic of turbulent flow being an indicator of the magnitude of turbulence (Equation (23)). Table 8 indicates that there is a reasonable degree of consistency between the overall (cross section integrated) turbulence intensity components in each experiment and at each cross section. This suggests balanced turbulence activities along the channel sections, particularly between CRS2 and CRS3.

Cross Sections	Streamwise Turbulent Intensity (I_u)	Lateral Turbulent Intensity (I_v)	Vertical Turbulent Intensity(I_w)
EXPT1CRS1	0.166	0.127	0.073
EXPT1CRS2	0.167	0.127	0.074
EXPT1CRS3	0.167	0.127	0.074
EXPT2CRS1	0.159	0.133	0.071
EXPT2CRS2	0.158	0.134	0.070
EXPT2CRS3	0.159	0.134	0.069

Table 8: Integrated Channel Mean Turbulent Intensities for all the three Directions

In keeping with the existing literature (Jesson, 2011; Nezu and Nakagawa, 1993) the magnitude of the vertical turbulent intensity (I_w) is significantly lower than the streamwise (I_u) and lateral (I_v) turbulent intensities, the results for all the cross sections demonstrates that $I_u > I_v > I_w$. This is attributed to the damping of the vertical fluctuations by the channel boundaries and the channel's aspect ratio. From Table 8; the increased lateral turbulence intensity (I_v) in EXPT2 relative to EXPT1 suggests enhancement of lateral momentum

transfer at the roughness boundary region in comparison to EXPT1 (further discussion in section 4.8).

Figures 85 and Figure 86 present the lateral distributions of streamwise turbulent intensities I_u for the three cross-sections in both EXPT1 and EXPT2. At all the lateral distances $\left({}^{y}/_{B}\right)$ close to the channel bed, the distribution of the streamwise turbulence intensities varies with respect to flow depth $\left({}^{z}/_{H}\right)$, demonstrating the influence of bed roughness on streamwise turbulent intensities close to the channel bed, whilst at the upper region of the flow, the intensities are observed to be approximately roughness independent.

The largest magnitudes of streamwise turbulence intensity I_u in the channel cross-sections were obtained over the vegetated bed $\left(0.5 \leq {}^{y}/_{B} \leq 1.0\right)$ for both EXPT1 and EXPT2, with the greatest magnitudes in EXPT1 occurring across a large proportion of the vegetated region (Figure 85); the maximum values for EXPT2 are located close to the boundary region (Figure 86). Both of these regions correspond to low areas of mean streamwise velocities (Figures 74 and 75). The value of I_u is approximately three times as high over the vegetated bed compared to the gravel bed.

The streamwise turbulence intensity I_u over the vegetated bed for higher flow rate $(40l/s)$ in EXPT1 is somewhat reduced in magnitude (Appendix E (Figure 170)) in comparison to the lower flow rate (Figures 85). This is attributed to the reduced inflection (Appendix E (Figure 167)) due to higher flow rate.

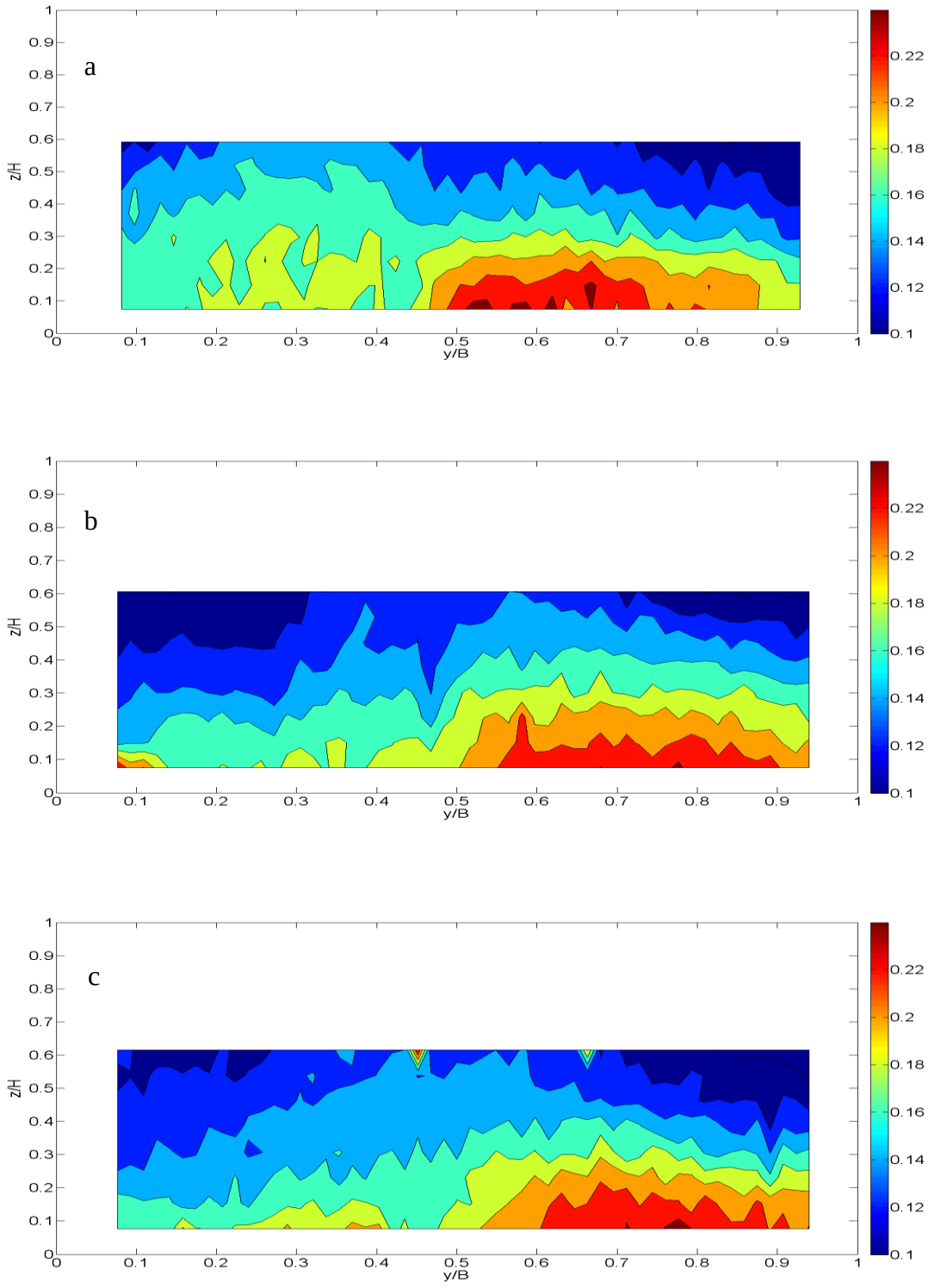

Figure 85: Relative streamwise turbulence intensity, CRS1 (a) to CS3 (c) (EXPT1)

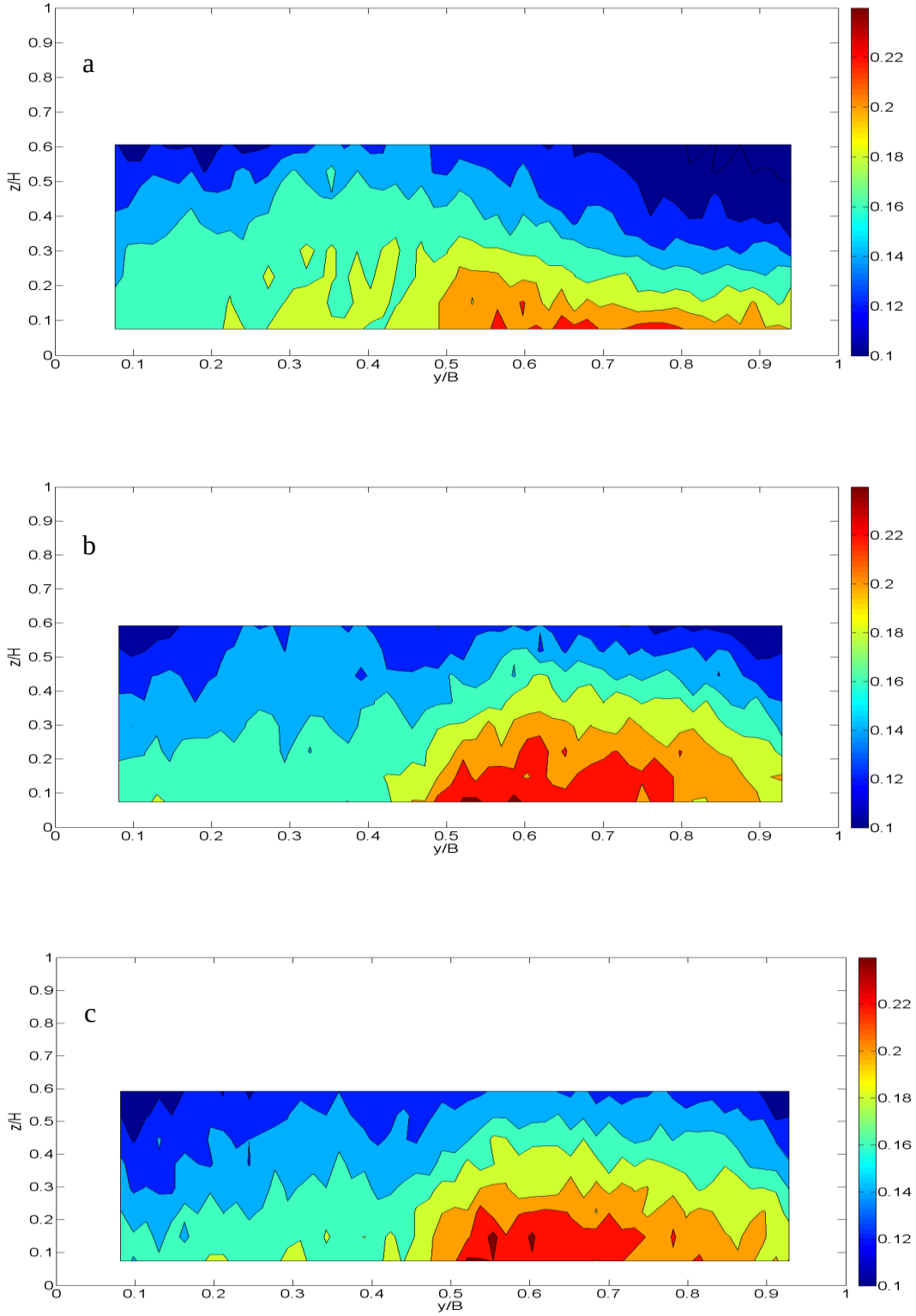

Figure 86: Relative streamwise turbulence intensity, CRS1 (a) to CS3 (c) (EXPT2)

Figure 87 and Figure 88 show similar distribution of lateral turbulence intensity I_v to the streamwise turbulence intensity I_u. However, in contrast to the distribution of streamwise turbulence intensity I_u for both experiments, there is an increased magnitude of lateral turbulence intensity I_v in EXPT2 relative to EXPT1 (Figure 87 and Figure 88). The presence of sparse vegetation stem in EXPT2 with lateral heterogeneous bed roughness can be attributed to the relatively high lateral turbulence intensities.

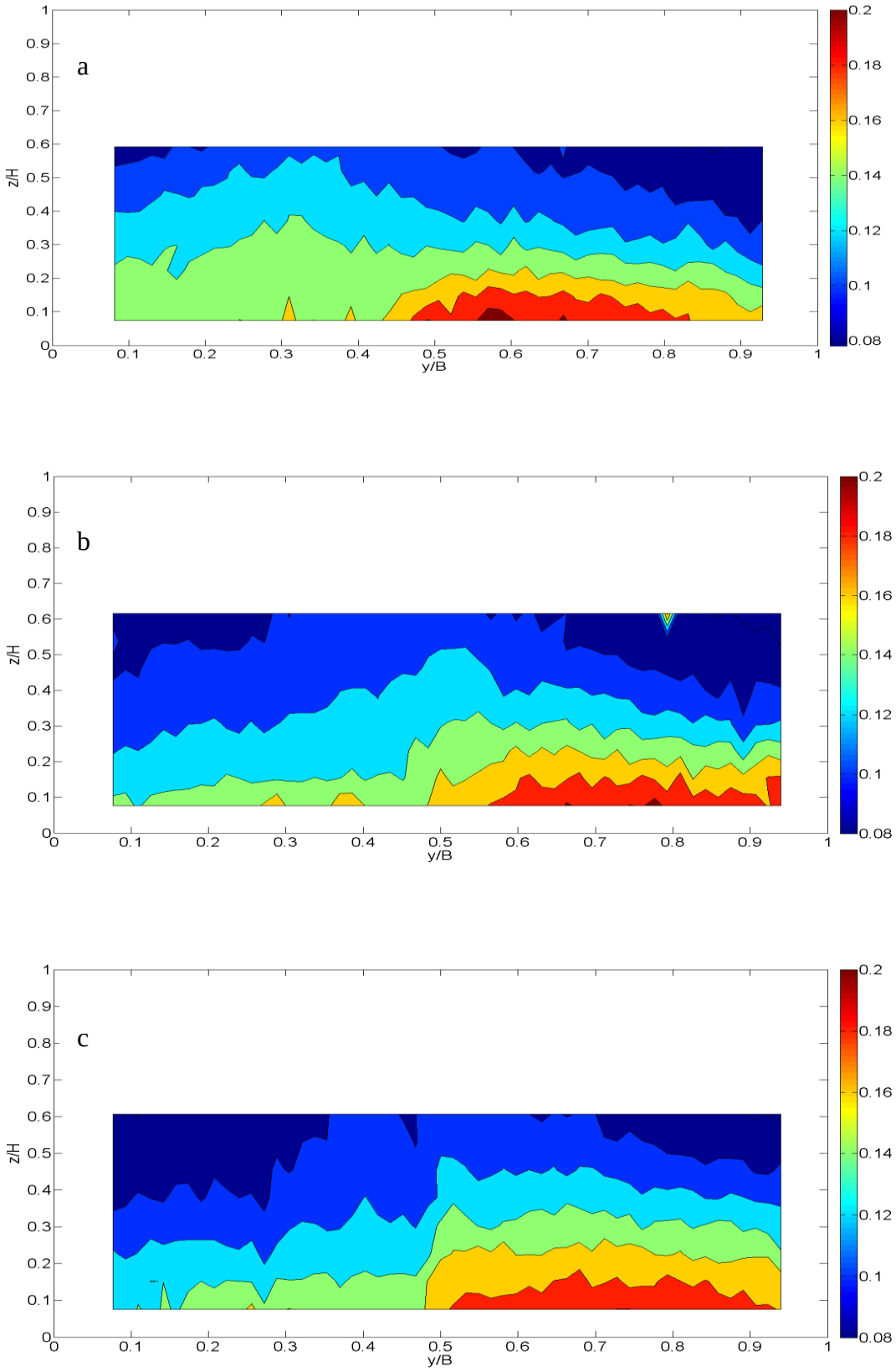

Figure 87：Relative lateral turbulence intensity, CRS1 (a) to CS3 (c) (EXPT1)

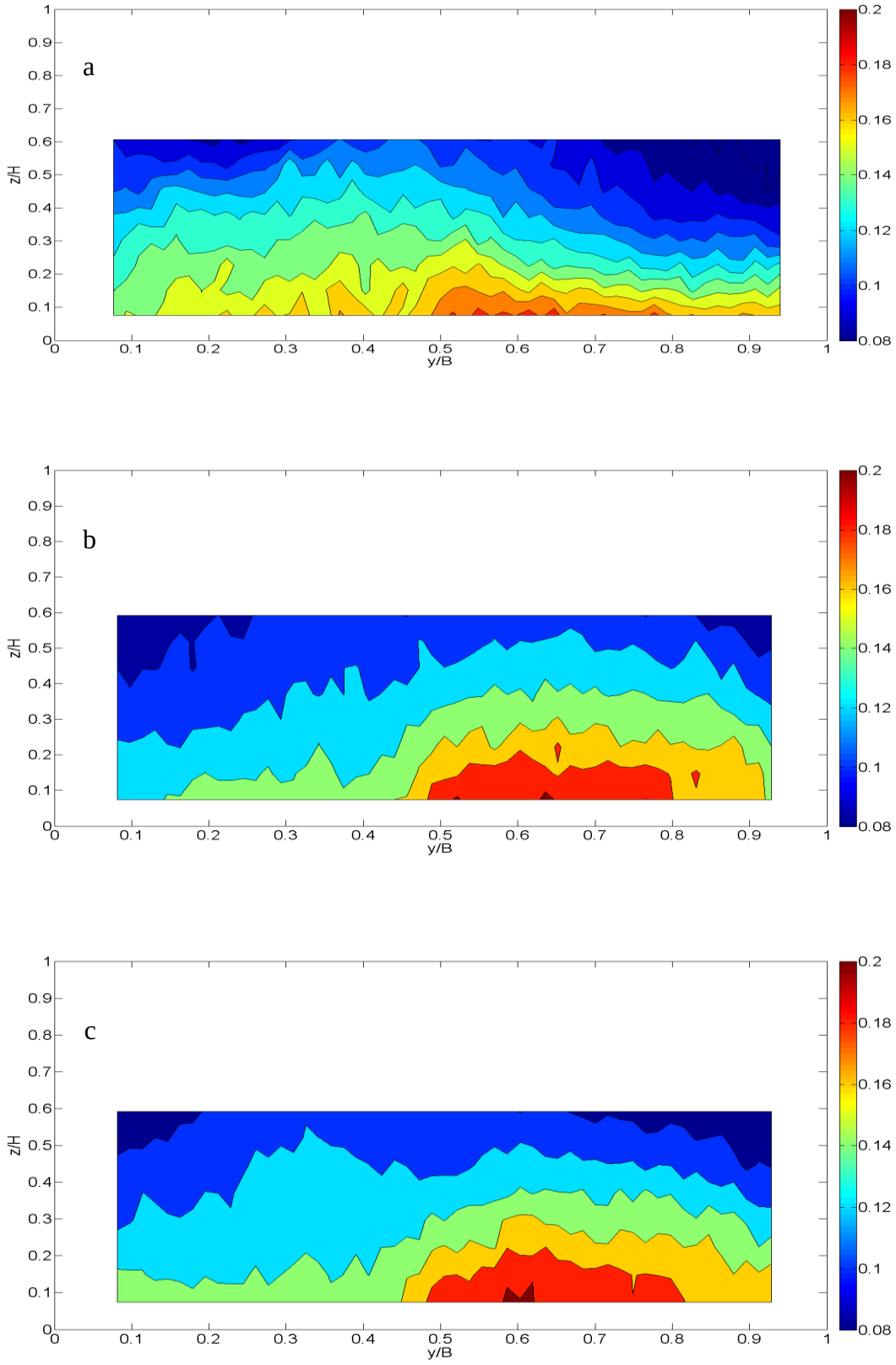

Figure 88：Relative lateral turbulence intensity, CRS1 (a) to CS3 (c) (EXPT2)

The vertical turbulent intensity (I_w) however shows a different distribution from the streamwise and lateral turbulent intensities (Figure 89 and Figure 90) as the figures indicates change in the contour levels. In EXPT1 the vertical turbulent intensity peaked over the gravel bed, this may be attributed to the secondary flow redistributing the flow laterally upward towards the gravel bed thus increasing vertical turbulence intensity within the region $\left(0.2 \leq {}^{y}/_{B} \leq 0.4\right)$ (consistent with the findings of McClelland et al., (1999).

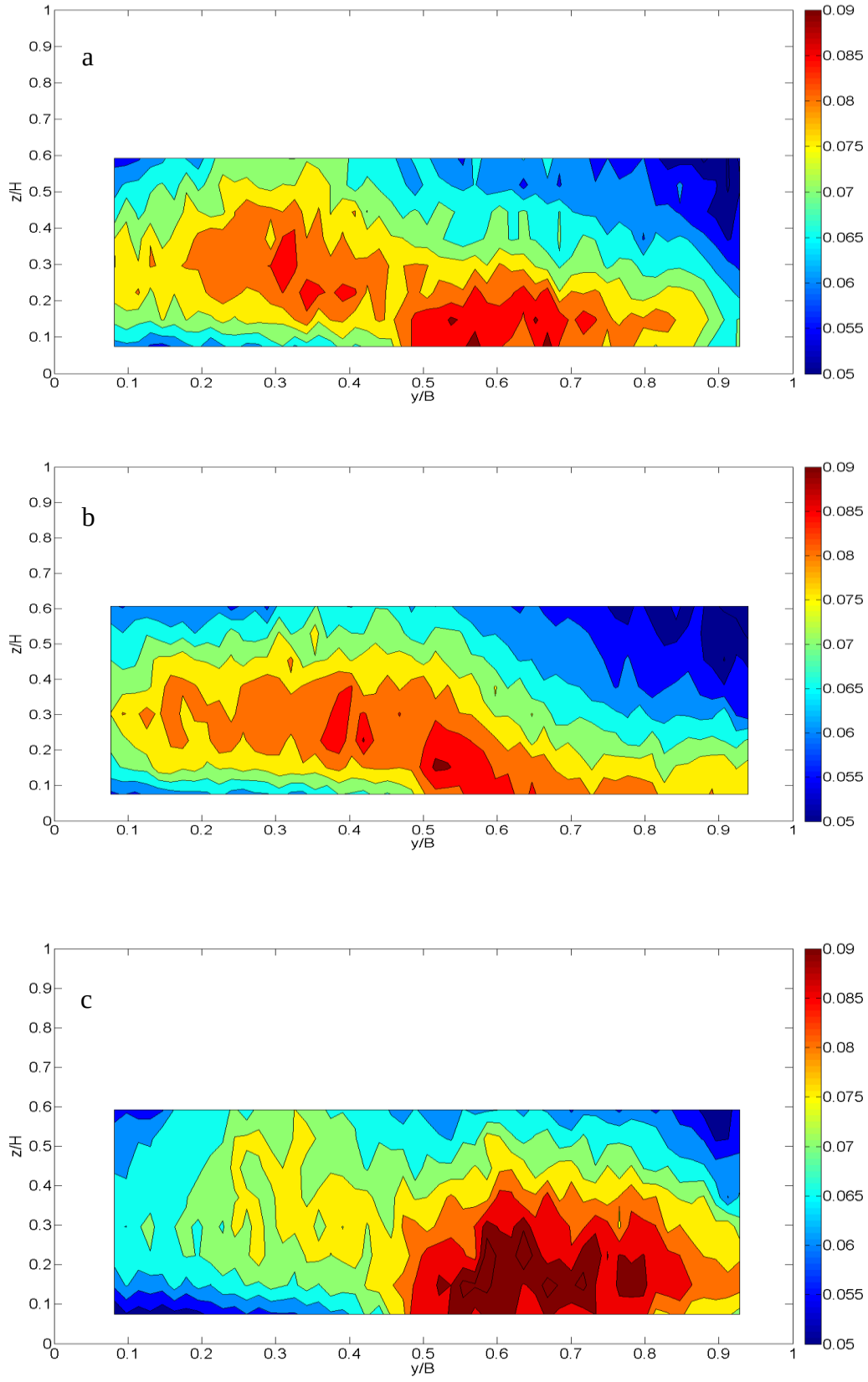

Figure 89: Relative vertical turbulence intensity, CRS1 (a) to CS3 (c) (EXPT1)

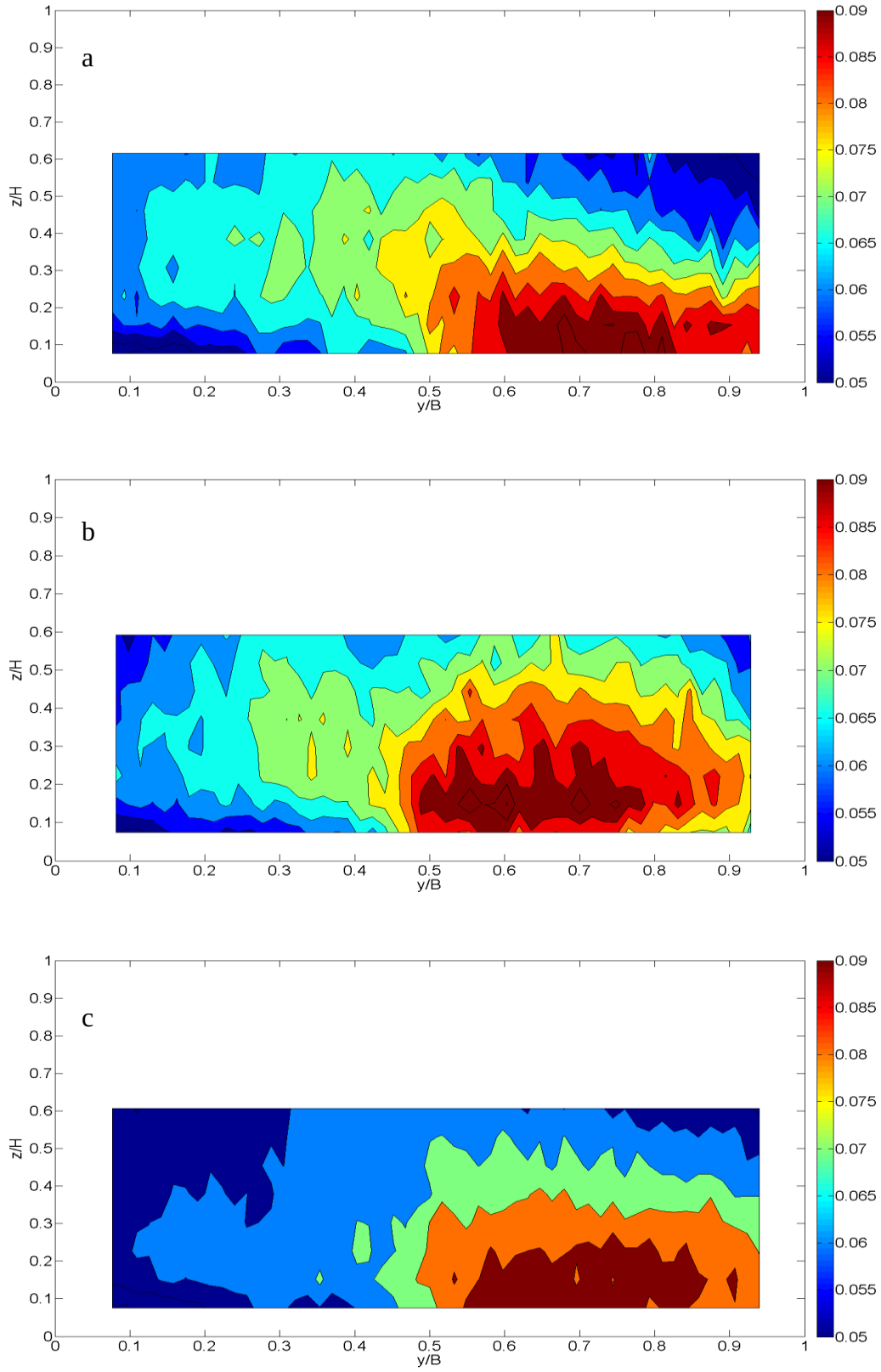

Figure 90：Relative vertical turbulence intensity, CRS1 (a) to CS3 (c) (EXPT2)

The vertical distributions of turbulent intensities at three locations are shown in Figure 91 and 92. In contrast to Jesson et al. (2013), the results show differences in the components of turbulence intensities across the channel, confirming the variations in the numerically integrated values for each component as presented in Table 8. This is an indication of apparent shear in the mean component of the flow in the current work. As would be expected, due to velocity gradient and turbulence generation, the relative turbulence intensities reached the maximum values near the bed $\left({}^{z}/_{H} \leq 0.2\right)$ and in the region near the water surface $\left(0.4 \leq {}^{z}/_{H} \leq 0.6\right)$, the vertical turbulence intensity I_w is approximately constant. This is attributed to the free surface effect on the vertical turbulent fluctuation. The peak relative turbulence intensities are obtained over the vegetated bed $(0.5 \leq y/B \leq 1.0)$ (Figure 91c) with lower values recorded at the boundary $\left({}^{y}/_{B} = 0.5\right)$ and the gravel $(0 \leq y/B \leq 0.5)$ bed regions respectively. This further suggests relatively large fluctuations from mean over the vegetated bed. In EXPT1, the values and magnitude of turbulence intensities over the gravel bed $(0 \leq y/b \leq 0.5)$ (Figure 91a) and at the boundary region $\left({}^{y}/_{B} = 0.5\right)$ (Figure 91b) are similar; indicating that roughness interaction processes do not significantly affect the turbulence intensity values at the roughness boundary region. This fact implies that the lateral interaction between the gravel and flexible vegetated bed in EXPT1 is relatively less important at the roughness boundary region. This is contrary to previous studies on heterogeneous roughness (Jesson et al., 2013; 2012) which indicated that turbulence intensities increase significantly at the roughness boundary region. In EXPT2, local peak in turbulence intensity values are recorded at the roughness boundary $\left({}^{y}/_{B} = 0.5\right)$ (Figure 92b) relative to EXPT1 (Figure 91b). In general the results can be explained from the minimum mean streamwise velocity U obtained at the roughness boundary region and the differences in the vegetation roughness where the density and oscillation of vegetation stems increases the

roughness in EXPT1 thereby intensifying the increase in turbulence intensities over the vegetated region relative to the boundary and gravel regions. The apparent changes of relative turbulence intensity in all three directions were obtained for the vertical turbulence intensity near bed. It can be seen that within the range of $\left({}^{z}/_{H} \leq 0.25\right)$, the vertical turbulence intensity decreases as the bottom of the channel is approached over the gravel bed (Figure 91a and 92a), and in contrast, increases towards the channel bed over the vegetated region Figure (91c and 92c), this may be attributed to the porosity over the vegetated bed which enhances vertical velocity fluctuation relative to the gravel bed. It is suggested that the damping of vertical fluctuation over the gravel bed can be attributed to a stable broader surface area and the viscous stress dissipating vertical turbulence fluctuation more effectively near the bed relative to the vegetated bed.

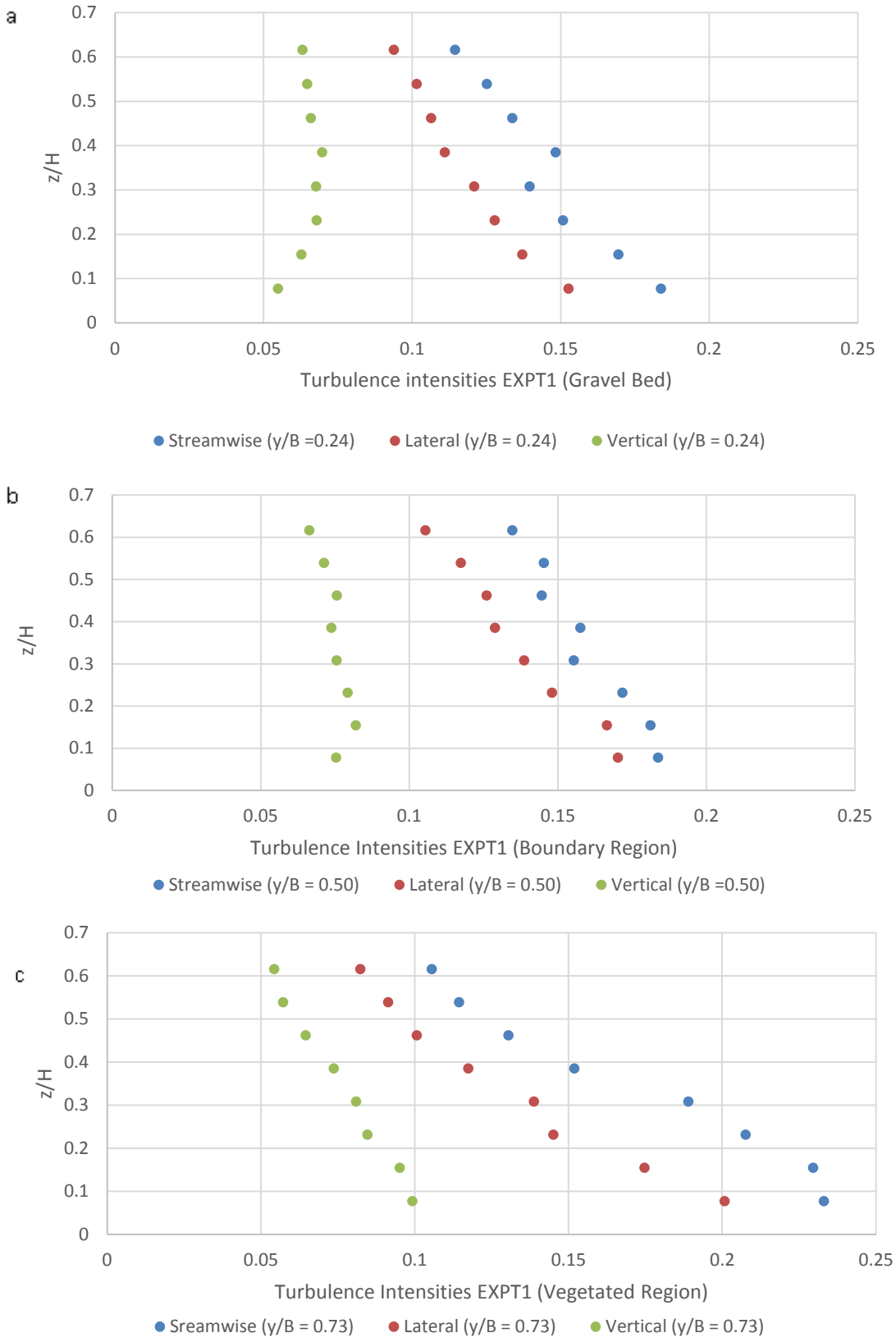

Figure 91: Vertical Distribution of the Relative Turbulence Intensities (EXPT1), (a) Gravel bed to (c) Vegetated bed

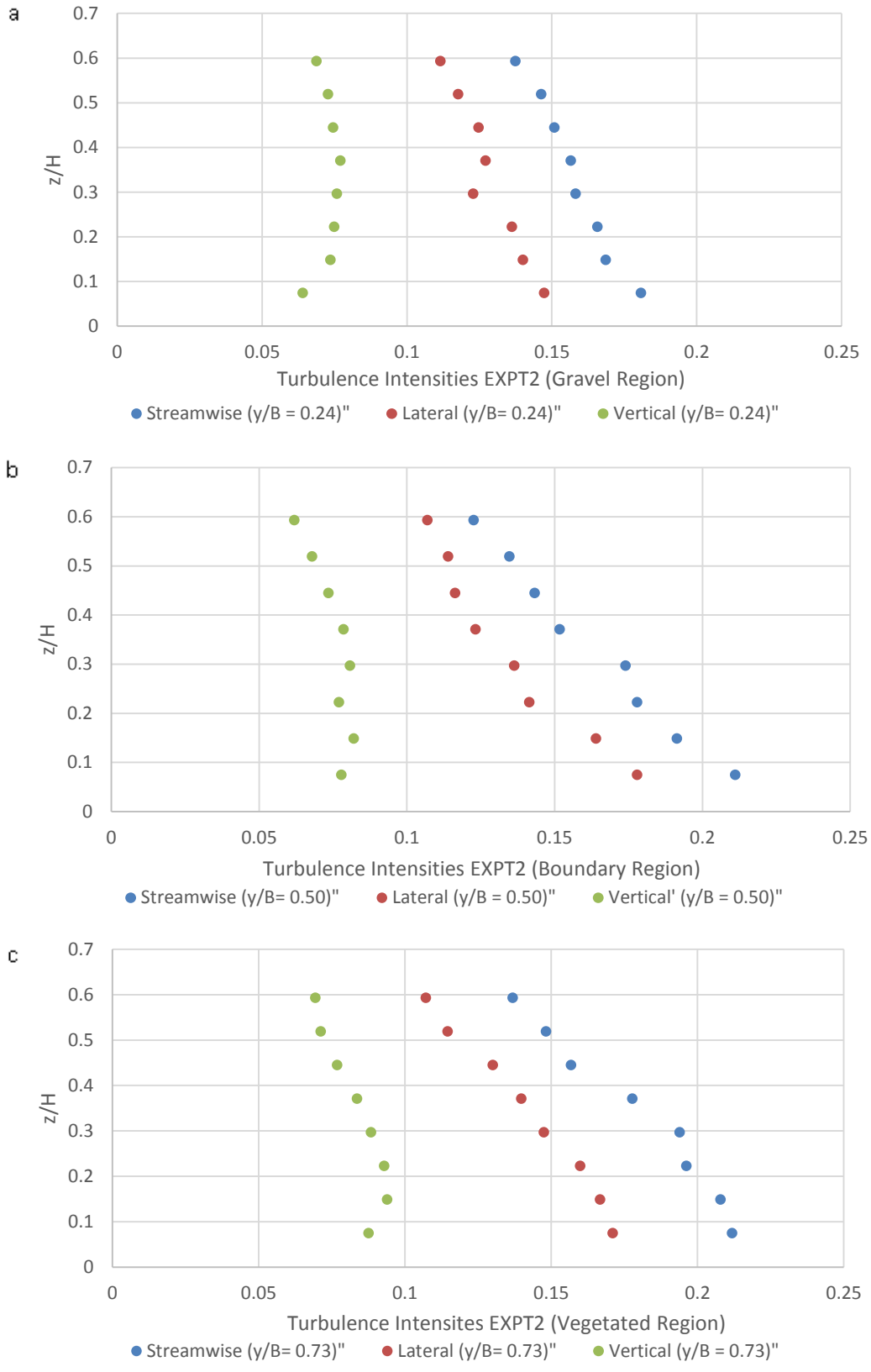

Figure 92: Vertical Distribution of the Relative Turbulence Intensities (EXPT2), (a) Gravel bed to (c) Vegetated bed

4.6 Turbulence Kinetic Energy (K)

With turbulence being transferred by the turbulent kinetic energy (K), the K relates the mean kinetic energy per unit mass of fluid with the turbulent eddies; this is characterized by the three dimensional turbulence intensities. The turbulent kinetic energy $K = \frac{1}{2}(u'^2 + v'^2 + w'^2)$ was obtained on the basis of the turbulence intensity values along the streamwise, lateral, and vertical directions. Figures 93 and 94 show the lateral distribution of the turbulent kinetic energy. The contribution of the streamwise velocity fluctuation to turbulent kinetic energy (K) dominates and ranges from 60 to 75% for both EXPT1 and EXPT2, hence the lateral distributions of turbulent kinetic energy (K) in Figures 93 and 94 are identical to the distributions of the relative turbulence intensity in the streamwise direction (Figure 85 and Figure 86).

Figure 93 shows that the maximum value of turbulent kinetic energy (K) occurs near bed $\left({}^{z}/_{H} \leq 0.2\right)$ over the vegetated zone. For depths greater than ${}^{z}/_{H} \cong 0.2$, the turbulent kinetic energy value reduces towards the free surface. However, the turbulent kinetic energy (K) value over gravel region in EXPT2 remains approximately constant with flow depth (Figure 94). The highest turbulent kinetic energy was calculated for flexible vegetation arrangement compared to the rigid vegetation.

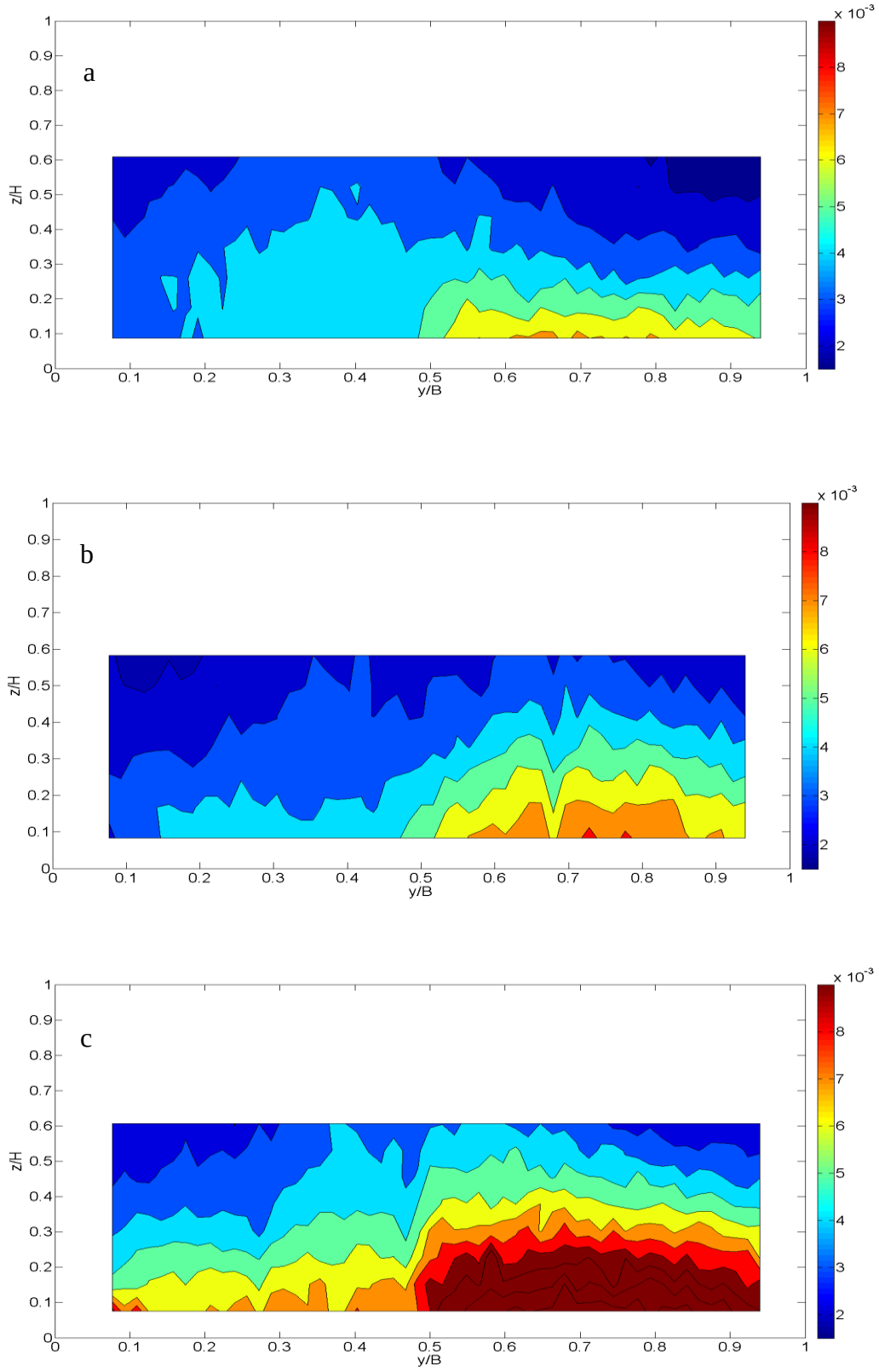

Figure 93: Lateral disribution of turbulent kinetic energy (K) CRS1 (a) to CS3 (c) EXPT1

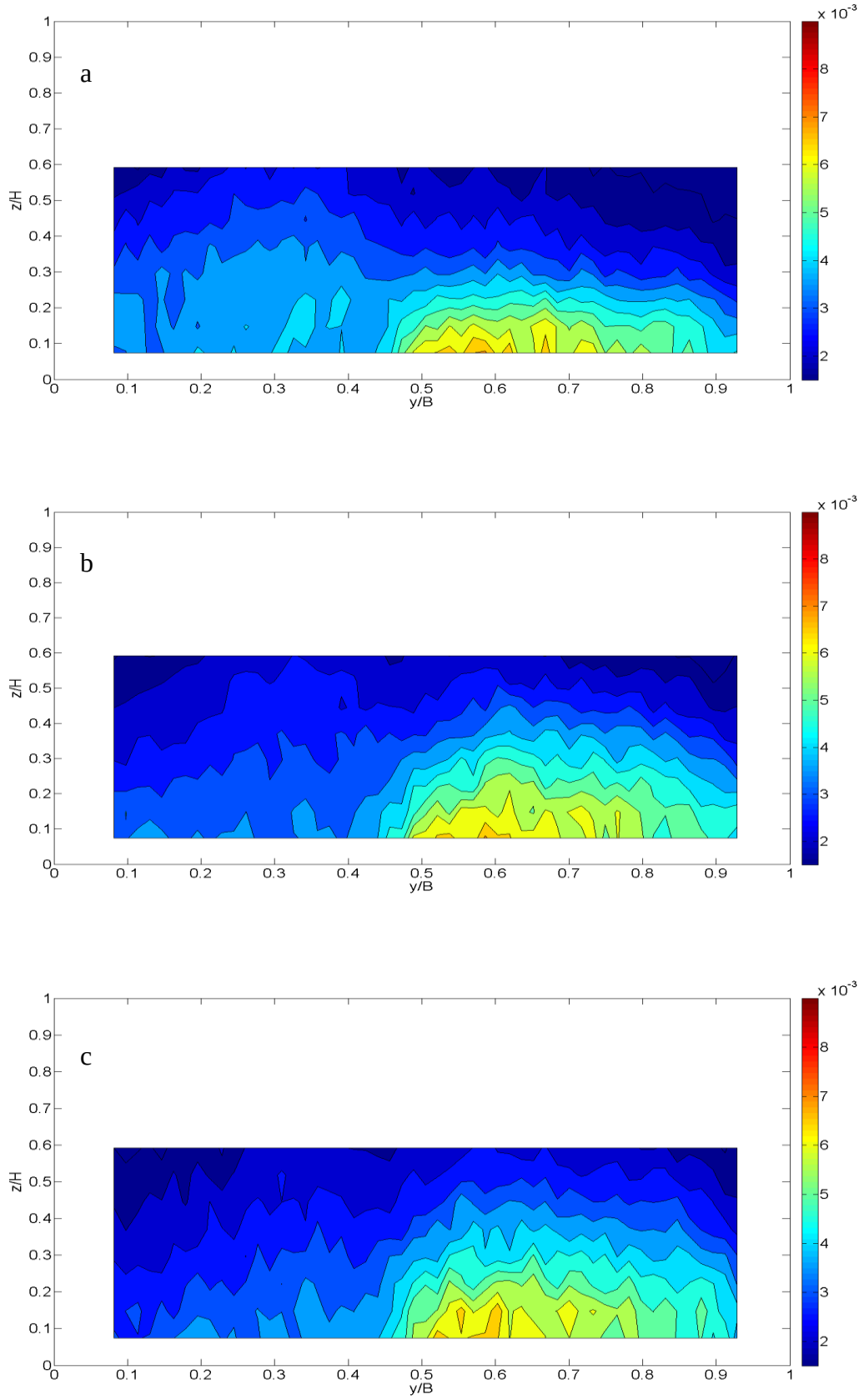

Figure 94：Lateral disribution of turbulent kinetic energy (K) CRS1 (a) to CS3 (c) EXPT2

To clarify further the structure of turbulence in the flow, the turbulent energy terms were explored using the velocity data to explain the relative significance of the processes that control the turbulent flow. The turbulence kinetic energy was obtained as described in section 4.6, the vertical turbulence transport (vertical flux) was obtained as $T_r = \frac{\partial w\prime K}{\partial Z}$, the turbulence production $P = -\overline{uw}\,\frac{\partial U}{\partial Z}$ and dissipation $E = \nu\left(\frac{\partial U}{\partial Z}\right)^2$ where ν is the kinematic viscosity (Nezu and Nakagawa, 1993). Figure 95 and Figure 96 show the turbulence terms for the flow, with the values normalized by the depth of flow. Both the turbulence production and the turbulence kinetic energy attained maxima near the bed, and decrease towards the free surface (Figure 95 and Figure 96). In contrast, the turbulence transport T_r tends to increase towards the free surface when compared with other turbulence terms; this indicates the transport of the near bed turbulent energy towards the free surface. Similar mechanisms have been observed by others (Nezu and Nakagawa, 1993). Hence, in this region, T_r serves as source of turbulence compensating for reduced turbulence production at the free surface. However, it should be noted that the high turbulence intensity near the bed over the vegetated region (Figure 91c) in EXPT1 indicates an inflection point; this becomes an essential source of turbulence generation hence enhancing turbulence production and kinetic energy over the vegetated bed relative to gravel bed. It can be observed that the higher values of turbulence production are recorded over the vegetated bed in EXPT1 (Figure 95b). However, comparison with Figure 91c shows that this is enhanced by the vertical velocity fluctuating component of the flow. Turbulence production over the vegetated bed in EXPT2 is comparable to the turbulence production over the gravel bed with similar magnitude of production terms (Figure 96a and 96b). The dissipation rate exhibits faster decay of turbulence kinetic energy over the vegetated bed in comparison to the gravel bed (Figure 95 and 96).

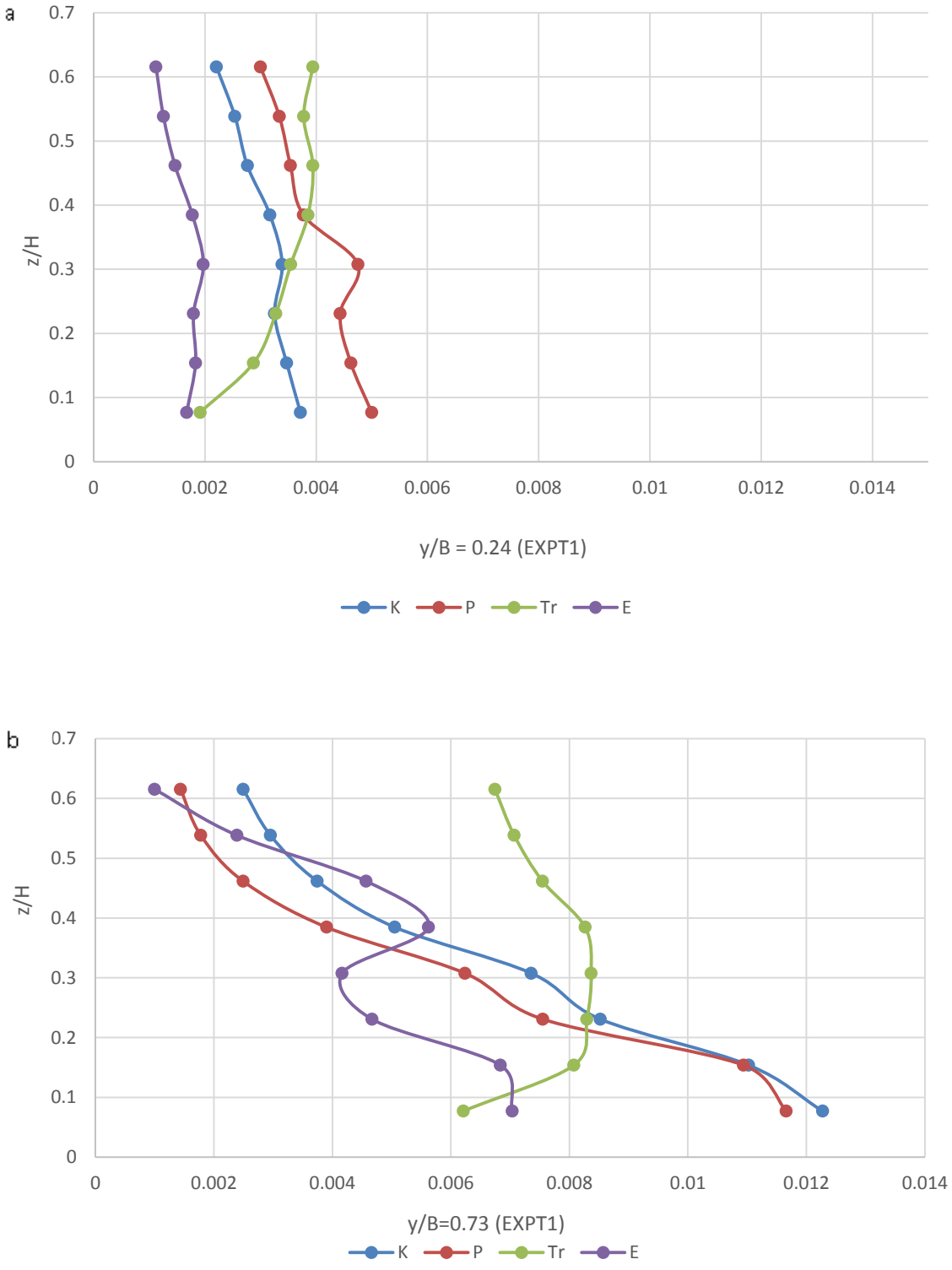

Figure 95：Vertical Distribution of the Turbulent Energy Terms (EXPT1): (a): Gravel Bed (b): Vegetated Bed

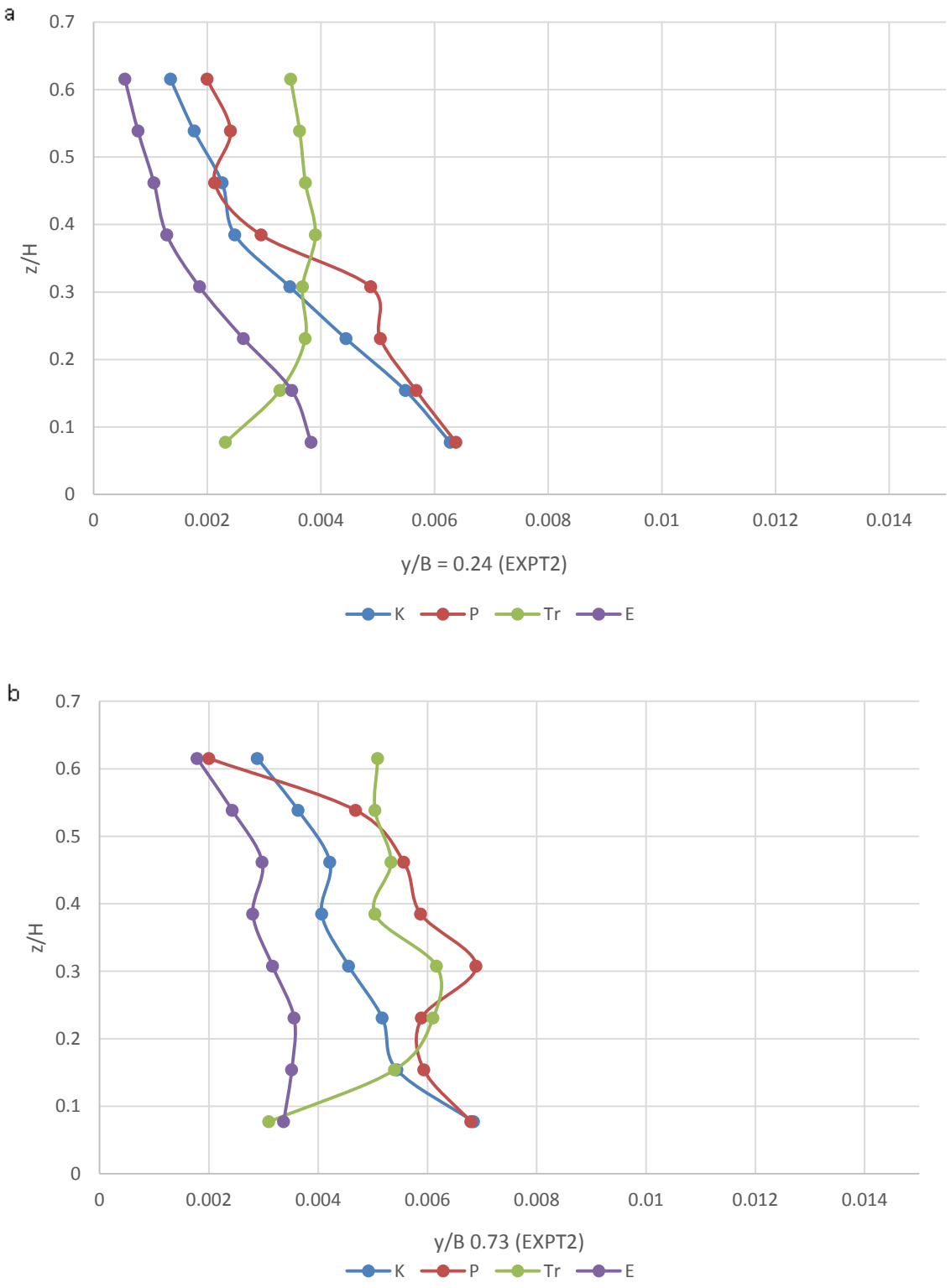

Figure 96: Vertical Distribution of the Turbulent Energy Terms (EXPT2): (a): Gravel Bed (b): Vegetated Bed

4.7 Reynolds Stress Distribution

The results of the vertical and horizontal Reynolds stresses (VRS and HRS respectively) are normalized by the theoretical boundary shear stress, $\bar{\tau_b} = \rho g R S_0$, where ρ is the water density, g is the acceleration due to gravity, R is the hydraulic radius and S_0 is the bed slope. The numerically integrated values corresponding to each cross-section are presented in Table 9.

CROSS SECTIONS	$\boldsymbol{VRS_i}$	$\boldsymbol{HRS_i}$
EXPT1CRS1	0.891	-0.072
EXPT1CRS2	0.863	-0.044
EXPT1CRS3	0.845	-0.044
EXPT2CRS1	0.645	0.099
EXPT2CRS2	0.642	0.096
EXPT2CRS3	0.621	0.096

Table 9: Integrated Mean Reynolds stresses and the Mean Boundary shear stress

Analysis of the Reynolds stresses for EXPT1 and EXPT2 provides an understanding of the shear turbulence dispersion within the flow. It is shown in Table 9 that the magnitudes of the integrated channel-mean vertical Reynolds stress (VRS_i) are larger in EXPT1 relative to EXPT2 for all the channel cross-sections. It should be noted from Table 9, that the value of the VRS decreases downstream along the channel section with CRS1 having a higher magnitude which reduces as the distance from change in roughness increases. This is

attributed to the effects of the bed roughness configuration (due to the preceding vegetated bed roughness) on the vertical VRS distribution.

Figures 97 and 98 illustrate the cross-sectional distribution of the vertical Reynolds stress, whilst Figures 99 and 100 show the vertical distribution of VRS at selected transverse positions. However, the position of maximum VRS is located near bed over the vegetated zone. This again provides an indication that the vegetated bed serves as the primary source of turbulence. Comparison of both EXPT1 and EXPT2 showed a qualitatively consistent distribution of this parameter over the vegetated bed but greater magnitude in EXPT1, with maximum relative vertical Reynolds stress of 0.89 and 0.65 for EXPT1 and EXPT2 respectively.

The vertical Reynolds stress for higher flow rate $(40l/s)$ as shown in Appendix E (Figure 172 and 173) is somewhat different with a reduced inflection (Appendix E (Figure 167)) given rise to lower magnitude of vertical Reynolds stress in comparison to Figures 97 and 98 for lower flow rate. This suggests diminishing (or intermittent) vertical shear over the vegetated bed for higher flow rate due to boundary layer interference.

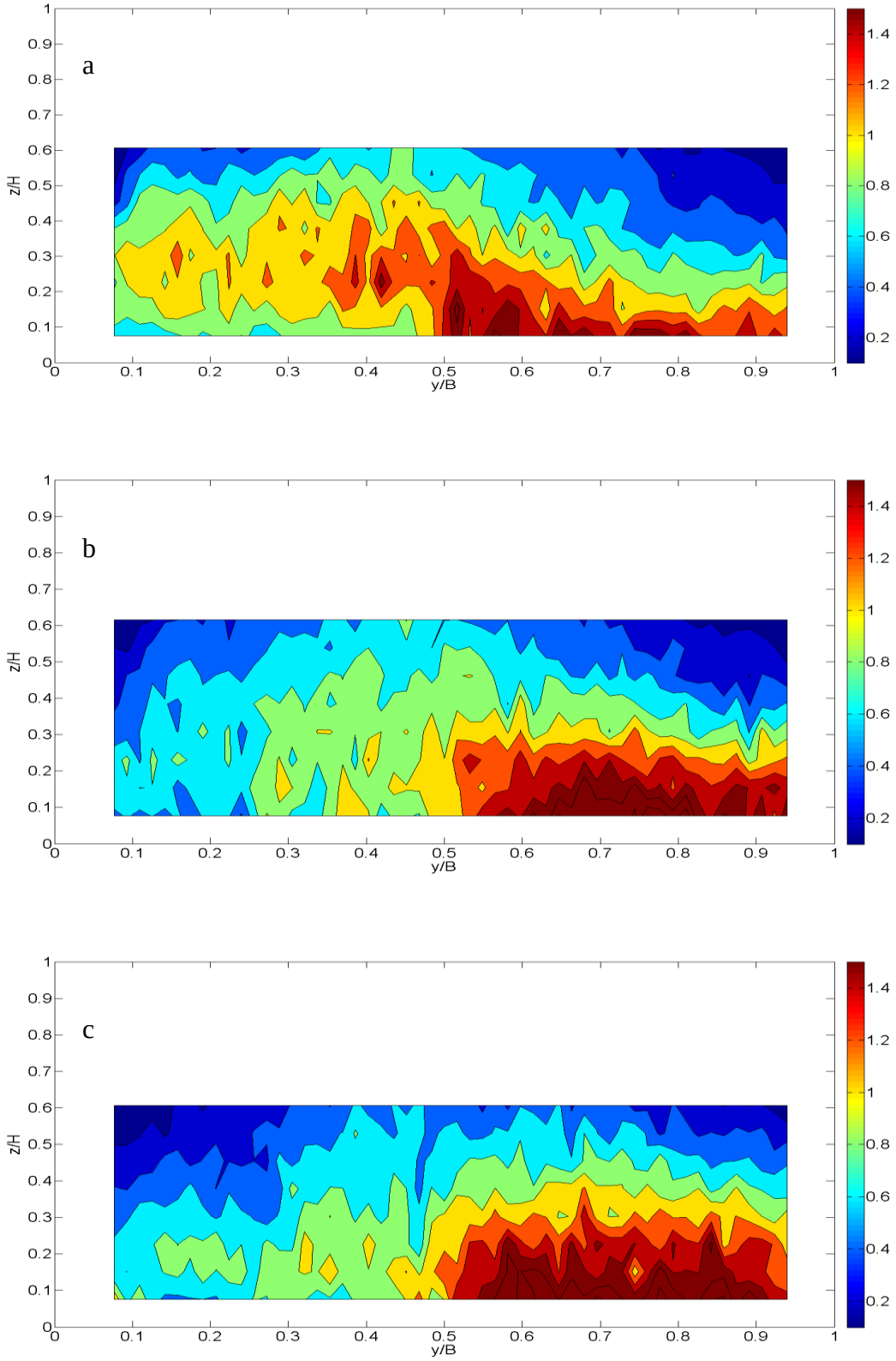

Figure 97: Lateral distribution vertical Reynolds stress; CRS1 (a) to CS3 (c) EXPT1

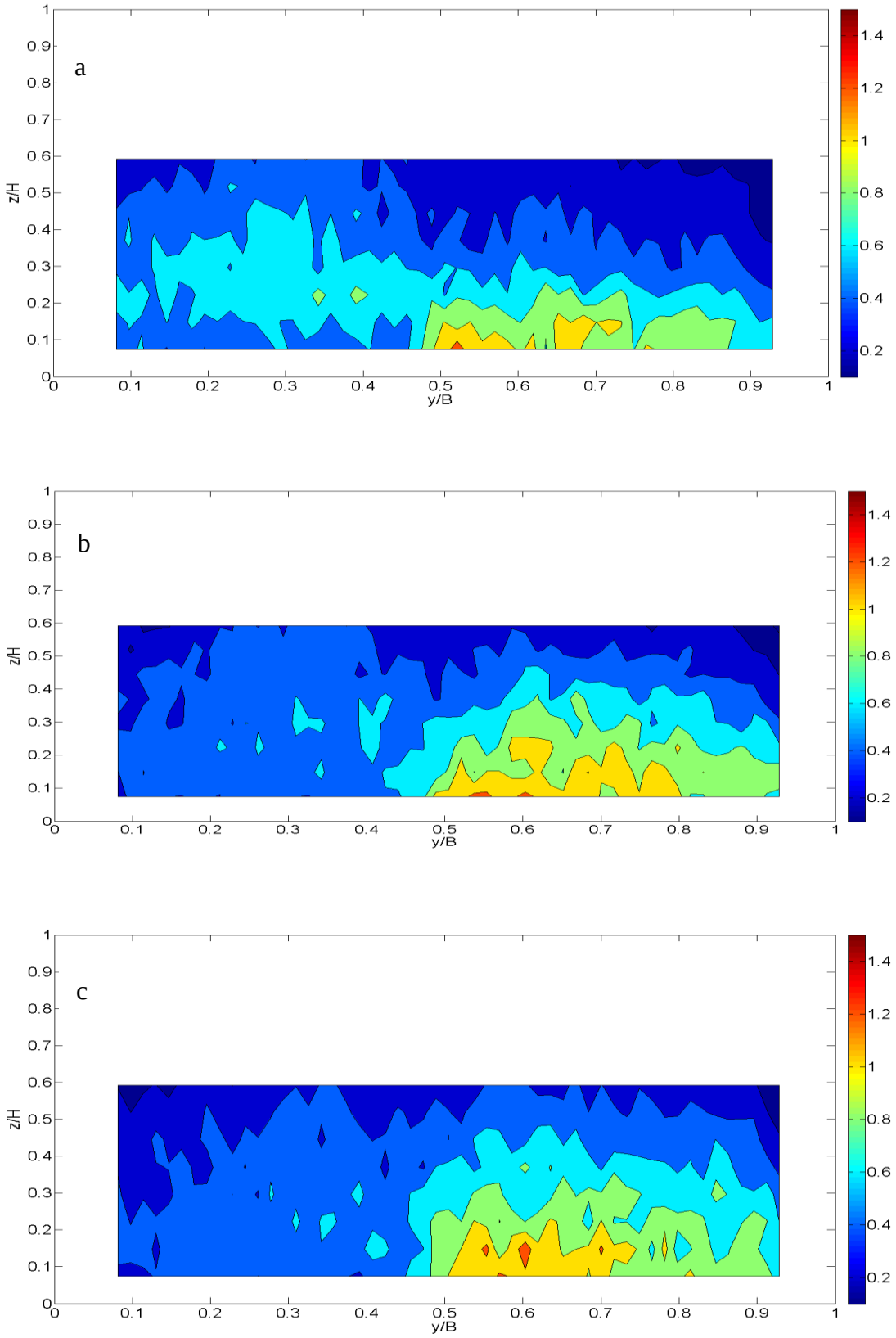

Figure 98: Lateral distribution vertical Reynolds stress; CRS1 (a) to CS3 (c) EXPT2

Figures 99 and 100 compares the vertical profiles of the normalised vertical Reynolds stress; Over the gravel bed $\left(0 \leq {}^{y}/_{B} \leq 0.5\right)$, the vertical Reynolds stress has a local maximum above the bed at approximately $\left({}^{z}/_{H} \cong 0.2\right)$, after which it decays approximately in a linear fashion towards the channel bed and the free surface from the maximum point. This is in good agreement with the wall region as defined by (Nezu and Nakagawa, 1993). In this region the vertical Reynolds stress decreases towards the channel bed due to the presence of non-negligible viscous shear stress induced by the bed surface (Nezu and Nakagawa, 1993). Moreover, the near bed momentum transport from gravel bed to the vegetated bed as shown in Figure 83 is assumed to have contributed to the reduced value of the near bed vertical Reynolds shear stress over the gravel bed. This is suggested to have contributed to the momentum balance in the near bed flow region (Shiono and Knight, 1991).

Over the vegetated bed, the vertical Reynolds stress is consistently linear over the measured section, with a maximum value located close to the channel bed. This behaviour is consistent with an inflection point in a submerged vegetation which is characterized by a maximum shear layer and confirm the existence of a ‘wake layer’ below the vegetation surface roughness as illustrated in Figure 79; thus, the effective height of the bed lies below the vegetation roughness crest (Nezu and Nakagawa, 1993).

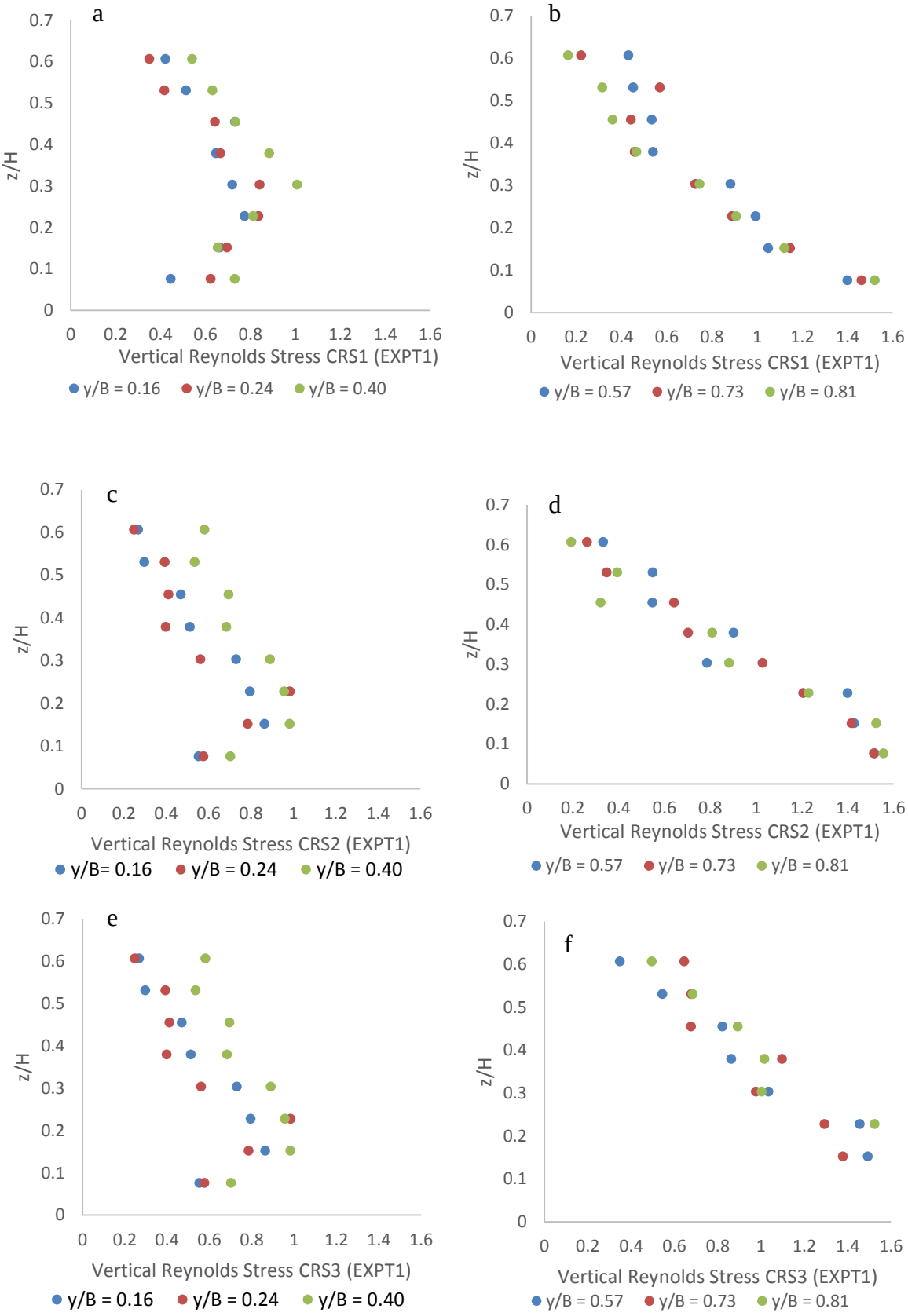

Figure 99: Vertcal distribution of relative verical Reynolds stress by bed region (EXPT1) Gravel (a-c-e), Vegetated region(b-d-f)

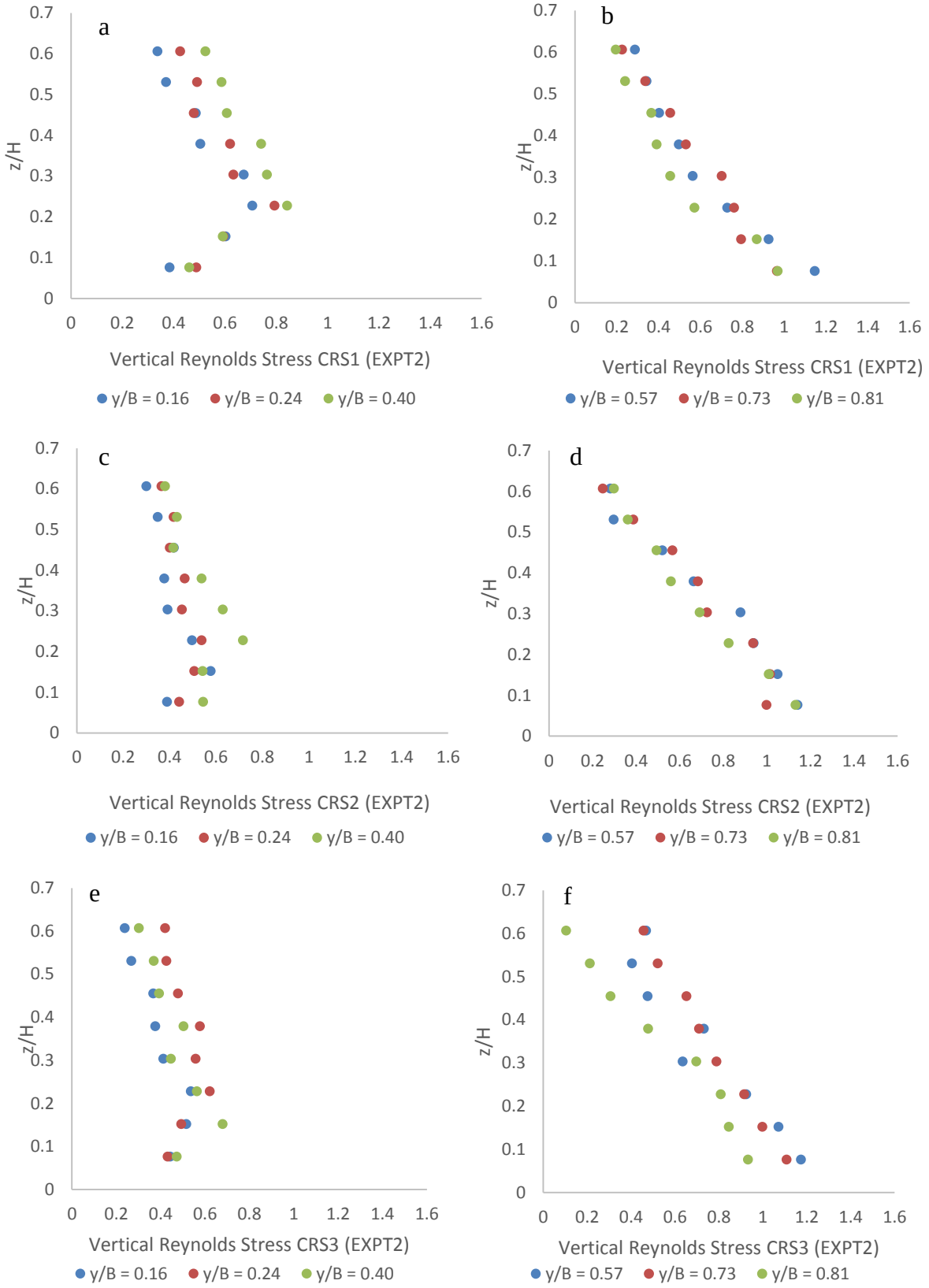

Figure 100: Vertcal distribution of relative vertical Reynolds stress by bed region (EXPT2) Gravel (a-c-e), Vegetated region(b-d-f).

Figure 101 and Figure 102 illustrates the contours of the horizontal Reynolds stress ($-\rho\overline{u'v'}/\tau_b$). These figures indicate the existence of the horizontal Reynolds stress over the vegetated bed. The shear propagation across the bed and towards the gravel zone is apparent and may be attributed to the vertical orientation of vegetation stems enhancing small scale horizontal turbulence due to stem wakes within vegetation. Comparing Figures 83 and 101, it can be seen that the region of negative horizontal Reynolds stress correspond with the up-flow regions. In addition, the horizontal Reynolds stress is maximized at the roughness boundary region $\left({}^{y}/_{B} = 0.5\right)$ of the flow in EXPT2.

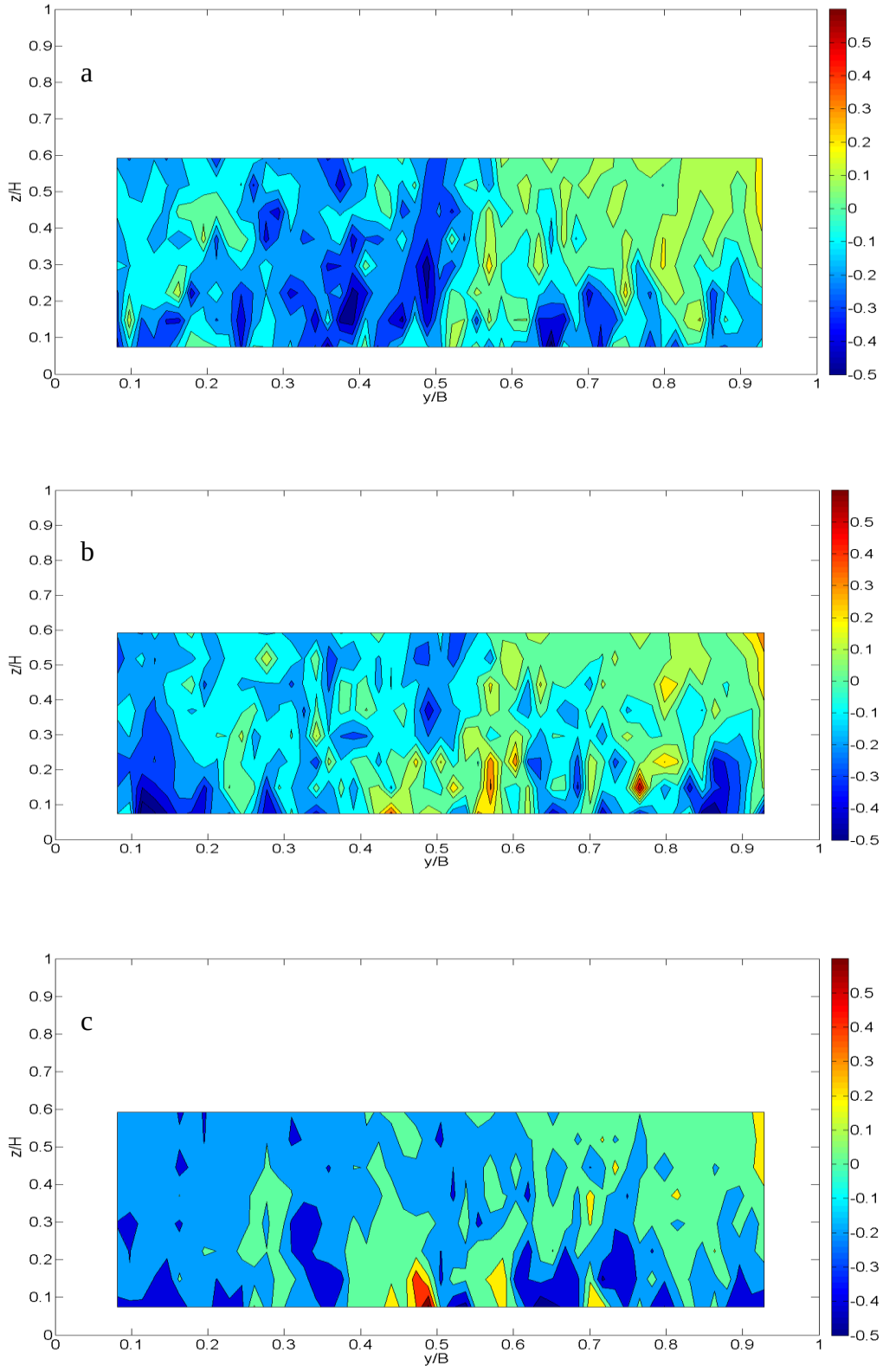

Figure 101：Lateral distribution of Horizontal Reynolds stress (HRS) EXPT1，(a) CRS1 to (c) CRS3

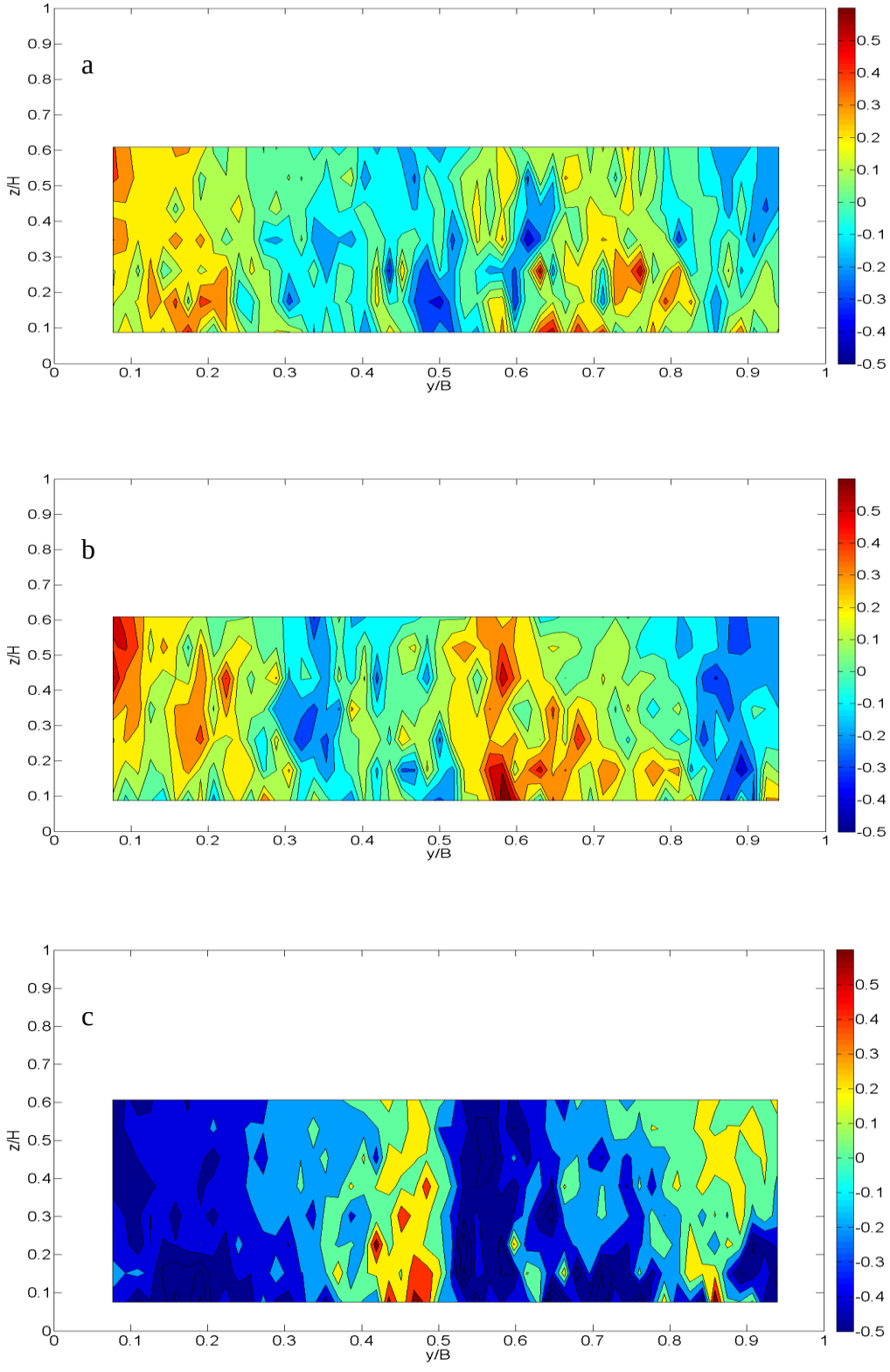

Figure 102: Lateral distribution of Horizontal Reynolds stress (HRS) EXPT2, (a) CRS1 to (c) CRS3

4.8 Shear Stresses Distributions

The dominant factor influencing turbulent transport in open channel flow is the degree of velocity shear due to different roughness sections. In the research work presented here in, Reynolds stresses are assumed as indicators of turbulence transport effects (Shiono and Knight, 1991; Shucksmith et al., 2010; Davidson, 2004).

The presence of both vertical and horizontal shear is notable in this work from Figures 79 and 80; efficient vertical transport of momentum across the shear layer through the vegetation-water interface region $\left({}^{z}/_{H} \leq 0\right)$ relative to gravel bed is expected due to the vertical shear over the vegetated bed as suggested in Figure 79. Similarly, there is evidence of horizontal shear at the roughness boundary regions $\left({}^{y}/_{B} = 0.50\right)$ as shown by the lateral velocity profiles (Figure 80). In such condition, turbulence transfer is expected over the roughness boundary region.

Referring to Figures 99 and 100, the vertical profiles of Reynolds stress exhibit a strong peak at the position of the vegetation top; this height coincides with the inflection point in the velocity profile in Figure 79. The shear layer is featured in this work by the point of the maximum Reynolds stress at the top of vegetation as shown in the vertical distributions of the vertical Reynolds stress (VRS) in Figures 99 and 100. It should be noted from the figures that the vertical Reynolds stress exhibits more peak over the vegetated bed in EXPT1 relative to EXPT2.

Figures 103 and 104 compare the depth averaged vertical and horizontal shear stresses. These figures can be seen to illustrate greater magnitude of vertical shear over the flexible vegetated bed $\left(0.5 \leq {}^{y}/_{B} \leq 1.0\right)$ relative to the gravel bed $\left(0 \leq {}^{y}/_{B} \leq 0.5\right)$ in EXPT1 (Figure 103); this is assumed to enhance turbulence in the vertical plane due to increased vegetation density. Also noted in Figure 103 is the negative lateral momentum transport at the boundary

region $\left({}^{y}/_{B} = 0.5\right)$, the vertical shear over vegetated bed in EXPT1 is assumed to have suppressed the level of lateral shear at the boundary region in contrast to Jesson et al. (2012) where the momentum transfer is maximized at the rough-smooth boundary. In EXPT2, the lateral turbulent shear stresses attain a maximum at the roughness boundary region $\left({}^{y}/_{B} = 0.5\right)$ as illustrated in Figure 104. The increased turbulent intensities at the boundary region in Figure 92 assumed to enhance the lateral shear in EXPT2 relative to EXPT1.

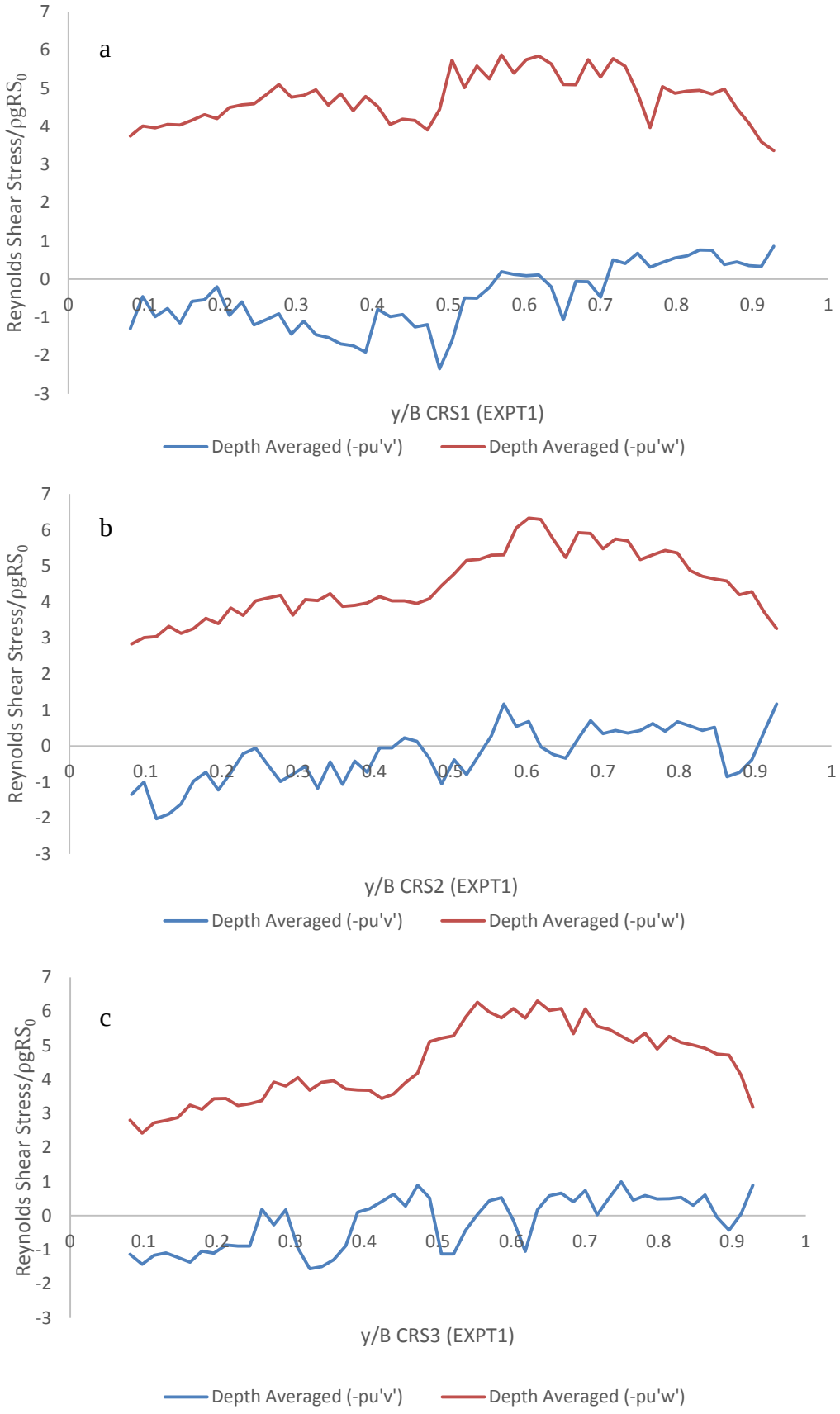

Figure 103: Lateral Distribution of depth averaged horizontal and vertical shear stresses for EXPT1, (a) CRS1 to (c) CRS3

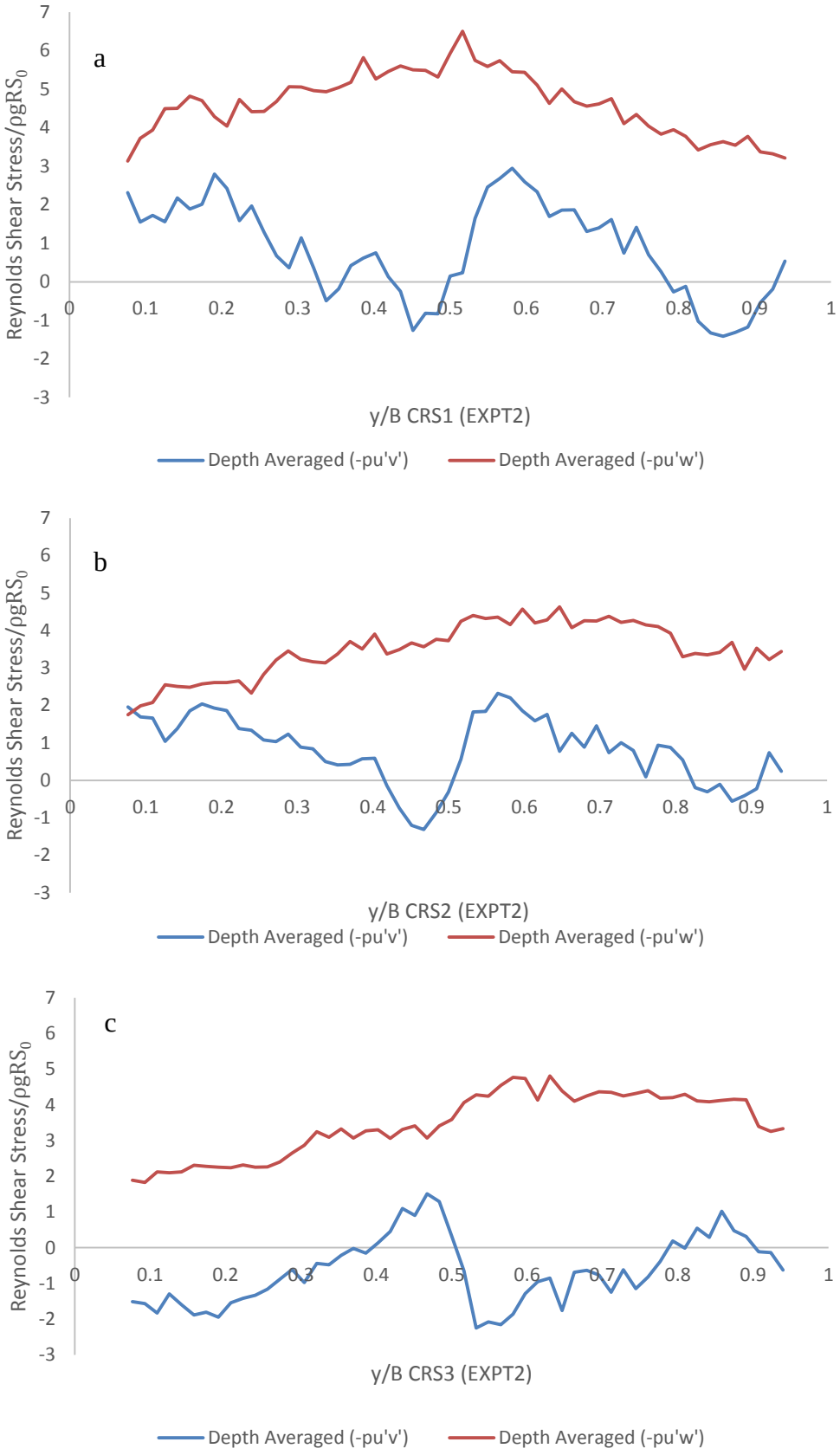

Figure 104: Lateral Distribution of depth averaged horizontal and vertical shear stresses for EXPT2, (a) CRS1 to (c) CRS3

5 Turbulence Structures and Boundary Shear Stress

5.1 Bursting Mechanism by Quadrant Analysis

To investigate the structure and distribution of turbulence due to the shear layer induced by the bed roughness, a quadrant analysis first introduced by Lu and Willmarth (1973) was used. A mean quadrant event, such as the quadrant Reynolds shear stress denoted as QRS_i is defined as in Equation (69):

$$QRS_i = lim\frac{1}{T}\int_o^T \big(u'(t).w'(t)\big)I(t)dt \qquad (i = 1,2,3,4) \tag{69}$$

where i indicates quadrant number and T = time interval. In this technique, the velocity fluctuations are decomposed and paired into four quadrants based on the signs of the fluctuating velocity components (Sterling et al., 2003; Lu and Willmarth, 1973). The existence of paired fluctuating components (u', w') defines an event in quadrant i, I provides indication of event in a quadrant i. If fluctuating components (u', w') exist in a quadrant i, then $I_i = 1$, otherwise $I_i = 0$. Each quadrant is defined as follows:

$i = 1(u' > 0, w' > 0)$: Outward interaction of relatively high velocity

$i = 2, (u' < 0, w' > 0)$: Ejections of relatively low velocity flow

$i = 3, (u' < 0, w' < 0)$: Inward interactions of relatively low velocity flow

$i = 4(u' > 0, w' < 0)$**:** Sweep

In order to examine the relative magnitude of the momentum transfer in each region, the overall contribution is analysed by introducing a "hole" into the quadrant analysis. The hole size, J, is an integer value used to scale the product of the standard deviations of u and w. Only events for which the absolute product of u' and w' exceeds a constant limit

$|u'w'|>J\sigma u\sigma$w (Sterling et al., 2003; Novak et al., 2000) are included in the analysis. In keeping with the work of Sterling et al. (2003), the contributing magnitude of the Reynolds shear stress $u'w'$ from the four quadrants are calculated from the normalised quadrant Reynolds shear stress Equation (70),

$$QRS_{i,J} = \frac{1}{\sigma_u \sigma_w T} \int_0^T u'(t)w'(t)I_{i,J}\, dt \qquad (70)$$

The plot of the normalised quadrant shear stress against hole size gives the indication of the magnitude of the shear stress within each quadrant. Figures 105 - 110 illustrate the normalised quadrant Reynolds shear stress for the four events directly above the bed roughness $\left({}^{z}/_{H} = 0.07\right)$. In these Figures the values of QRS_{ij} have been normalised by the maximum value of (QRS_{max}) for each cases respectively. The normalised quadrant Reynolds shear stress as a function of hole size illustrated in Figures 105 -Figure 110 are in general similar. Overall, the figures illustrate the contribution of QRS_1 (outward) and QRS_3 (inward) as both smaller in all the cross-sections, while those of QRS_2 (ejection) and QRS_4 (sweep) are both larger in magnitude. In EXPT1 (Figures 105 - 107), the sweep (QRS_4) and ejection (QRS_2) have their maximum values over both the gravel $(y/B = 0.24)$ and the vegetated bed $(y/B = 0.73)$ respectively; nevertheless, ejections (QRS_2) dominate sweeps (QRS_4) over the flexible vegetated bed $(y/B = 0.73)$, demonstrating larger proportion of momentum transfer over the vegetated bed $(y/B = 0.73)$ in EXPT1 with the burst dominated motion and largest contribution to the Reynolds shear stress. It should be noted that the ejection motions transport the low velocity flow over the flexible vegetated bed up to the free surface; this supports the upward secondary flow observed in Figure 83. Above the gravel bed $(y/B = 0.24)$ however, ejection plays a less important role in momentum transfer relative to sweep. This is associated with the reduced vertical turbulence fluctuations noted over the gravel bed (Figure 91 and 92). However, Figures 105 - Figure 107 show similar evidence of

of momentun transport at the roughness boundary region $\left({}^{y}/_{B} = 0.5\right)$ with ejection and sweep demonstrating similar magnitude of events, this indicates that there are relatively equal magnitude of quadrant events occuring at the roughness boundary region in EXPT1 and suggests that the momentum flux is not as efficiently transported at this region relative to vegetated region $\left({}^{y}/_{B} = 0.73\right)$ where ejection dominates and have greatest contribution to the Reynolds shear stress.

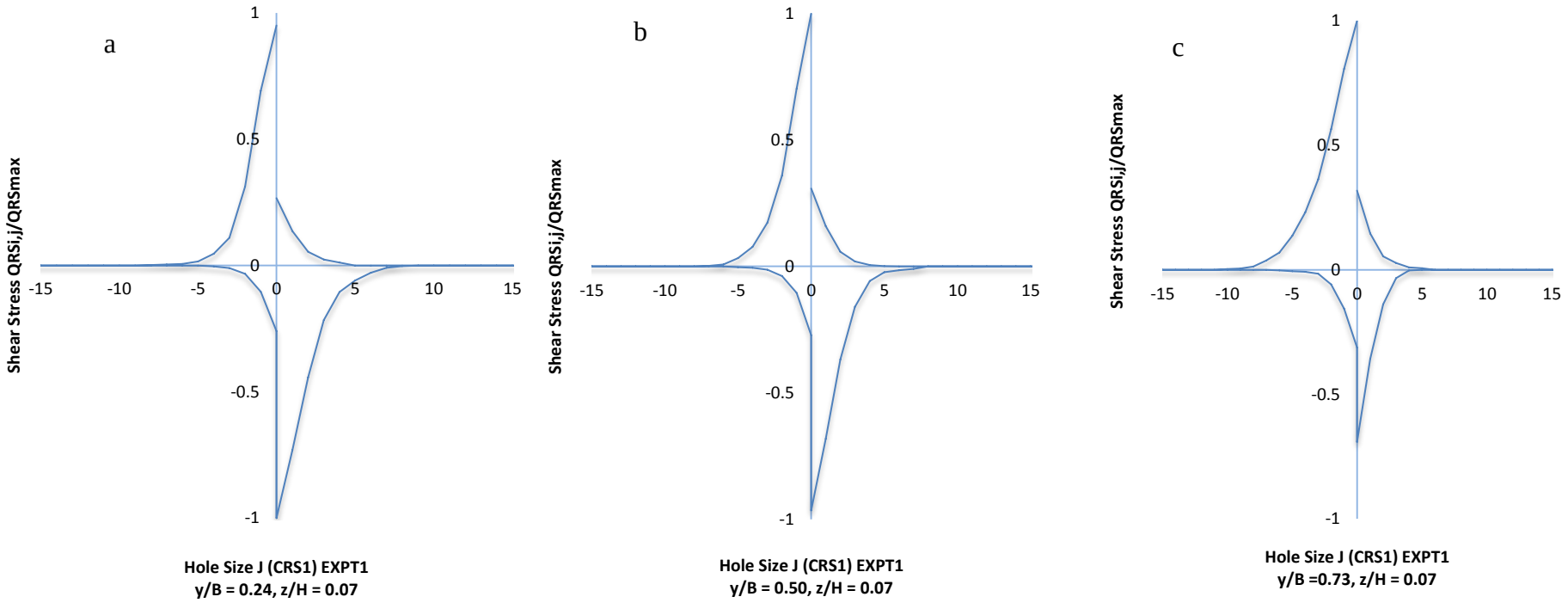

Figure 105：Quadrant Hole analysis of Reynolds shear stress magnitudes from quadrant events (CRS1 EXPT1), (a) Gravel bed, (b) boundary region, and (c) Vegetated bed

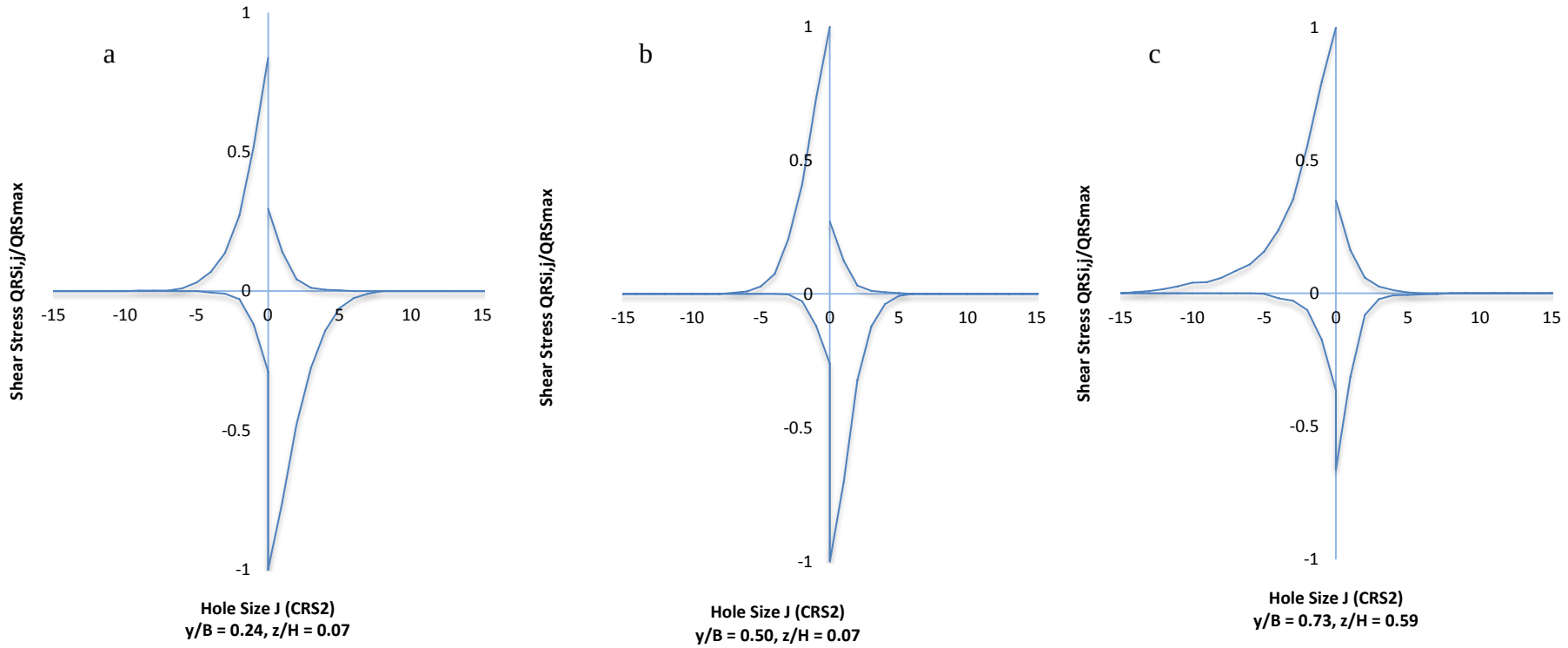

Figure 106: Quadrant Hole analysis of Reynolds shear stress magnitudes from quadrant events (CRS2 EXPT1), (a) Gravel bed, (b) boundary region, and (c) Vegetated bed

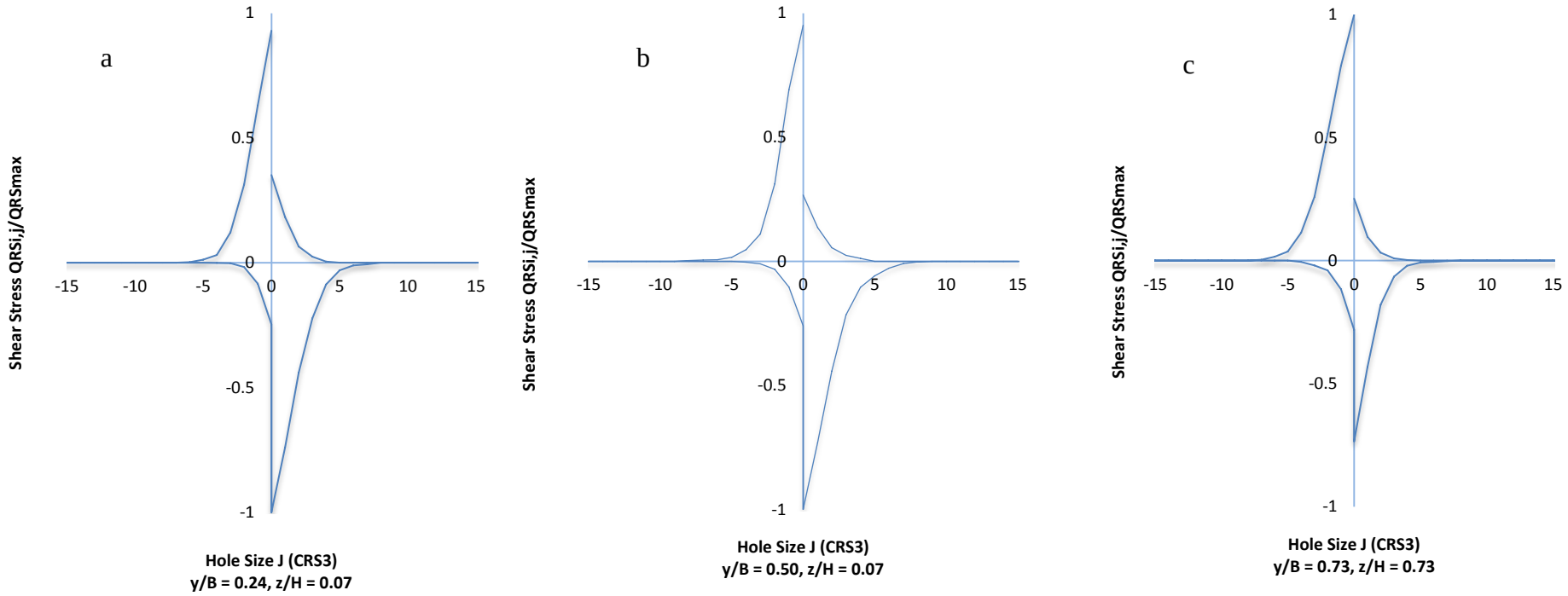

Figure 107: Quadrant Hole analysis of Reynolds shear stress magnitudes from quadrant events (CRS3 EXPT1), (a) Gravel bed, (b) boundary region, and (c) Vegetated bed

In EXPT2 (Figures 108 - 110) ejections can be seen to have comparable shear stress magnitude with sweep for all the hole sizes over the rigid vegetated bed in all the cross-sections. However, sweeps have a slightly larger shear stress magnitude above the vegetated bed $\left({}^{y}/_{B} = 0.73\right)$ similar to gravel region $\left({}^{y}/_{B} = 0.24\right)$. As for the boundary region $\left({}^{y}/_{B} = 0.50\right)$, ejections have relatively larger shear stress magnitude. Relative to EXPT1, the peak values of ejection (QRS_2) in EXPT2 (Figure 108-110) are somewhat reduced; this supports the observation of smaller vertical momentum exchange in EXPT2 compared to EXPT1. As observed in the literature (Nepf and Ghisalberti, 2008), the vertical shear layer generation is directly proportional to the density and distribution of vegetation elements.

The results overall demonstrate differences in turbulence structure between EXPT1 and EXPT2 with ejection contributing most to the vertical momentum transport over the vegetated bed in EXPT1 relative to EXPT2. This suggests stronger ejection above a dense flexible vegetated bed, while sweep become stronger above the gravel and sparsely rigid vegetated bed in EXPT2.

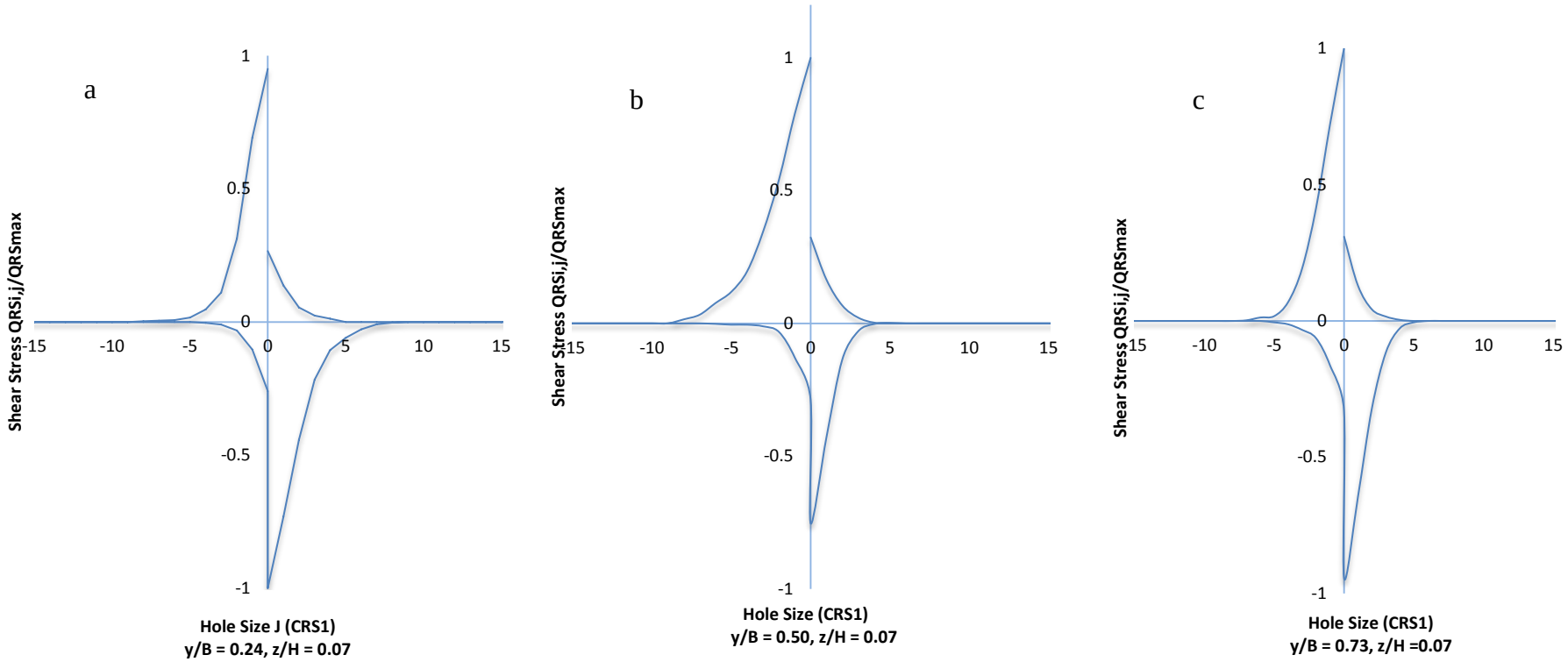

Figure 108: Quadrant Hole analysis of Reynolds shear stress magnitudes from quadrant events (CRS1 EXPT2), (a) Gravel bed, (b) boundary region, and (c) Vegetated bed

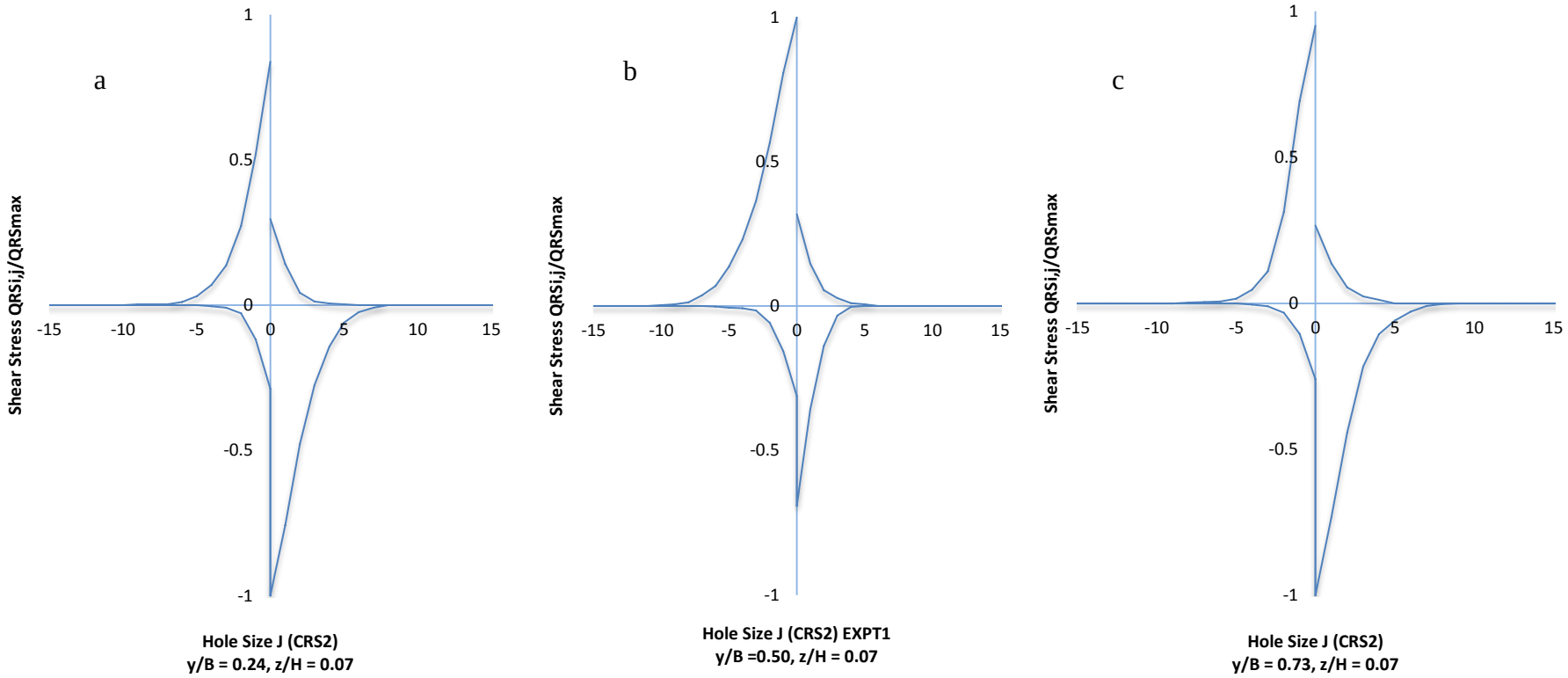

Figure 109: Quadrant Hole analysis of Reynolds shear stress magnitudes from quadrant events (CRS2 EXPT2), (a) Gravel bed, (b) boundary region, and (c) Vegetated bed

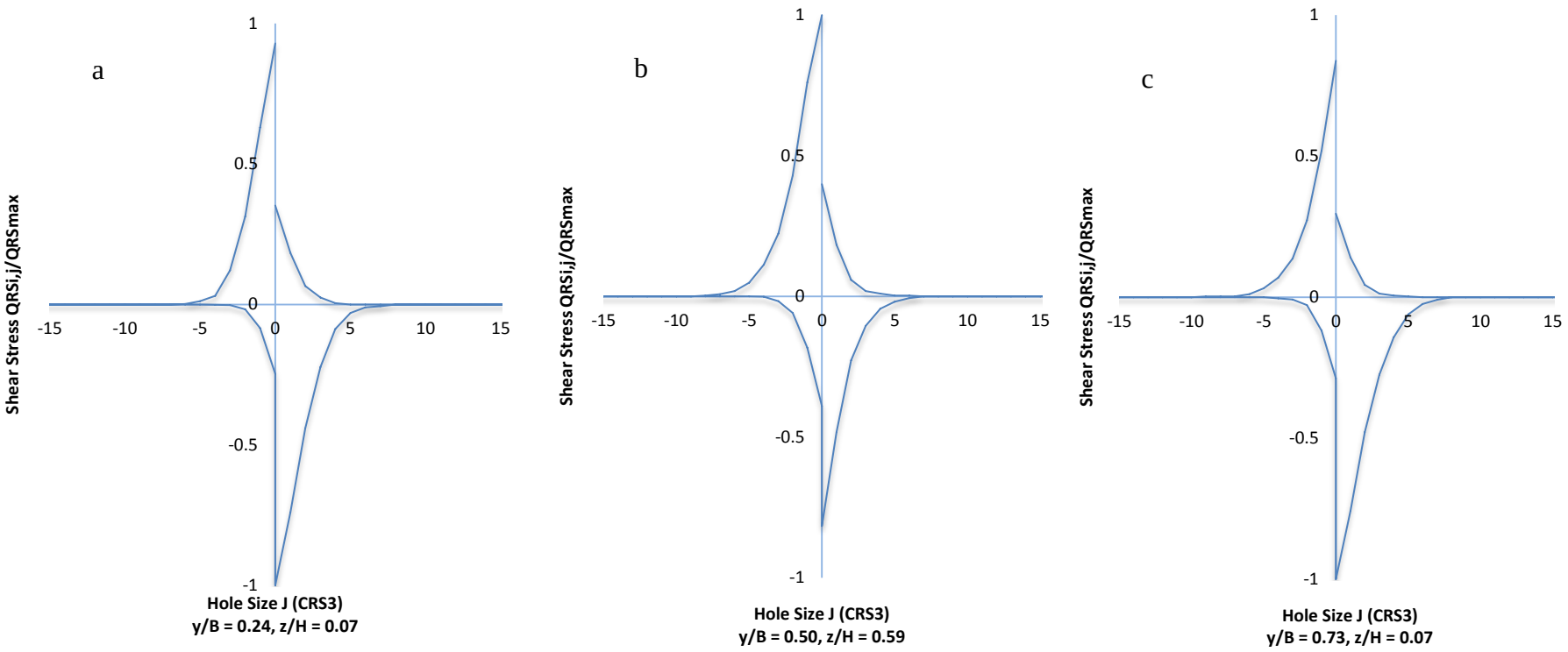

Figure 110: Quadrant Hole analysis of Reynolds shear stress magnitudes from quadrant events (CRS3 EXPT2), (a) Gravel bed, (b) boundary region, and (c) Vegetated bed

5.2 Boundary Shear Stress

The near bed velocity gradient over the gravel and vegetated beds (Figure 79) and in particular the lateral distribution of the mean streamwise velocity (Figure 80) suggests existence of a lateral variation in the distribution of the boundary shear stress τ_b. Jesson et al. (2013) successfully used a Preston tube for boundary shear stress measurements in heterogeneous channels but these measurements were restricted to the non-gravel regions. Some studies extend the use of the Preston technique to measure flows rough surfaces (Sun and Shiono, 2009, Ming, 1995, Hwang and Laursen, 1963), however the applications to rough surfaces has not been proven to be as robust. The vegetation surface roughness made it more complicated and prevented the use of this technique to provide reasonable results. The limitation of the technique is due to not only the obstructions by the relatively large vegetation roughness elements but the difficulty and uncertainty of the reference datum since Preston tube techniques computes boundary shear stress by locating it directly on the bed of the channel at the point of measurement.

However, a number of methods for estimating boundary shear stress from the turbulent kinetic energy and Reynolds stress techniques have been suggested (McLelland et al., 1999; Jesson et al., 2013; Nezu and Nakagawa, 1993), and similar methods have been applied to the experimental data in the current work. These include:

- Extrapolating a least square linear regression from measurement of the vertical Reynolds stress.
- Extrapolating a least square linear regression from measurement of vertical Reynolds stress at the four points nearest to bed.
- Using the mean value of bottom three points nearest to bed of the vertical Reynolds stress VRS.

- Using the mean value of bottom two points of the vertical Reynolds stress VRS
- Application of log law to the lower 30% of the flow.

The evaluation of the bed shear stress by log law of the wall must suggest that the universal logarithmic law for velocity distribution exists both for the gravel and vegetated bed, essentially a law of the wall function is assumed to be valid from which the shear stress is interpreted (Sterling et al., 2008). The difficulty in the evaluation of Nikuradse k_s, (the equivalent roughness height) over vegetated bed due to the associated form drag make k_s impracticable to represent the physical size of the vegetation elements (a detailed discussion can be found in section 2.2).

Extrapolation of Reynolds shear stress and the near bed mean values represents direct flow measurements; hence, these techniques were applied to the ADV experimental data to calculate the lateral distribution of the boundary shear stress.

The percentage difference of the calculated average boundary shear stress $\overline{\overline{\tau_b}}$based on the Reynolds stress techniques and the theoretical boundary shear stress given by $\overline{\tau_b} = \rho g R S_0$ are illustrated in Table 10 and 11. It should be noted from the values presented in Table 10 that the Reynolds stress techniques relative to the theoretical boundary shear stress underestimated the boundary shear stress across all the sections and are somewhat susceptible to errors.

The average side-wall shear stress $\overline{\overline{\tau}}_w$ was obtained by considering the overall force balance in the flow direction (Guo and Julien, 2005) as given in Equation (71)

$$2H\overline{\overline{\tau}}_w + B\overline{\overline{\tau_b}} = \rho g B H S_0 \quad (71)$$

where the first term on the left-hand side represent the shear stress on the two side walls, the second term is the boundary (channel bed) shear stress, and the right-hand side is the weight component in the flow direction. Equation (71) gives the average side-wall shear stress as:

$$\bar{\bar{\tau}}_w = \frac{\rho g B H S_0 - B\bar{\bar{\tau}}_b}{2H} \quad (72)$$

Comparing the experimental measurements with the theoretical boundary shear stress, the first approximation without the wall shear stress considerably underestimated the measured averaged boundary shear stress $\bar{\bar{\tau}}_b$, hence significantly smaller than the standard value ($\rho g R S_0$) for the flow by more than 30% (Table 10). The estimated difference is relatively high with the maximum percentage difference approximately 32% for EXPT1 and 29% for EXPT2 based on the theoretical boundary shear stress.

A second approximation was undertaken to include the wall shear stress [Equation (72)] in the calculation of the average boundary shear stress. The second approximation yields better agreement with the theoretical 2-dimensional value with a reduced maximum difference of 19% as shown in Table 11. This can be attributed to the contribution of the secondary flow effect in Equation (72) on the boundary shear stress.

These differences between the Reynolds stress techniques and the theoretical boundary shear stress values are attributed not only to the experimental error such as the restriction in using the ADV near the channel bed but also the reduction in the vertical Reynolds stress VRS that occurs within the inner region of the boundary layer close to bed as recorded for gravel bed (Figure 99 and 100) in the current work (section 4.7). This reduction was ignored by assuming that the near bed value and linear profile of the vertical Reynolds stress VRS can be taken as an indication of the boundary shear stress. However, the bottom 4 points extrapolation method provides better results relative to the mean bottom 2 and 3 points. It should also be noted that

the underestimation of boundary shear stress relative to the theoretical standard value $\rho g R S_0$ would suggest reduction in channel bed scour and erosion with the roughness configuration, this is consistent with the finding of Sun and Shiono (2009).

CROSS SECTION	Mean Bottom 2pts	Mean Bottom 3pts	Bottom 4pts Extrapolation
EXPT1CRS1	30	25	21
EXPT1CRS2	27	26	23
EXPT1CRS3	29	27	21
EXPT2CRS1	26	24	22
EXPT2CRS2	29	25	24
EXPT2CRS3	26	26	24

Table 10: First Approximation Percentage Difference in Bed Shear Stress Values

CROSS SECTION	Mean Bottom 2pts	Mean Bottom 3pts	Bottom 4pts Extrapolation
EXPT1CRS1	19	14	12
EXPT1CRS2	15	15	15
EXPT1CRS3	17	17	12
EXPT2CRS1	15	14	14
EXPT2CRS2	15	15	14
EXPT2CRS3	12	15	14

Table 11: Second Approximation Percentage Difference in Bed Shear Stress Values

Previous work by Jesson et al. (2013) measured the boundary shear stress of the smooth side of the channel with an estimated error of $0.05Nm^{-2}$ using a Preston tube, and estimated the boundary shear stress over the rough bed using vertical Reynolds stress methods with a maximum error approximately 22%. Based on 95% confidence interval using the standard error in the current research, the average value of uncertainties for the estimated shear stress values were obtained as $\pm 0.081Nm^{-2}$ and $\pm 0.077Nm^{-2}$ for the methods in EXPT1 and EXPT2 respectively as illustrated in Figure 111 using the bottom 4 points linear extrapolation. The results in each cross-section were found to be consistent with one another and the uncertainties are within the accepted experimental error.

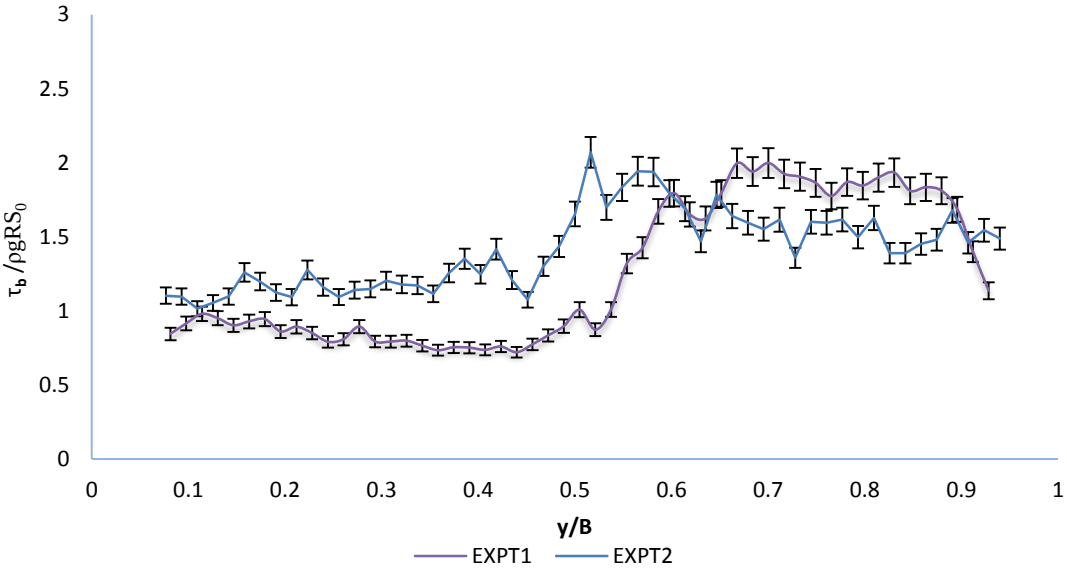

Figure 111: Uncertainties in the estimated shear stress values for both EXPT1 and EXPT2

Figure 112 and 113 illustrates the lateral distribution of the boundary shear stress calculated using the Reynolds stress profile methods and normalised by the theoretical boundary shear stress $\bar{\tau}_b = \rho g R S_0$. For each cross-section, the Reynolds stress methods give similar distribution of the boundary shear stress. The figures illustrates an increase in boundary shear stress from a minimum over the gravel bed $(0 \leq y/b \leq 0.5)$, to a maximum over the vegetated bed $(0.5 \leq y/b \leq 1.0)$, with the profiles demonstrating rapid increase in bed shear stress at the roughness boundary region $\left({}^{y}/_{B} = 0.5\right)$ between gravel and vegetated zone. Similar phenomenon was pointed out by Jesson et al. (2013) at the rough-smooth boundary. It is noted in EXPT1 that the boundary shear stress over the vegetated section is much larger than the corresponding gravel section, with the mean over the gravel section being approximately 40% of the vegetated section (Figure 112). The vertical shear and the amount of near bed lateral momentum transport from the gravel towards the vegetated bed as shown in Figure 83 suggests the higher magnitude of boundary shear stress over the vegetated bed. The relatively low values of the boundary shear stress over the gravel bed of the channel $(0 \leq$

$y/b \leq 0.5$) arise as a result of the low values of relative turbulence intensities over the gravel bed as illustrated in Figure 91a and 92a, this is consistent with the observation of Hofland and Battjes (2006) who assumed the statistics of the drag force on particle roughness as directly proportional to the statistics of the fluctuations of the shear stress. Comparison of the boundary shear stress with the location of the peak value indicates the peak in the boundary shear stress to be higher in EXPT1 (Figure 112) relative to EXPT2 (Figure 113). This can be attributed not only to the vertical shear but also the contribution of upflow over the vegetated bed in EXPT1 in consistent with the results as illustrated in Figure 83. This was in keeping with previous work (Nezu and Nakagawa, 1993) who observed perturbations in the trend of the boundary shear stress profile due to secondary flow structure over the rough bed. The increase in boundary shear stress at the vegetated section further demonstrates the formation of shear layer due to vegetation drag (Nepf and Vivoni, 2002) over the top of vegetation surface layer resulting in high shear stress at the vegetated section. This is an indication that distribution of boundary shear stress is roughness dependent and controlled by roughness elements distribution.

Figure 112: Lateral Distributions of Bed Shear Stress (EXPT1)

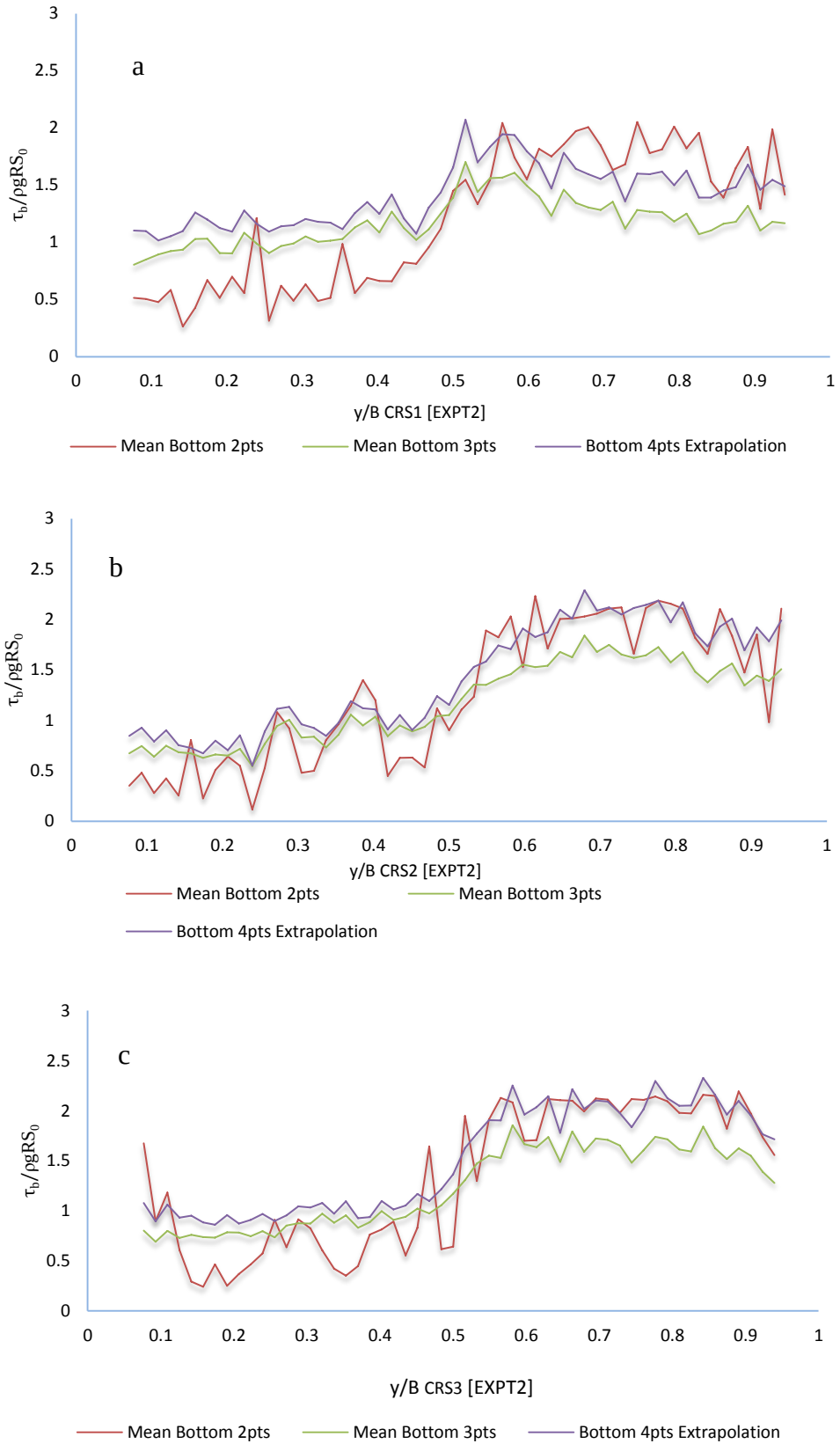

Figure 113: Lateral Distributions of Bed Shear Stress (EXPT2)

In reference to previous work, the location of the maximum boundary shear stress has shifted from the gravel bed, which indicates that the gravel bed is no longer the primary source of turbulence generation as postulated by Jesson et al, (2013); rather it is now dominated by the vertical shear over the vegetated bed. However, this is still consistence with Jesson et al, (2013) taking the most hydraulically rough surface at the dominant one.

5.3 Turbulence Scale

To characterize eddies transporting momentum in the flow, the streamwise temporal and length spatial scales of turbulent eddies are examined for efficient mass and momentum transfer and other transport processes in the flow. Evaluation of the length scale of eddies is preceded by determining the time scale, to achieve this, autocorrelation function for streamewise velocity component $R_{(uu)}$ was used. The two point correlation between the streamwise velocities fluctuations defined in section 2.5.3 is expressed as in Equation (73);

$$R_{uu}(\tau = \Delta t) = \frac{\int_0^T u\prime_{(t)} u\prime_{(t+\Delta t)} dt}{\int_0^T u\prime_{(t)}^2 dt} \tag{73}$$

where u' represents the streamwise turbulent fluctuation, and Δt is the time lag.

The autocorrelation functions versus the time lag(Δt) given as $\Delta t = 0.005s$ (time interval between consecutive measurements) are shown in Figure 114 and 115 for the near bed region of the flow. In EXPT1 near bed $\left({}^{z}/_{H} = 0.07\right)$(Figure 114), the decay rate of autocorrelation functions over the gravel bed is relatively small compared to the vegetated bed (Figure 114). For EXPT2, the decay rate is approximately constant over the gravel and vegetated section of the channel (Figure 115); however the fluctuating velocities exhibit relative stronger turbulence connection over the gravel bed in both EXPT1 and EXPT2 respectively, suggesting lower rate of turbulence dissipation relative to vegetated bed. For the sake of clarity,

autocorrelation functions are only presented for the near bed $\left({}^{z}/_{H} = 0.07\right)$ region as the upper region of the flow $\left({}^{z}/_{H} = 0.59\right)$ exhibited similar behaviour for the cross-sections.

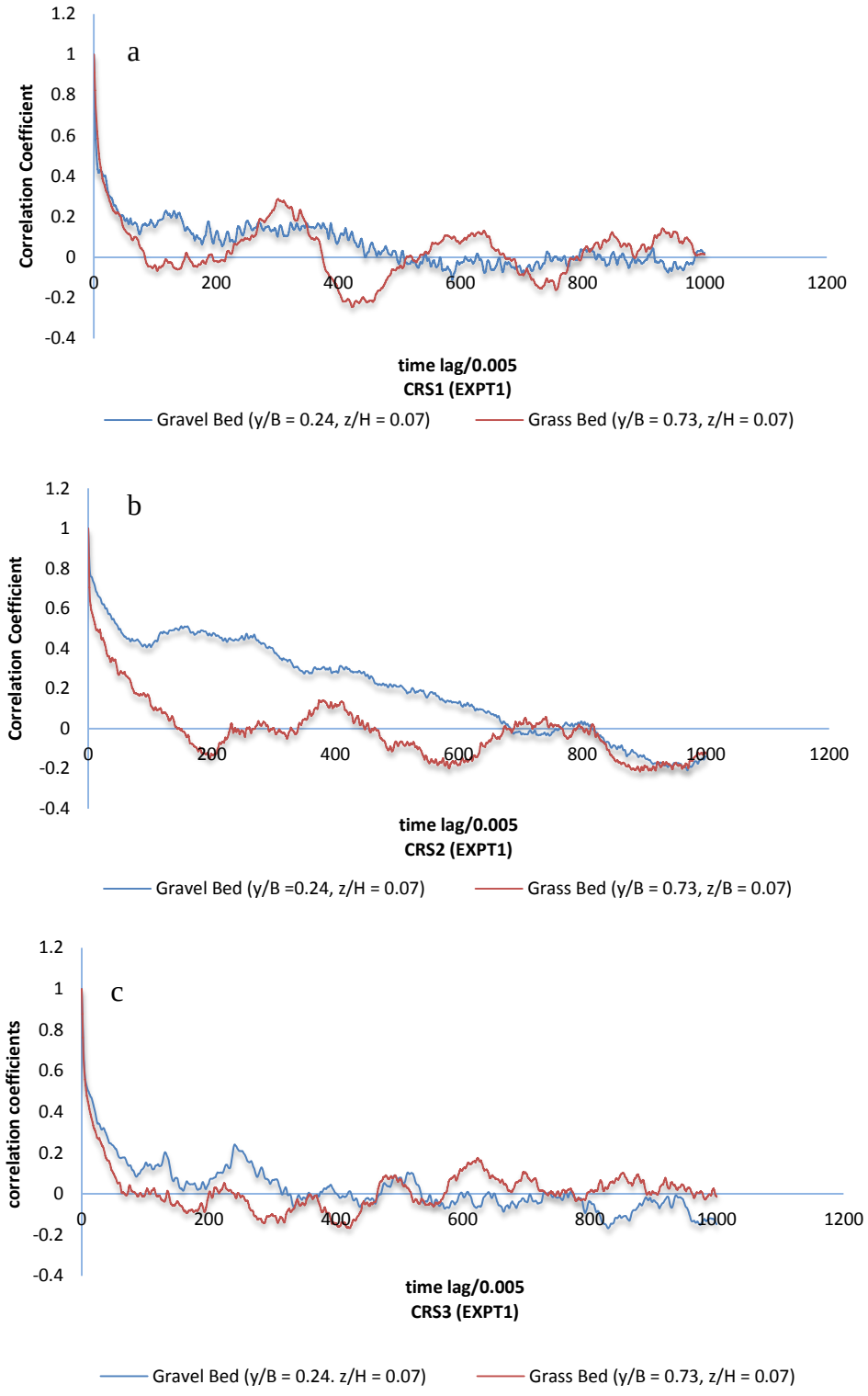

Figure 114: Autocorrelation Functions over Gravel and Grass Bed for Lower Region EXPT1, (a) CRS1 to (c) CRS3

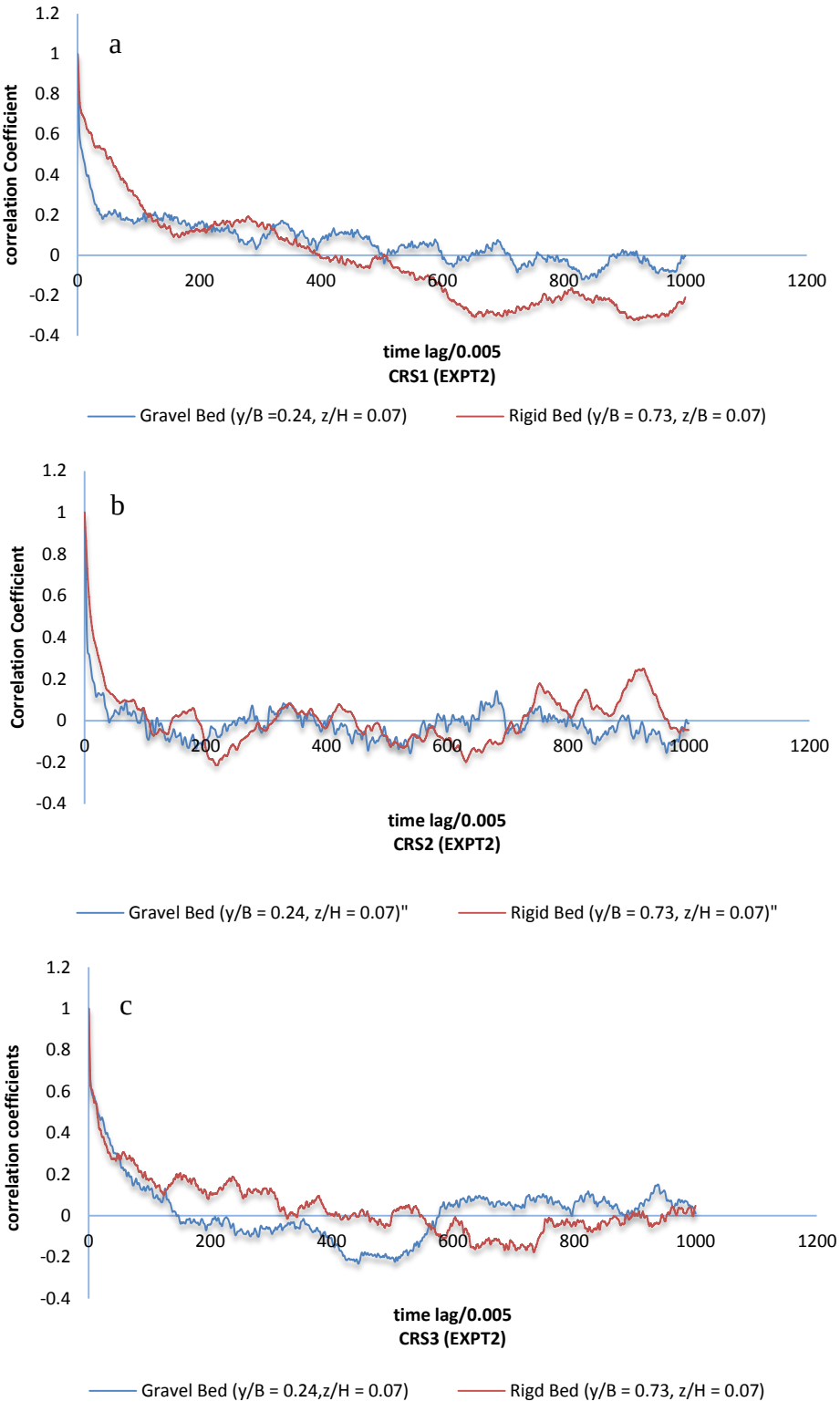

Figure 115: Autocorrelation Functions over Gravel and Grass Bed for Lower Region EXPT2, (a) CRS1 to (c) CRS3

Using the autocorrelation functions of the streamwise velocity component in Equation (73), the integral time scale is obtained by evaluating the area under the autocorrelation function. Integrating numerically the autocorrelation functions using the expression in Equation (74):

$$T_u = \int_0^t R_{uu}(t)dt \tag{74}$$

Lacey and Roy (2008) described integral time scale T_u as an indication of the temporal scale of turbulent eddies. As shown in Table 12 for the near bed $\left({}^{z}/_{H} = 0.07\right)$ and the upper region $\left({}^{z}/_{H} = 0.59\right)$. The maximum time scale T_u values detected near bed are $0.16s$ and $0.18s$ over the gravel bed in CRS3 for EXPT1 and EXPT2 respectively. In the upper region of the flow, the maximum time scale for EXPT1 and EXPT2 are $0.28s$ and $0.32s$ detected over the vegetated bed respectively demonstrating the largest values of timescale located in the upper region of the flow. The temporal scale of eddies generally increase at the upper region of the flow for all the cross-sections reaching maximum value over the vegetated region in CRS3. The lower magnitudes of time scale near bed may be attributed to occurrence of shear and turbulence production near bed. The time scale is noted to be generally greater in EXPT2 relative to EXPT1.

Cross-Section	Gravel Bed (time scale (s))		Vegetated Bed (time scale (s))	
	$y/B = 0.24$ $z/H = 0.07$	$y/B = 0.24$ $z/H = 0.59$	$y/B = 0.73$ $z/H = 0.07$	$y/B = 0.73$ $z/H = 0.59$
EXPT1CRS1	0.12	0.23	0.08	0.24
EXPT1CRS2	0.14	0.22	0.08	0.24
EXPT1CRS3	0.16	0.24	0.08	0.28
EXPT2CRS1	0.16	0.26	0.12	0.26
EXTP2CRS2	0.16	0.28	0.14	0.29
EXPT2CRS3	0.18	0.30	0.16	0.32

Table 12: Table Showing Integral Time Scale Values (EXPT1 and EXPT2)

The integral length scale L_u corresponds to the size of fluctuating eddy motions that exists in turbulent flows, the streamwise integral length scale L_u is obtained from the streamwise integral time scale using Equation (75);

$$L_u = U\,T_u \tag{75}$$

Figure 116 and 117 illustrates vertical profiles of the normalized turbulent integral length scales over the gravel and vegetated bed. These figures demonstrate a general increase in depth with large variations around this trend. From Figure 116, eddies generated near the channel bed $\left(z/H \leq 0.2\right)$ over the vegetated bed in EXPT1 are much smaller than eddies over the gravel bed, this is attributed to the size of the vegetation stem and the burst (ejection)

producing the turbulent eddies over the vegetated bed as discussed in section 5.1 (Figures 105 - 107). The vertical shear over the vegetated bed is presumed to increase the concentration of vorticity (due to shear) in these small eddies thereby generating turbulence whose energy is dissipated rapidly due to the smaller size of eddies over the vegetated bed. Over the gravel bed, larger eddies generated contributes to the high velocity downflow as illustrated in Figure (83), while the smaller eddies over vegetated bed are dominated by the burst like upward fluid motions. The results however indicated that, the closer the eddies originate to the bed, the smaller their size in comparison to the upper region. This supports previous work by Yalin (1972) who observed the largest eddies did not occur near bed, however the experimental results demonstrate vortex stretching and the corresponding interaction thereof with other eddies as supported by the large variation (Figure 116). In EXPT2, the length scale is larger relative to EXPT1 and approximately constant over the gravel and vegetated bed. The larger length scale in EXPT2 is attributed to the vegetation stem spacing which allow the growth of eddies relative to EXPT1. A number of similar distributions of integral length scales can also be seen at the cross-sections. The finding is important because it provides an approximation of eddy structure size in the flow.

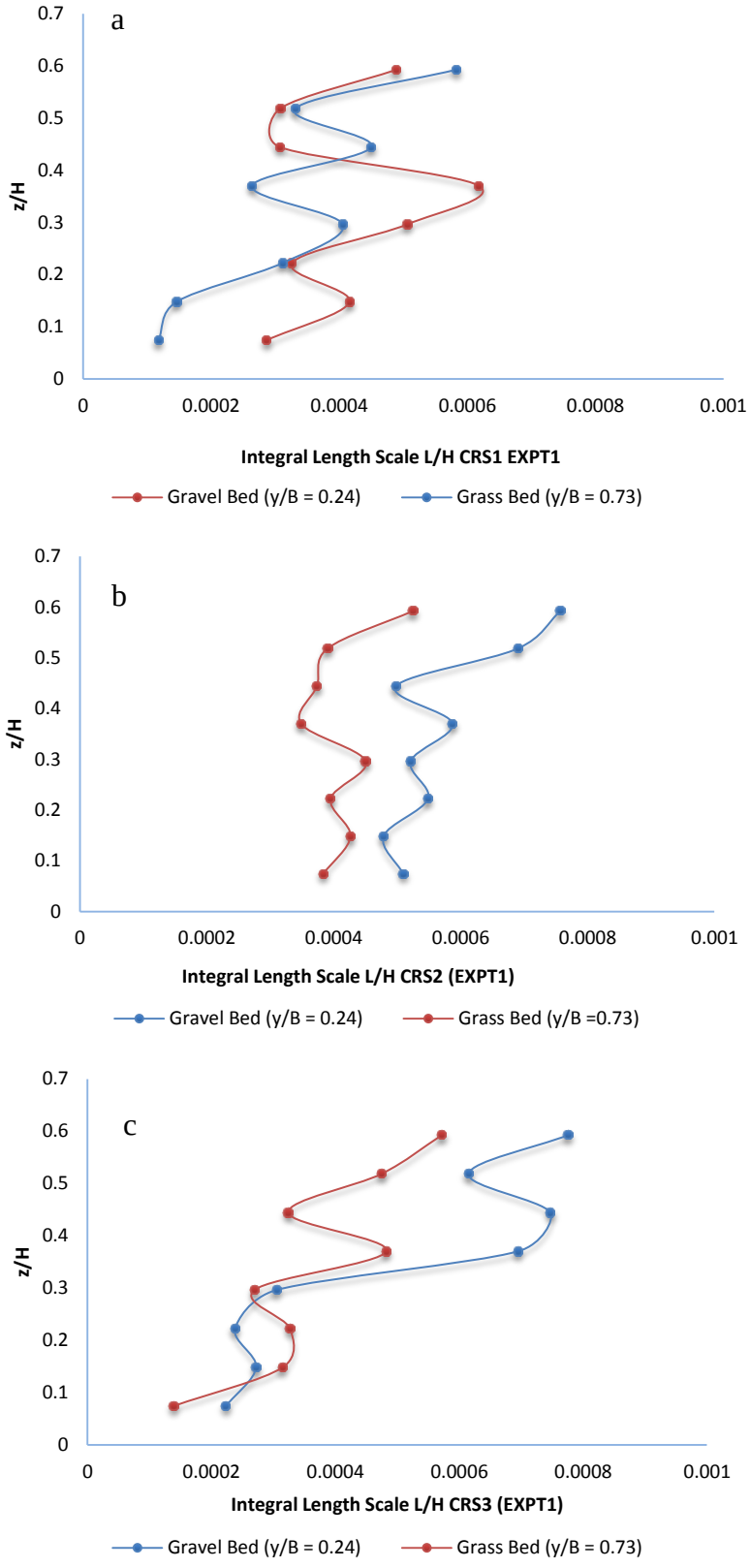

Figure 116: Integral Length Scale over Gravel and Grass Bed (EXPT1), (a) CRS1 to (c) CRS3

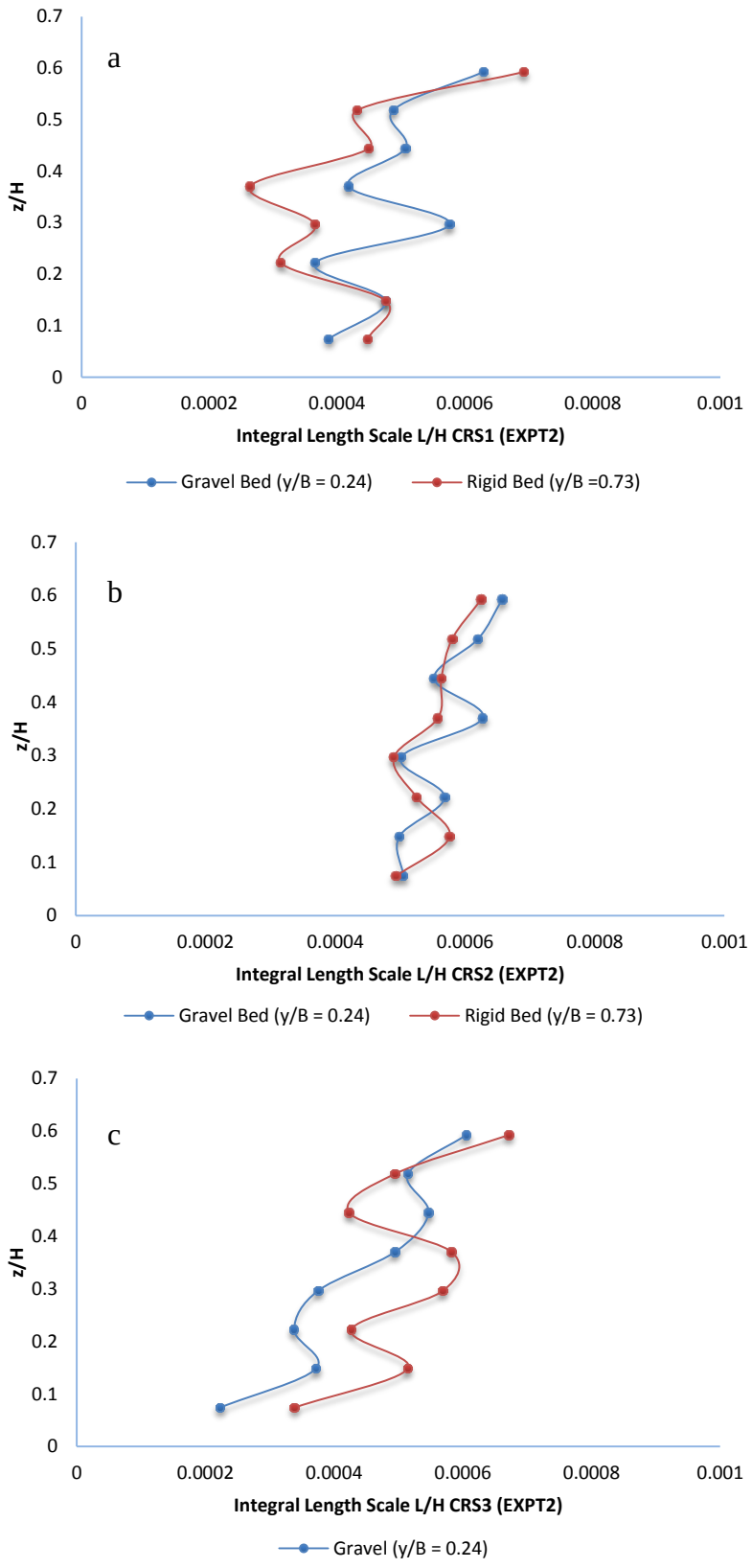

Figure 117: Integral Length Scale over Gravel and Grass Bed (EXPT2), (a) CRS1 to (c) CRS3

5.4 Energy Power Spectral Density (EPSD) Distribution

The energy power spectrum was studied in order to explore which scales were mostly responsible for various level of turbulence. Figures 118 and 119 display power spectral $S(K_u)$, where K_u is the energy resulting from the streamwise velocity components defined for the near channel bed $\left({}^{z}/_{H} = 0.07\right)$ at lateral positions$\left({}^{y}/_{B} = 0.24\ (left),\ and\ {}^{y}/_{B} = 0.73\ (right)\right)$ over the gravel and vegetated bed respectively.

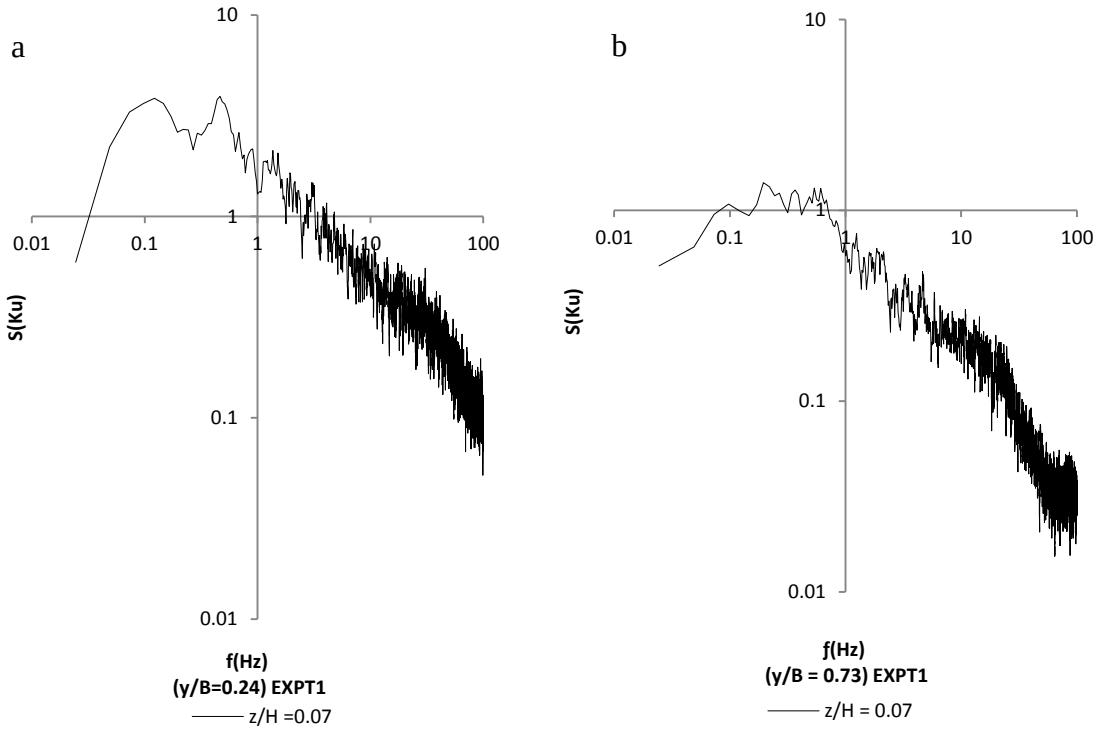

Figure 118: Energy Spectral Distribution near the Channel Bed $\left({}^{z}/_{H} = 0.07\right)$ at $\left({}^{y}/_{B} = 0.24\ (left), and\ {}^{y}/_{B} = 0.73\ (right)\right)$ (EXPT1CRS3)

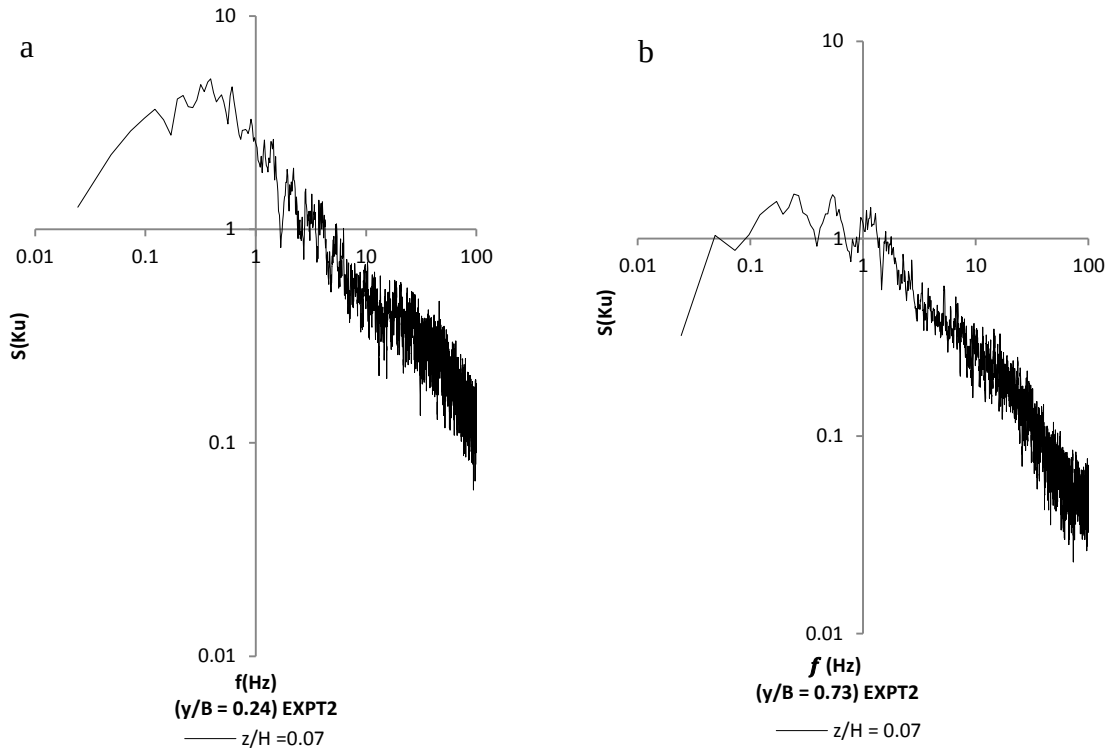

Figure 119: Energy Spectral Distribution near the Channel Bed ($^{z}/_{H} = 0.07$) at $\left(^{y}/_{B} = 0.24\ (left), and\ \ ^{y}/_{B} = 0.73\ (right)\ \right)$ (EXPT2CRS3)

From Figures 118 and 119, it is evident that the peak frequencies f occurs within the range $0.3 - 0.5Hz$. Near the channel bed $\left(^{z}/_{H} = 0.07\right)$, the spectral distributions on the gravel section $\left(^{y}/_{B} = 0.24\right)$ obey the $^{-5}/_{3}$ power law with a wider occurrence of inertial subrange over a range of frequencies $1\ Hz < f < 60Hz$ (Figure 118a and 119a). However, over the near bed vegetated section $\left(^{y}/_{B} = 0.73\right)$, the spectral distribution fits to the $^{-5}/_{3}$ power law in a narrow range ($40Hz < f < 70Hz$) Figures 118b and 119b). The inertial subrange is negligible at the upper region $\left(^{z}/_{H} = 0.59\right)$ of the flow relative to the near bed region (Figure 157 and 158) (Appendix B). However, these figures demonstrate an increased spectral energy over the gravel bed relative to vegetated bed as illustrated in Figure 118 and 119, supporting the presence of the larger turbulence length scale over the gravel region as discussed in section (5.3). However, at the upper region of the flow $^{z}/_{H} = 0.59$ (Figures 157 and 158) (Appendix

B), the energy spectrum is observed to be approximately constant as it does not decay significantly with frequency. It is shown from the figures that the inertia sub-range is wider near bed over the gravel section relative to vegetated section, and this becomes smaller as the distance from the bed increases to the upper region for both roughness sections.

5.5 PIV Measurements

In the current work, the pulse separation Δt range was calculated for the flow by noting that the camera resolution was set at 640×480 pixels with a magnification of $0.78mm$ per pixels ($i.e. 0.788mm/px$) (PIV, 2009). In keeping with the recommendations (PIV, 2009), seven pixels was set as the minimum distance which could be transverse between laser pulses (i.e., 5.5mm). Based on the average mean bulk velocity for the flow ($U_b = 0.152m/s$) using a discharge of $7.5\ l/s$ and a flow depth $80mm$, the time taken to move a distance $5.5mm$ was equal to 37ms, therefore the laser pulse separation Δt was adjusted within the range 37ms to 40ms. The laser pulse *width* δt is theoretically be no greater than one tenth $\left({}^{1}/_{10}\right)$ of the laser pulse *separation* Δt (PIV, 2009), this was approximately obtained as 4ms for the experiment. These timings were adjusted until a displacement of 5-10 pixels was recorded. The laser thickness (ray) is $3mm$ (PIV, 2009) and facilitated the transmission of light and illumination of the flow field of view (FOV). The flow field of view (FOV) was imaged with camera having a focal length range $50mm$ to $400mm$ (PIV, 2009) with vertical resolution of 480 pixel and horizontal resolution of 640 pixel (480 × 640) (Adrian, 1991, PIV, 2009). The camera and laser were adjusted to obtain field of view (FOV) for the measurement as schematized in the general set up shown in Figure 120.

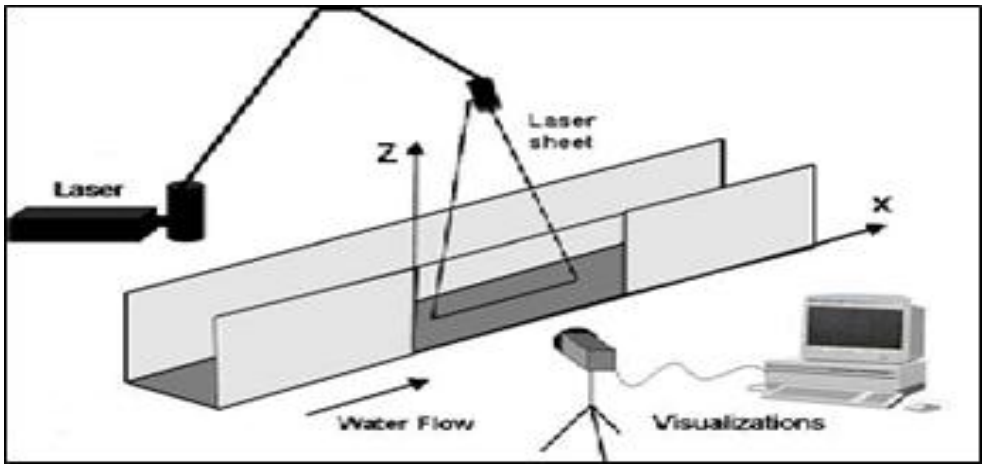

Figure 120: Schematic diagram for PIV general set-up (PIV, 2009)

Given the geometry of the PIV measuring domain, the measurements were confined to the xz and xy planes as showing in Figure 121. The two different planes of measurement in the current work (Figure 121) are shown in blue and yellow. The planes of measurements are determined through the orientation and access of optical light when making the PIV measurement. It is important to note that the PIV adopted only 2-velocity components. These components are represented using the small black arrows in the enclosed blue and yellow planes. Based on the coordinate system applied in this research work, the illumination access considerations for each plane are described below:

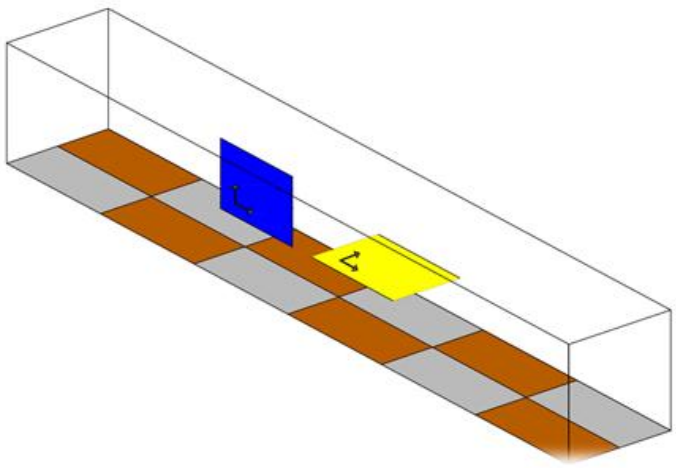

Figure 121: PIV Measurement Planes

- Blue (vertical) plane defines the (xz) axis. In this case, the camera was orientated and views the flow through the side wall of the flume, while the laser is perpendicular to the channel bed and illuminates the flow from above the water surface.
- Yellow (lateral) plane defines the (xy) axis. In this case, the laser illuminates through the sidewall of the flume and the camera mounted above the water surface perpendicular to the channel bed. Consideration is given to the water surface under the camera. Being a small scale turbulence measurement, the surface ripple problem was mitigated by using a transparent plastic bottom box through which the camera viewed the illuminated flow.

Once the camera has been set to properly focus and the laser set up as shown in Figure 120, the calibration of the experiment was undertaken to set a scale factor in the PIV software in order to interpret the distance between the camera and the experimental plane. The PIV software records the measurements in pixel light intensity maps; it processes these and outputs the particle mean displacement for each sub-window area in terms of camera pixels. In order for the PIV software to provide velocity measurements in physical units (i.e. mm/s), the scale factor are provided to translate between the pixels of the camera image and the millimetres in physical units by allowing the velocity vectors to be converted from pixels per second to millimetres per second. This was carried out by clicking on two points of known distance apart using a ruler and the distance provided in millimetres to define the field of view (FOV) positions in millimetres as illustrated in Figure 122 for xy (upper) and xz (bottom) planes respectively. Figure 122 provides the scale factor set in the PIV acquisition software for the experiments.

a

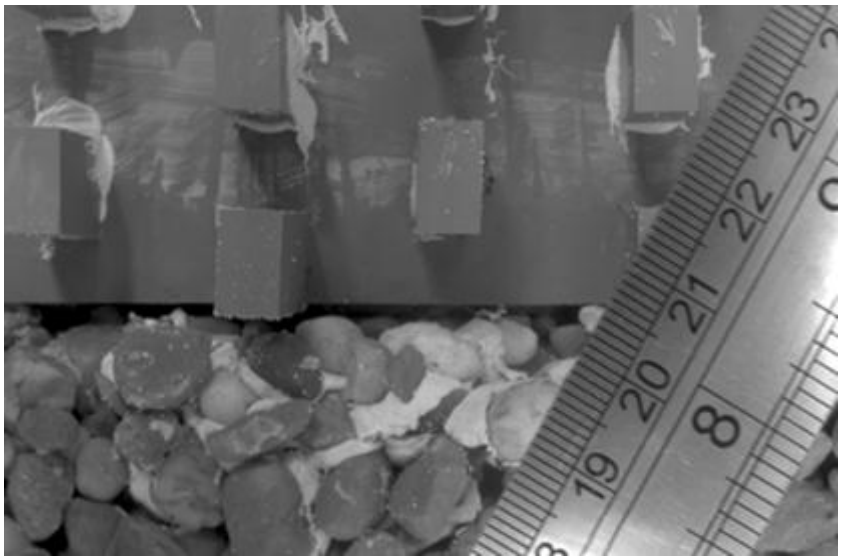

b

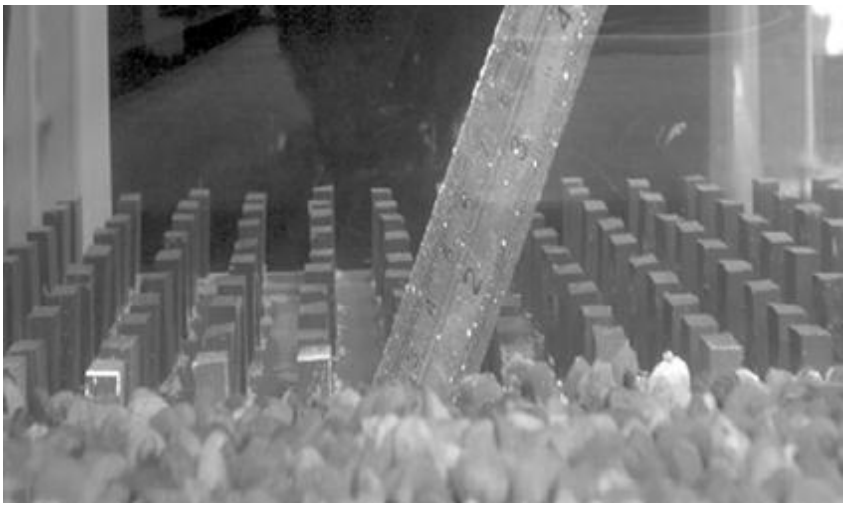

Figure 122: Calibration procedures for xy (upper) and xz (bottom) planes

5.5.1 Experimental Condition

Velocity measurements were undertaken over an approximately $90mm \times 70mm$ field of view for xy and $110mm \times 80mm$ for xz plane using a constant discharge $7.5\ l/s$ and depth of flow $80mm$. Experiments were performed for both roughness configurations and for the sake of brevity, selected results for configuration two (EXPT2) (Figure 123) are presented. Whilst additional results for both EXPT1 and EXPT2 presented in Appendix C.

Two lateral planes at different height, near bed $\left({}^{z}/_{H} = 0.25\right)$ and at upper region near the free surface $\left({}^{z}/_{H} = 0.75\right)$ were measured for plane xy as indicated by the rectangular shape in Figure 123. The figure also indicates the three longitudinal planes measured at $50mm$ interval over the gravel region$\left({}^{y}/_{B} = 0.42\right)$, at the boundary region $\left({}^{y}/_{B} = 0.50\right)$ and vegetated region$\left({}^{y}/_{B} = 0.58\right)$ for plane xz, where y represent lateral distance perpendicular to the streamwise flow and B is the channel width.

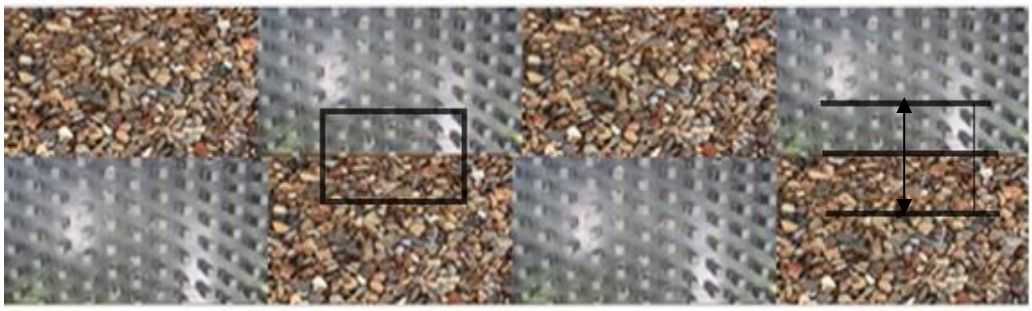

Figure 123: Showing the longitudinal and lateral sections measured

The vertical distance $\left({}^{z}/_{H}\right)$ is defined as the vertical field of view (FOV), where H represents the depth of flow, the lateral distance $\left({}^{y}/_{B}\right)$ is defined as the lateral field of view (FOV) and the streamwise distance $\left({}^{x}/_{D_x}\right)$ defined as the streamwise field of view (FOV), x is the position in streamwise length distance and D_x is the total streamwise length measured.

5.5.2 Data Processing

The PIV images were acquired for five hundred (500) frames (1000 double exposed PIV photographs). The PIV software "rtControl" was used to control the whole procedure of PIV measurements after setting up the locations of camera and laser sheet as discussed in section 5.5. The PIV data was collected by adjusting the camera and laser objects to obtain a field of view of $90mm$ in x-direction and $70mm$ in y-direction for xy plane and $110mm$ in x-

direction and $80mm$ in z direction for xz plane with each point providing a time series for $180s$ at a temporal resolution of $15Hz$. $180s$ was examined to obtain more than 250 frames which provides the statistical quantity of measurements adequate for the analysis of turbulent flow (Adrian, 1991). A two-dimensional (2D) velocity map is obtained by cross-correlating two consecutive images separated by a time interval ranging from 37ms to 40ms selected optimally according to the flow speed as discussed in section 5.5. The PIV software and MATLAB were used to analyse the PIV images for velocity and turbulent field.

The image filtering was performed using the data acquisition software rtControl by enabling the vector filtering advanced settings to accept vectors that are within the mean of neighbours plus or minus root mean square multiply by a standard value of 1.3, i.e., $\pm RMS \times 1.3$ as recommended for velocity measurement (PIV, 2009). Vectors were replaced with interpolated data from neighbours (PIV, 2009). Statistical accuracies were calculated based on the total number of samples (N), sampling variance, and the 95% confidence interval for each point over the planes. In each of data processing, the standard error was used to determine the accuracy of the data based on the 95% confidence interval, the uncertainty in the mean velocity U were estimated to be approximately $\pm 5\%$ or less. This statistical error was calculated using Equation (76):

$$S_d = \pm \frac{\sigma_u}{\sqrt{N}} \tag{76}$$

where N is the number of valid measurements.

As illustrated by the vertical distribution of the mean velocity U in Figure 124, the PIV measurements in the xz plane are within the experimental error of 5%.

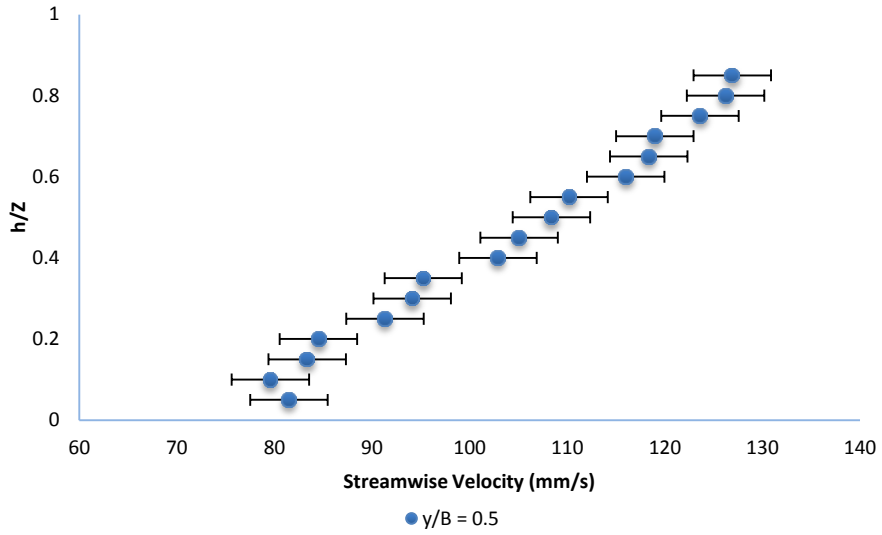

Figure 124: Experimental Errors in the Mean Streamwise Velocity Measurement

The image analysis was performed using the cross-correlation technique (PIV, 2009). Once a sequence of two light exposures is recorded, the images are divided into small sub-windows; the images in each sub-window are cross-correlated with each other pixel by pixel. The correlation produces a signal peak (Figure 125), identifying the common displacement of the tracer particle.

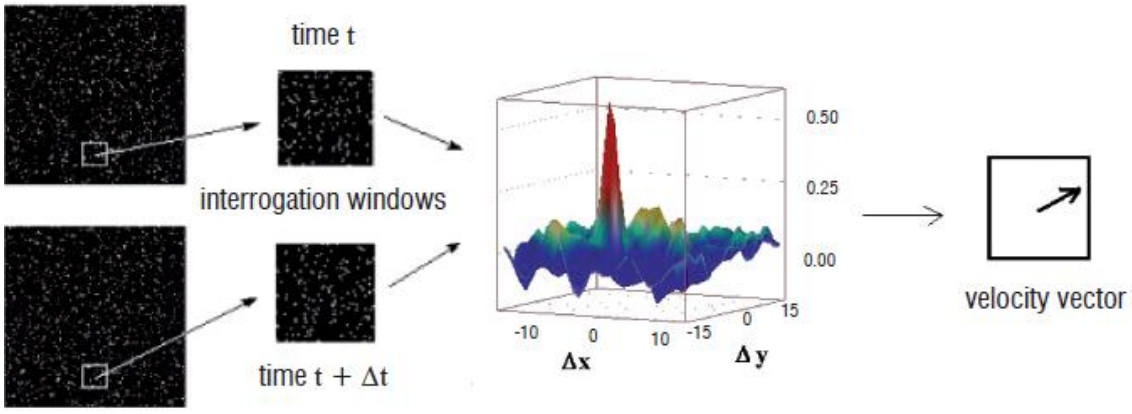

Figure 125: Image cross-correlations and degree of match (PIV, 2009)

In the analysis of the images, the following correlation settings were used in the PIV software, the PIV rtControl software offered sub-windows of the following sizes as measured in camera pixels; (i) 16×16, (ii) 32×32, and (iii) 64×64. The size of the sub-window used for constructing the velocity field and vector maps in this experiment was set as 32×32 and 50% overlapped in each direction. The choice of the sub-window was undertaken by examining the sub-window sizes for images that will produce a high quality correlation map. A 32×32 pixel wide sub-windows provided higher image correlations compared to a larger sub-window size where the image particles are further apart and are less correlated, while the image particles spread out in the smaller sub-window. The overlap of the sub-windows is to build up the vector maps and to mitigate against holes being created in the maps through the loss of data around the boundaries of these regions. Figure 126 illustrates the instantaneous mean velocity and vector distributions respectively using 32×32 sub-window and 50% overlap.

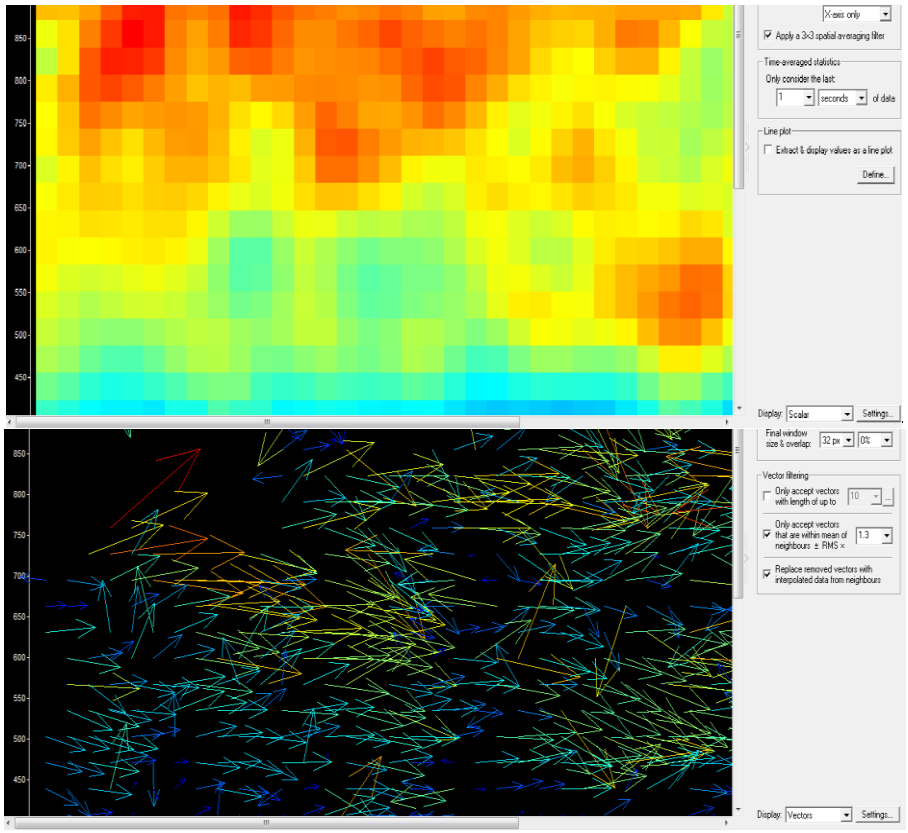

Figure 126: Instantaneous streamwise velocity and vector maps for the flow in xz plane

The 1000 instantaneous velocity fields were post processed to obtain the mean velocities and turbulence properties of the flow through a code written in MATLAB.

In summary, the data processing involves the following steps:

- The camera recorded pairs of valid 500 images and processes them in 640×480 pixels
- The images are cross-correlated to yield common particle displacement using 32×32 sub-window area.
- The average particle displacement for each sub-window is divided by the pulse separation (delay) time Δt to create the velocity vectors.
- The maps of velocity vectors are then built by overlapping the sub-windows and filtered based on their magnitude.

- The velocity maps are further post processed using codes written in MATLAB for better results.

5.5.3 Results

As noted in Figure 123, velocity measurements were undertaken over two independent different planes (xy) and (xz) with the results showing the time averaged streamwise U and lateral velocity V for the xy plane and time average streamwise U and vertical velocity W for the xz plane. The theoretical velocity was compared with the integrated channel mean velocity over the full depth of the channel with a difference of 5% which falls within the experimental error. In the figures presented in this section, the flow depth H is used as the normalising length scale for vertical FOV $\left({}^{z}/_{H}\right)$, while the total streamwse length measured (D_x) is used as the normalizing length scale for the streamwise FOV $\left({}^{x}/_{D_x}\right)$ and the lateral width used to normalise the lateral FOV $\left({}^{y}/_{B}\right)$.

Figure 127 illustrates the distribution of the time averaged streamwise velocity U in the xy plane (lateral plane) for the measured field of view (FOV) $90mm \times 70mm$ for xy plane. The boundary region between gravel and vegetated region is demarcated with lines. From Figure 127, it can be seen that, the lateral distribution of mean velocity U responds to change in bed roughness in xy plane. In the near bed plane $\left({}^{z}/_{H} = 0.25\right)$ (Figure 127b), U is apparently retarded over the gravel bed $(0 \leq lateral\ FOV \leq 0.5)$ relative to the vegetated bed $(0.5 \leq lateral\ FOV \leq 1.0)$ (Figure 127b). This provides an evidence of significant effect of roughness on the near bed flow. The upper plane region of the flow $\left({}^{z}/_{H} = 0.75\right)$ (Figure 127a) shows little difference in U distribution over the bed regions with the flow demonstrating acceleration over the vegetated bed relative to the gravel bed; the results at the upper plane region indicates that this region of the flow is less affected by the channel bed roughness relative to near bed. The lateral profile of mean streamwise U in xy plane is shown

in Figure 128. The mean streamwise velocity distributions reveal similar trends seen in those of the ADV measurements in Figure 81. In the figure, there is evidence of the central dip at the boundary region (lateral $FOV \approx 0.50$) as seen in the ADV measurements (Figure 81). Its existence is attributed to the momentum transport due to lateral shear in this region. From the mean velocity U results, the velocity distributions taken with the ADV and PIV are qualitatively consistent showing similar distributions of mean velocities.

a

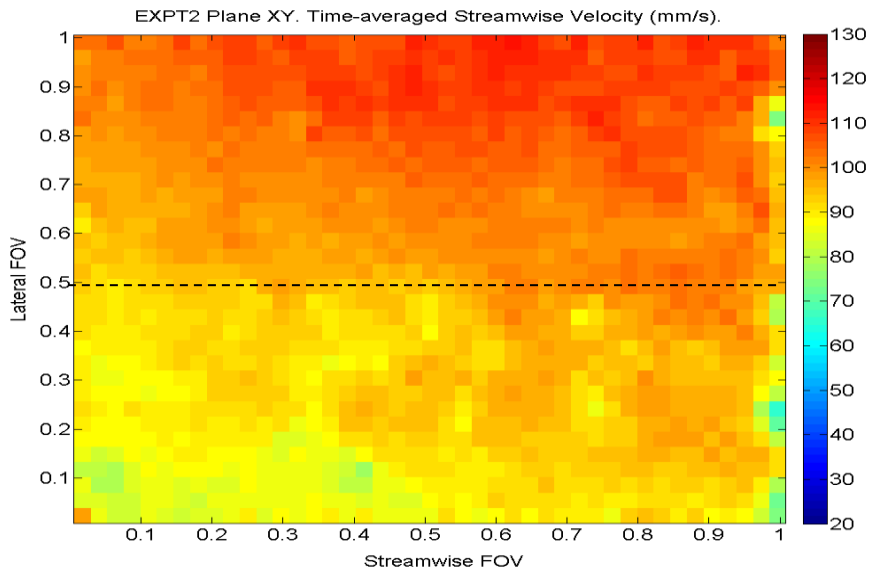

b

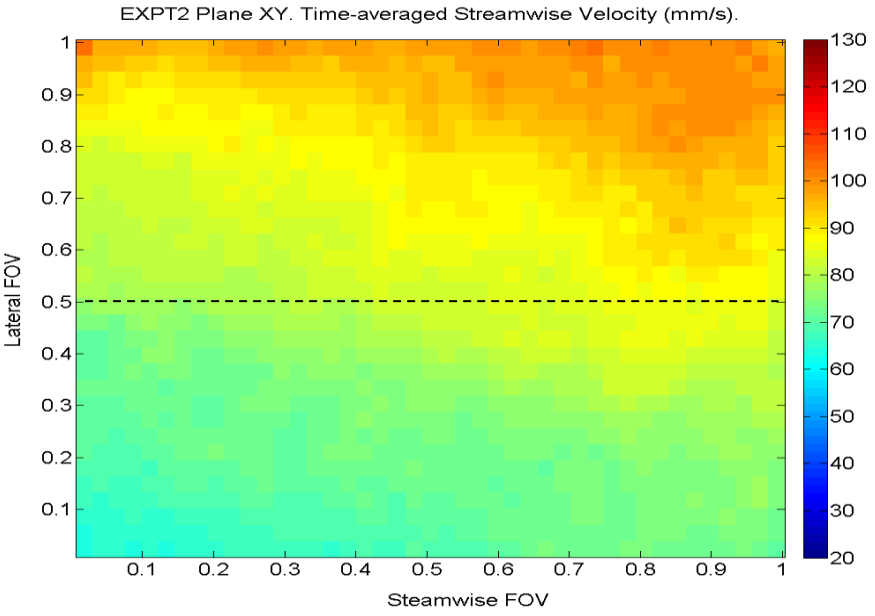

Figure 127: Mean Streamwise velocity in xy (lateral) plane, upper region $\left({}^{z}/_{H} = 0.75\right)$ plane (a) near bed $\left({}^{z}/_{H} = 0.25\right)$ plane (b)

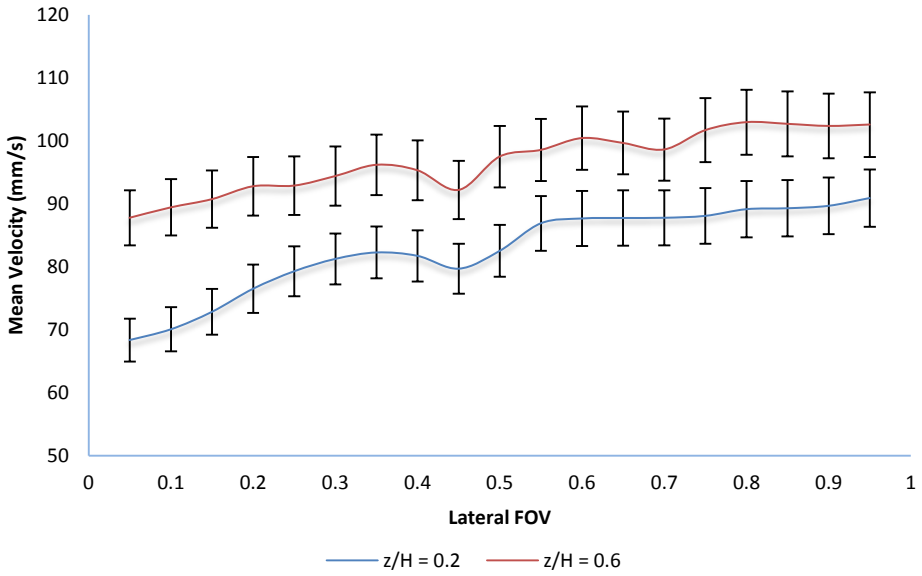

Figure 128: Lateral (FOV) distribution of the mean streamwise velocity.

For the xz plane, Figure 129 illustrates the images of the mean streamwise velocity U at three representative positions over the gravel, roughness boundary and vegetated regions in the xz plane. The velocity values (mm/s) are measured over the FOV 110mm long and 80mm high. The figures provide direct comparison between each lateral position measured. The first position is located laterally over the gravel $\left({}^{y}/_{B} = 0.42\right)$ bed, the second and third positions are located at the roughness boundary region $\left({}^{y}/_{B} = 0.50\right)$ and over the vegetated bed $\left({}^{y}/_{B} = 0.58\right)$ respectively. The three measured regions are $50mm$ laterally separated as shown in Figure 123. As noted from the roughness configuration, these positions are noted as regions for the roughness interaction and shear turbulence generation.

By visual inspection of the velocity maps and regions of the flow field, the region of low velocity can be identified at the boundary region $\left({}^{y}/_{B} = 0.50\right)$ (Figure 129b), the results suggest that, the bed roughness exerts more influence on the flow at the boundary region $\left({}^{y}/_{B} = 0.50\right)$ with the existence of lateral momentum transfer and lower average streamwise

velocities at this region. The flow accelerates at the free surface over the vegetated region $\left({}^{y}/_{B} = 0.58\right)$ (Figure 129c) relative to the gravel region$\left({}^{y}/_{B} = 0.42\right)$ (Figure 129a) which is consistent with the result for the xz plane in Figure 127 and in reasonable agreement with the ADV results as shown in the lateral distribution of the mean streamwise velocity U in Figure 80 and 81 where the lower streamwise velocity is measured at the boundary region $\left({}^{y}/_{B} = 0.50\right)$ for EXPT2. The lower velocity at the boundary region is attributed to the effect of both roughness elements on the flow and the lateral momentum transfer due to change in bed roughness. Similarly, previous work that investigated the central region containing the boundary between the rough and smooth beds has observed lower velocities at the boundary region (Jesson et al., 2013). In addition from the figures, the velocity measurements in these planes indicate the downstream development of the mean streamwise velocities along the streamwise (FOV) distance.

The low quality at the most left hand sides of the images is attributed to the different rough bed sections upstream of the plane measured,

a

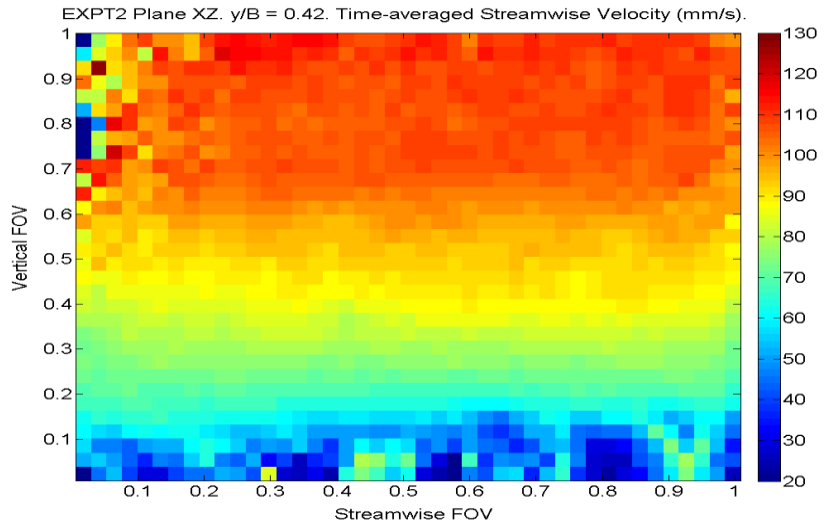

b

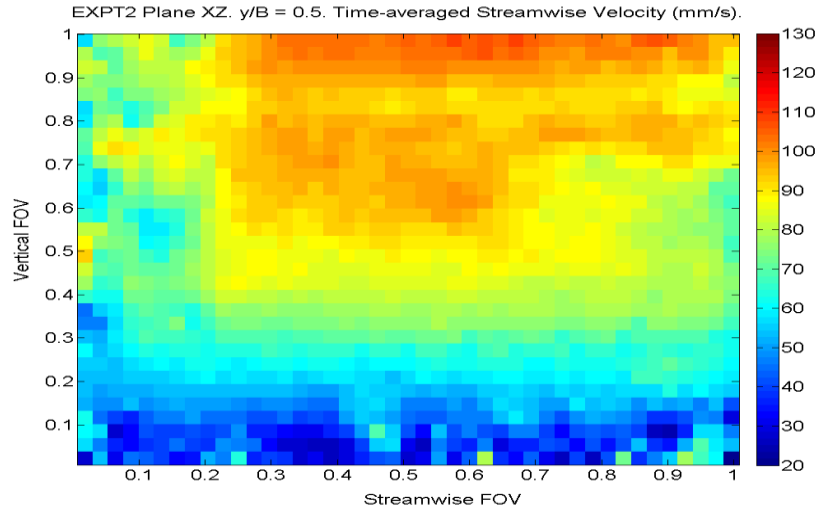

c

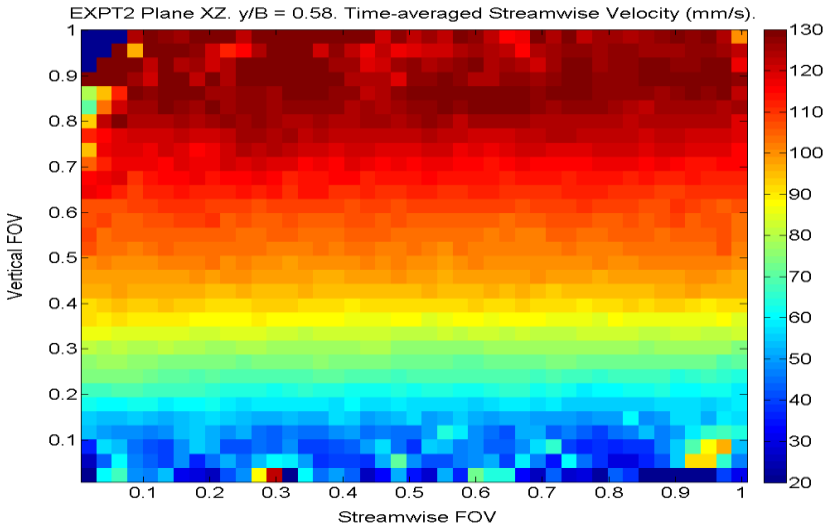

Figure 129: Mean Streamwise velocity distributions in xz (vertical plane) over the gravel region $\left({}^{y}/_{B} = 0.42\right)$ (a), the boundary region $\left({}^{y}/_{B} = 0.50\right)$ (b) and the vegetated region $\left({}^{y}/_{B} = 0.58\right)$(c)

Figure 130 illustrates the vertical profiles of the mean streamwise velocity U at three representative streamwise locations $x/D_x = 0.30$, $x/D_x = 0.50$, and $x/D_x = 0.80$. The distributions collapse over the gravel $(y/B = 0.42)$ (Figure 130a) and vegetated region $(y/B = 0.58)$ (Figure 130c). At the boundary region $(y/B = 0.50)$ (Figure 130b) where the flow shows to be more disturbed, differences occur in the vertical profiles of the mean streamwise velocity U. The divergence of the distribution at the boundary region $(y/B = 0.50)$ further suggest velocity shear at this region. Furthermore, it can be seen that the near bed mean streamwise velocity is lower over the gravel $(y/B = 0.42)$ and boundary regions $(y/B = 0.50)$ relative to the vegetated region $(y/B = 0.58)$. This is consistent with the results in the xy-plane and the ADV data as illustrated in Figure 127 and Figure 80. Figure 130 further demonstrate large scale flow becoming increasingly accelerated near the free surface over the vegetated bed $(y/B = 0.58)$ relative to gravel $(y/B = 0.42)$and boundary regions $(y/B = 0.50)$. This becomes more evident if Figure 130 is thoroughly compared with the velocity map in Figure 129.

a

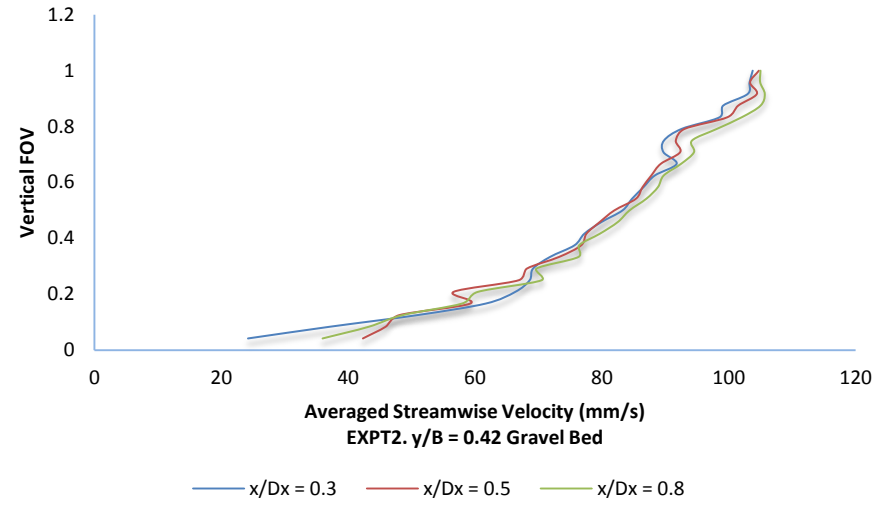

b

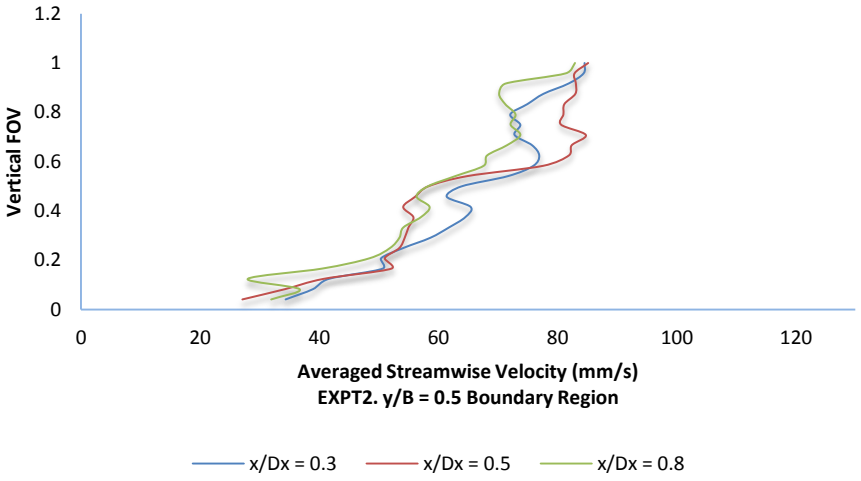

c

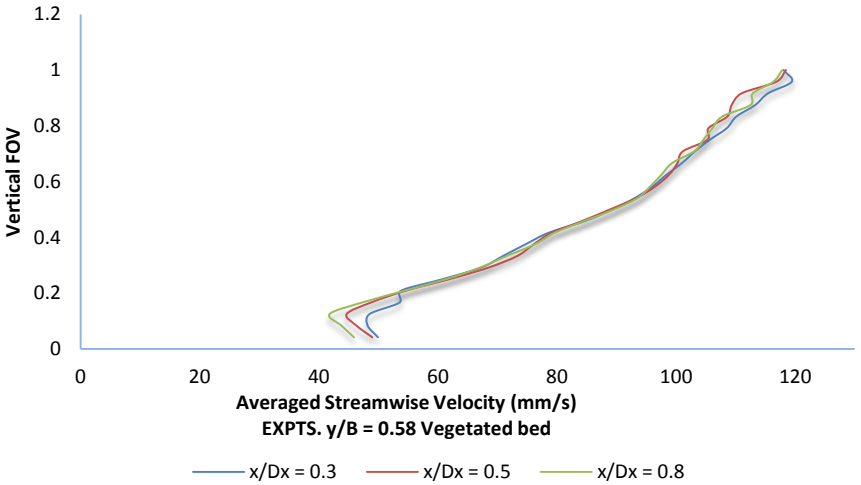

Figure 130: Mean Streamwise Velocities over gravel$\left(\frac{y}{B} = 0.42\right)$ (a), boundary$\left(\frac{y}{B} = 0.5\right)$ (b), and vegetated$\left(\frac{y}{B} = 0.58\right)$ (c) regions.

The streamwise turbulence intensity over the entire experimental xy-plane tended to remain as shown in Figure 131 constant at the upper plane region of the flow $\left({}^{z}/_{H} = 0.75\right)$ Figure 131a, however at the near bed plane region $\left({}^{z}/_{H} = 0.25\right)$ Figure 131b, the result showed a small increase in streamwise turbulence intensity over the gravel region of the flow $(0 \leq lateral\ FOV \leq 0.5)$. An explanation for this constant streamwise turbulence intensity at the upper plane region is of the little influence of the boundary roughness on the flow near the free surface over the xy-plane.

The distributions of turbulence intensities over the xz-plane are shown in Figure 132 for streamwise turbulence intensity. From Figure 132, turbulence intensity was calculated as being highest at the boundary region $\left({}^{y}/_{B} = 0.50\right)$ (Figure 132b) with the magnitude of turbulence intensity extending the depth of flow. This is not too surprising as the results supports the principle of shear turbulence at the boundary region and provides further indication of velocity shear at the boundary region in EXPT2. The results further indicate greater magnitude of near bed streamwise turbulence intensity over the gravel bed $\left({}^{y}/_{B} = 0.42\right)$ (Figure 132a) relative to the vegetated region $\left({}^{y}/_{B} = 0.42\right)$ (Figure 132c). Regions of higher turbulence intensity in Figure 132 exhibited lower mean velocities as shown in Figure 129.

a

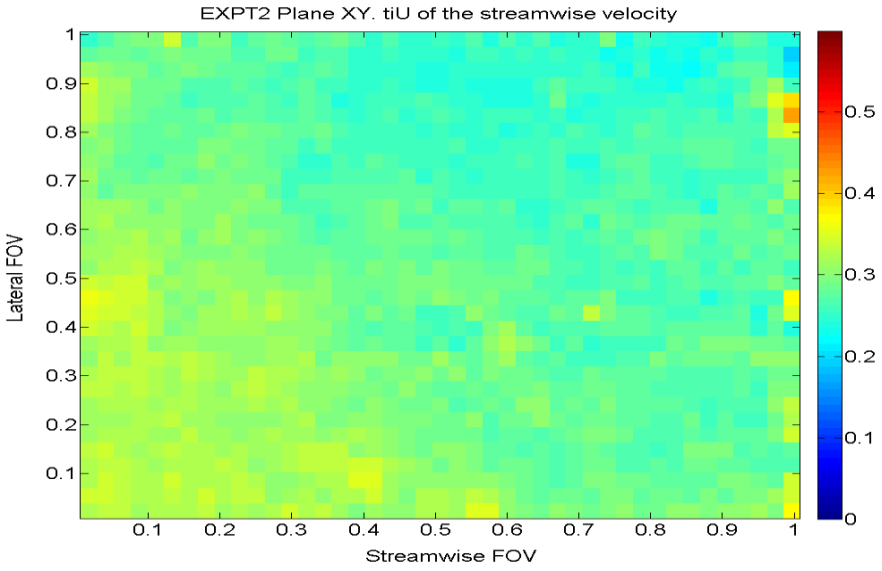

b

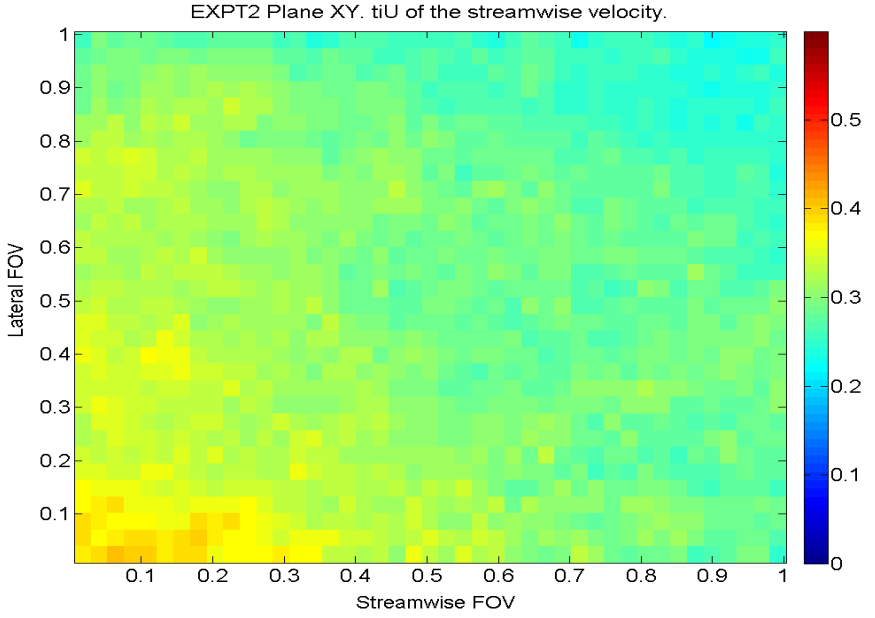

Figure 131: Streamwise turbulence intensity in xy (lateral) plane, upper region $\left(z/H = 0.75\right)$ plane (a), and near bed $\left(z/H = 0.25\right)$ plane (b).

a

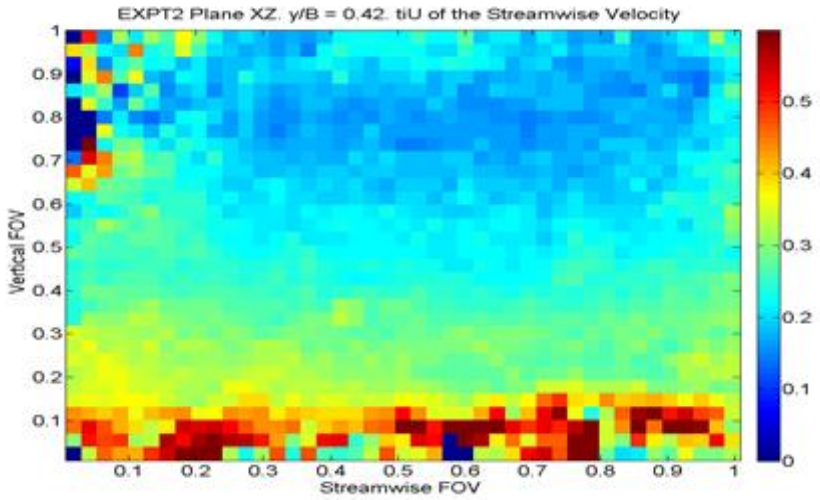

b

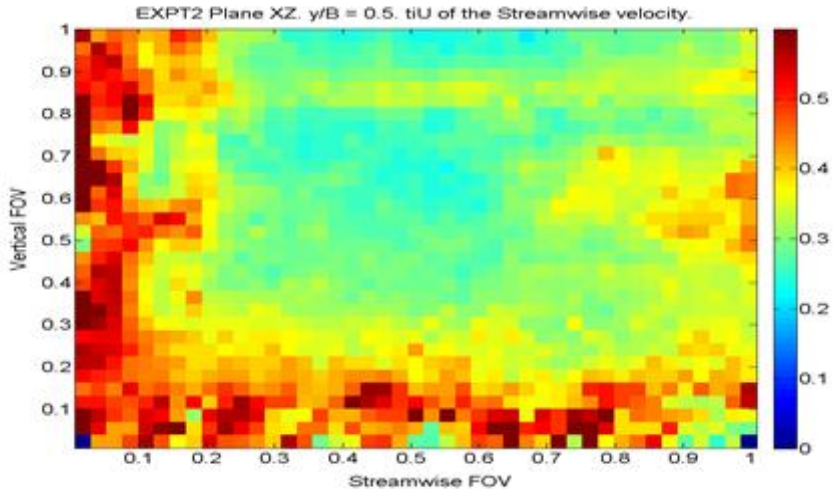

c

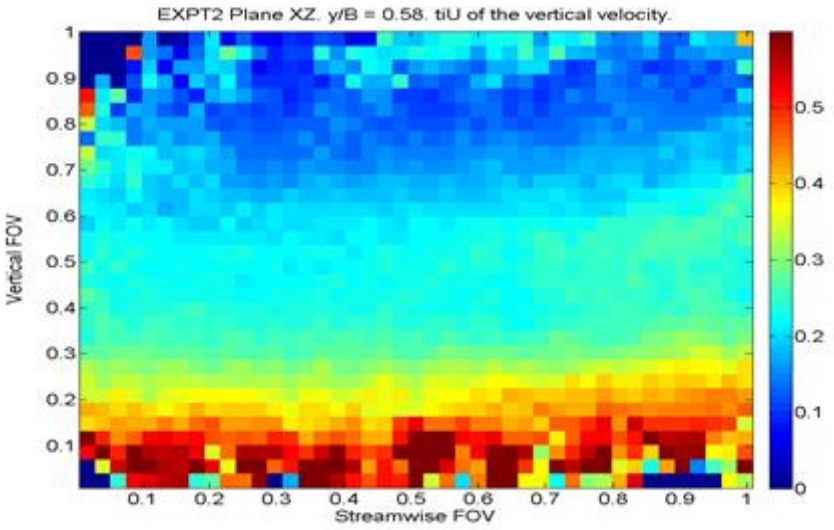

Figure 132: Streamwise turbulence intensities (tiU) in xz (vertical) plane over the gravel region $\left({}^{y}/_{B} = 0.42\right)$ (a), the boundary region $\left({}^{y}/_{B} = 0.50\right)$ (b) and the vegetated region $\left({}^{y}/_{B} = 0.58\right)$(c)

The vertical profiles of turbulence intensities of the streamwise velocity, for xz plane at representative points with respect to the streamwise distance are shown in Figure 133. The figures compare the vertical profiles of streamwise turbulence intensity in different streamwise locations. The shear stress τ_b was evaluated here as the weight component theoretical 2-dimensional boundary shear stress $\rho g R S_0$ and the friction velocity U_* calculated from $U_* = \sqrt{\tau_b/\rho}$, where ρ is the water density. This method is consistent with the method of vegetated flow as studied by Finnigan (2000). The following theoretical equation derived from 2-D equation of motion on the basis of the equilibrium-state equations of turbulent kinetic energy (Nezu and Onitsuka, 2001) as included in Figure 133 is applied to approximate the distribution of the streamwise turbulence intensity with height:

$$\sigma_u/U_* = 1/\ln\left(z/z_0\right) \tag{77}$$

The figures exhibit some local variations with downstream distance. Considering the streamwise positions $x/D_x = 0.30$, $x/D_x = 0.50$, $x/D_x = 0.80$ (Figure 133). The distribution of the streamwise turbulence intensities indicates for all cases an increase in the turbulence intensities near bed and attains maximum value at $(vertical\ FOV \leq 0.2)$, then decreases from the maximum value towards the free surface. The streamwise turbulence intensity near the free surface over the vegetated bed (Figure 133c) decreases further relative to gravel (Figure 133a) and boundary region (Figure 133b). The intensity value gradually increases near bed with streamwise distance as shown in Figure 133.

However, higher turbulent intensity is observed for the boundary region $\left(y/B = 0.50\right)$ of the flow (Figure 133b). The result supports evidence that the boundary region is a source of turbulence in EXPT2 as discussed in session 4.8. It should be noted that the streamwise turbulence intensities coincides well with the theoretical Equation (77). In contrast, over the

vegetated bed (Figure 133c), the streamwise turbulence intensity values decreases further near the free surface, irrespective of the streamwise location relative to the theoretical Equation (77). This is attributed to the shear velocity U_* obtained from the theoretical 2-dimensional boundary shear stress $\rho g R S_0$ representing average value over the whole cross-section which is likely to vary with changes in bed roughness and also the uniform value of z_0 used for the computation of the theoretical equation. This trend however overestimated the streamwise turbulence intensity at the free surface by the theoretical Equation (77) above the vegetated region.

a

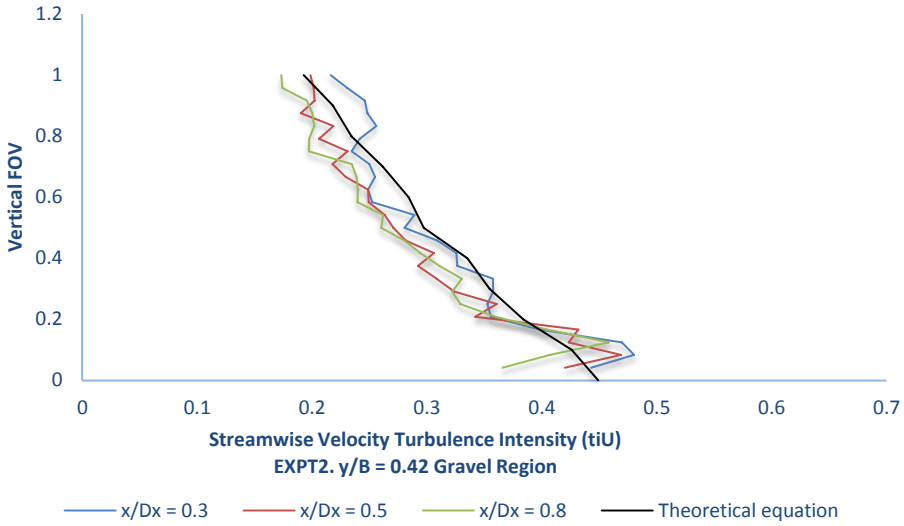

b

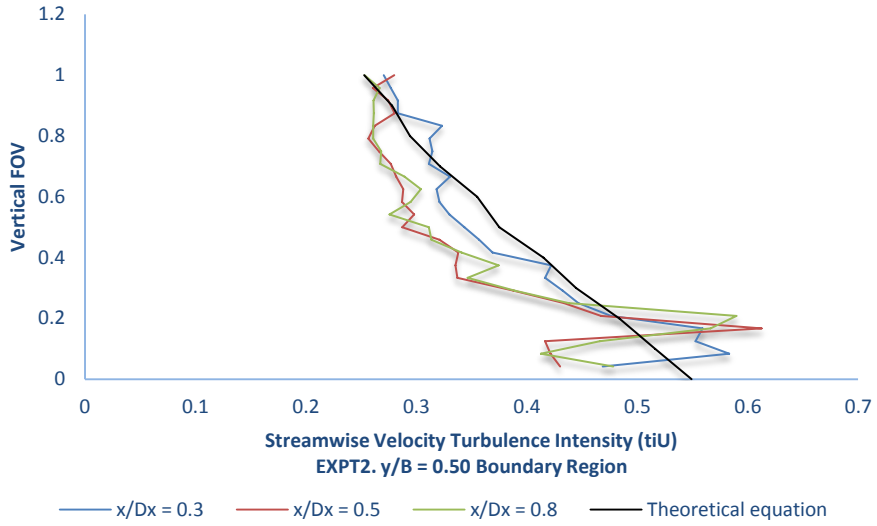

c

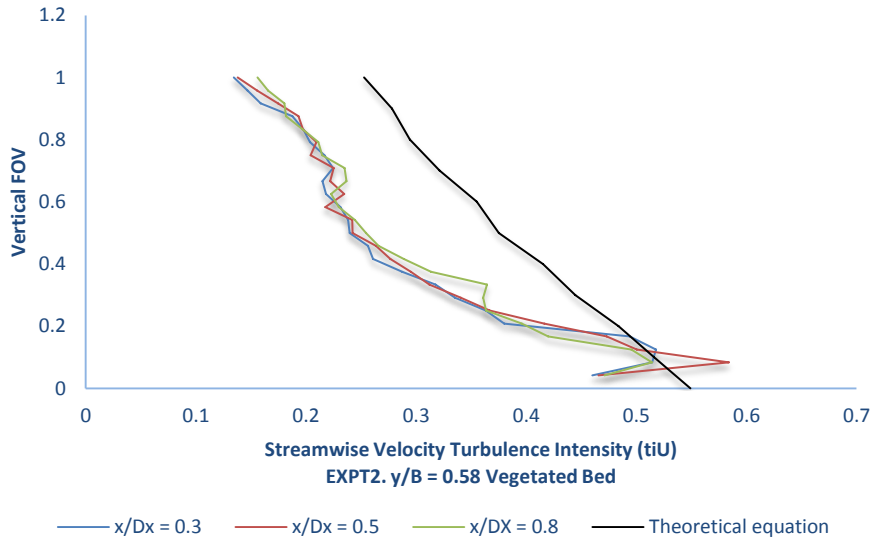

Figure 133: Vertical profiles of streamwise turbulence intensities over the gravel $\left(\frac{y}{B} = 0.42\right)$(a), boundary$\left(\frac{y}{B} = 0.5\right)$ (b) and vegetated$\left(\frac{y}{B} = 0.58\right)$(c) regions.

Figure 134 shows the velocity vector maps for the xy plane within the measured FOV, it can be seen from the vector figures that, at the upper region $\left({}^{z}/_{H} = 0.75\right)$ of the experimental plane for xy, the vectors are entirely in the streamwise direction. The flow indicates well-defined mean streamlines and organised motion as shown in Figure 134a which illustrates the upper flow region in xy-plane. The figure demonstrates that turbulence has been dissipated at this region and the main flow is relatively undisturbed. This trend is confirmed at the upper region ($vertical\ FOV\ \geq 0.3$) of the flow in the xz-plane (Figure 135). From Figure 134, it can be seen that the turbulence arising near bed $\left({}^{z}/_{H} = 0.25\right)$ (Figure 134b) form the separation in vector streamlines in comparison to the upper region (Figure 134a). This is attributed to the influence of shear due to high velocity gradient near bed.

Figure 135 shows the velocity vector plots for the xz plane. Similar to Figure 134, within the upper half of the experimental plane for xz planes ($vertical\ FOV\ \geq 0.3$), the vector shows well defined mean velocity streamlines entirely in streamwise direction. The flow can be seen to be highly turbulent near bed with the presence of structure such as burst type mechanism (large velocity fluctuation) appearing at the lower middle of the channel and grow larger farther downstream the streamwise FOV. However, larger portion of the flow region is disrupted over the gravel region $\left({}^{y}/_{B} = 0.42\right)$ (Figure 135a) and at the boundary region $\left({}^{y}/_{B} = 0.50\right)$ (Figure 135b). The flow disturbance is confined only to the lower region over the vegetated bed $\left({}^{y}/_{B} = 0.58\right)$ (Figure 135c). These regions correspond to the regions of low mean velocity and high turbulence intensity as shown in Figure 129 and Figure 132 respectively. For all the measured planes, this phenomenon of burst event appears to be the most noticeable near bed as it occurs in similar regions and exhibited consistency for all the planes measured.

a

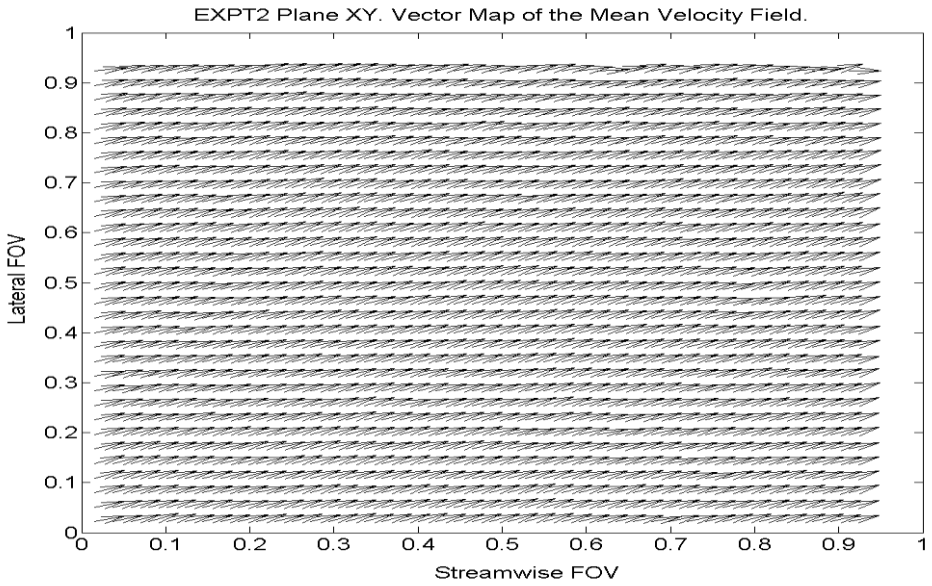

b

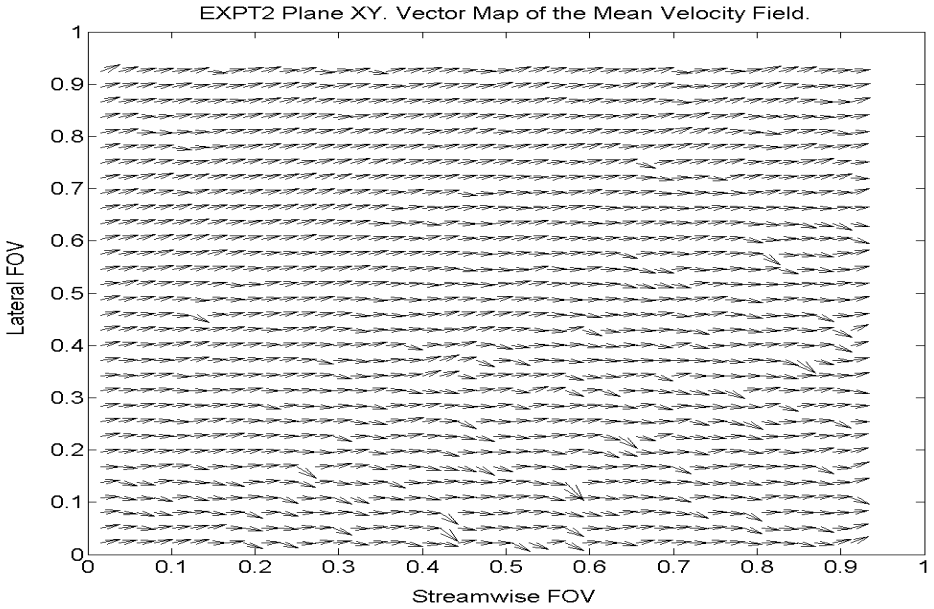

Figure 134: Mean velocity vectors in xy (lateral) plane, upper region $\left({}^{z}/_{H} = 0.75\right)$ plane (a), and near bed $\left({}^{z}/_{H} = 0.25\right)$ plane (b)

a

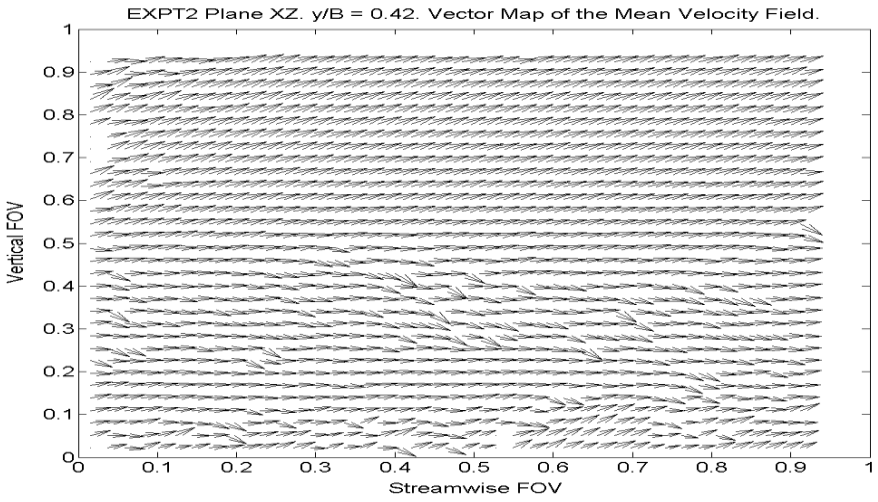

b

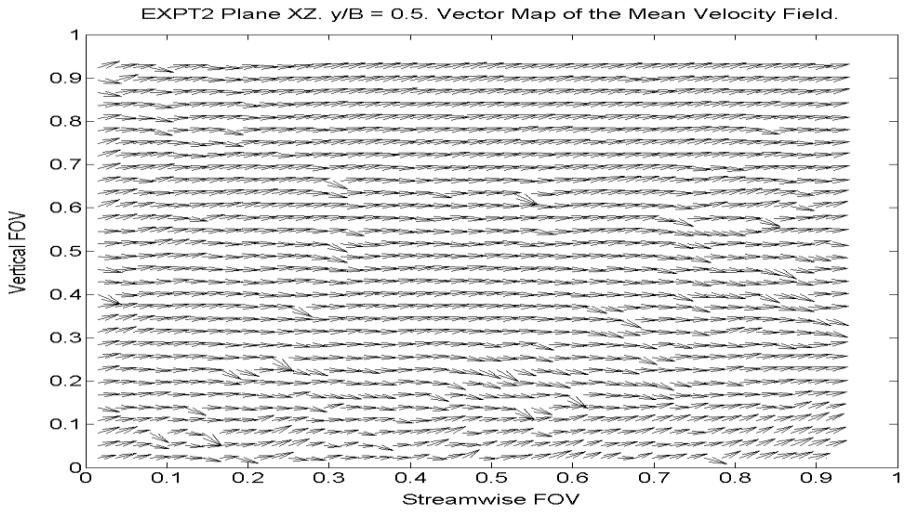

c

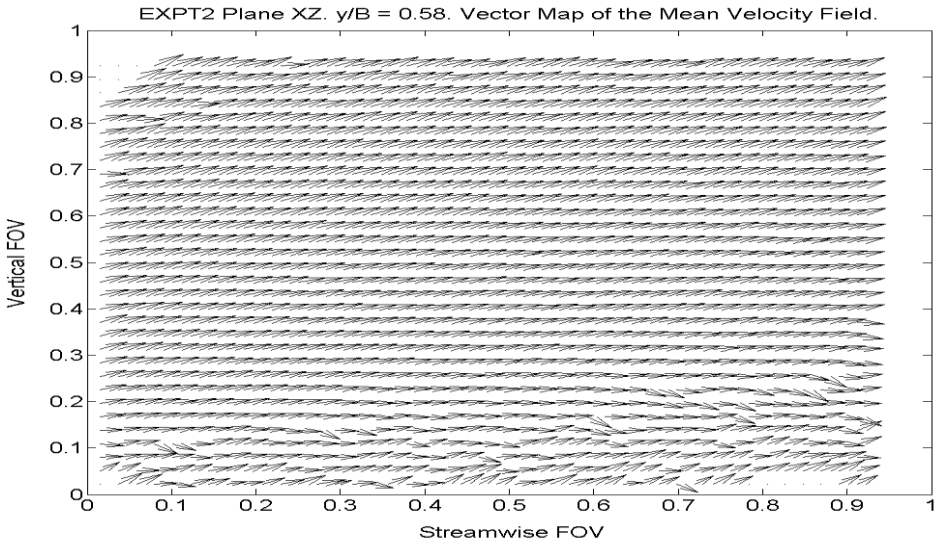

Figure 135: Mean velocity vector plot in *xz* (vertical) plane over the gravel region $\left({}^{y}/_{B} = 0.42\right)$ (a), the boundary region $\left({}^{y}/_{B} = 0.50\right)$ (b) and the vegetated region $\left({}^{y}/_{B} = 0.58\right)$(c)

6 Numerical Modelling of Experimental Data

6.1 Introduction

This chapter examines the applicability of the Shiono and Knight method (SKM) to model the physical experiments. The lateral variation of the SKM parameters for both EXPT1 and EXPT2 and the proposed calibration and panelling procedure for the model are presented. Results are expressed in terms of the depth-averaged velocity and boundary shear stress.

6.2 Modelling Depth-Averaged Velocity and Boundary Shear Stress Distribution

6.2.1 Analytical Solution

The depth-averaged velocity at a given lateral distance is expressed by Equation (46). To apply the SKM, the channel is normally divided into a number of sub-sections or panels and the constants A1 and A2 in Equation (46) are evaluated from the relevant boundary conditions. λ is typically taken as 0.07 (Elder, 1954) but can also be estimated from the experimental data using (Shiono and Knight, 1991; Jesson et al., 2013):

$$\lambda = \frac{-\rho\overline{u'v'}}{\rho H U_* \frac{\partial U}{\partial y}} \tag{78}$$

whilst the secondary flow term Γ is given by:

$$\Gamma = \frac{\partial H(\rho UV)_d}{\partial y} \tag{79}$$

Using the boundary shear stress data obtained from the experiments, the lateral distribution of friction factor f was calculated using:

$$f = \frac{8\tau_b}{\rho U_d^2} \tag{80}$$

The boundary conditions applied between the panels include (Shiono and Knight, 1991):

- Continuity of the depth averaged velocity U_d

$$U_d^{(i)} = U_d^{(i+1)} \tag{81}$$

- Based on Knight et al. (2004) and Omran (2005), the boundary conditions between two adjacent panels given as the continuity of the lateral gradient of depth averaged velocity

$$\mu_{(i)} \frac{\partial U_d^{(i)}}{\partial y} = \mu_{(i+1)} \frac{\partial U_d^{(i+1)}}{\partial y} \tag{82}$$

where $\mu = \lambda \sqrt{\frac{f}{8}}$

μ is applied in (82) for smoothing spikes caused by abrupt changes in the local friction and dimensionless eddy viscosity (Omran, 2005).

- The last boundary condition is specified as a no-slip condition at the channel walls

$$\frac{\partial U_d^i}{\partial y} = \frac{\partial U_d^{i+1}}{\partial y} = 0 \tag{83}$$

Considering two adjacent panels, these boundary conditions are solved and are represented mathematically by Equations (84) - (86), in which y_1 is the left-most measured point looking downstream of the channel and the panel numbers are represented by the subscripts.

$$A_1 e^{\gamma y_2} + A_2 e^{-\gamma y_2} - A_3 e^{\gamma y_2} - A_4 e^{-\gamma y_2} = k_2 - k_1 \tag{84}$$

$$\mu_1 \gamma_1 A_1 e^{\gamma y_2} - \mu_1 \gamma_1 A_2 e^{-\gamma y_2} - \mu_2 \gamma_2 A_3 e^{\gamma y_2} + \mu_2 \gamma_2 A_4 e^{-\gamma y_2} = 0 \tag{85}$$

$$A_1 e^{\gamma y_1} + A_2 e^{-\gamma y_1} = (U_d(y = y_1))^2 - k_1 \tag{86}$$

The SKM boundary condition are generally expressed in matrix formed and solved.

6.2.2 Calibration coefficients

The model calibration was undertaken by evaluating the predicted lateral distributions of U_d and τ_b with the experimental data for various values of f, λ and Γ. In the current work, the SKM simulations were performed using a maximum of eight panels distributed across the sections (including additional panels located at the boundary region due to velocity dip in EXPT2, further details are given in section 6.3). In what follows, the approach for obtaining the calibration parameters and the panel structures are described.

6.2.3 Dimensionless Eddy viscosity Coefficient (λ)

The distributions of the λ calculated from the experimental data are shown in Figures 136 and 137 for EXPT1 and EXPT2 respectively at each cross-section. As shown in these figures, the values of λ do appear not to follow any specific pattern across the channel sections. However, the magnitude of the average value of λ in EXPT1 is lower over the vegetated bed $\left(0.5 \leq \frac{y}{B} \leq 1.0\right)$ compared to the gravel bed $\left(0 \leq \frac{y}{B} \leq 0.5\right)$ (Figure 136), while the value of λ shows greater scatter in EXPT2 (Figure 137). The average magnitude values obtained for each of the cross-section are shown in Table 13. These values are within the range of the standard value 0.07 (Elder, 1954). The analysis of this parameter value confirms the previous findings (Omran and Knight, 2006; Tang et al., 2011) by showing that the standard value 0.07 of λ can be applied to the SKM modelling. The value of 0.07 has been widely reported in the literature (Shiono and Knight, 1991; Elder, 1954) to represent the dimensionless eddy viscosity λ and used to simulate different flow situations with accurate results in comparison to measured data. The effect of variation of the dimensionless eddy viscosity on simulations has also been reported to be negligible for flow in the main channel and the flood plain respectively (Knight et al., 2009). As shown in Table 13, the averaged value of λ recorded in EXPT1 and EXPT2 differs by less than 3%.

CROSS-SECTION	AVERAGE (λ)	CROSS-SECTION	AVERAGE (λ)
CRS1EXPT1	0.087	**CRS1EXPT2**	0.089
CRSEXPT1	0.067	**CRS2EXPT2**	0.073
CRS3EXPT1	0.065	**CRS3EXPT2**	0.071

Table 13: Mean Magnitude Values of λ

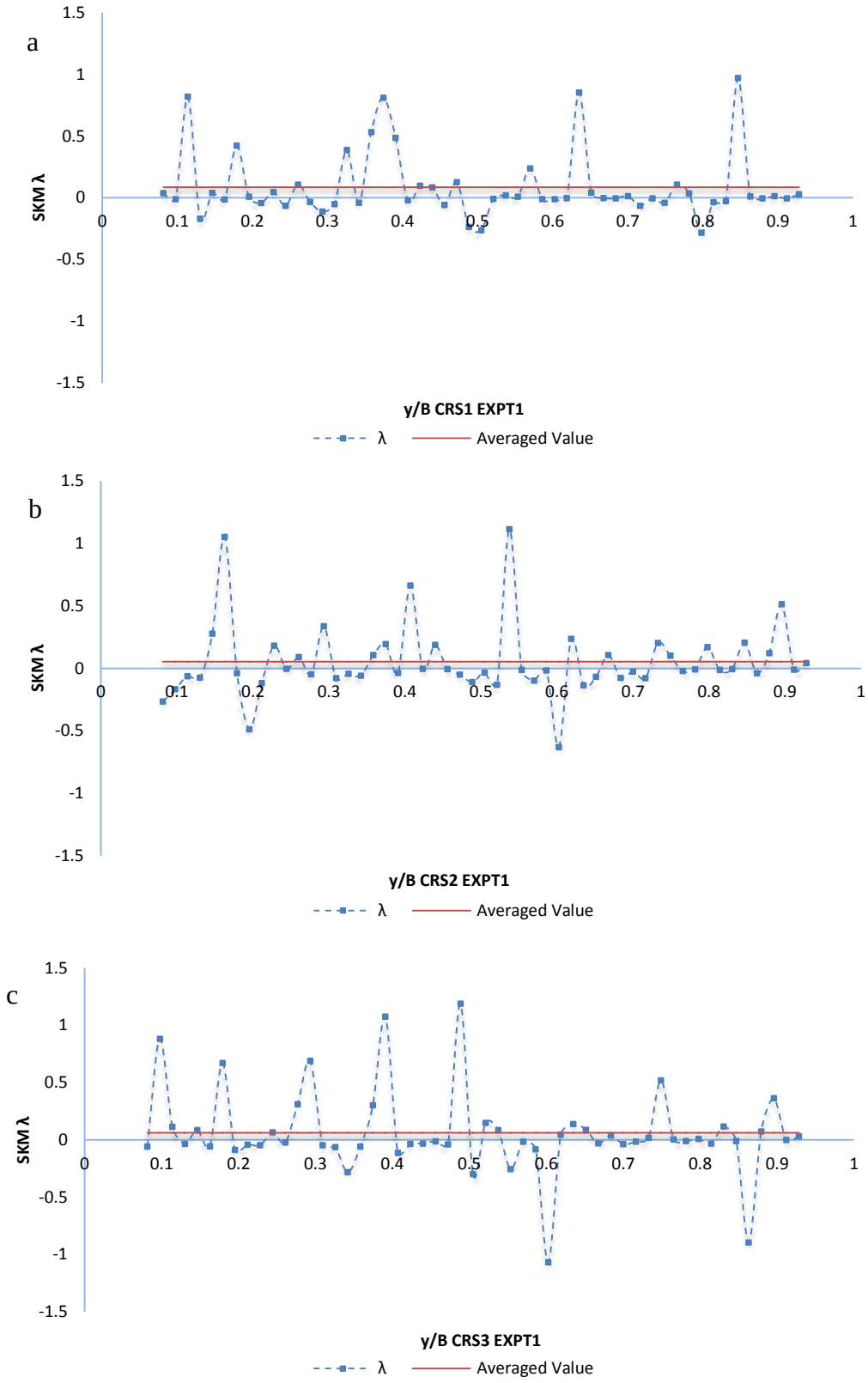

Figure 136: Lateral Distribution of λ CRS1 (a) to CRS3 (c) EXPT1

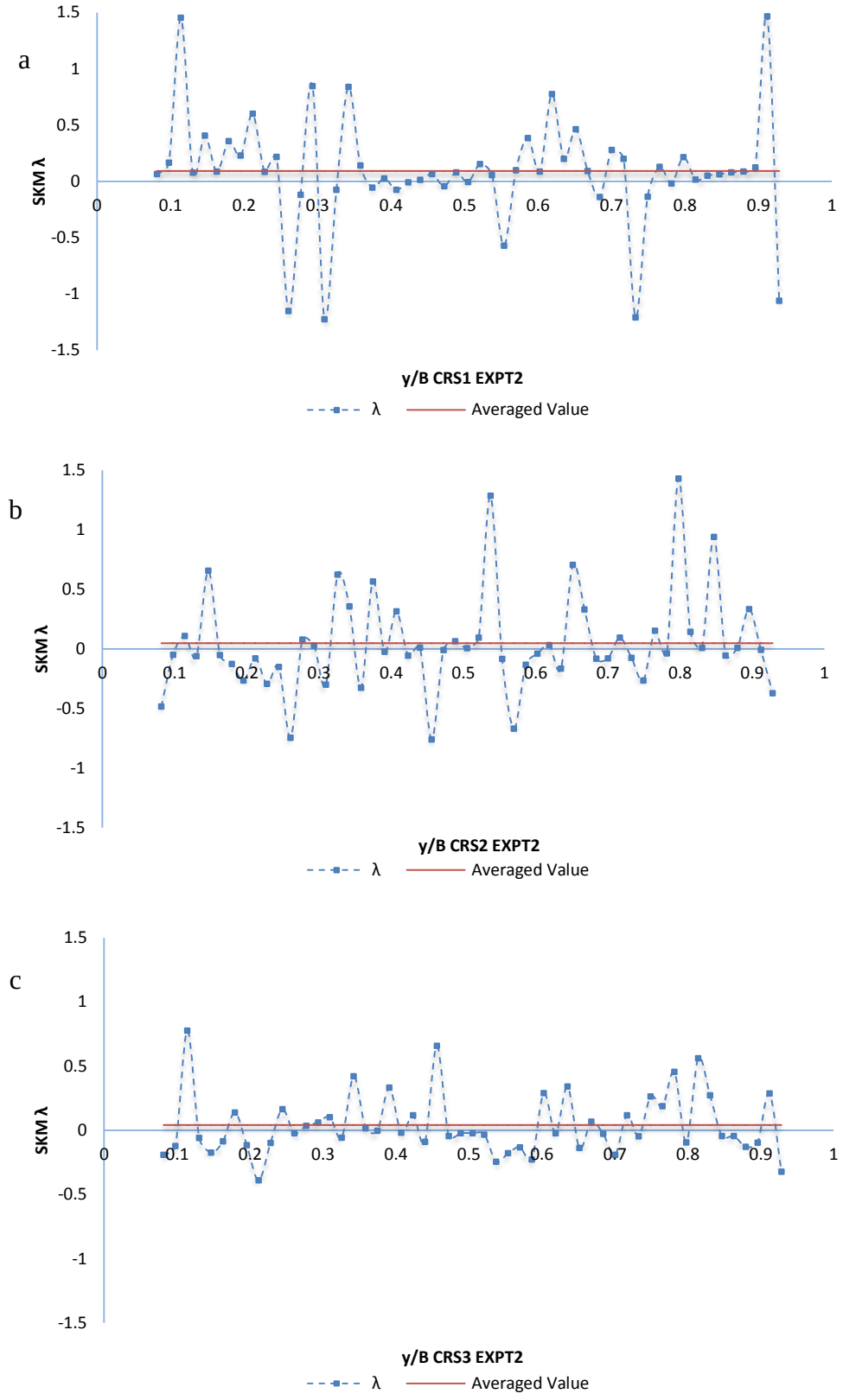

Figure 137: Lateral Distribution of λ CRS1 (a) to CRS3 (c) EXPT2

To examine the sensitivity of λ on the modelling, the outputs of the SKM are examined when applied to the cross-sections using six (6) panel boundaries based on secondary flow fluctuations (further details about panel boundaries are discussed in section 6.2.5). The panels are distributed in accordance with the variation of the secondary flow term Γ.

In Figure 138, the standard λ value of 0.07 and the values obtained from the actual experimental data are used to examine the sensitivity of λ. The common friction factor f values are adopted at the panel boundaries and vary linearly within each panel (further details about friction factor are given in session 6.2.6). These values are given in Table 14 for CRS3, whilst the Γ value is obtained from Equations (87) and (88) (Shiono and Knight, 1991).

The results of these simulations are illustrated in Figure 138 for both EXPT1 and EXPT2 using CRS3 with the conclusions applicable to other cross-sections. Although neither simulation predict the distribution reasonably well, given the parameter section, the constant value of λ performs better (Figure 138) in the distribution of depth averaged velocity U_d. This is supported by the low values of the Root Mean Squared Error (RMSE) i.e. 4% difference between the simulated results and experimental data when the standard value of $\lambda = 0.07$ was adopted (Figure 138). Henceforth the standard λ value of 0.07 is adopted.

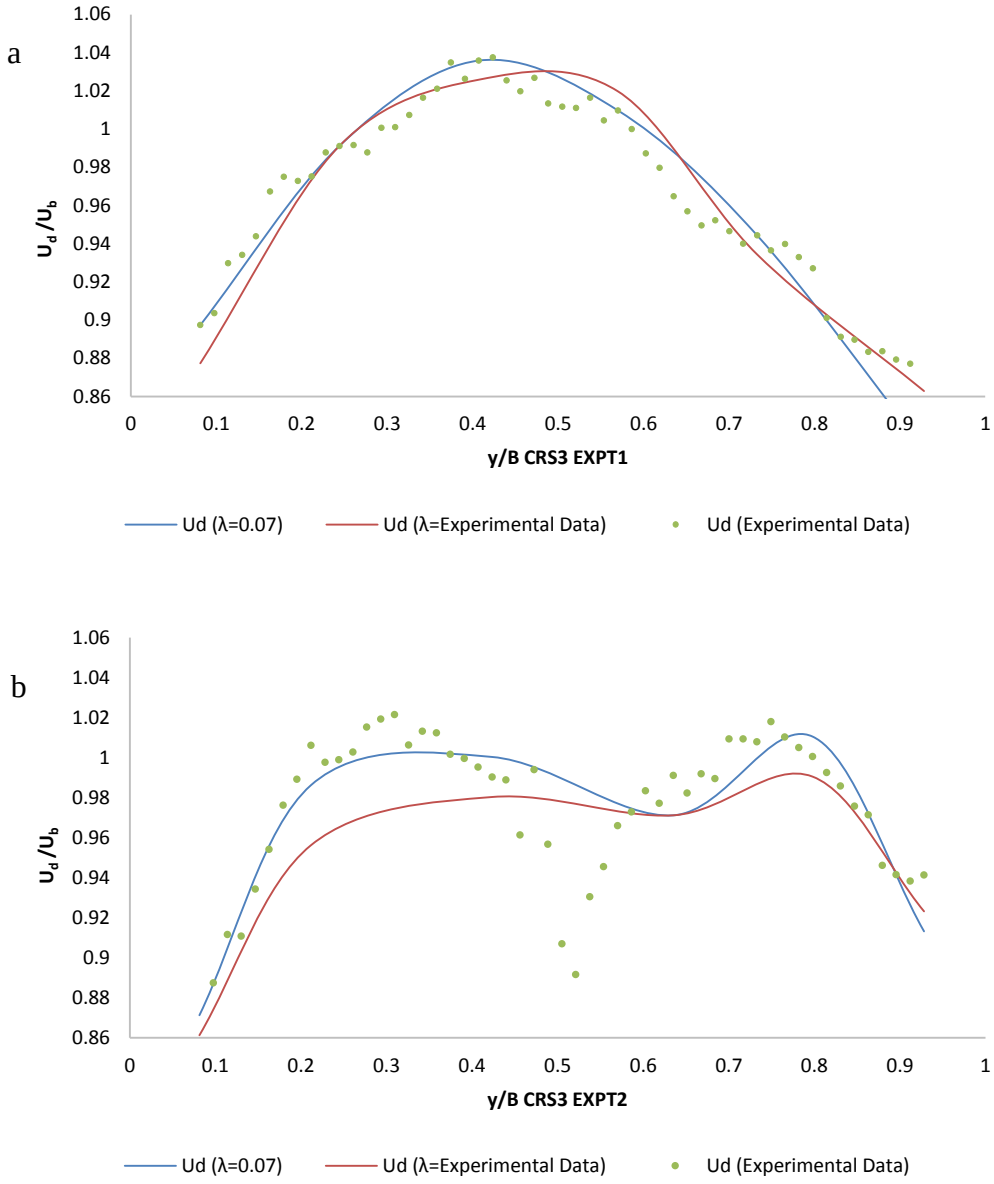

Figure 138: U_d Distribution Using λ Standard Value (0.07) and calculated λ from Experiemtal Data. EXPT1 (a) and EXPT2 (b)

6.2.4 Secondary Flow Term Γ

The values of Γ obtained from the experimental data were calculated using Equation (79) and are shown in Figures 139 and 140. These figures include the depth-averaged relative streamwise velocity U_d. The lateral variations are complex and show frequent positive and negative values. This is consistent with the behaviour of secondary flow since the depth averaged values of $(UV)_d$ can either be positive or negative (Omran and Knight, 2006) which

can be attributed to the direction of the secondary flow cells. From these figures, the magnitude of secondary flow term Γ is generally lower in EXPT1 relative to EXPT2. In EXPT2 the maximum fluctuating magnitude of Γ occurs at the roughness boundary region (Figure 140); this region corresponds with the region of upflow as shown in Figure 84 and dip velocity (Figure 81). In comparison to EXPT1, the fluctuating secondary flow between positive and negative values at the boundary region is approximately 51.6% higher in EXPT2, demonstrating weaker secondary flow in EXPT1 relative to EXPT2 (Figure 140).

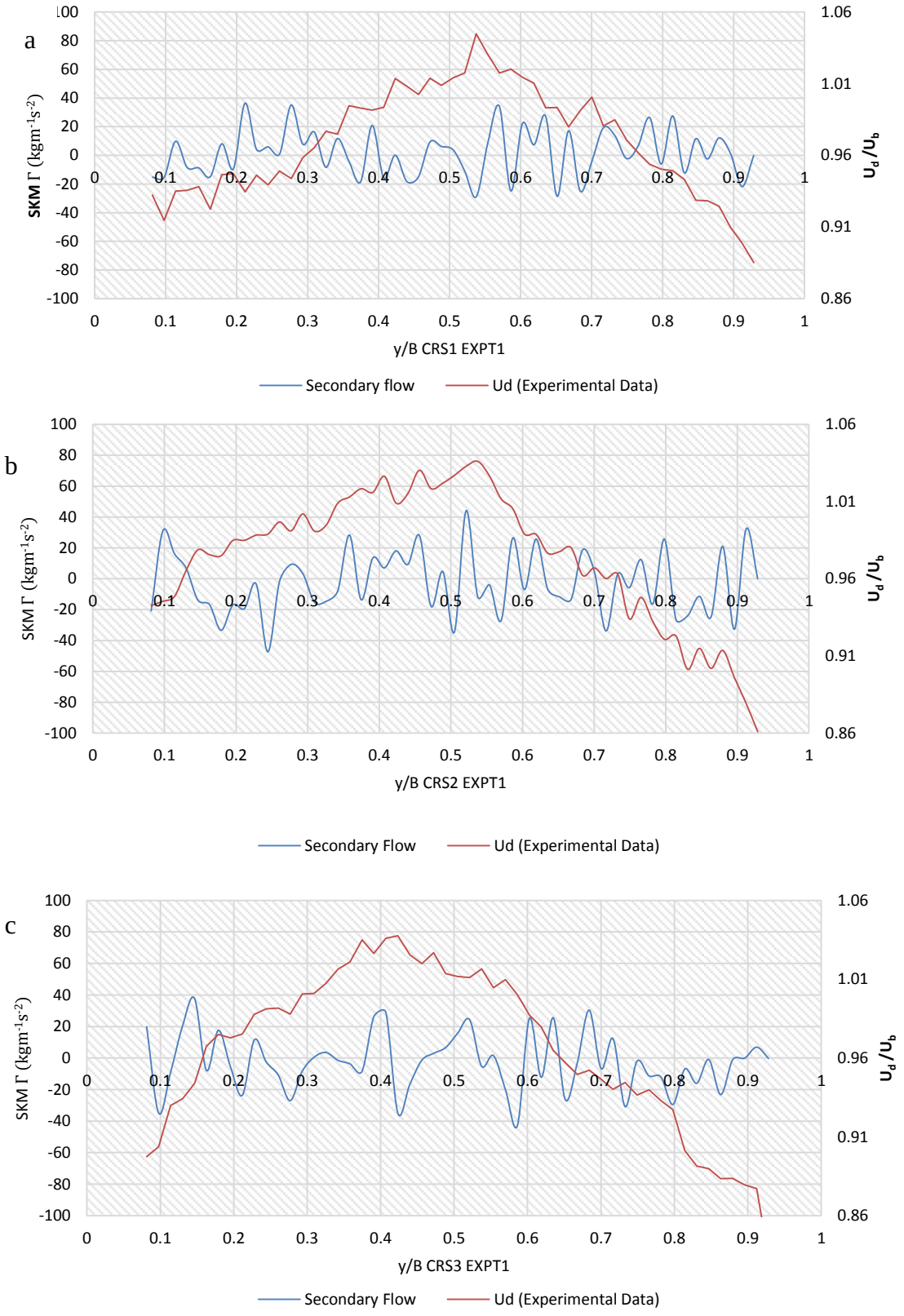

Figure 139: Lateral Distribution of Γ CRS1 (a) to CRS3 (c) EXPT1

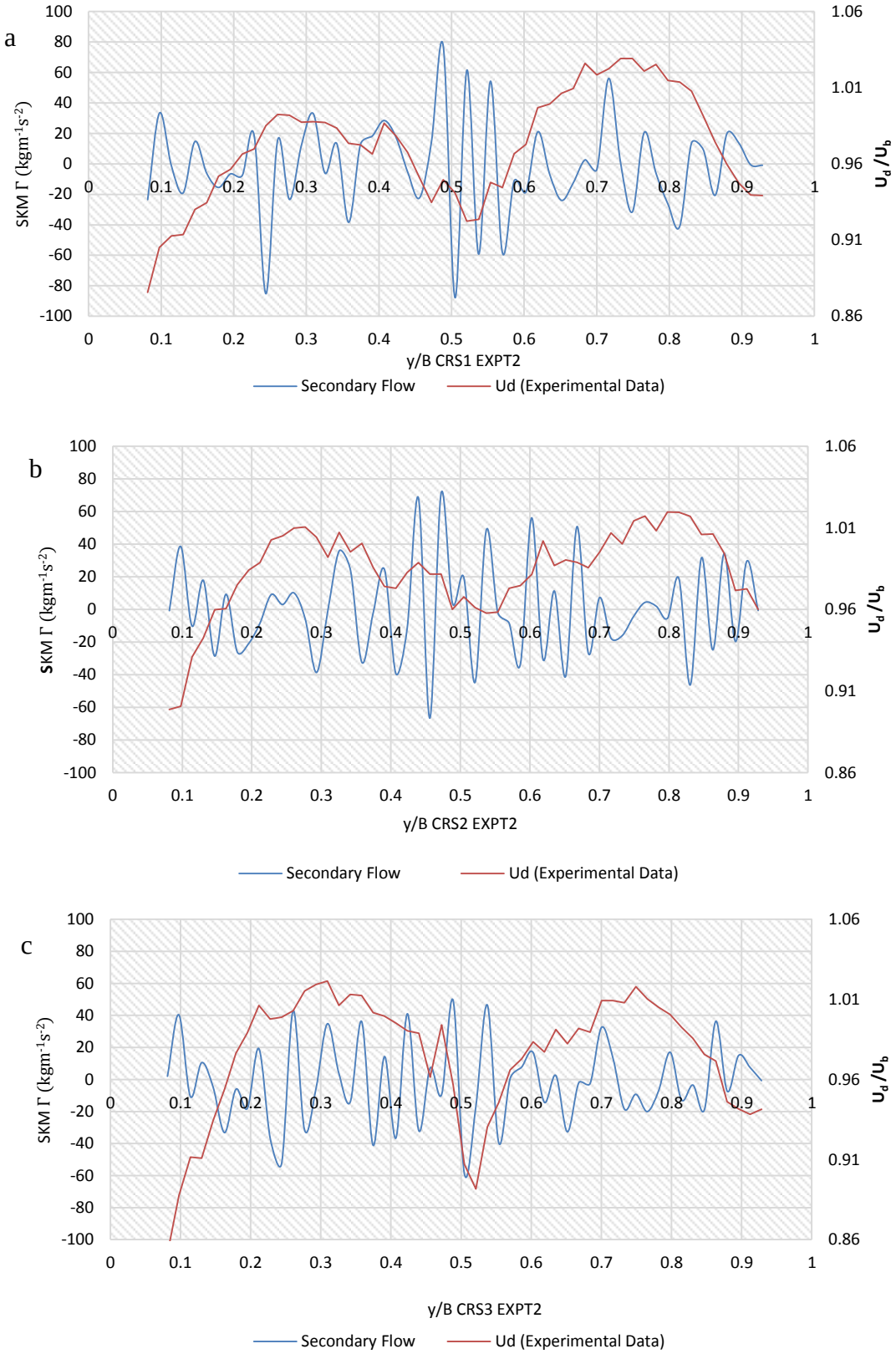

Figure 140: Lateral Distribution of Γ CRS1 (a) to CRS3 (c) EXPT2

Using the same test parameters as adopted for λ sensitivity, Figure 141 illustrates the depth-averaged velocity using the calculated values of Γ from the experimental data with Equation (79). It can be seen from Figure 141 that as the value of Γ increases, the distribution of U_d becomes more unrealistic. The calculated Γ values used in the simulation yielded extremely large values of simulated U_d particularly over the vegetated bed, thereby losing the required modelling accuracy. This can be attributed to the lateral velocity gradient sensitivity to small changes.

However, in order to calculate the secondary flow values for the SKM simulation, recourse was made to the suggestions of Shiono and Knight (1991), Abril (1996) and Abril and Knight (2004) who examined two staged channels. In the main channel and floodplain regions Γ was obtained from the linear approximation to a plot of the force per unit length $H\rho(UV)_d$ and given as:

$$\Gamma = 0.15H\rho gS_0 \tag{87}$$

$$\Gamma = -0.25H\rho gS_0 \tag{88}$$

Although the current situation is a single stage channel, it is postulated that the differential roughness is hydraulically equivalent to that which occurs in the two stage channels of Shiono and Knight (1991). Hence, equation (87) and (88) was used to obtain Γ values over the gravel and vegetated sections respectively. In keeping with the work of others (Gunawan, 2010), the values of Γ were then adjusted until the predicted U_d distribution was improved (discussed more fully in sections 6.2.5 and 6.3) and the discharge obtained from simulation was within 5% of the measured value. However, it is acknowledged that in Figure 141 the distribution is far from ideal and this will be examined further in section 6.3.

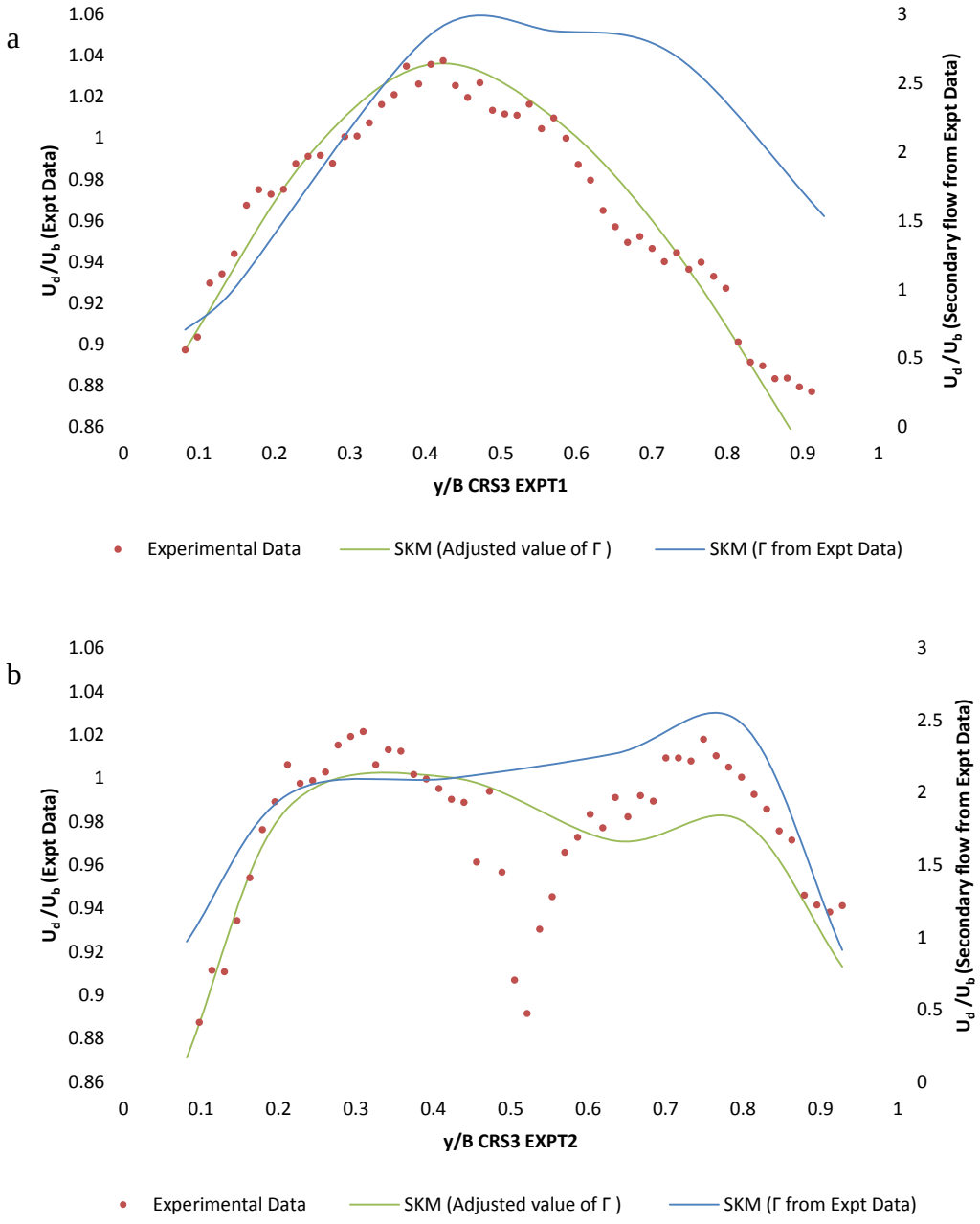

Figure 141: U_d Distribution Using Γ Adjusted Values and Γ from Experiemtal Data, EXPT1 (a) and EXPT2 (b).

6.2.5 Panelling Approach

In keeping with the work of Shiono and Knight, (1991) and Knight et al. (2007), the channel was divided into a number of panels in order to enable simulations to occur. In previous work

(Shiono and Knight, 1991, Knight et al., 2007, Omran and Knight, 2006) the secondary flow term Γ has been used to determine the number of panels required. The number of panels depends on the pattern and rotational direction of the secondary flow cells determined by mean U and V values (Omran and Knight, 2006). Knight et al. (2007) suggested that the sign of the secondary flow values to determine the number of panels required for undertaking SKM simulation. As the streamwise velocity U increases with vertical distance from the channel bed and is always positive, whilst the lateral velocity V a small fraction of U can either be positive when rotation is clockwise and negative when the rotation is counter clockwise indicates that the product term and the depth averaged values of (UV_d) can either be positive or negative depending on the position and the rotational sense of the secondary flow cells (Knight et al., 2007, Tang et al., 2011) (Figure 142).

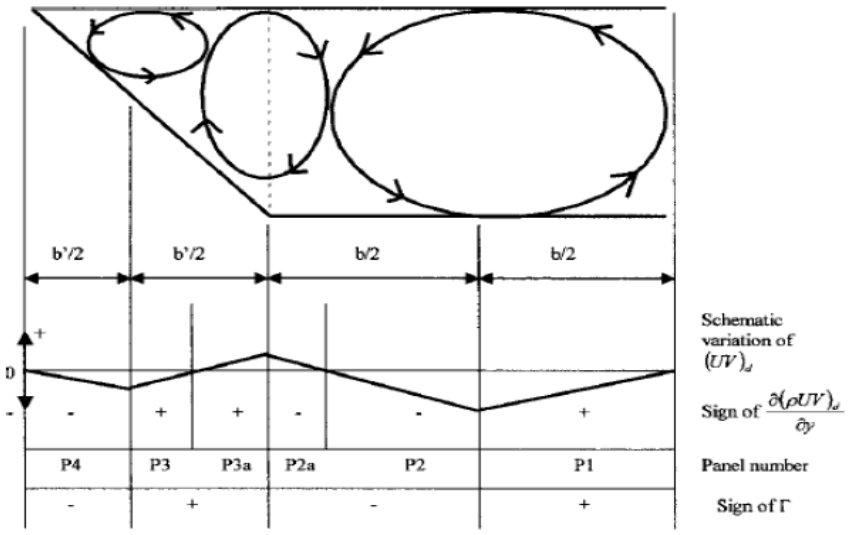

Figure 142: Number of panels and signs of secondary current term (Omran and Knight, 2006, Knight et al., 2007).

The lateral variation of (UV_d) gives the sign of the secondary flow term for a constant depth domain as shown in Figure 142. However, due to the lack of an identifiable secondary flow structure in each cross section (Figures 83 and 84) the exact size, rotation and position of secondary flow cells could not be established in the current work.

In keeping with the previous work (Omran and Knight, 2006, Knight et al., 2007) the number of panels in the current work varied between five and eight (including an additional panel at the roughness boundary region conditioned by the velocity dip in EXPT2) and was cross section dependant. Figures 143 and 144 summarise the number of panels identified for each cross-section. This panel structure follows from an interpretation of the secondary flow fluctuations which in turn depends on the positive and negative values.

a

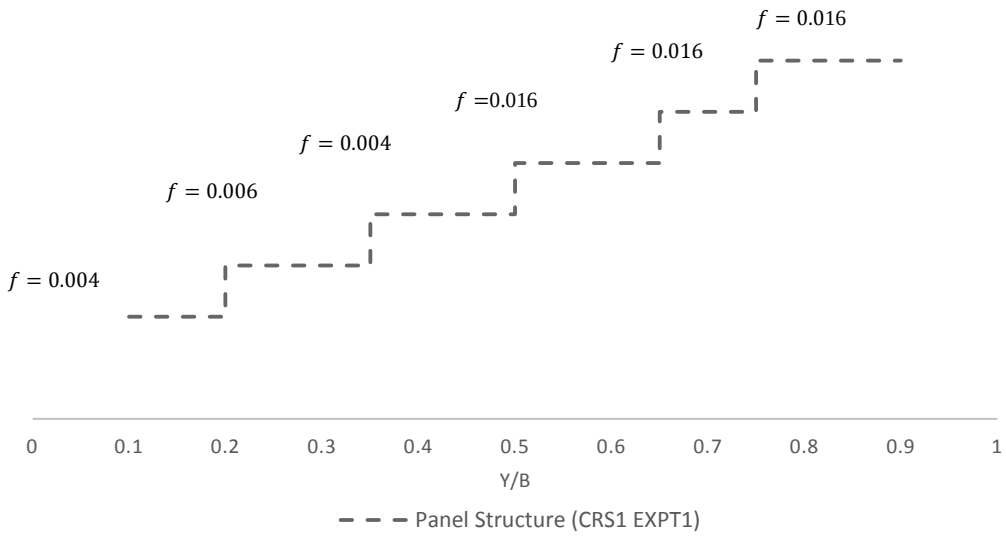

b

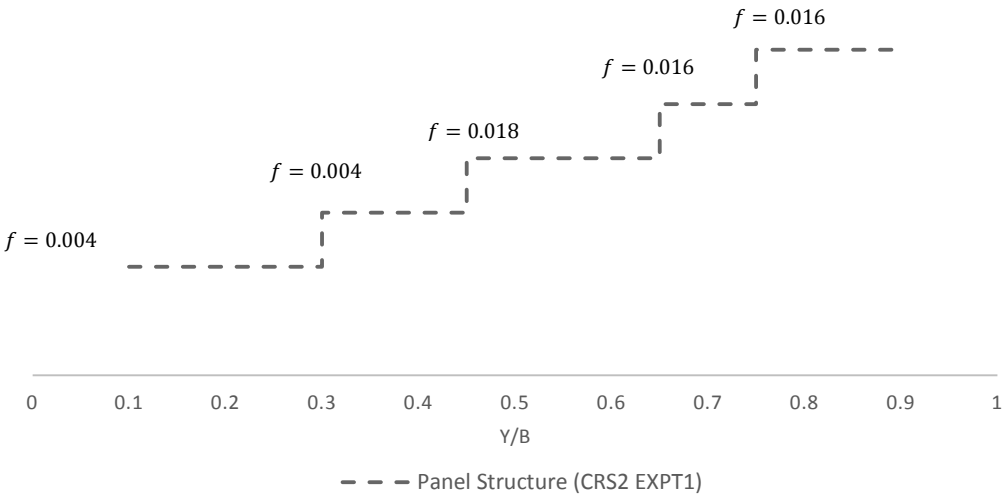

c

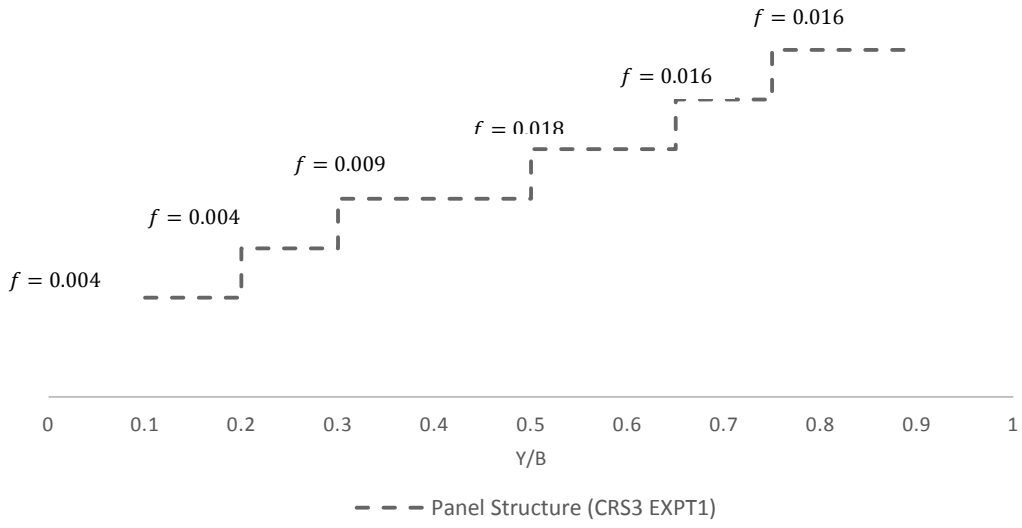

Figure 143: The Panel Boundaries Identified by the Secondary Flow Fluctuation CRS1 (a) to CRS3 (c) (EXPT1)

a

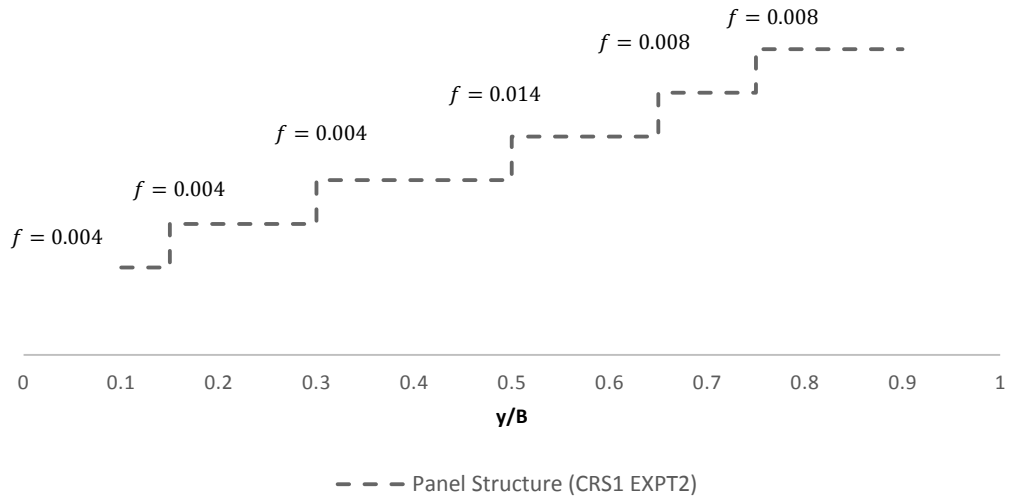

b

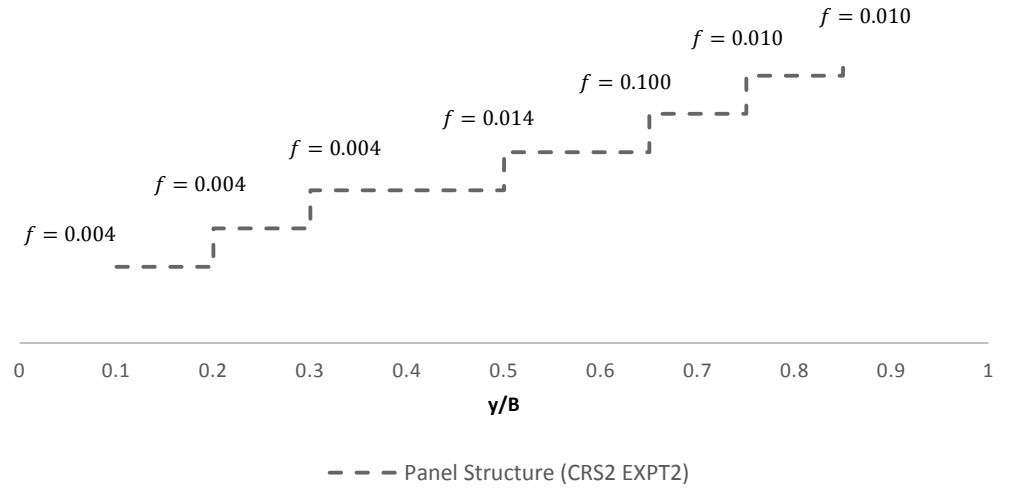

c

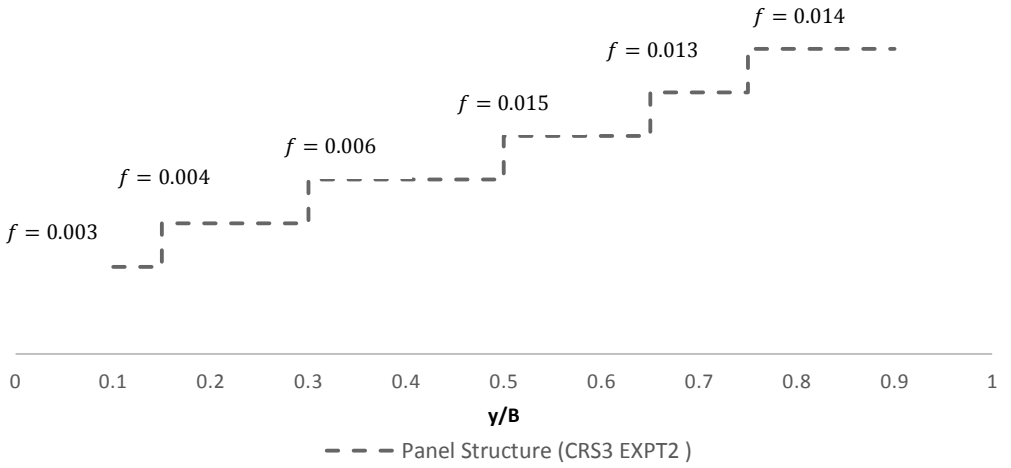

Figure 144: The Panel Boundaries Identified by the Secondary Flow Fluctuation CRS1 (a) to CRS3 (c) (EXPT2)

It can be seen from Figure 145 that the panel boundaries show good agreement with the experimental data, though the slight difference between the simulated results and the experimental data is noted. Initial analysis revealed that introducing panels with constant width for the cross-sections indicate differences within 4% in comparison with the panels based on the secondary fluctuations (Figure 145); however, the modelled depth-averaged velocity distributions for constant width panels demonstrates a slight shift in the position of panel boundaries relative to the panels from secondary flow fluctuations, therefore, the solutions were obtained using the panel structures based on the secondary flow fluctuations. The panel structure interpreted from secondary flow fluctuations (Figure 143 and 144) ranged from five to seven which are cross-section dependant (excluding the panel conditioned by the velocity dip in EXPT2). However, it is clear that the EXPT2 is still not adequately captured; this will be examined further in section 6.3

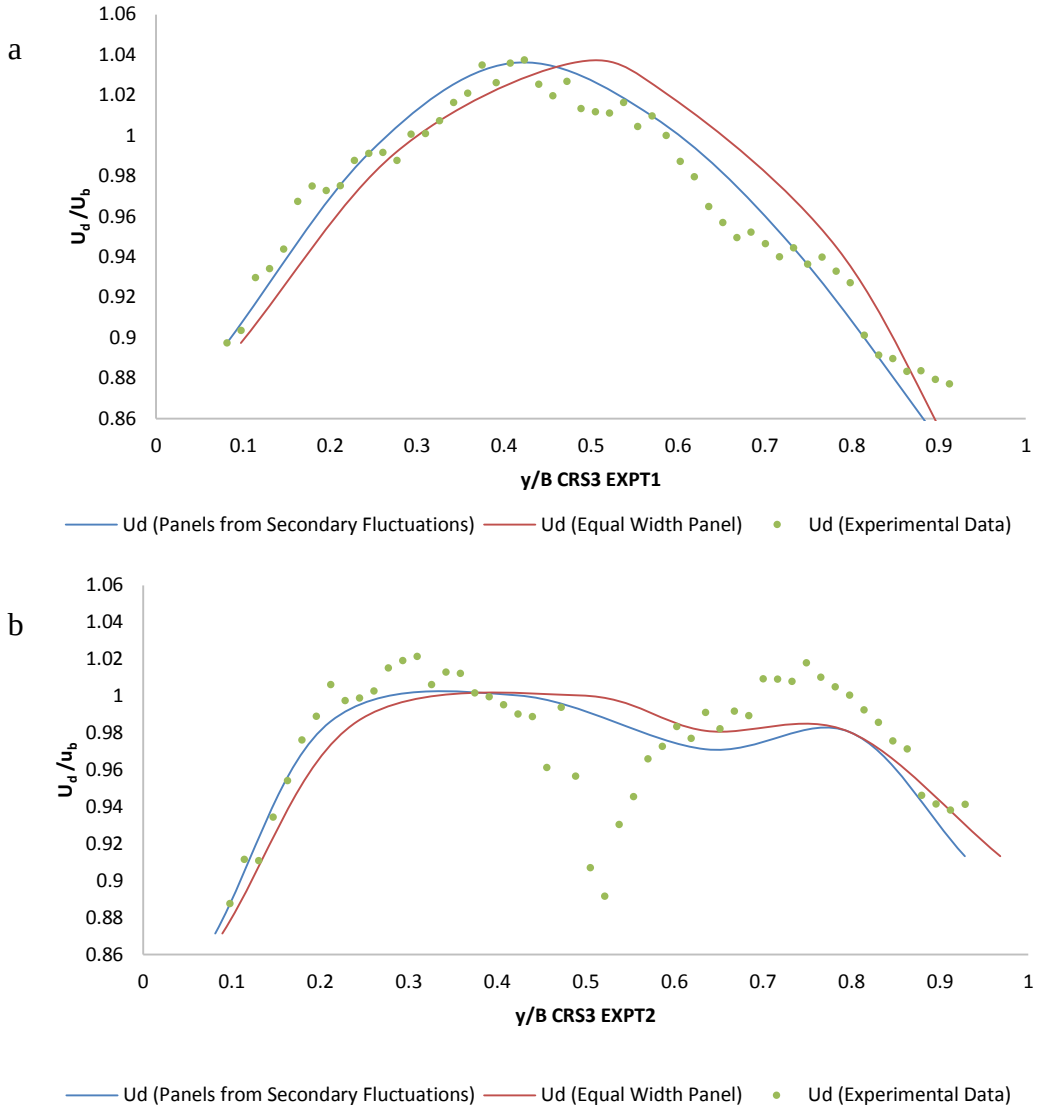

Figure 145: U_d Distribution Using Panel Boundaries from Γ Fluctuation and Equal Width, EXPT1 (a) and EXPT2 (b).

It should be noted that, the number of panels was considered to give a trade-off between accuracy and complexity of the simulation, examination of the number of panels revealed that introducing additional panels to the ones specified by the secondary flow fluctuations (and the panel conditioned by the velocity dip at the boundary region in EXPT2) show negligible improvement.

6.2.6 Friction Factor f

The friction factor f is evaluated using Equation (80) for each panel based on the boundary shear stress value obtained from the experimental data. In previous studies, the friction factor f has often been taken to be constant in each panel (Omran and Knight, 2006, Knight et al., 2007, Tang et al., 2011). Jesson et al. (2013) observed a reduction in f near the rough smooth boundary (RSB) and recommended the location of a panel at the RSB ${}^{y}/_{B} = 0.50$ based on the distribution of the friction factor f, and observed the panel at the roughness boundary ${}^{y}/_{B} = 0.50$ as the only panel position conditioned by the friction factor f distribution.

The calculated friction factor f distributions for each cross section are shown in Figures 146 and 147. It can be seen from the figure that there is a reduction in f over the gravel region $\left(0 \leq {}^{y}/_{B} \leq 0.5\right)$ relative to the vegetated region$\left(0.5 \leq {}^{y}/_{B} \leq 1.0\right)$, with f increasing with distance from the roughness boundary region towards the vegetated region for both EXPT1 and EXPT2. The increase in f is greater over the vegetated region in EXPT1 than in EXPT2 as shown in the figures and Table 14. Critical examination of the figures shows that the f value laterally increases from the gravel region to the vegetated region, then appears to remain relatively constant over each of the bed regions.

In keeping with Knight et al., 2007, it may be appropriate to select an average f value over each panel boundary and vary f linearly within each panel to avoid discontinuity of the shear stress at boundaries and junctions between panels (Omran and Knight, 2006).

The data do not indicate reduction in f near the roughness boundary as reported in (Jesson et al., 2013). In the SKM calibration, the f value was assumed to be constant at the panel boundaries to express the resistance associated with the different panel section of the channel

for accurate prediction of the lateral distributions of the depth-averaged streamwise velocity and the boundary shear stress.

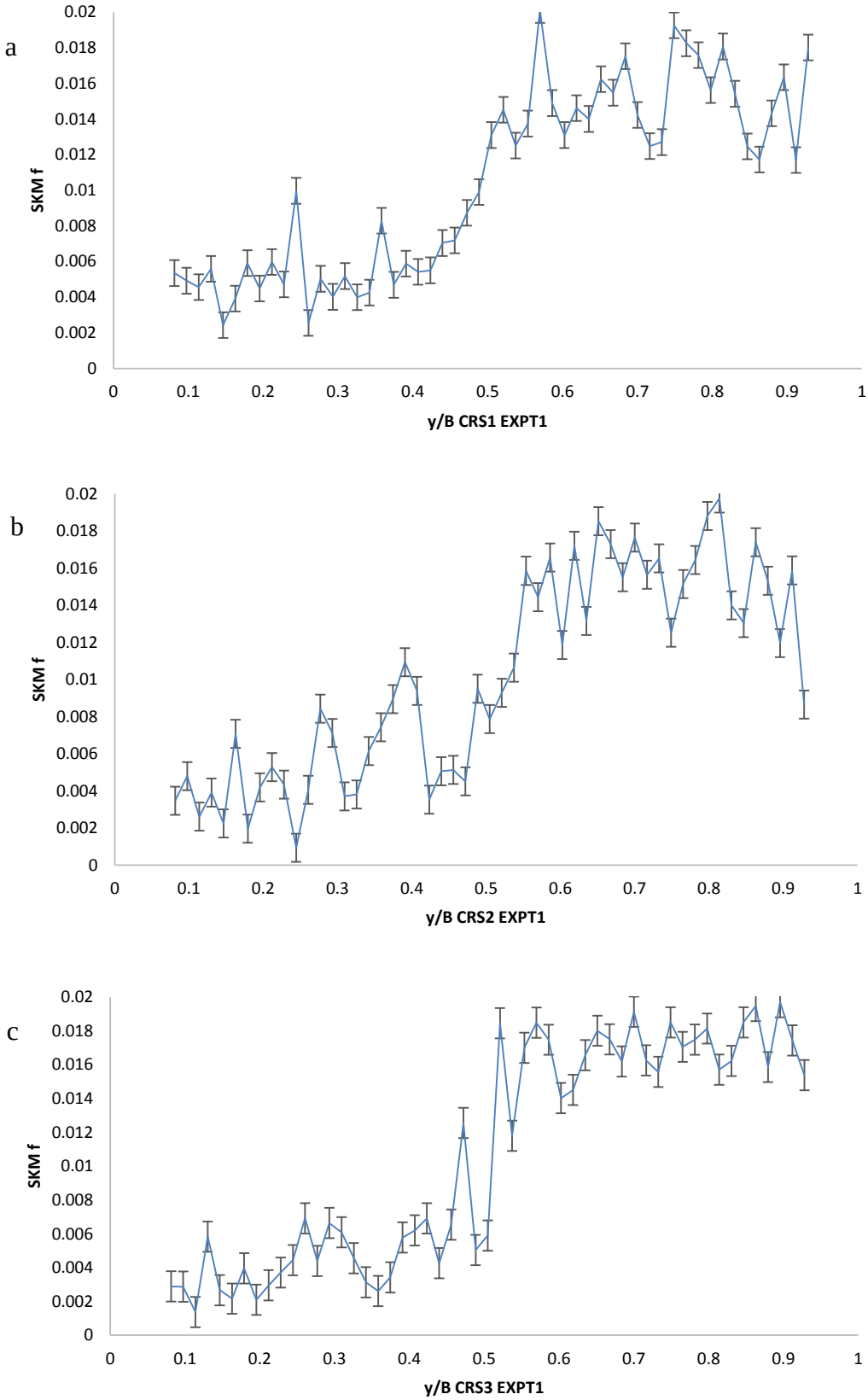

Figure 146: Lateral Distribution of f CRS1 (a) to CRS3 (c) EXPT1

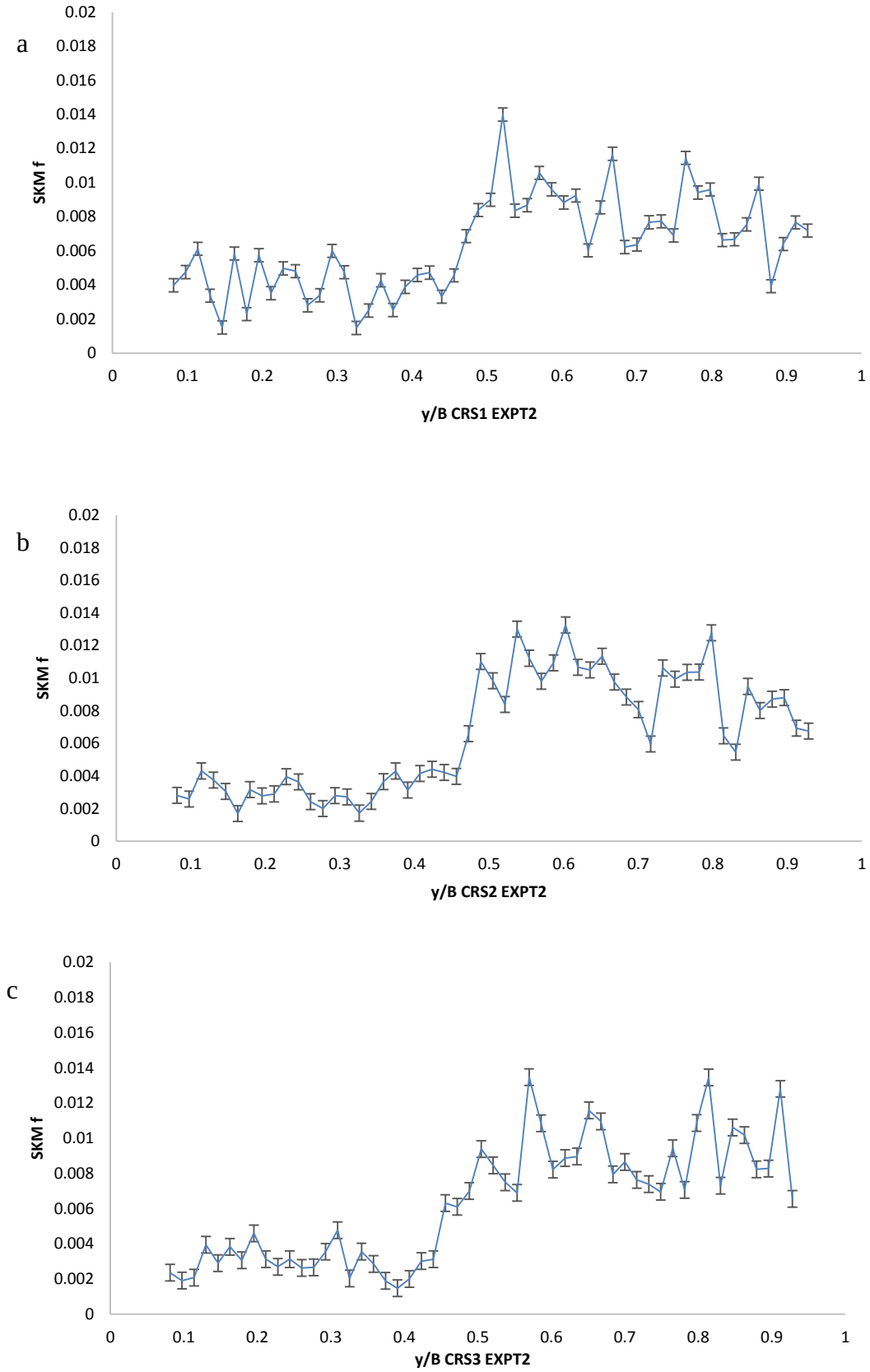

Figure 147: Lateral Distribution of f CRS1 (a) to CRS3 (c) EXPT2

	EXPT1 (CRS3)			EXPT2 (CRS3)		
Panel	f	λ	k	f	λ	k
1	0.0042	0.07	0.58	0.0038	0.07	0.91
2	0.0048	0.07	0.58	0.0042	0.07	0.91
3	0.0085	0.07	0.58	0.0064	0.07	0.70
4	0.0173	0.07	0.51	0.0146	0.07	0.70
5	0.0181	0.07	0.51	0.0139	0.07	0.86
6	0.0186	0.07	0.51	0.0141	0.07	0.86

Table 14: Example of SKM parameter values for CRS3 (EXPT1 and EXPT2) using 6 panels

The effect of constant f between panels on boundary shear stress has been investigated to introduce abrupt changes in the shear stress distribution (Knight et al., 2007). The constant values of f has led to discontinuities in bed shear stress τ_b since changes in friction factor f between panels leads to changes in bed shear stress. Knight et al. (2007) evaluated the linear variation of friction f as a solution to the discontinuities in boundary shear stress by adopting a common f factor value at panel boundaries and varied f linearly within each panel to correspond to these values. This resulted in accurate distribution of the boundary shear stress (Omran and Knight, 2006). In keeping with the work of Omran and Knight, (2006), this method was adopted in the current research to avoid discontinuity at the panel boundaries for shear stress distribution. The method as adopted consisted of computing the average value of f at the boundary between the panels as the average between the individual values of adjacent panels and joining these averaged values by a linear line to determine linear equations representing the lateral variation of the friction factor across the channel (Figure 148). The resulting shear stress distributions are presented in section 6.3.

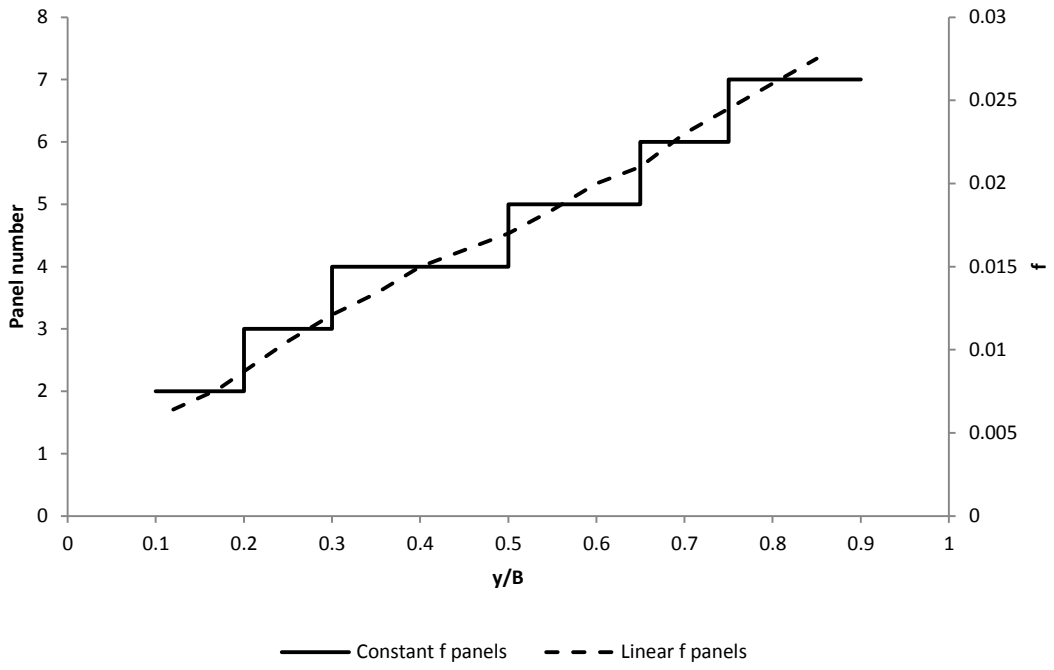

Figure 148: Linear Friction Factor

6.3 Depth-average velocity U_d and boundary shear stress distribution

The results of the numerical model of the depth-averaged streamwise velocity and the experimental data are illustrated in Figure 149 and 150, using the adjusted value of Γ as obtained from Equation (87) and (88), and constant f panel boundaries. For all the cross sections, the results indicate the simulated depth-averaged velocity to be in reasonable degree of consistency with the experimental data. However in EXPT2, the dip in the depth-averaged velocity profile at the boundary region cannot be adequately captured by the model (Figure 150). This is attributed to the constant Γ value across the panel sections and the lateral momentum transfer at this region. As shown in Figure 140 for EXPT2, the value of Γ increases with high magnitude of fluctuation at the roughness boundary region relative to EXPT1 (Figure 139). Given the existence of shear and the scale of lateral momentum transfer and velocity retardation at the boundary region in EXPT2, constant value of Γ may be unable to adequately predict the depth averaged-velocity at this region. However, another approach

was adopted in order to simulate the velocity dip at the roughness boundary region in EXPT2 for optimum U_d distribution. This is examined further in the following paragraph, a sink term (i.e, a drag coefficient) is added at this location with an additional panel introduced and located at the roughness boundary region. This is the only panel position conditioned by the velocity distribution.

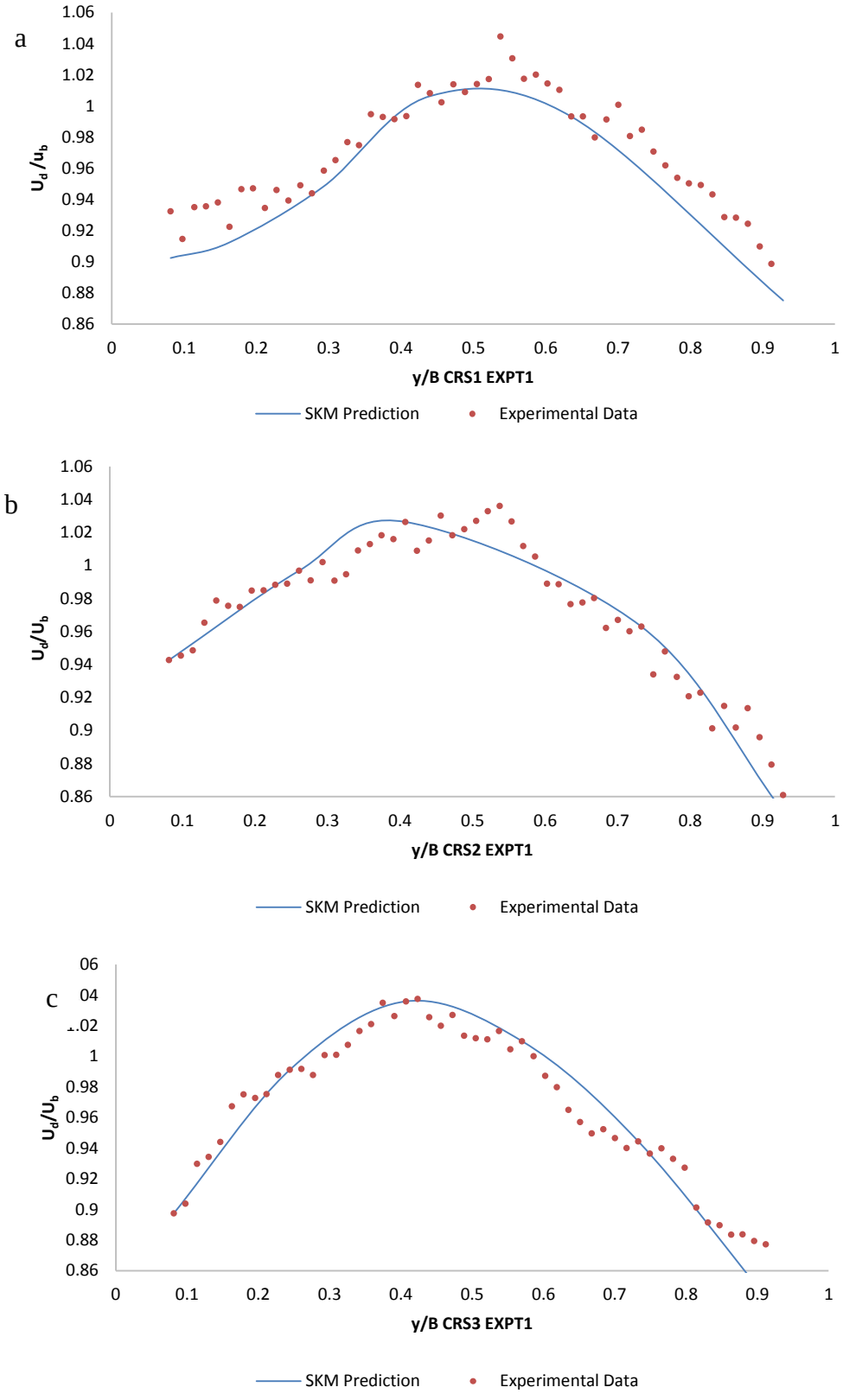

Figure 149: U_d Didtributions CRS1 (a) to CRS3 (c) EXPT1

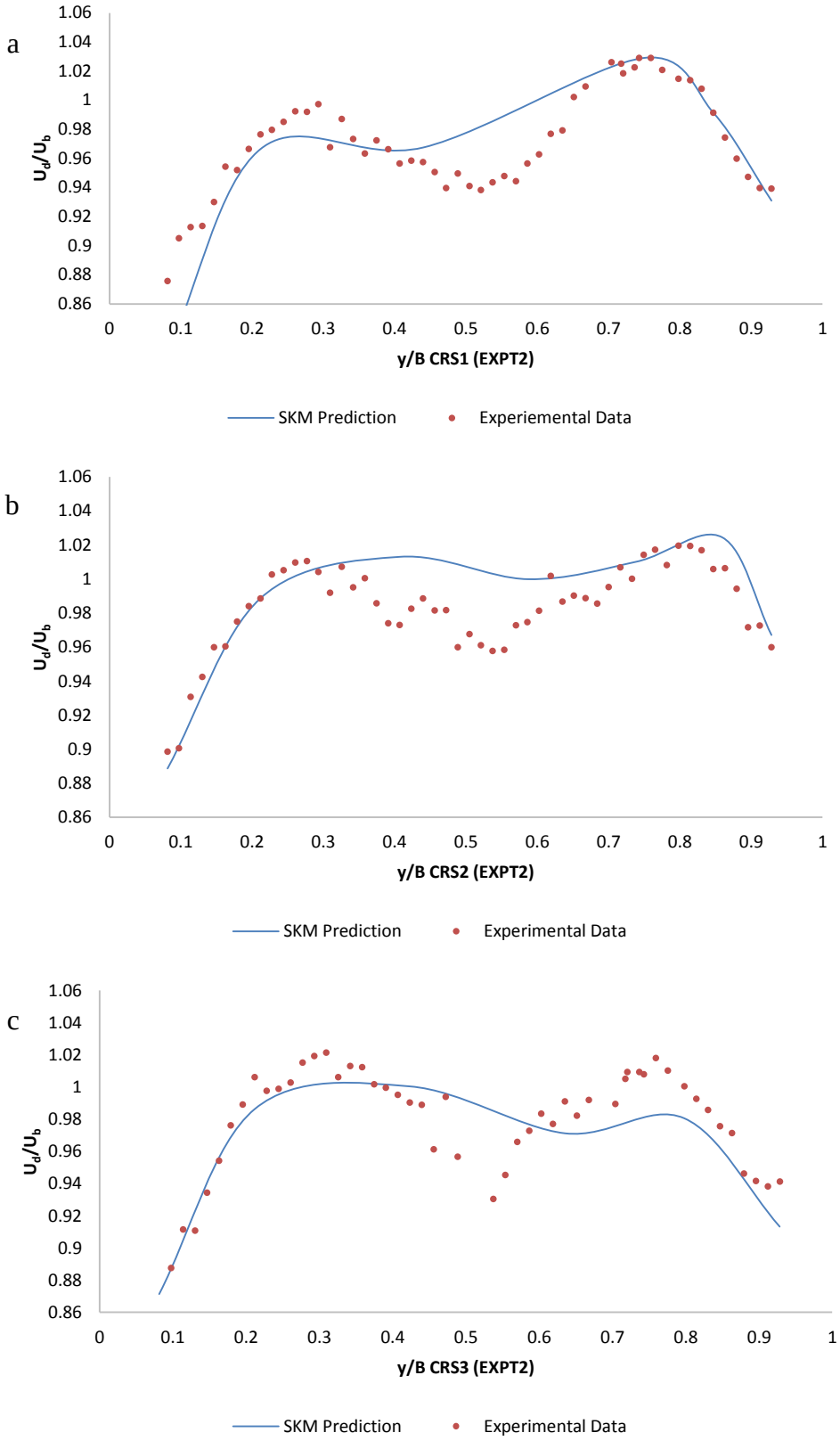

Figure 150: U_d **Distributions CRS1 (a) to CRS3 (c) EXPT2**

In order to address the velocity dip which exists in EXPT2, an additional sink term (i.e., drag force) in the momentum equation in streamwise direction was included:

$$\frac{\partial H(\rho UV)_d}{\partial y} = \rho H g S_o + \frac{\partial H(-\rho\overline{u'v'})_d}{\partial y} - \tau_b \left(1 + \frac{1}{s^2}\right)^{\frac{1}{2}} - F_d \quad (89)$$

where F_d is the drag force per unit fluid per unit volume due to vegetation and in the model expressed as:

$$F_d = \frac{1}{2}\rho C_d a_v H U_d^2 \quad (90)$$

where a_v is the vegetation frontal area per unit volume expressed in Equation (54). The analytical solution to Equation (89) was obtained based on eddy viscosity model and thus becomes (Shiono et al., (2012) :

$$U_d = [A_1 e^{\gamma y} + A_2 e^{-\gamma y} + k_v]^{\frac{1}{2}} \quad (91)$$

where

$$k_v = \frac{g S_0 H}{\left(\frac{f}{8} + \frac{1}{2} C_d a_v H\right)} (1 - \beta) \quad (92)$$

$$\gamma = \left[\frac{\left(\frac{f}{8} + \frac{1}{2} C_d a_v H\right)}{\frac{\lambda}{2}\sqrt{\frac{f}{8}} H^2}\right]^{\frac{1}{2}} \quad (93)$$

β and Γ are as defined in section 2.10.

In order to apply Equation (91) to predict the depth averaged velocity over the vegetated bed, the drag coefficient C_d and the vegetation frontal area per unit volume a_v are required. In keeping with the works of (Nepf and Vivoni, 2000), the average C_d value of 0.15 for submerged vegetation was used to model depth average velocity in EXPT2. Finally, an

additional panel was introduced between $0.5 \leq \frac{y}{B} \leq 0.6$ since the velocity dip is governed by the roughness elements in this region.

Figure 151 demonstrates the improvement in the simulated U_d distribution over Figure 150 using this approach (~91% agreement with the experimental data). With the inclusion of the sink term and introduction of additional panel at the roughness boundary region, the localised velocity dip at this region was adequately captured. The root mean square difference of the simulated U_d is within 6% of the experimental data for both EXPT1 and EXPT2 respectively.

Generally the result demonstrates the sensitivity of SKM to lateral momentum transfer with the simple approach appearing to work for EXPT1 with less lateral momentum transfer at the boundary region (Figure 103). Whilst in EXPT2, the momentum transfer at the roughness boundary region requires additional momentum sink term (drag coefficient) to simulate the velocity dip at the boundary region due to efficient lateral momentum transfer at this region.

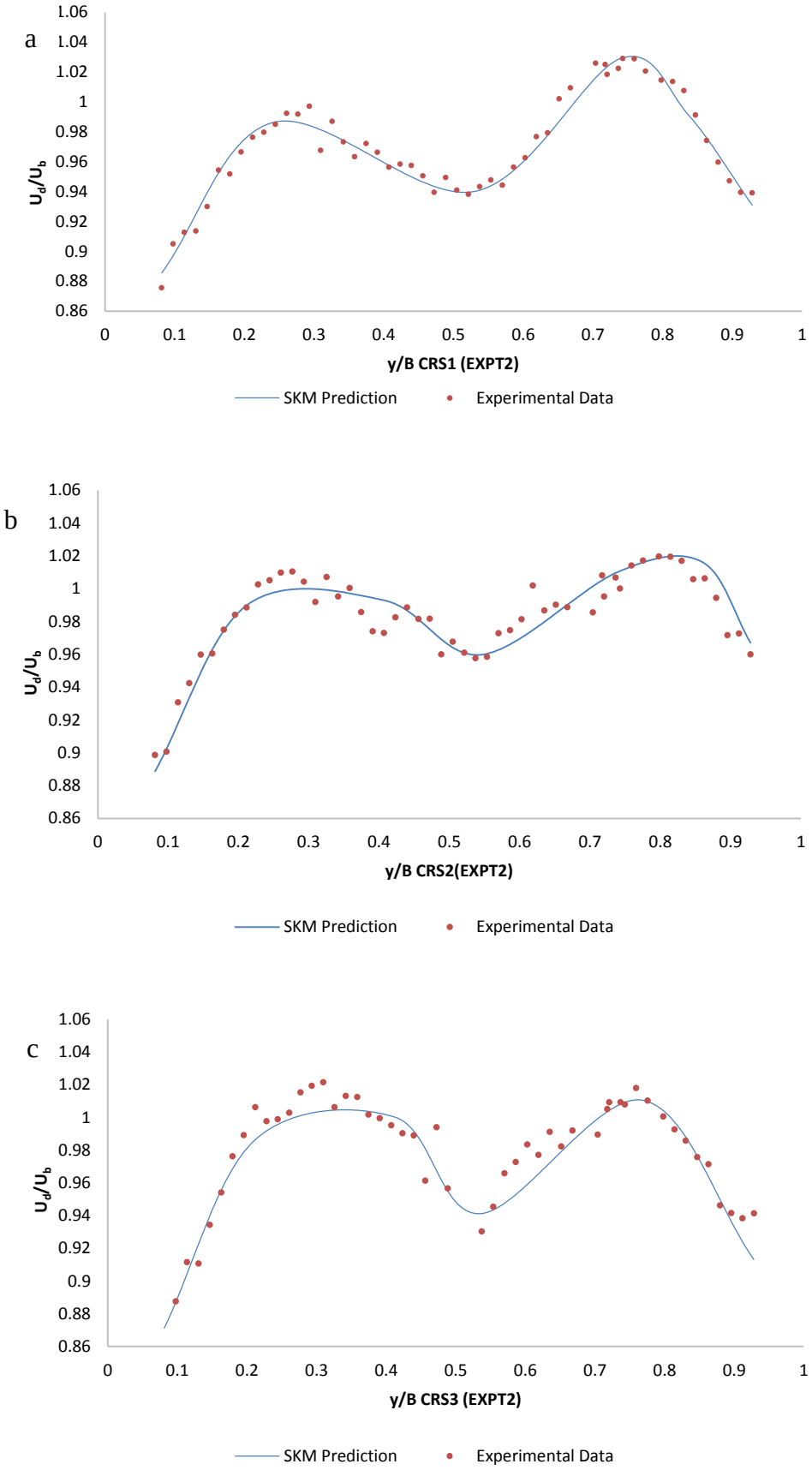

Figure 151: U_d Distributions CRS1 (a) to CRS3 (b) EXPT2

6.3.1 Boundary Shear Stress Distribution

The shear stress was modelled based on the linear variation of the friction factor f (Knight et al., 2007) as illustrated in Figure 148 for linear f panels. The numerical results of the bed shear stress distribution with the experimental data are shown in Figure 152 and 153. The figures illustrate approximately 85% agreement between the predicted and experimental results. Thus, a simple linear variation of f based on the constant values for each panel boundary was able to simulate and predict the boundary shear stress. Table 14 illustrates examples of the numerical value of the SKM parameters adopted in the current research for CRS3.

From the results, the boundary shear stress is slightly under-predicted over the vegetated bed in EXPT1. This can be attributed to the constant value of Γ applied between panels which may not adequately simulate the upflow activities over the vegetated bed in EXPT1. However, it should be appreciated that the experimental data over the roughness surface is far from robust.

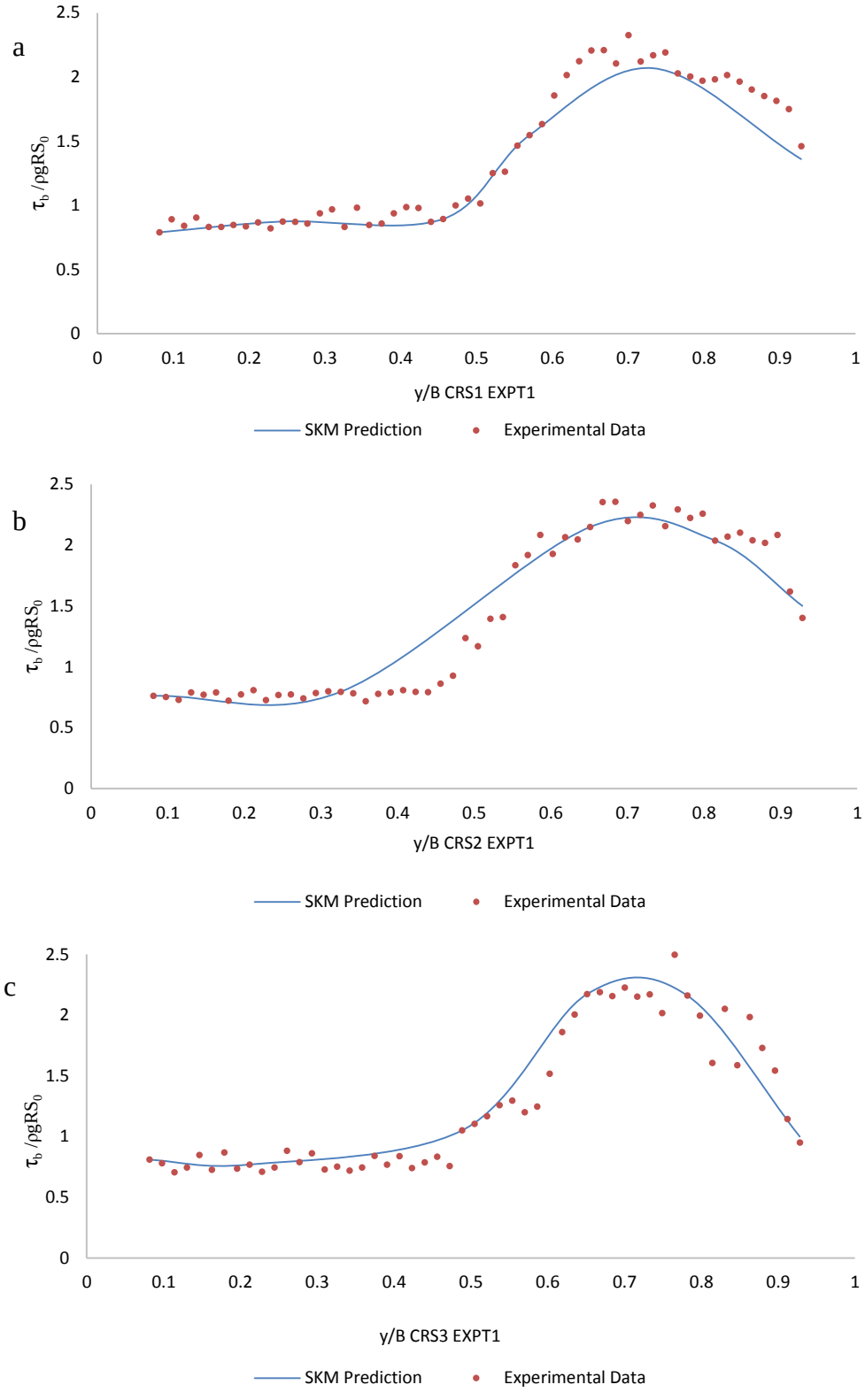

Figure 152: Boundary Shear Stress Didtributions CRS1 (a) to CRS3 (b) EXPT1

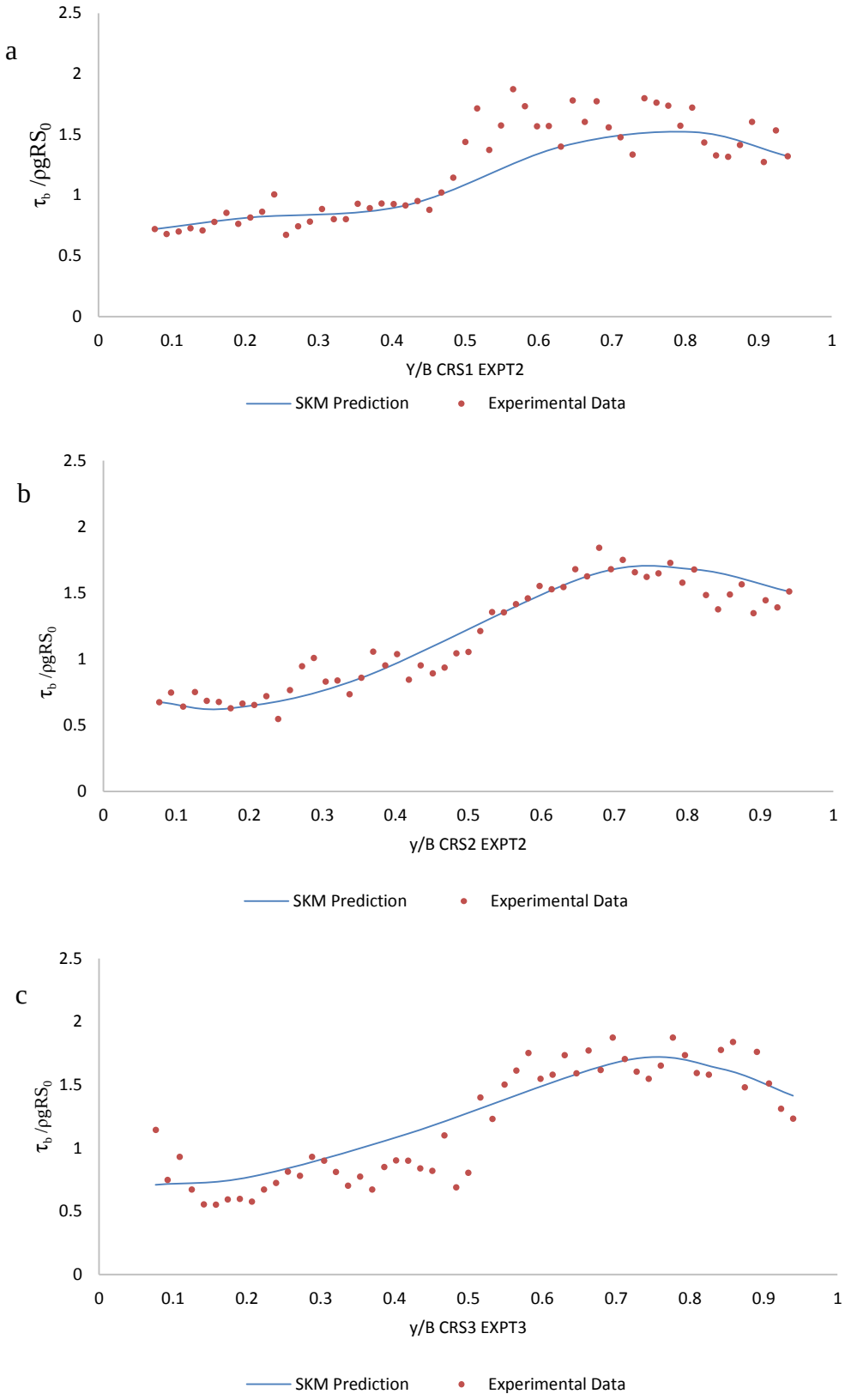

Figure 153: Boundary Shear Stress Didtributions CRS1 (a) to CRS3 (c) EXPT2

Figure 154 compares the SKM calculated discharge with the measured discharge. It should be noted that there is a small discrepancy between the measured and predicted discharge. Relative to the measured discharge, the SKM slightly under predicted the discharged (maximum difference of 3% and 5% for both EXPT1 and EXPT2 respectively). Generally, the differences are similar across the channel sections for both EXPT1 and EXPT2. Figure 154 further confirms that the SKM can be simulated using the standard value 0.07 for λ.

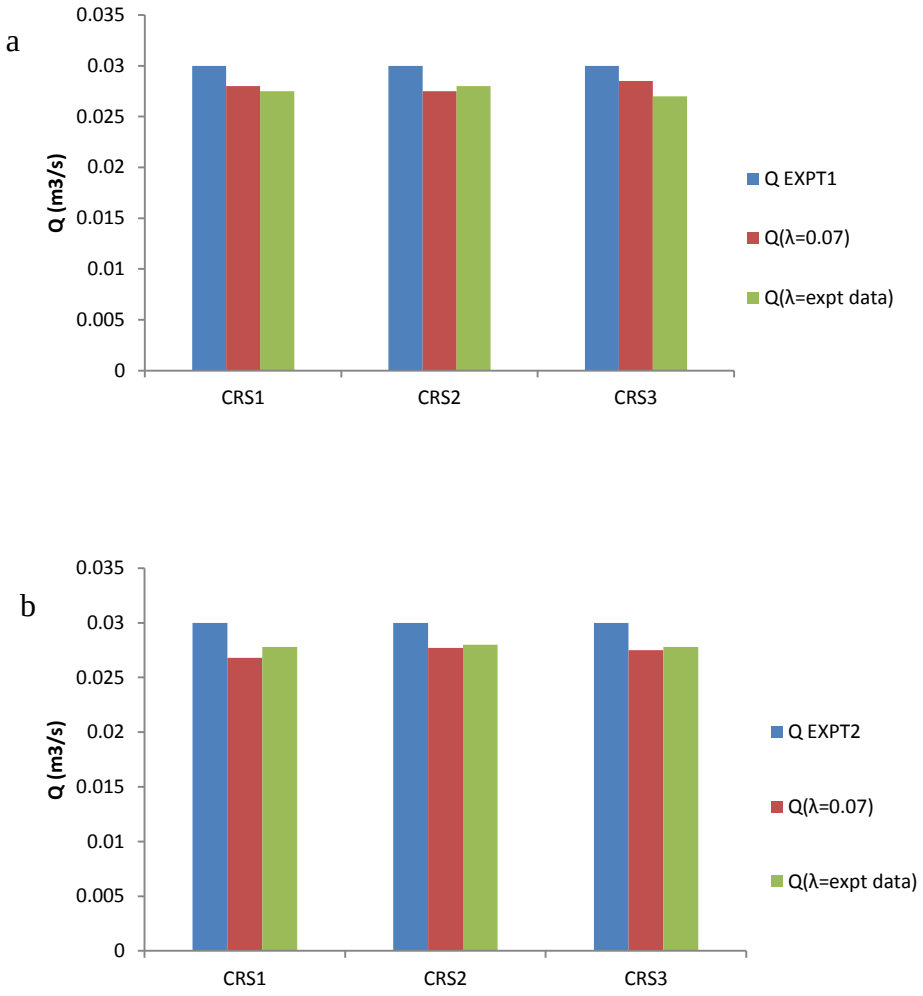

Figure 154: Experimental and Modelled Discharge by Cross-sections

7 Discussions, Conclusions and Recommendations for Future Work

7.1 Discussion

The overall aim of the research was to evaluate how the dynamics of the flow field change when heterogeneous roughness involving vegetation is present. In order to achieve this aim both the mean and turbulence structure in a patchy vegetated open channel has been examined. Specifically, the research had six objectives:

i. *To investigate the influence that rigid vegetation (akin to 'shrubs') and flexible vegetation (akin to 'grass') have on turbulence generation within an idealised open channel with a patchy roughness distribution.*
ii. *To evaluate the channel's resistance through calculation of traditional resistance parameters (e.g. Manning's roughness coefficient n and Darcy-Weisbach friction factor f in order to assess the conveyance capacity of the channel).*
iii. *Detailed high frequency 3-dimensional velocity measurement over three cross-sections of the channel using the Acoustic Doppler Velocimetry (ADV) in order to understand the mean and turbulence characteristics of the flow properties.*
iv. *To determine the variability of momentum transport and mechanisms responsible due to changes in roughness characteristics*.
v. *To map the flow field with Particle Image Velocimetry (PIV) to determine the 2-dimensional spatial correlations of the flow variables*.
vi. *To investigate the applicability of a numerical model (SKM) to reproduce the depth-averaged streamwise velocity and the boundary shear stress.*

The current research demonstrated that vegetation in EXPT1 are dominated by vertical shear which supresses the lateral shear at the boundary region $\left({}^{y}/_{B} = 0.50\right)$ (Figure 103) thereby balancing the depth-averaged momentum equation. This is in contrast to other work (Jesson et

al., 2013) who found the lateral shear to be the most dominant. In addition, the current research demonstrates the impact of roughness distribution on turbulence generation, i.e. the flexible vegetation resulted in more vorticity (due to shear) which had an impact on the hydraulic resistance. This in part is related to two-layer flow which arose in the flexible vegetation and the corresponding vertical shear induced therein (see Figure 79). In addition, there exists evidence of velocity difference at the roughness boundary region $^{y}/_{B} = 0.50$ between the gravel and vegetated bed (Figure 80) resulting in lateral shear.

As identified in the current work, the contributing mechanisms controlling the momentum exchange between the gravel and vegetated bed roughness includes the secondary flow driven by turbulence anisotropy, which aids the turbulent transport in the lateral direction by transferring momentum from the decelerating flow over the vegetated bed relative to the accelerating flow over the gravel bed (Figure 83) in EXPT1. The secondary flow indicates that at the lower portion ($z/H \leq 0.3$) of the flow, the transverse motion is directed from the gravel bed to the vegetated bed, transporting the high velocity flow from gravel bed towards grass vegetated bed (Figure 83), while at the upper portion, the low velocity occurring over the flexible vegetated bed moves up and transported laterally in the opposite direction. In EXPT2, the secondary flow over the gravel, vegetated and boundary regions maximized the momentum transfer between the bed regions (Figure 84). Another mechanism involves vertical and horizontal Reynolds stresses due to shear formation which actively transport momentum in vertical and horizontal directions respectively. From the results, it is observed that the vertical shear induced by the vegetation elements dominated the flow in EXPT1 by vertical momentum transport over the vegetated bed (Figure 103). It is also observed that the vegetation stems created some localized lateral Reynolds stress over the vegetated bed (Figures 101 and 102) attributed to stem vertical orientation which generates some small scale non-isotropic wakes and eddies over the vegetated bed. However, a reduction in lateral

Reynolds stress at the roughness boundary region is observed in EXPT1 relative to EXPT2 (Figure 103).

In contrast to a gravel bed where the velocity shear and turbulence is dominated by the bed surface roughness effects, the primary source of velocity shear over the vegetated bed is the interaction between the vegetated zone and the free zone at the top of vegetation which created a free shear layer over the vegetated bed. The higher vegetation density in EXPT1 does increase the vertical velocity shear over vegetated bed, while in EXPT2; the vertical shear is reduced relative to EXPT1 due to sparse distribution of vegetation elements (Figures 103 and 104). It should be noted that, the velocity inflection point which governs the shear layer formation over the vegetated bed only exists for vegetation with $C_d a_v h_v > 0.1$ (Ghisalberti and Nepf, 2006, Ghisalberti and Nepf, 2004), where C_d represent the drag coefficient, a_v represent stem patch-scale density and h_v is the stem height. This condition is satisfied by the vegetated bed (EXPT1) in the current research with $C_d a_v h_v > 0.1$.

The maximum shear value as indicated by the maximum Reynolds shear stress is located over the vegetated bed in EXPT1 (Figure 99). This suggests that the turbulence generated by shear layer in dense flexible vegetated bed in EXPT1 do not penetrate below the vegetation surface due to stem density (Figure 99). In this case the vertical momentum transport is comparably higher $(\approx 65\%)$ over vegetated bed. In EXPT2, the relatively sparse vegetation reduces the turbulence due to shear between vegetated and free flow layer (Raupach et al., 1996) (Figure 100). In this case vertical momentum transport is comparably low (Nepf and Vivoni, 2000). Relative to EXPT2, the flexible vegetation in EXPT1 reduces the lateral shear at the roughness boundary region $\left({}^{y}/_{B} = 0.50\right)$ (Figures 103 and 104) suggesting a less significant source of momentum transport at the roughness boundary region in contrast to Jesson et al. (2013) with smooth and gravel roughness.

7.2 Conclusions

Based on the measurements, the main findings of the research are highlighted as follows to satisfy the objectives defined in section 7.1.

7.2.1 Objective (i)

1) In addition to the general discussion above, it can be seen from Figures 70 and 71 that, the scale and shape of the pdf distribution of the streamwise turbulent velocities varies laterally within the channel. This highlights the variation in casual mechanism pertaining to velocity fluctuations.
2) In EXPT1, the flow deceleration of the streamwise velocity component due to flexible vegetation produces an asymmetric velocity fluctuation over the vegetated bed (Figure 70c), this is attributted to a more distortion of large scale structures due to stem density and oscillations which becomes more asymmetric and in turn manifested in the actual velocity fluctuations.
3) The large (negative) values of skewness over the flexible vegetated region ($^{y}/_{B} = 0.73$) in EXPT1 and roughness boundary region ($^{y}/_{B} = 0.50$) in EXPT2 (Table 6) suggests that the velocity fluctuation in these regions do not follow Gaussian distribution and has long negative tails, these regions of high negative skews are assumed to be the shear regions for the flow.

7.2.2 Objective (ii)

4) The variation of the Manning's roughness coefficient indicates a non-uniform distribution with respect to flow depth, i.e., the maximum value occurs near bed and decreases as the water surface is approached. In addition, based on the standard (absolute) n value for vegetation roughness, it can be postulated from the results that the gravel roughness interaction reduces the absolute resistance effect of the vegetation

roughness on the flow with maximum n values 0.030 and 0.025 (Figure 50) for the flow.

7.2.3 Objective (iii)

5) Given the short length and density of the vegetation elements which may have reduced its flexibility in EXPT1, the oscillating nature of grass stem however generate some significant differences between the flexible and rigid patchy roughness, in particular the distribution of the depth averaged streamwise velocity in which the flexible vegetation appears to decelerate the flow and the rigid vegetation accelerate the flow (Figures 77c and 78c). The oscillating stem are assumed to be moving against the flow and absorbed more mean energy relative to rigid stem, consequently, the distribution shows different regions of maximum velocity for each of the experiments.
6) However, the flow resistance at the roughness boundary is seen to be apparent in rigid patchy roughness with a velocity dip at the boundary region when compared with the case of flexible vegetation (Figure 81).
7) In keeping with the previous work (Jesson et al., 2012), the lateral interaction is achieved by the secondary flow, at the lower region $\left({}^{z}/_{H} \leq 0.2\right)$ of the flow, the transverse motion is directed from the gravel bed towards the grass bed, and at the upper region $\left({}^{z}/_{H} > 0.2\right)$, the flow is transported laterally in the opposite direction in EXPT1 (Figures 83). The secondary vector in EXPT2 suggests the appearance of developing cells circulating in clockwise direction as illustrated in Figure 84. In addition, the upward flow over the vegetated bed in EXPT1 can be attributed to the flow retardation and pressure around the vegetation stems due to high stem density (Figure 83).

8) The vegetated bed controls the flow structure supplied to the gravel bed in flexible patchy roughness with the turbulence transport sourced from the shear layer developed over the vegetated bed due to increased turbulence intensities (Figure 91c).
9) The magnitude of the flow structures change over the gravel bed with the turbulence intensities becoming smaller relative to vegetated bed. In particular, the vertical velocity fluctuation increases towards the vegetated bed in EXPT1 and decreases over the gravel bed (Figure 91a and 91c).

7.2.4 Objective (iv)

10) In EXPT1, the presence of vegetation promotes vertical shear and the resulting dominance of vertical momentum transport as illustrated in Figure 103, hence turbulence is enhanced in the vertical direction in EXPT1 over the vegetated bed with an increased near bed value of vertical fluctuation. Applying a force balance to the depth averaged momentum equation; the dominance of vertical momentum transport over the vegetated bed is shown to suppress the lateral momentum transport at the roughness interface $\left({}^{y}/_{B} = 0.5\right)$ as shown in Figure 103.
11) In EXPT2, the distribution and spacing of the vegetation elements created less a dense flow domain within the vegetation which reduced the vertical shear over the vegetated bed relative to EXPT1 (Figure 104). A relatively local maximum of turbulence intensities is associated with the boundary region in EXPT2 (Figure 92b), this is assumed to enhance the lateral momentum transfer at the roughness interface region similar to Jesson et al. (2013) as illustrated in Figure 104. However, in general the magnitude of turbulence intensity appears to be a maximum in different regions in EXPT1 and EXPT2. This indicates that the roughness distribution has an enhanced impact on turbulence generation compared to the magnitude of the surface roughness.

12) The general trend in the integral length scale is an increase in depth with large variations around this trend, however, the large variation indicates vortex stretching and the corresponding interaction thereof with other eddies (Figures 116 and 117).

13) It can be seen from the integral length scale that eddies generated near bed are smaller over the vegetated bed in EXPT1 relative to EXPT2 (Figures 116 and 117). This may initially suggest that the sizes of vegetation stems are likely to play a large part in the sizes of eddy formation, hence generating eddies with a length scale similar to the size of the vegetation stems. However, it is possible to deduce that the eddy generated encounters the size of the roughness elements creating them. Hence, higher time scale over the gravel bed suggests longer turbulence connection relative to the vegetated bed.

14) The vertical shear over the vegetated bed in EXPT1 is presumed to increase the concentration of vorticity (due to shear) in these small eddies, thereby generating turbulence whose energy is dissipated rapidly due to the smaller size of eddies over the vegetated bed (Figure 116). Over the gravel bed, larger eddies generated contributes to the high velocity downflow as illustrated in Figure 83, while the smaller eddies over vegetated bed are dominated by the burst like upward fluid motions (Figure 83).

15) Quadrant hole analysis was used to examine the propagation of turbulence through the flow. Relative to EXPT1, the peak values of ejection motions (QRS_2) in EXPT2 are somewhat reduced; this supports the observation of smaller vertical momentum exchange in EXPT2 compared to EXPT1.

16) Figures 105 - 107 demonstrate relatively equal magnitude of quadrant events at the roughness boundary region in EXPT1, this provides an evidence of similar occurence of momentun transport at the roughness boundary region $({}^{y}/_{B} = 0.50)$ with both ejection and sweep demonstrating similar magnitude of events. This implies that much of the momentum flux is less transported at this region relative to vegetated region

$(0.5 \leq y//B \leq 1.0)$ where ejection dominates and have greatest contribution to the Reynolds shear stress.

17) As shown in Figure 112 and 113, the velocity shear and turbulence resulting from the boundary effect over the gravel bed are dominated by the vegetation generated turbulence.

7.2.5 Objective (v)

18) In agreement with the ADV measurements in EXPT2, the streamwise velocities are generally lower at the boundary region $\left({}^{y}/_{B} = 0.50\right)$ indicating a region of lateral momentum transfer as confirmed by the PIV measurement (Figure 129).

19) The velocity vector plots for both xy and xz plane demonstrate a well-defined mean velocity streamlines entirely in streamwise direction at the upper region of the flow (Figure 135). The flow is seen to be turbulent near bed with the presence of structure such as burst type mechanism (large velocity fluctuation) appearing at the lower region of the channel and grow larger farther downstream the streamwise FOV.

20) The turbulence properties of the flow as measured by PIV confirm the potentials of boundary region as the primary source of turbulence to the flow in EXPT2.

21) Generally, the research demonstrates that relative to turbulence distribution, the vegetated bed exerts a major influence on the flow.

22) From the results, local regions of efficient moment transport can be predicted in natural rivers with similar patches of roughness.

7.2.6 Objective (vi)

23) Figures 149 and 150 indicate that the SKM is capable of predicting the distribution of the depth-averaged streamwise velocity in a patchy vegetated channel using (for example) the calibration values presented in Table 14 for CRS3. The lateral distribution of depth averaged velocity for EXP1 was predicted reasonably well with

an overall agreement of 91%. However, in EXPT2 the simulations failed to predict the velocity dip at the boundary region and which impacted on the overall lateral distribution. This is attributed to the lateral momentum transfer at the boundary region, hence velocity dip due to retardation and the lack of a sink term. However, Figure 151 demonstrates an improvement in the simulated U_d distribution over Figure 150 with approximately 91% agreement with the experimental data. With the inclusion of the sink term (F_d) and introduction of additional panel at the roughness boundary region, the localised velocity dip at this region was adequately captured by the numerical model as illustrated in Figure 151. The root mean square difference of the simulated U_d is within 6% of the experimental data for both EXPT1 and EXPT2 respectively.

24) The boundary shear stress distribution was approximately 85% predicted by the model with a slight shift of the peak distribution over the vegetated bed in EXPT2 (Figure 152 and 153).

25) The initial Γ values for the gravel and vegetated region calculated from Equations (87) and (88) respectively are considerably lower than those calculated from the experimental data using Equation (79).

26) The pattern of the secondary flow term Γ is found to have positive and negative fluctuations (Figures 139 and 140). This change in the sign of Γ can be interpreted as a change in the rotating direction of secondary flow cells. The maximum fluctuating magnitude of secondary flow is observed at the roughness boundary region in EXPT2. The lateral variation of Γ over the gravel bed is similar to that of the vegetated bed in EXPT1. Generally, higher values of Γ are found for the panels in EXPT2, this indicates higher levels of secondary circulation in EXPT2 relative to EXPT1. This is consistent with the findings obtained from the experimental data in section 4.4

27) The average magnitude value obtained for λ ranged between 0.065 and 0.089. These values are close to the standard value 0.07 found in the literature. Varying this value did not significantly improve the simulations.

28) The lateral variation of the friction factor f for both EXPT1 and EXPT2 showed that values of f increases over the vegetated bed relative to the gravel bed, with f values approximately constant over each of the bed region (Figure 146 and 147). The f values calculated for each panel indicated f to be greater in EXPT1 relative to EXPT2. Generally, the friction factor increases towards the vegetated region from the gravel region.

29) The modelled velocity and shear stress distribution agree with the experimental data. The root mean square of the difference between the experimental results and numerical model results was estimated to be within 8% for both EXPT1 and EXPT2. Such difference is within the limits observed by Jesson et al., (2013), Tang et al., (2011), Omran and Knight, (2006). The good agreement between the experimental and modelled data suggests the model as an appropriate tool for vegetated flow simulations for river management and flood control.

7.3 Recommendations for Future Work

1) The current research has a great potential for further investigation of the frequency of waving motion of the flexible vegetation stems in EXPT1, this will provide additional information about the biomechanical structure of the vegetation for model development.

2) In natural rivers, aquatic vegetation in many cases re-establishes spatial distribution of their morphology due to growth (height, size, etc.). The knowledge of the morphology and dynamic processes is therefore necessary for predicting the impact of vegetation

growth on the shear and transport processes, a much higher vegetation height relative to the one for this research is required to investigate this phenomenon.

3) The channel bed roughness can be reconfigured to investigate the absolute effect of the vegetation types currently used in this research in comparison to the relative and interactive effects examined in the current research.
4) The implication of the current investigated flow for scalar transfer can further be examined through the introduction and distribution of sediment into the flow.
5) A method for direct measurement of the shear stress over submerged vegetated bed is required. Estimation of shear based on the region of high Reynolds stress as used in this research may neglect some important variables introduced to the flow due to vegetation characteristic (e.g. vegetation height).
6) The SKM panel distribution in accordance with the variation of the secondary flow term Γ can further be investigated.

References

ABRIL, B. & KNIGHT, D. 2004. Stage-discharge prediction for rives in flood applying a depth-averaged model. *Journal of Hydraulic Engineering,* 42**,** 616–629.

ADRIAN, R. J. 1991. Particle imaging techniques for experimental fluid mechanics. *Annual Rev. Fluid Mechanics,* Vol 23**,** 261-305.

AFZALIMEHR, H. & DEY, S. 2009. Influence of bank vegetation and gravel bed on velocity and Reynolds stress distributions. *International Journal of Sediment Research,* 24**,** 236-246.

ANDERSON, J. 1995. Introduction to Computational Fluid Dynamics. *McGraw Hill,* Edition 6.

ARCEMENT, G. J. & SCHNEIDER, V. R. 1984. Guide for selecting Manning's roughness coefficients for natural channels and flood plains. *United States Geological Survey Water-supply Paper 2339 Metric Version***,** 1-67.

BOXALL, J. B. & GUYMER, I. 2007. Longitudinal mixing in meandering channels: New experimental data set and verification of a predictive technique. *Water Resource. Res,* 41**,** 341-354.

BRACA, G. 2008. Stage-discharge relationships in open channels: Practices and problems *Agency for Environmental Protection and Technical Services, Rome, Italy* 1-32.

BUFFING-BELANGER, T. & ROY, A. G. 2005. 1 min in the life of a river: Selecting the optimal record length for the measurement of turbulence in fluvial boundary layers *Geomorph.,,* 68**,** 77-94.

CAROLLO, F. G., FERRO, V. & TERMINI, D. 2005. Analyzing turbulence intensity in gravel bed channels. *Journal of Hydraulic Engineering,* 131**,** 1050-1061.

CEA, L., PUERTAS, J. & PENA, L. 2007. Velocity measurements on highly turbulent free surface flow using ADV. *Experiments in Fluids* 42**,** 333-348.

CHANSON, H., TAKEUCHI, M. & TREVETHAN, M. 2007. High-frequency suspended sediment flux measurements in a small estuary. *6th International Conference on Multiphase Flow, ICMF 2007, Leipzig, Germany*.

CHENG, N.-S., NGUYEN, H. T., TAN, S. K. & SHAO, S. 2012. Scaling of velocity profiles for depth-limited open channel flows over simulated rigid vegetation. *Journal of Hydraulic Engineering,* 138**,** 673-683.

CHOW, V. T. 1959. Open-Channel Hydraulics. *McGraw-Hill Singapore*.

CHU, C. R., PARLANGE, M. B., KATUL, G. G. & ALBERTSON, J. D. 1996. Probability density functions of turbulent velocity and temperature surface layer. *Water Resources Research,* 32**,** 1681-1688.

DANIEL, E., DOMBROSKI & JOHN, P. C. 2007. The accuracy of acoustic Doppler velocimetry measurements in turbulent boundary layer flows over a smooth bed. *Limnol. Oceanogr.: Methods,* 5**,** 23-33.

DAVIDSON, P. A. 2004. Turbulence - an introduction for scientists and engineers. *Oxford University Press*.

ELDER, J. W. 1954. The dispersion of marked fluid in turbulent shear flow. *Cavendish Laboratory, University of Cambridge***,** 544-560.

FINNIGAN, J. 2000. Turbulence in plant canopies. *Journal of Fluid Mechanics,* 32**,** 519-571.

GHISALBERTI, M. 2009. Obstructed Shear Flows: similarities across system and scales. *J. Fluid Mech,* 641**,** 51-61.

GHISALBERTI, M. & NEPF, H. 2006. The structure of the shear layer over rigid and flexible canopies. *Environmental Fluid Mechanics,* 6**,** 527-551.

GHISALBERTI, M. & NEPF, H. M. 2004. The limited growth of vegetated shear layers. *Water Resource. Res,* 40**,** 1-12.

GHISALBERTI, M. & NEPF, H. 2002. Mixing layers and coherent structures in vegetated aquatic flow. *Journal of Geophysical Research-Earth Surface,* 107**,** 527-551.

GORING, D. G. & NIKORA, V. I. 2002. Despiking acoustic Doppler velocimeter data. *Journal of Hydraulic Engineering,* 128**,** 117-126.

GUO, J. & JULIEN, P. 2005. Shear Stress in Smooth Rectangular Open-Channel Flows. *journal of Hydraulic Engineering,* 131**,** 30-37.

HA, H. K., MAA, J. P.-Y., SHAO, Y. Y. & HOLLAND, C. W. 2009. Using ADV backscatter strength for measuring suspended cohesive sediment concentration. *Continental Shelf Research,* 29**,** 1310–1316.

HARDY, J. R., BEST, L. J., LANE, N. S. & CARBONNEAU, E. P. 2009. Coherent flow structures in a depth limited flow over a gravel surface: The role of near bed turbulence and influence of Reynolds number. *Journal of Geophysical Research,* 114**,** 1-18.

HAYWOOD, L. 1996. Airline Turbulence: Staying Safe in the Air. *dspace.mit.edu*.

HINZE, J. O. 1975. Turbulence. *McGraw-Hill series in mechanical engineering*.

HOFLAND, B. & BATTJES, J. 2006. Probability density of instantaneous drag forces and shear stresses on a bed. *Journal of Hydraulic Engineering,* 132**,** 1169-1175.

HWANG, L. & LAURSEN, E. M. 1963. Shear measurements technique for rough surfaces. *Journal of Hydraulic Engineering,* 89**,** 19-37.

IGARASHI, T. 1984. Characteristics of the flow around two circular cylinders. *Bull JSME,* 27**,** 2380-2387.

IKEDA, S., M., K., K. & OHTA 1995. Flow over flexible vegetation and 3-D structure of organized vortex associated with honami. *Journal of Hydraulic, Coastal and Environmental Enginerring,* 515**,** 33-43.

IKEDA, S., OHTA, K. & HASEGAWA, H. 1994. Instability –induced horizontal vortices in shallow open channel flows with an inflexion point in skewed velocity profile. *Journal of Hydroscience and Hydraulic Engineering,* Vol.12**,** 69-84.

ISHIGAKI, T., MUTO, Y. & SHIONO, K. 2010. Flow structure and resistance in compound open channel. *Nagare,* 29**,** 177-186.

JACKSON, J. L., WEBSTER, D. R., RAHMAN, S. & WEISSBURG, M. J. 2007. Bed-roughness effects on boundary-layer turbulence and consequences for odor-tracking behavior of blue crabs (Callinectes sapidus). *Limnol. Oceanogr,* 52**,** 1883–1897.

JAMES, C. S., GOLDBECK, U. K., PATINI, A. & JORDANAVOA, A. A. 2008. Influence of foliage on flow resistance of emergent vegetation *Journal of Hydraulic Engineering,* 46**,** 536-542.

JARVELA, J. 2002. Flow resistance of flexible and stiff vegetation: a flume study with natural plants. *Journal of Hydrology* 269**,** 44–54.

JESSON, M., STERLING, M. & BRIDGEMAN, J. 2010. Turbulent structures in heterogenous channels and their effects on conyeyance. *First IAHR European Div. Congress., International Association for Hydro-Environment Engineering and Research (IAHR), Madrid, Spain*.

JESSON, M., STERLING, M. & BRIGDEMAN, J. 2013. Modelling flow in an open channel with heterogeneous bed roughness. *Journal of Hydraulic Engineering,* 139**,** 195-204.

JESSON., M. 2011. The effect of heterogeneous roughness on conveyance capacity and application of the Shiono-Knight Method Method. *PhD, University of Birmingham*.

JESSON., M., STERLING M. & BRIDGEMAN, J. 2012. An experimental study of turbulence in a heterogeneous channel. *Water Management Proceedings of the Institution of Civil Engineers,* 166**,** 16-26.

JIMENEZ, J. 2004. Turbulent flows over rough walls. *Fluid Mech,* 36**,** 173-96.

KAIMAL, J. C. & FINNIGAN, J. J. 1994. Atmospheric Boundary Layer Flow, . *Oxford University Press*.

KNIGHT, D. W., MCGAHEY, C., LAMB, R. & SAMUELS, P. G. 2010. Practical Channel Hydraulics. *London, CRC Press/Balkena, Taylor & Francis Group*.

KNIGHT, D., TANG, X., STERLING, M., SHIONO, K. & MCGAHEY, C. 2010a. Solving open channel flow problems with a simple lateral distribution model. *In Riverflow 2010, Proceedings of Riverflow 2010***,** 41-48.

KNIGHT, D. W., AYA, S., IKEDA, S., NEZU, I. & SHIONO, K. 2009. Flow structure in flow and sediment transport in compound channels,. *IAHR Monograph. IAHR Spain.*

KNIGHT, D. W., OMRAN, M. & TANG, X. 2007. Modeling depth-averaged velocity and boundary shear in trapezoidal channels with secondary flows. *Journal of Hydraulic Engineering, ,* 133**,** 39-47.

KNIGHT, D. W. & OMRAN, M. 2004. Boundary conditions between panels in depth-averaged flow models revisited. *Proc. 2nd Int. Symp,on River flow, IAHR, Naples, Italy, Jun., ,* 473-483.

KNIGHT, D. W. & ABRIL, B. 1996. Refined calibration of a depth-averaged model for turbulent flow in a compound channel. *Proceedings of the Institution of Civil Engineers, Water, Maritime and Energy Division,,* 118 (3)**,** 151-159.

KNIGHT, D. W. & DEMETRIOUS, J. D. 1983. Floodplain and main channel flow interaction. *Journal of Hydraulic Engineering,* 109**,** 1073-1092.

KOUWEN, N. & UNNY, T. E. 1980. Flexible roughness in open channels. *Journal of Hydraulic Engineering-Asce,* 99**,** 713-727,.

LACEY, R. W. J. & ROY, A. G. 2008. Fine-scale characterization of the turbulent shear layer of an instream pebble cluster. *Journal of Hydraulic Engineering,* 137**,** 925-926.

LANE, S. N., BIRON, P. M., BRADBROOK, K. F., BUTLER, J. B., CHANDLER, J. H., CROWELL, M. D., MCLELLAND, S. J., RICHARDS, K. S. & ROY, A. G. 1998. Three-Dimensional measurement of river channel flow processes using acoustic Doppler velocimetry. *Earth Surface Processes and Landforms,* 23**,** 1247-1267

LANE, T., SHARMAN, R. D., TRIER, S. B., FOVELL, R. G. & WILLIAMS, J. K. 2012. Recent advances in the understanding of near-cloud turbulence. *Advances in numerical modeling and new observations***,** 499-515.

LEONARD, L. & LUTHER, M. 1995. Flow Hydrodynamics in Tidal Marsh Canopies. *Lomnol.Oceanography,* 40**,** 1474-1484.

LIU, D., DIPLAS, P., FAIRBANKS, J. D. & HODGES, C. C. 2008. An experimental study of flow through rigid vegetation. *JOURNAL OF GEOPHYSICAL RESEARCH,* 113**,** 1-16.

LOHRMANN, A., CABRERA, R. & KRAUS, N. C. 1994. Acoustic Doppler velocimeter (ADV) for Laboratory Use. Fundamentals and Advancements in Hydraulic Measurements and Experimentation. *Buffalo, New York. ASCE***,** 351-365.

LOPEZ, F. & GARCIA, M. 1998. Open-channel flow through simulated vegetation: suspended sediment transport modelling. *Water Resour. Res,* 34**,** 2341-2352.

LU, S. S. & WILLMARTH, W. W. 1973. Measurements of the structure of the Reynolds Stress in a Turbulent Boundary Layer. *J. Fluid Mech,* 60**,** 481-511.

LUHAR, M., ROMINGER, J. & NEPF, H. 2008. Interaction between flow, transport and vegetation spatial structure. *Environmental Fluid Mechanics,* 8**,** 423-439.

MANES, C., POKRAJAC, D., MCEWAN, I. & NIKORA, V. 2009. Turbulence structure of open channel flows over permeable and impermeable beds: A comparative study. *Physics of Fluids,* 21**,** 125109(1-12).

MCCONVILLE, A. C. 2008. The physical simulation of thunderstorm downbursts.

MCLELLAND, S. J., ASHWORTH, P. J., BEST, J. L. & LIVESEY, J. R. 1999. Turbulence and secondary flow over sediment stripes in weakly bimodal bed material. *Journal of Hydraulic Engineering,* 125**,** 463-473.

MCLELLAND, S. J. & NICHOLAS, A. P. 2000. A new method for evaluating errors in high frequency ADV measurements. . *Hydrological processes.,* 14**,** 351-366.

MING, J. 1995. Boundary shear stress measurements by two tubes. *Journal of Hydraulic Research,* 33**,** 385-395.

MORVAN, H., KNIGHT, D., WRIGHT, N., TANG, X. & CROSSLEY, A. 2008. The concept of roughness in fluvial hydraulics and its formulation in 1D, 2D and 2D Numerical Simulation Models. *Journal of Hydraulic Research,* 46**,** 191-208.

NAKAGAWA, H., NEZU, I. & UEDA, H. 1975. Turbulence of Open channel flow over smooth and rough beds. *Proceedings of JSCE,* 241**,** 155-168.

NAOT, D. & RODI, W. 1981. Calculation of secondary currents in channel flow. *ASCE, JHydraulic s Div,* 108**,** 948–68.

NEPF, H. M. 2012. Hydrodynamics of vegetated channels. *Journal of Hydraulic Research,* 50**,** 262-279.

NEPF, H. & GHISALBERTI, M. 2008. Flow and transport in channels with submerged vegetation. . *Acta Geophysical,* 56**,** 753-777.

NEPF, H. M. 2004. Vegetated flow dynamics. *Coastal and Estuarine Studies,* 59**,** 137-163.

NEPF, H. M. & VIVONI, E. R. 2000. Flow structure in depth-limited, vegetated flow. *Journal of Geophysical Research,* 105**,** 28,547-28,557.

NEZU, I. & SANJOU, M. 2008. Turburence structure and coherent motion in vegetated canopy open-channel flows. *Journal of Hydro-Environment Research,* 2**,** 62-90.

NEZU, I., SANJOU, M. & OKAMOTO, T. 2006. *Turbulent structure and dispersive properties in vegetated canopy open-channel flows*.

NEZU, I. & ONITSUKA, K. 2001. Turbulent structures in partly vegetated open-channel flows with LDA and PIV measurements. *Journal of Hydraulic Research,* 39**,** 629-642.

NEZU, I. & NAKAGAWA, H. 1993. Turbulence in open-channel flows,. *Rotterdam, A.A. Balkema.*

NEZU, I., TOMINAGA, A. & NAKAGAWA, H. 1993. Field measurements of secondary currents in straight rivers. *Journal of Hydraulic Engineering-Asce,* 119**,** 598--614.

NEZU, I. & RODI, W. 1986. Open channel measurements with a Laser Doppler Anemometer. *Journal of Hydraulic Engineering,* 112**,** 335-355.

NEZU, I. & NAKAGAWA, H. 1984. Cellular secondary currents in straight conduit. *Journal of Hydraulic Engineering.,* 110, 173-193.

NEZU, I. 1977. Turbulence intensities in open-channel flows. *Journal of JSCE,* 261**,** 67-76.

NIKORA, N. & NIKORA, V. 2010. Flow penetration into the canopy of the submerged vegetation: definitions and quantitative estimates. *River Flow 2010 - Dittrich, Koll, Aberle & Geisenhainer***,** 438-444.

NIKORA, V. 2009. Hydrodynamics of aquatic ecosystems: an interface between ecology, biomechanics and enviromental fluid mechanics. *River Research and Applications,* 26**,** 367-384.

NIKORA, V. I., GORING, D. G., MCEWAN, I. & GRIFFITHS, G. 2001. Spatially-averaged open-channel flow over a rough bed. *Hydraulic Engineering,* 127**,** 123-133.

NIKORA, V. I. & GORING, D. G. 1998. ADV Measurements of turbulence: can we improve their interpretation. *Journal of Hydraulic Engineering,* 124**,** 630-634.

NIKURADSE, J. 1933. Law of Flow in Rough Pipes. *available in http://ntrs.nasa.gov/archive/nasa/casi.ntrs.nasa.gov/19930093938_1993093938.pdf*.

NORTEK 2004. Vectrino Velocimeter User Guide. *Nortek AS, Vangkroken 2, NO-1351 RUD, Norway*.

NOVAK, B. S., WARLAND, J. S., ORCHANSKY, A. L., KETLER, R. & GREEN, S. 2000. Wind Turnnel and Field Measurements of Turbulent Flow in Forests. Part 1. *Boundary Layer Meterology,* 95**,** 457-497.

OKAMOTO, T. & NEZU, I. 2009. Turbulence Structure and Monami Phenomena in Flexible Vegetated Open Channel Flows. *Journal of Hydraulic Engineering,* 47**,** 798-810.

OMRAN, M. & KNIGHT, D. W. 2006. Modelling the Distribution of Boundary Shear Stress in Open Channel Flows. *FERREIRA, ALVES, LEAL & CARDOSO (eds.) River Flow 2006. London: Taylor & Francis Group*.

OMRAN, M. 2005. Modelling stage-discharge curves, velocity and boundary shear stress distributions in natural and artificial channels using a depth-averaged approach. *PhD, University of Birmingham.*

PELTIER, Y., PROUST, S., RIVIERE, N., PAQUIER, A. & SHIONO, K. 2013. Turbulent flows in straight compound open-channel with a transverse embankment on the floodplain. *Journal of Hydraulic Research,* 0022-1686. DOI: 10.1080/00221686.2013.796499.

PIV 2009. User Manual and Quick Start Guide. *The TechnoCentre, Puma Way Coventry*.

PRANDTL, L. 1952. Essentials of fluid dynamics.

RAHMAN, S. & WEBSTER, D. R. 2005. The effect of bed roughness on scalar fluctuations in turbulent boundary layers *Experiments in Fluids,* 38**,** 372–384.

RAMESHWARAN, P. & SHIONO, K. 2007. Quasi two dimensional model for straight overbank flows through emergent vegetation on floodplains. *Journal of Hydraulic Research,* 45**,** 392-315.

RAUPACH, M., FININGAN, J. & BRUNET, Y. 1996. Coherent Eddies and Turbulence in Vegetation Canopies: The Mixing Later Analogy. . *Boundary Layer Meteorology,* 60**,** 375-395.

RAUPACH, M. 1994. Simplified Expressions for Vegetation Roughness Length and Zero-Plane Displacement as Functions of Canopy Height and Area Index. . *Boundary Layer Meteorology,* 71**,** 211-216.

RAUPACH, M. & SHAW, R. 1981. Turbulence In and Above Plant Canopies *Annual Review of Fluid Mechanics,* 13**,** 97-129.

REIDENBACH, M. A., LIMM, M., HONDZO, M. & STACEY, M. T. 2010. Effects of bed roughness on boundary layer mixing and mass flux across the sediment-water interface. *Water Resource. Res,* 46**,** 1-15.

REYNOLDS, O. 1901. An Experimental Investigation of the Circumstances Which Determine Whether the Motion of Water Shall Be Direct or Sinuous, and of the Law of Resistance in Parallel Channels. *Papers on Mechanical and Physical Subjects. Cambridge*.

REYNOLDS, O. 1895. Philos.Trans.R.Soc.London. 186**,** 123-164.

ROUSE, H. 1965. Critical analysis of open channel resistance. *Journal of Hydraulic Engineering,* 91**,** 1-25.

SHAFI, H. S., ANTONIA, R. A. & KROGSTAD, P.-A. 1997. Heat flux measurements in a turbulent boundary layer on a rough wall. *Int J Heat Mass Transfer,* 40**,** 2989–2993.

SCHMIDT, A. R. & YEN, B. C. 2001. Stage-Discharge Relationship in Open Channels. *Proceedings of the 2001 International Symposium on Environmental Hydraulics ISEH and IAHR***,** 1-6.

SHIMIZU, Y. & TSUJIMOTO, T. 1993. Comparison of flood flow structure between compound channel and channel with vegetation zone. *Proceedings of 25th IAHR Congress, Tokyo,* 1 A-3-4**,** 97-104.

SHIONO, K., TAKEDA, M., YANG, K., SUGIHARA, Y. & ISHIGAKI, T. 2012. Modeling of vegetated rivers for inbank and overbank flows. *Proceeding of the International Conference on Fluvial Hydraulics – River Flow 2012,* 1**,** 263-269.

SHIONO, K., ISHIGAKI, T., KAWANAKA, R. & HEATLIE 2009. Influence of one line vegetation on stagedischarge rating curves in compound channel. *33rd IAHR Congress, Water Engineering for a sustainable Environment***,** 1475-1482.

SHIONO, K. & MUTO, Y. 1998. Complex flow mechanisms in compound meandering channels with overbank flow. *Journal of Fluid Mechanics,* 376**,** 221-261.

SHIONO, K. & KNIGHT, D. W. 1991. Turbulent open-channel flows with variable depth across the channel. *J. Fluid Mech,* 222**,** 617-646.

SHIONO, K. & KNIGHT, D. W. 1988. Two dimensional analytical solution for a compound channel. *In: IWASA, Y., TAMAI, N. & WADA, A., eds. 3rd International Symposium on Refined Flow Modelling and Turbulence Measurements, Tokyo. Universal Academy Press,* **,** 503-510.

SHUCKSMITH, J. D., BOXALL, J. B. & GUYMER, I. 2011. Determining longitudinal dispersion coefficients for submerged vegetated flow. *Water Resources Research,* 47**,** 1-13.

SHUCKSMITH, J. D., BOXALL, J. B. & GUYMER, I. 2010. Effects of emergent and submerged natural vegetation on longitudinal mixing in open channel flow. *Water Resource. Res,* 46**,** 1-14.

SHVIDCHENKOA, A. B. & PENDER, G. 2001. Macroturbulent structure of open-channel flow over gravel beds *Water Resource. Res,* 37**,** 709-719.

STERLING, M., BEAMAN, F., MORVAN, H. & WRIGHT, N. 2008. Bed-shear stress characteristics of a simple, prismatic, rectangular channel. *Journal of Engineering Mechanics,* 134**,** 1085-1094.

STERLING, M., BAKER, C. J., BERRY, P. M. & WADE, A. 2003. An experimental investigation of the lodging of wheat. *Agricultural and Forest Meterology,* 119**,** 149-165.

STETZNER, B., RESH, V. H. & ROUX, A. L. 1994. Ecology of the Upper Rhône River: a test of habitat templet theories. *Freshwater Biology,* 31**,** 253-554.

SUNCAN 2012. Introduction to compound channel flow analysis for floodplains. *SunCam online.*

SUN, X., HUANG, T., FU, X., YANG, K. & SHIONO, K. 2013. Application of Shiono and Knight method to compound open channel flow with one-line emergent vegetation. *Advanced Materials Research,* 663**,** 930-935.

SUN, X. & SHIONO, K. 2010. Flow characteristics in vegetated compound channel. *Enviromental Hydraulics***,** 233-239.

SUN, X. & SHIONO, K. 2009. Flow Resistance of One-line emergent vegetation along the floodplain of a compound open channel. *Advances in Water Resources,* 32**,** 430-438.

TANG, X., KNIGHT, D. W. & M., S. 2011. Analytical model for streamwise velocity in vegetated channels. *Engineering and Computational Mechanics,* 164**,** 91-101.

TENNEKES, H. & LUMLEY, J. L. 1972. A first course in turbulence. *The MIT Press Cambridge, Massachusetts, and London, England*.

TSUJIMOTO, T. 1999. Fluvial processes in streams with vegetation. *Journal of Hydraulic Research,* 37**,** 789-803.

VANONI, V., A. 1944. Transportation of suspended sediment by water. *Trans ASCE,* 111**,** 67–133.

VELASCO, D., BATEMAN, A., REDONDO, J. M. & DEMEDINA, V. 2003. An open channel flow experimental and theoretical study of resistance and turbulent characterization over flexible vegetated linings. *Flow Turbulence and Combustion,* 70**,** 69-88.

VERMAAS, D. A., UIJTTEWAAL, W. S. J. & HOITINK1, A. J. F. 2011. Lateral transfer of streamwise momentum caused by a roughness transition across a shallow channel. *WATER RESOURCES RESEARCH,* 47**,** doi:10.1029/2010WR010138.

VERMAAS, D. A., UIJTTEWAAL, W. S. J. & HOITINK, A. J. F. 2010. Lateral transfer of streamwise momentum caused by a roughness transition across a shallow channel. *WATER RESOURCES RESEARCH,* 47**,** 1-12.

VERMAAS, D. A., UIJTTEWAAL, W. S. J. & HOITINK, A. J. F. 2007. Effect of Heterogeneous Bed Roughness on the Conveyance Capacity of Floodplains. *Netherlands Centre for River Studies***,** 34-35.

VOULGARIS, G. & TROWBRIDGE, J. H. 1998. Evaluation of the Acoustic Doppler Velocimeter (ADV) for Turbulence Measurements. *J O U R N A L O F A T M O S P H E R I C A N D O C E A N I C T E C H N O L O G Y,* 15**,** 272-289.

WANG, Z. Q. & CHENG, N.-S. 2006. Time-mean Structure of Secondary Flows in Open Channel with Longitudinal Bedforms. *Advances in Water Resources,* 29**,** 634-1649.

WANG, Z.-Q. & CHENG, N.-S. 2005. Secondary Flows Over Artificial Bed Strips. *Advances in Water Resources,* 28**,** 441-450.

WILSON, C. A. M. E. & HORRITT, M. S. 2002. Measuring the flow resistance of submerged grass. *Hydrological processes.,* 16**,** 2589-2598.

WINANT, C. & BROWAND, F. 1974. Vortex Pairing the Mechanism of Turbulent Mixing-Layer Growth at Moderate Reynolds Number *Journal of Fluid Mechanics,* 63**,** 237-255.

WU, W., SHIELDS JR, F. D., BENNETT, S. J. & WANG, S. S. Y. 2005. A depth-averaged two-dimensional model for flow, sediment transport, and bed topography in curved channels with riparian vegetation. *Water Resources Research,* 41**,** W03015.

YALIN, M. S. 1972. Mechanics of Sediment Transport. *Pergamon Press, Oxford; New York:***,** 290.

YEN, B. C. 2002. Open channel flow resistance. *Journal of Hydraulic Engineering,* 128**,** 20-39.

Appendix A

Appendix A contains the TKE flux indicating the lateral dispersion of the TKE through the flow.

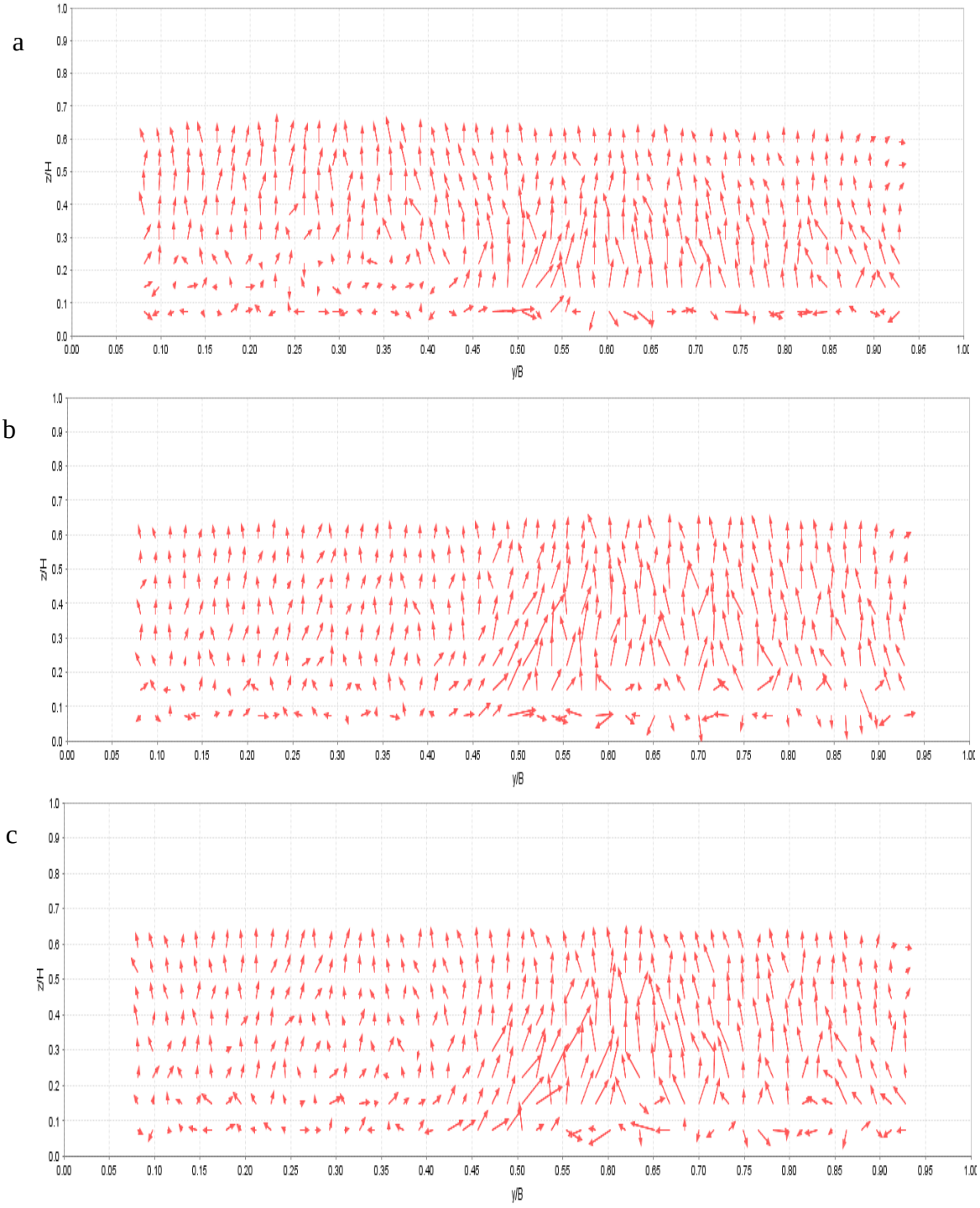

Figure 155: Lateral flux of turbulent kinetic energy (TKE) CRS1 (a) to CS3 (c) EXPT1

a

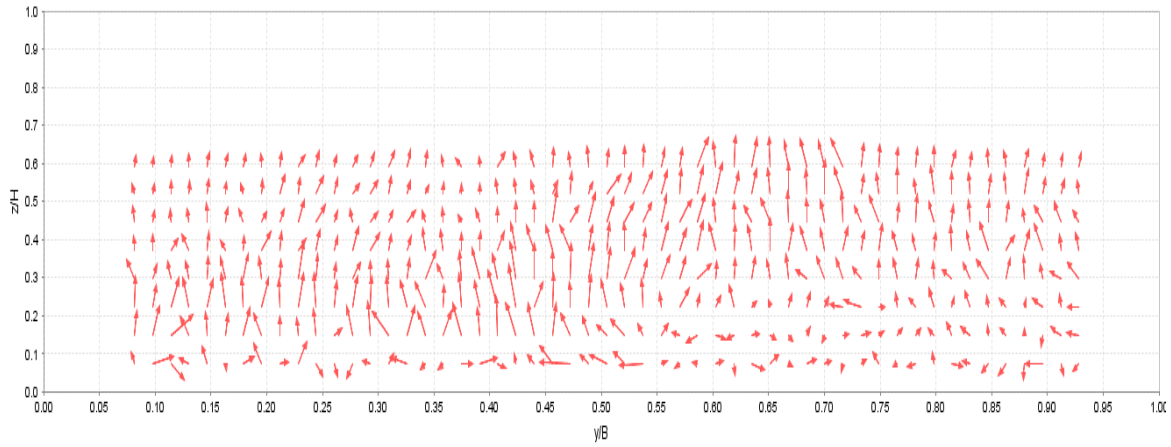

b

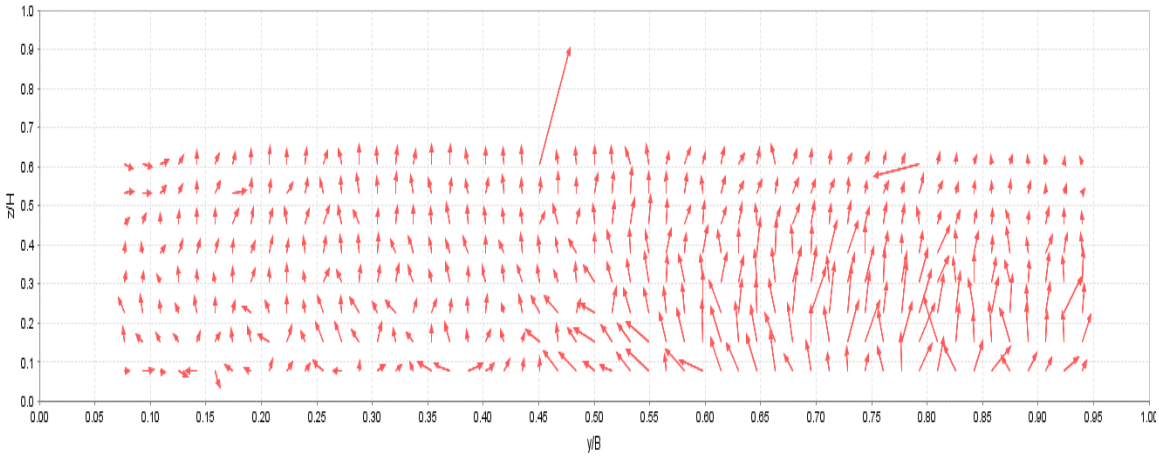

c

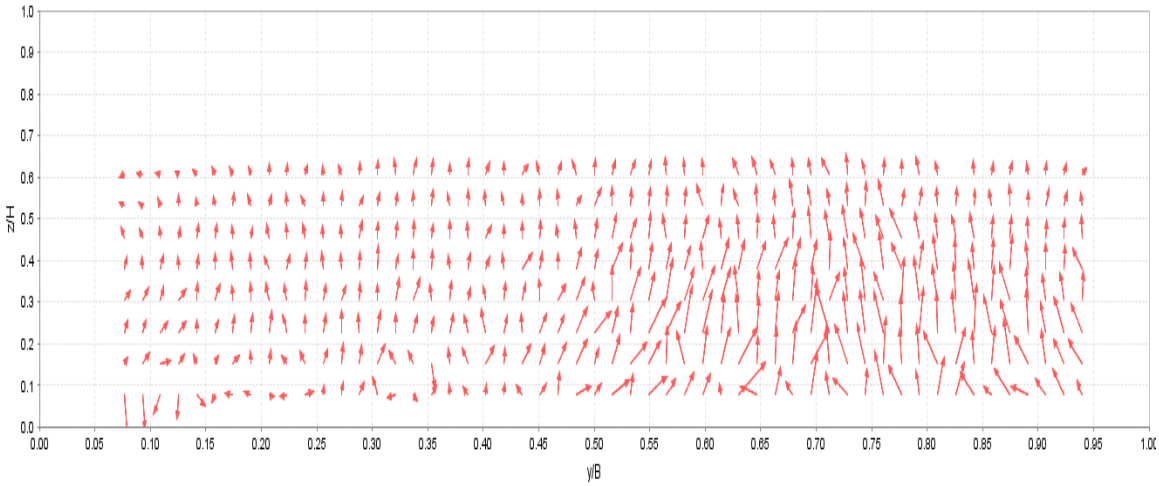

Figure 156: Lateral flux of turbulent kinetic energy (TKE) CRS1 (a) to CS3 (c) EXPT2

Appendix B

This appendix contains the energy spectral distribution at upper region of the flow.

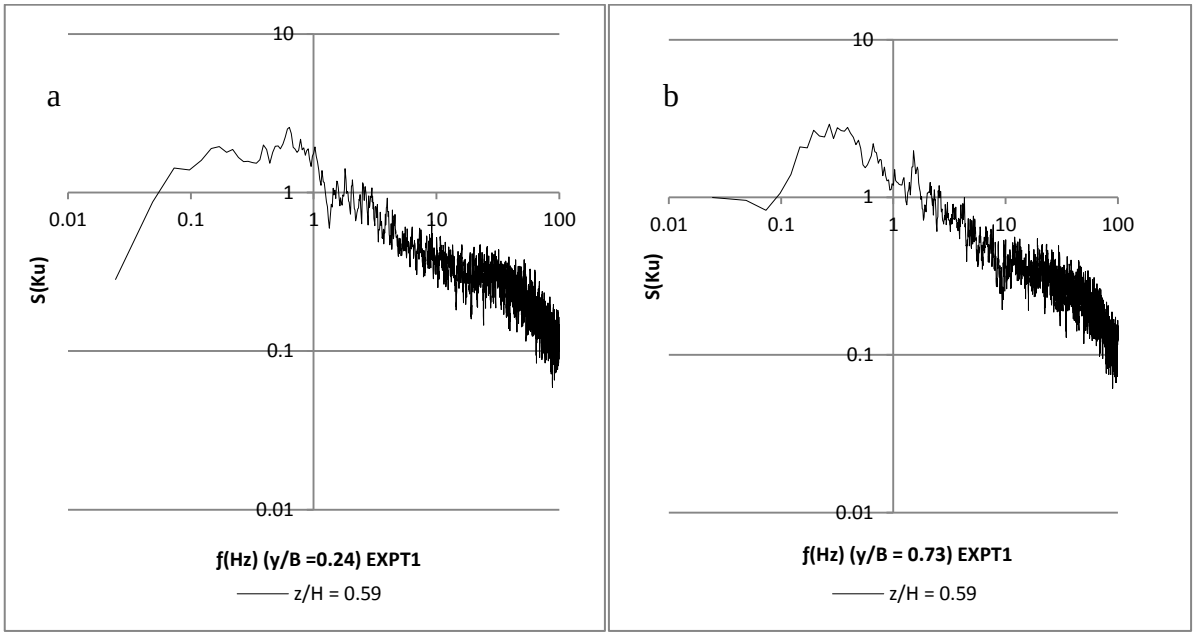

Figure 157: Energy Spectral Distribution at the Upper Region of the Channel ($^{z}/_{H} = 0.59$) at ($^{y}/_{B} = 0.24\ (a), and\ \ ^{y}/_{B} = 0.73\ (b)$) (EXPT1CRS3)

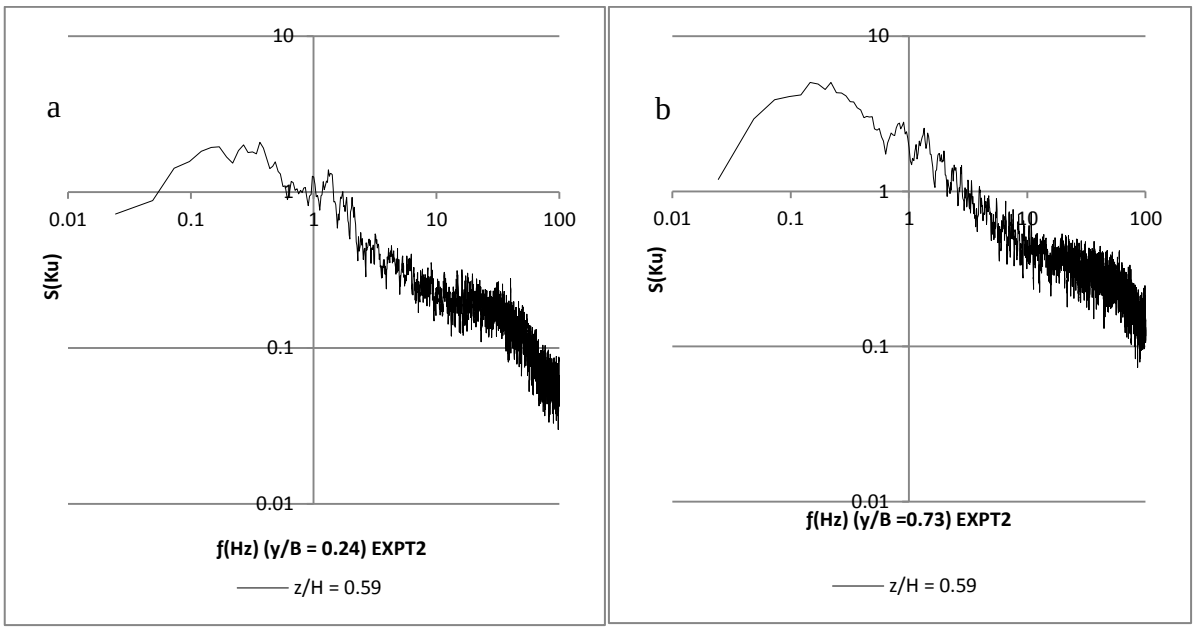

Figure 158: Energy Spectral Distribution at the Upper Region of the Channel ($^{z}/_{H} = 0.59$) at ($^{y}/_{B} = 0.24\ (a), and\ \ ^{y}/_{B} = 0.73\ (b)$) (EXPT1CRS3)

Appendix C

This appendix contains some selected figures from the PIV measurement to complete the presented results in Section 5.5.

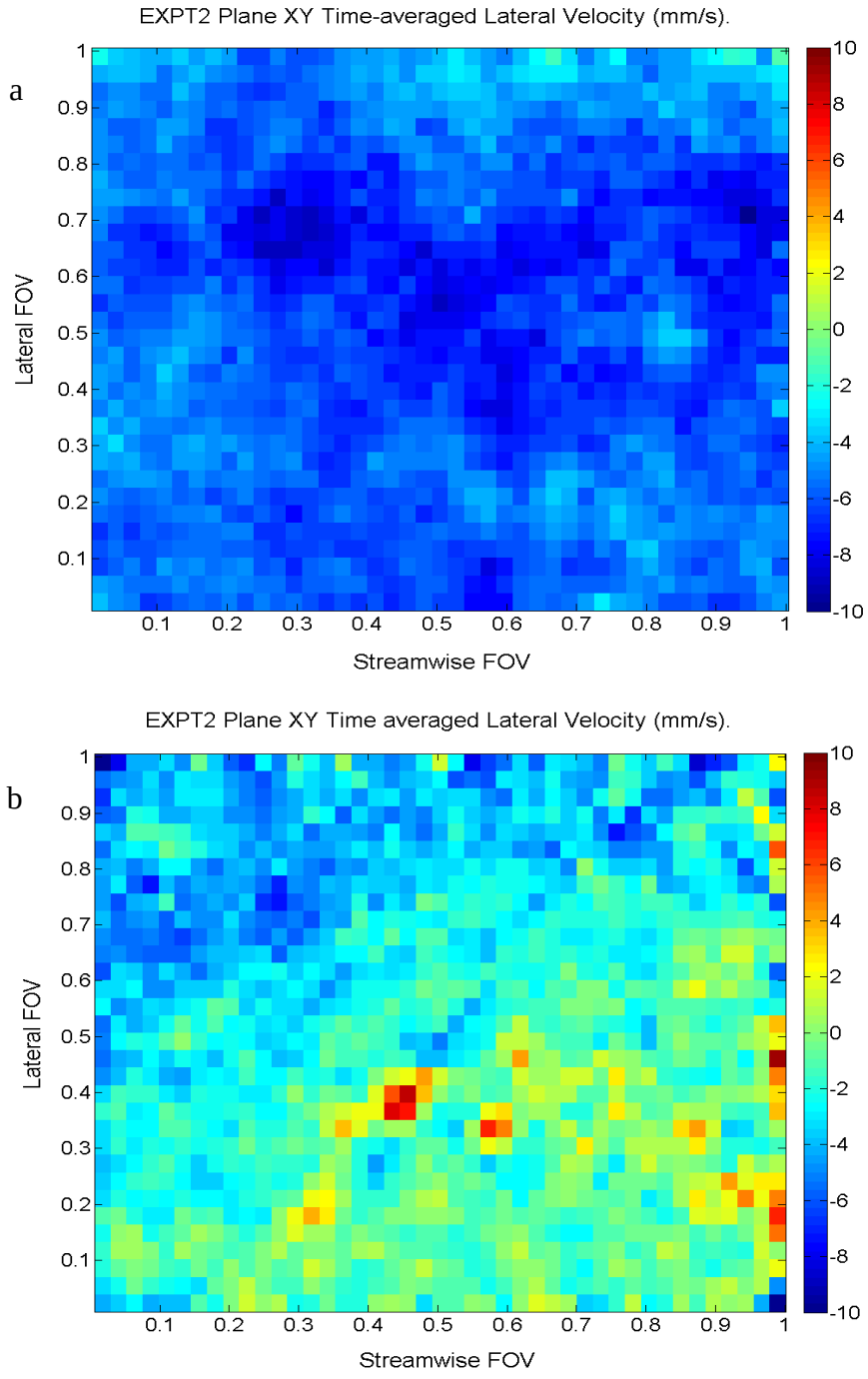

Figure 159: Mean Lateral velocity in *xy* (lateral) plane, upper region $(z/H = 0.75)$ plane (a) and near bed $(z/H = 0.25)$ plane (b)

a

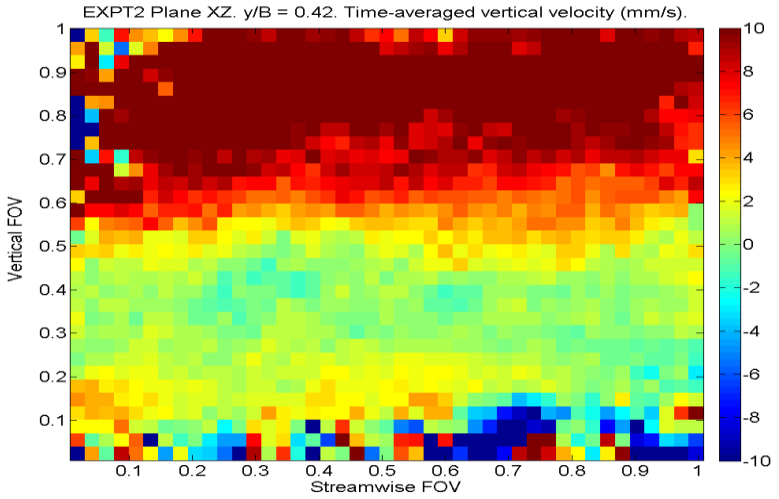

b

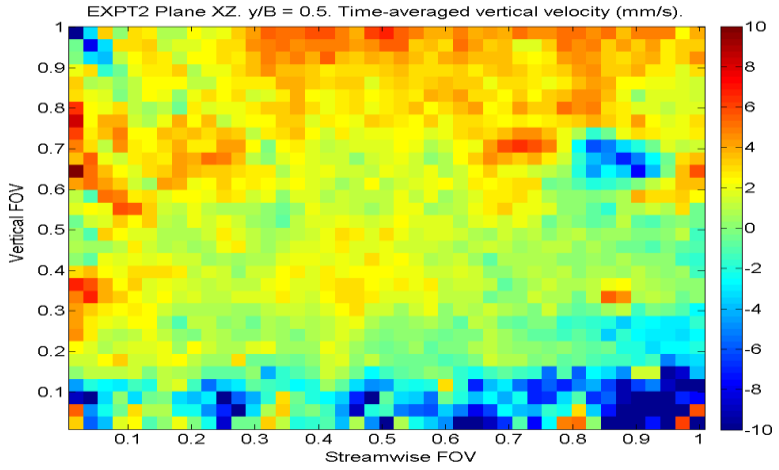

c

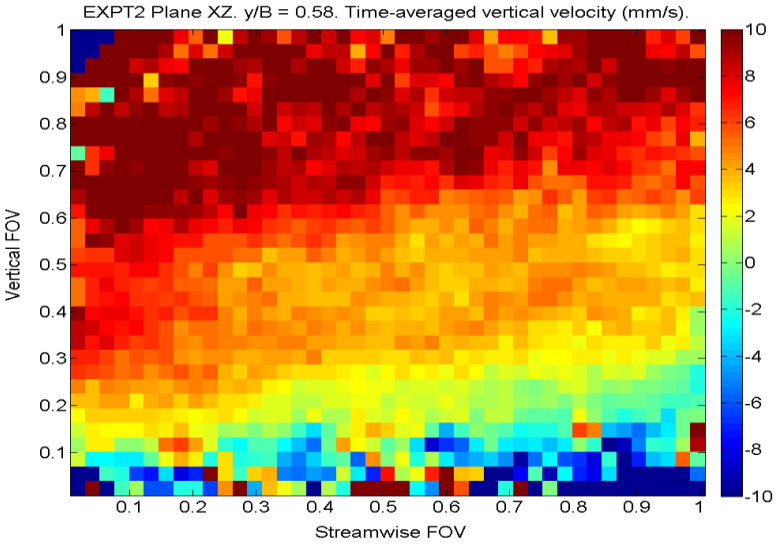

Figure 160: Mean Vertical Velocities in xz (vertical) plane over the gravel region $\left({}^{y}/_{B} = 0.42\right)$ (a), the boundary region $\left({}^{y}/_{B} = 0.50\right)$ (b) and the vegetated region $\left({}^{y}/_{B} = 0.58\right)$(c)

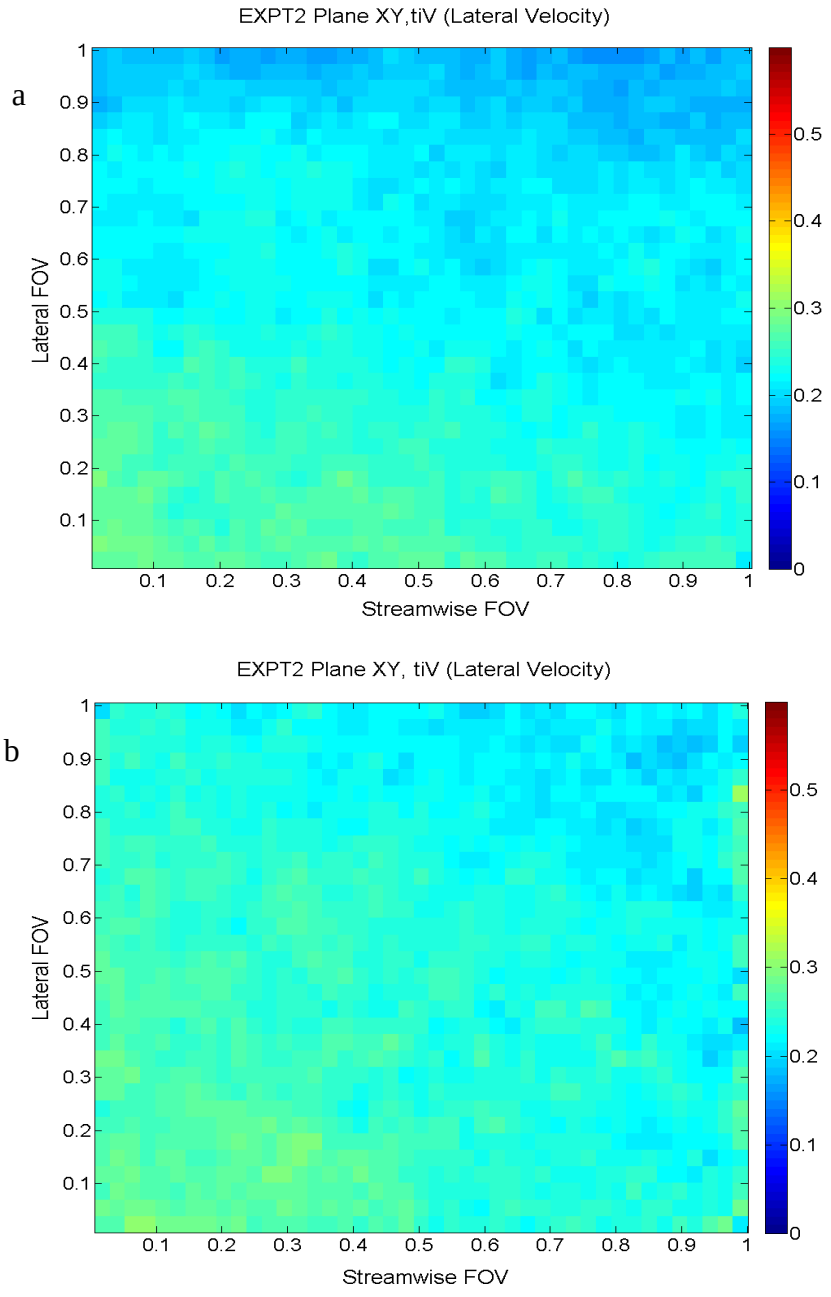

Figure 161: Lateral turbulence intensity in *xy* (lateral) plane, upper region $\left(z/H = 0.75\right)$ plane (a) and near bed $\left(z/H = 0.25\right)$ plane (b)

a

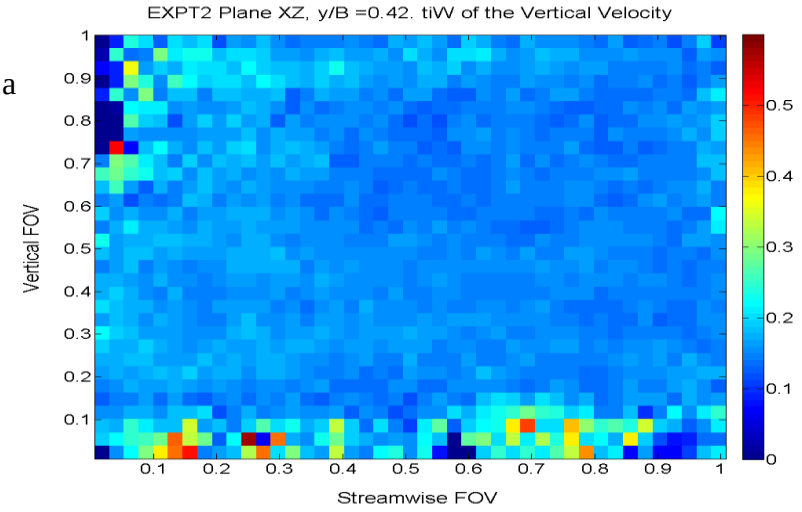

b

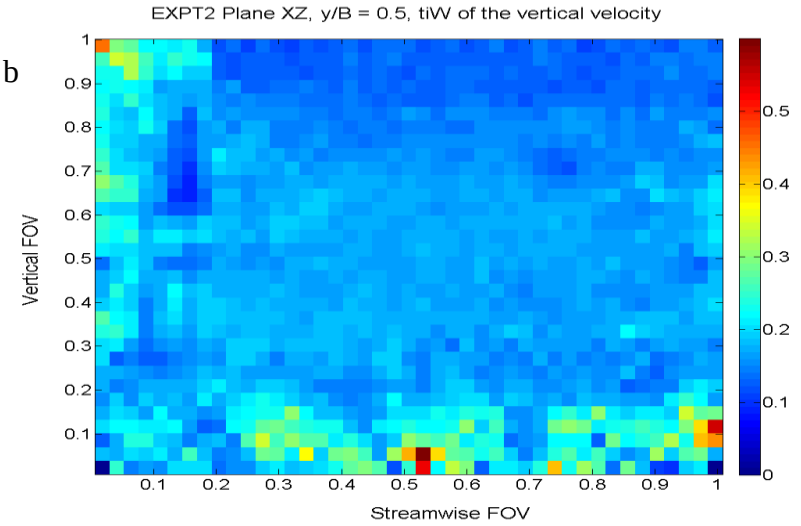

c

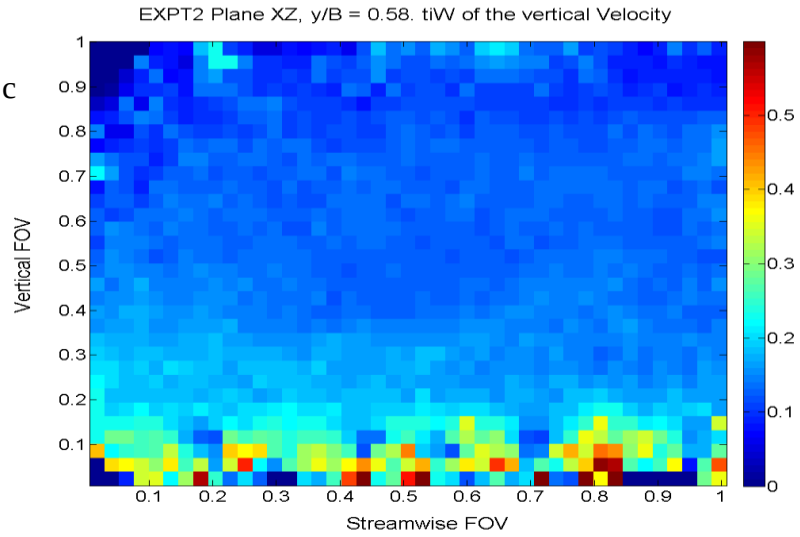

Figure 162: Vertical turbulenty intensities (tiU) in xz (vertical) plane over the gravel region $\left({}^{y}/_{B} = 0.42\right)$ (a), the boundary region $\left({}^{y}/_{B} = 0.50\right)$ (b) and the vegetated region $\left({}^{y}/_{B} = 0.58\right)$(c)

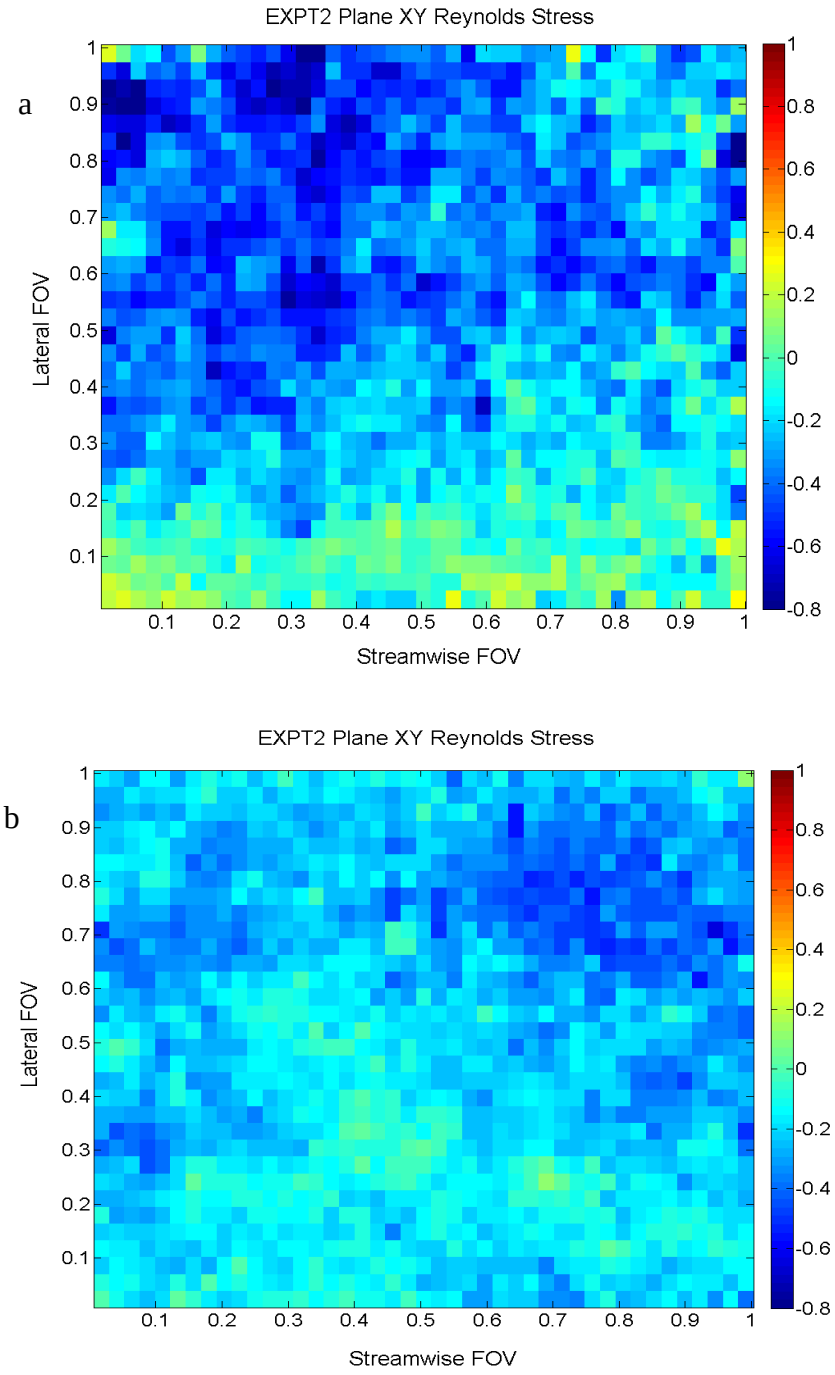

Figure 163: Reynolds stress in xy (lateral) plane, upper region $\left(z/H = 0.75\right)$ plane (a) and near bed $\left(z/H = 0.25\right)$ plane (b)

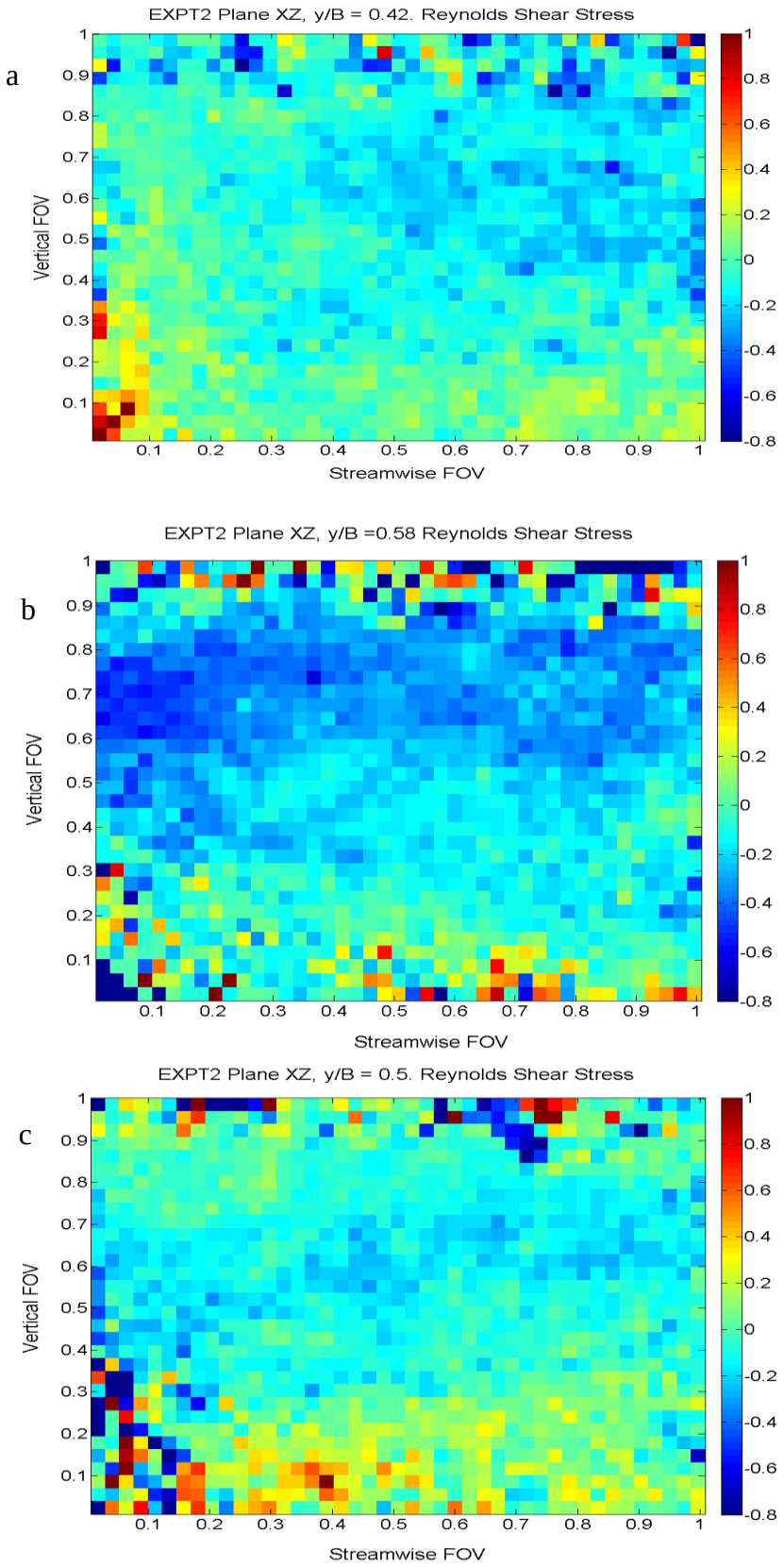

Figure 164 : Reynolds Stress in *xz* (vertical) plane over the gravel region $\left({}^{y}/_{B} = 0.42\right)$ (a), the boundary region $\left({}^{y}/_{B} = 0.50\right)$ (b) and the vegetated region $\left({}^{y}/_{B} = 0.58\right)$(c)

a

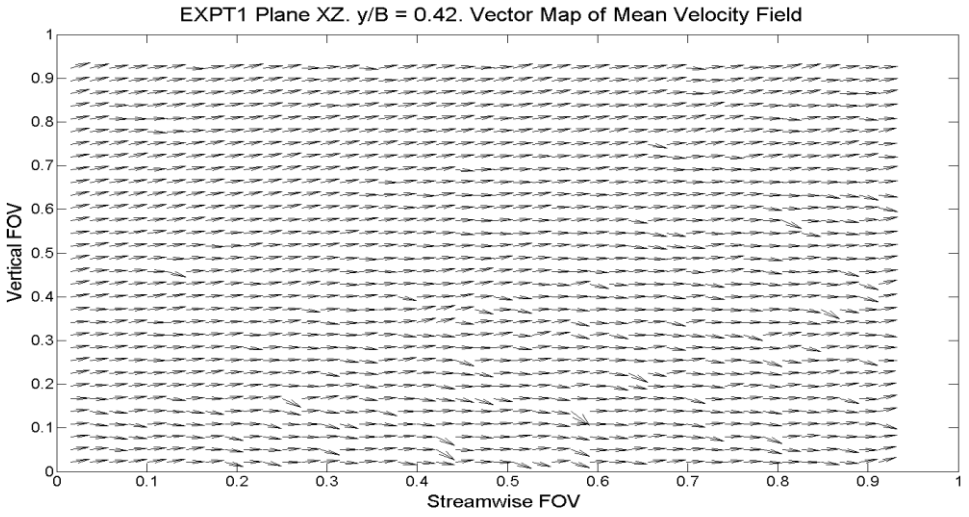

b

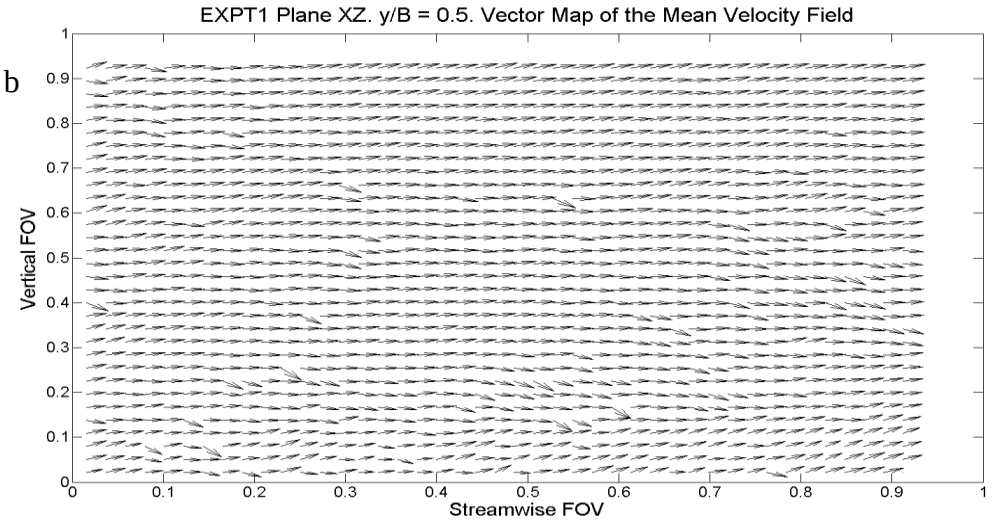

c

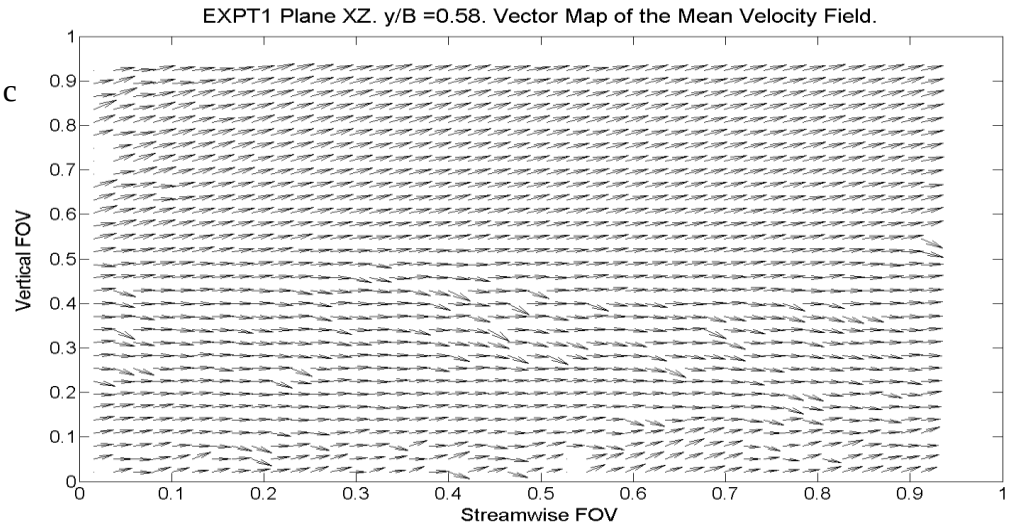

Figure 165: Mean velocity vector plot in *xz* (vertical) plane over the gravel region $\left({}^{y}/_{B} = 0.42\right)$ (a), the boundary region $\left({}^{y}/_{B} = 0.50\right)$ (b) and the vegetated region $\left({}^{y}/_{B} = 0.58\right)$(c) (Higher flow rate $40 l/s$)

Appendix D

Composite Channel Analysis Methods

1. Cox Method

$$n_c = \frac{\sum_1^N (A_N n_N)}{A} \quad (94)$$

2. Lotter Method

$$n_c = \frac{PR^{2/3}}{\sum_1^N \left(\frac{P_N R_N^{5/3}}{n_N} \right)} \quad (95)$$

3. Colebatch Method

$$n_c = \left(\frac{\sum_1^N (A_N n_N^{1.5})}{A} \right)^{2/3} \quad (96)$$

4. Segmented Conveyance Method

$$K_c = \sum_1^N \frac{K_n}{n_N} A_N {R_N}^{2/3} \quad (97)$$

Where n_c = composite Manning's roughness coefficient

A = channel cross-sectional area

n = Manning's roughness coefficient

N = Subscripts of individual subareas of the channel

P = Wetted perimeter

K_c = Channel conveyance

K_n = Coefficient equal to 1.49 (SunCam, 2012)

Appendix E

This appendix contains some ADV results using higher flow rate $(40l/s)$

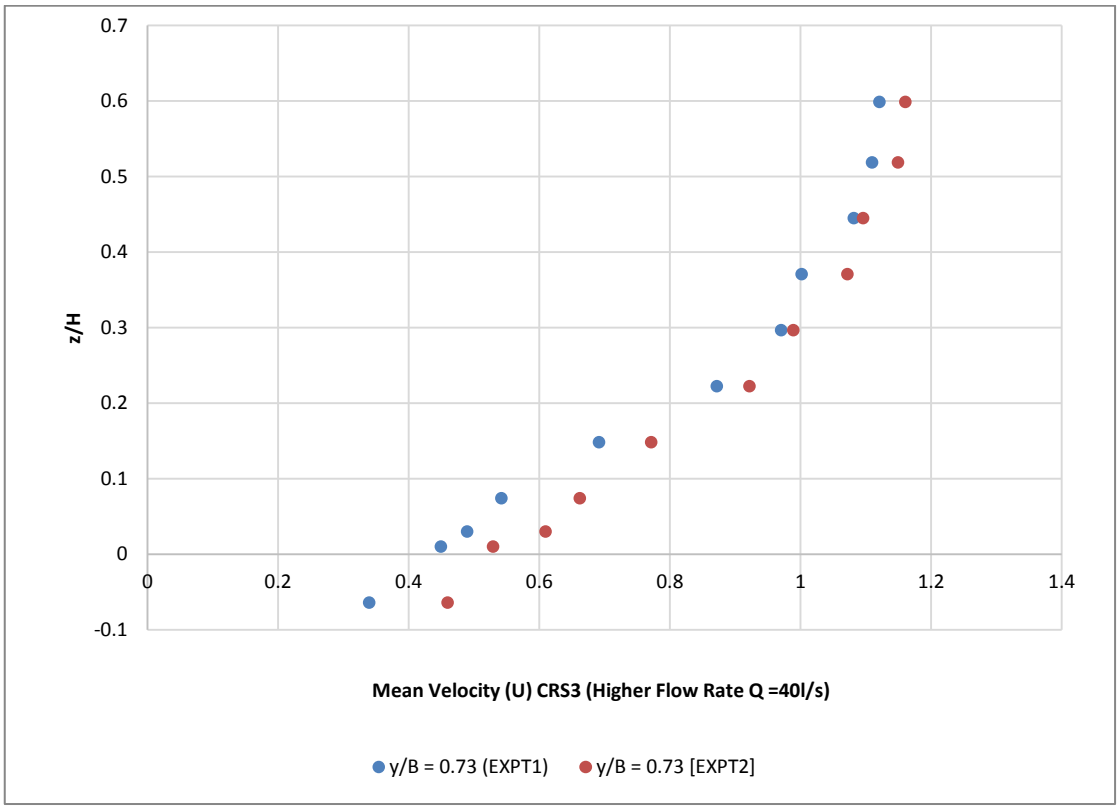

Figure 166: Vertical velocity profiles over vegetated bed with porous layer (EXPT1 and EXPT2), CRS3 (Higher flow rate $40l/s$)

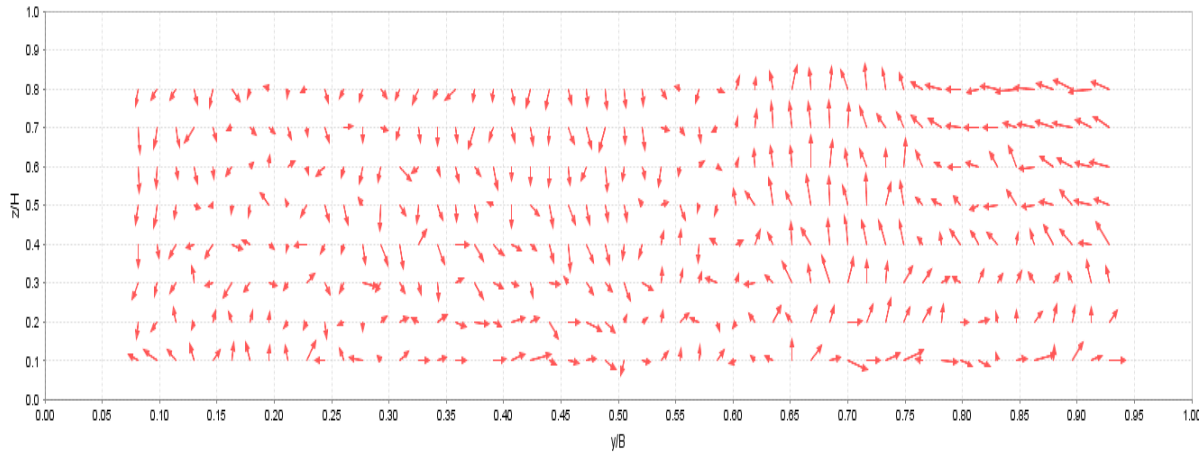

Figure 167: Lateral flow distributions (EXPT1) CRS3 (Higher flow rate $(40l/s)$)

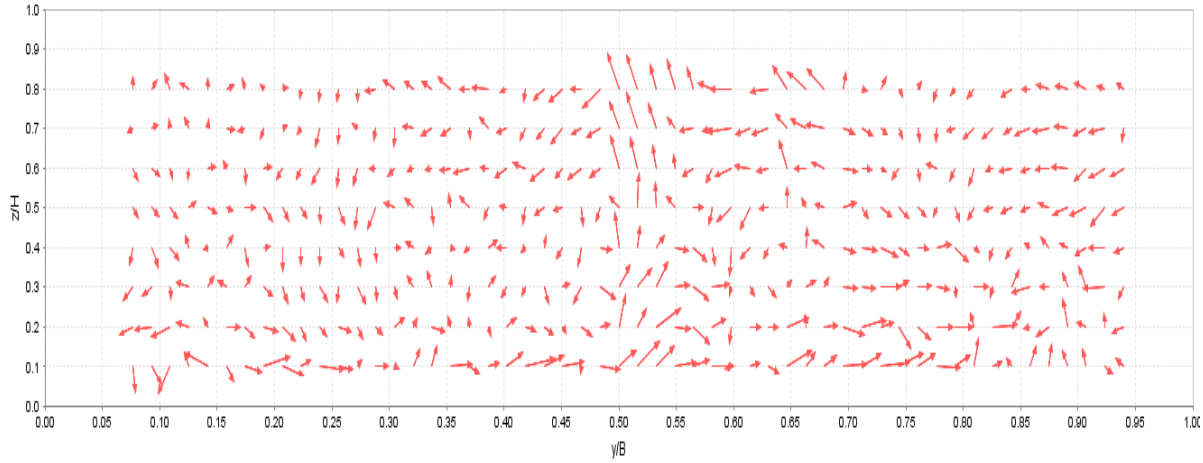

Figure 168: Lateral flow distributions (EXPT2) CRS3 (Higher flow rate $(40l/s)$)

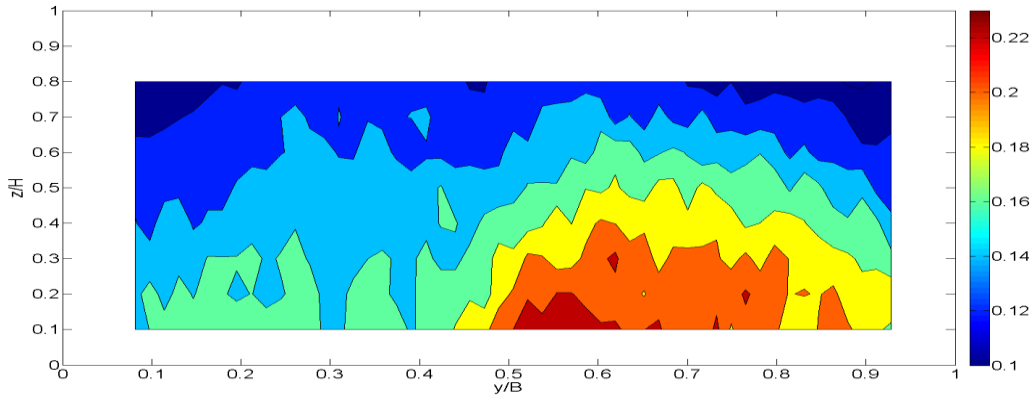

Figure 169: Relative streamwise turbulence intensity, CRS3 (EXPT1) (Higher flow rate $(40l/s)$)

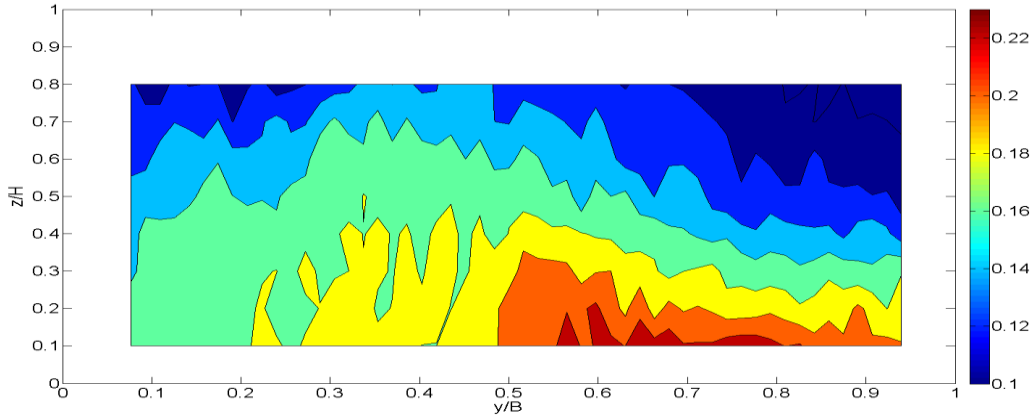

Figure 170: Relative streamwise turbulence intensity, CRS3 (EXPT2) (Higher flow rate $(40l/s)$)

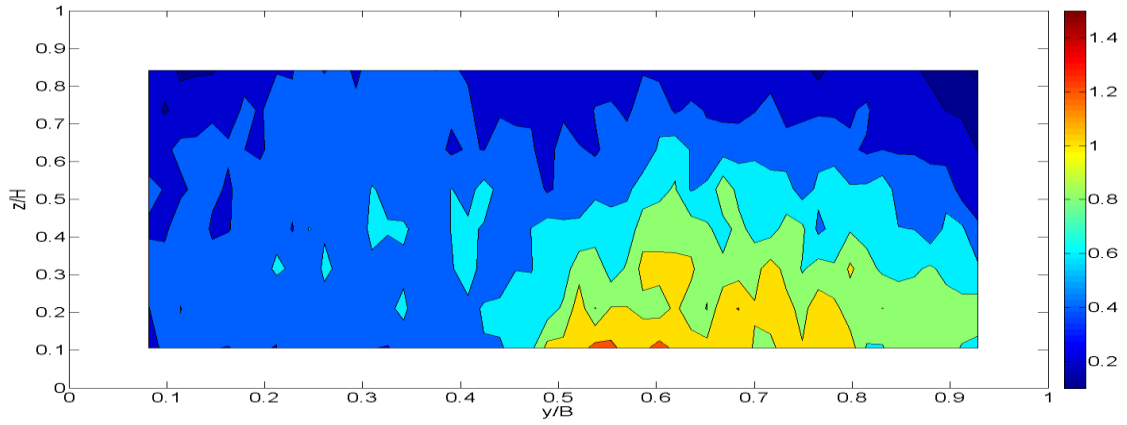

Figure 171: Lateral distribution vertical Reynolds stress; CRS3 (EXPT1) (Higher flow rate $(40l/s)$)

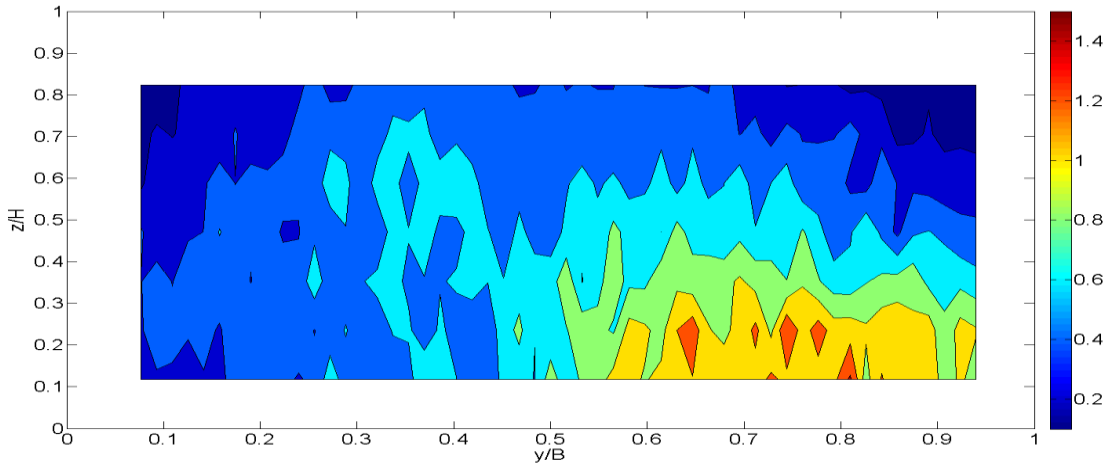

Figure 172: Lateral distribution vertical Reynolds stress; CRS3 (EXPT2) (Higher flow rate $(40l/s)$)

Appendix F

Publications in Conference Proceedings

1) Folorunso, J. Bridgeman and M. Sterling. 2014. Physically and numerically modelling turbulent flow in a patchy vegetated open channel. *Proceeding of the 7th International Conference on Fluvial Hydraulics – River Flow 2014-Schleiss et al. (Eds),* 383-392.
2) Folorunso, M. Sterling and J. Bridgeman. 2013. Shear layer flows over gravel and vegetated beds. *Proceedings of the Hydro 2013 International XVIII Conference on Hydraulics, Water Resources, Coastal and Environmental Engineering, 793-802.*